Engineering Biomimetic Nanoparticles for Biomedical Applications

by

Emine Sumeyra Turali-Emre

A dissertation submitted in partial fulfillment
of the requirements for the degree of
Doctor of Philosophy
(Biomedical Engineering)
in the University of Michigan
2021

Doctoral Committee:

Professor Nicholas A. Kotov, Chair
Associate Professor James Moon
Associate Professor Ariella Shikanov
Assistant Professor J. Scott VanEpps

Emine Sumeyra Turali-Emre

esumeyra@umich.edu

ORCID iD: 0000-0001-8166-0892

Dedication

This dissertation is dedicated to my beloved sons Talha (Sonic) Emre, born at the beginning of my PhD studies, and Taha Emre, born at the end of my PhD studies and the very first day of COVID entered MI.

Acknowledgments

This work would not have been possible without helpful guidance and support from a significant number of individuals. There is no way that I can express my full gratitude to everyone who has touched my life during this journey. Specifically, I would like to thank my research advisor, Prof. Nicholas A. Kotov, for providing incredible support and guidance both in and outside of the research setting. All the encouragement, generosity, creativity, and criticism I received from him has made this work possible. All these years, I learned a lot about balancing life and work, thinking critically, and most importantly, doing science from him. Without his presence and encouragement, I would not be able to accomplish this journey.

I would also like to thank all my committee members. I am grateful for Prof. Scott VanEpps' helpful guidance and insightful feedback during the entire thesis process. He humbly made himself available all the time that I need, even running between emergency room shifts. He was so patient and helpful with all my questions and encouraged me to overcome the challenges. Prof. Ariella Shikanov saw my potential and made me believe in myself. She also showed how significant the presence of female professors is essential in the field. She by herself is one of the biggest reasons I want to stay in academia and guide young individuals as she does. Prof. James Moon's humble guidance and discussions made this journey much easier for me. He was so supportive of all the choices that I made. I am thankful for him to stay behind and encourage me with all the obstacles that I encountered all the time.

I feel lucky to have wonderful friends and their support during my PhD. I am thankful to all previous and current Kotov Lab members; I learned a lot and truly enjoyed having discussions

full of science. Thanks to the diversity of Kotov Lab, I made many friends from all over the world. Particularly, this journey would not be the same without Mashid Chekini, Hee Jeong Jang, Erika Martinez, Gleiciani Queiros Silveira, Yichun Wang, Yue Wang, Elizabeth Wilson. Exclusively, I want to thank Usha Kadiyala, Naomi Ramesar, Minjeong Cha, Ji-Young Kim, John Soukar and all undergraduate students. Usha specifically helped and cheered me up during my qualification exam and writing my thesis. Naomi supported me in and outside the lab. Her friendship, specifically during the downtimes, made me stand up again. Minjeong believed in me starting a completely new project that she is unfamiliar. However, with her help and support, we concluded the project during the quarantine times while I was taking care of two kids at home. Ji-Young Kim showed me that a colleague could become a good friend who can rely on each other. Her friendship made me feel confident during this journey. John Soukar helped with many bacterial studies; made an excellent teammate accomplish a challenging task. I truly enjoyed mentoring all undergraduate students, specifically Brendan Knittle, Shivani Kozaker, Alienna Glenn, and William Brown. Their help in many projects made this work more accessible.

I appreciate administrative and technical support, especially Mary Beth Westin, Maria Steele, and Nadine Wang. They all have been so kind and generous to help me with many aspects of life. Without their support, I could not be full of myself. Additionally, I am grateful to all staff of Michigan Center for Material Characterization, and Microscopy Core. Their help advanced my imaging skills. Furthermore, I am indebted to all funding sources that allowed me to perform my research. Explicitly, BlueSky and scholarship from the Turkish Ministry of Education. With these two funding, I was able to meet many talents that changed my life. Another special thank you to the Center for Education of Women (CEW+) for the financial help on daycare during the pandemic.

I am also thankful for many great campus organizations, Graduate Rackham International (GRIN), Biomedical Engineering Graduate Student Society (BME-GSC), The Graduate Society of Women Engineers (GradSWE). All the members from these student organizations have offered a backbone of support and community throughout my graduate work. I had a chance to serve in many roles in those organizations where I connected to many hardworking and talented people at the campus other than my department and the lab. I would not have enjoyed my time at the U-M as much without a supportive community and many friendships from these organizations. I am also incredibly grateful to Rackham Professional Development Department for their support as well as to Diversity Equity and Inclusion Certificate Program; I attended many workshops that made me grow personally and professionally. And special thanks to the CEW+ Academic Coaching Pilot Program and my mentor Michele Randolf for helping me when I needed help the most. 2020 was not an easy year for anyone but specifically for caregivers. CEW + specifically design this program for caregiver students. I had a chance to join this incredible program during the lockdown where I was far behind putting myself together with a 5-year-old and an infant. With the support from my mentor and colleagues in similar situations, I was able to stand up and put things in order for graduation.

Of course, there are many people outside the lab-made this journey easier and filled it with joy. They are not just friends anymore; they all became family to me. Their support is priceless; I cannot thank you enough. But specifically, I want to express my sincerest gratitude to my friends Naomi, Usha, Minjeong, Ji-Young, Nejla, Elif, Ruhsar, and Ahu for their support during all these years but specifically during the time of quarantines. I do sincerely appreciate all the help and friendship I have received from each one of them.

Last but not least, I am immensely thankful to my family members. My parents, siblings, and grandparents all helped me follow my dreams. Without their encouragement, support and help, I would not have stood here. Special thanks to my mom Gulten Turali and dad, Abdullah Turali, for allowing their little girl to fly with her wings to the other side of the world. From the beginning, their endless support, prayers, and pride made me continue even when I faced obstacles. I am also specifically and incredibly grateful to Ahmet Emre, my partner, husband, classmate, lab mate, soul mate, and many more. Without his support, I would not even think about studying abroad, and this would not happen. His endless support, love, sacrifice are priceless and more than what I would ask. Finally, I am incredibly thankful for my sons Talha *aka* Sonic, and Taha, who constantly sacrificed to make my dreams come true; nothing would be as much fun without them. Their presence lifted me high so that I could fly; even on hard days, they cheered me up and made me stand through.

Preface

This dissertation summarizes research I have conducted over the last five years while working in Professor Nicholas Kotov's laboratory in collaboration with Professor J. Scott VanEpps's lab.

This thesis contains two main parts. Part I includes Chapters 2 and 3, and Part II includes Chapter 4.

Parts of Chapter 1, Chapter 2, and Appendix 1 have been adapted from the work that has been previously published as follows: Kadiyala, U., Turali-Emre, E. S., Bahng, J.H., Kotov, N. A., VanEpps, J. S. Unexpected insights into antibacterial activity of zinc oxide nanoparticles against methicillin resistant Staphylococcus aureus (MRSA). *Nanoscale* **10**, 4927–4939 (2018)

Chapter 3 is modified from the manuscript under final revisions for publication as follows: Turali-Emre, E.S*., Soukar, J*., Kadiyala, U*., Kotov, N. A., VanEpps, J. S., Membrane Dynamics of ZnO Nanoparticles in Methicillin-Resistant *Staphylococcus aureus* And Subsequent Effects on Cell Respiration. (*Equally contributed)

Chapter 4 is a manuscript under final revisions for publication as follows: Turali-Emre, E. S., Emre, A. E., Kadiyala, U., VanEpps, J. S., Kotov, N. A. Self-Organization of Iron Sulfide Nanoparticles into Multi-Compartment Supraparticles as Artificial Viruses for DNA Delivery.

Table of Contents

List of Tables

List of Figures

List of Abbreviations

In Order of Appearance

Nanoparticle ..... NP

Supraparticle ..... SP

Zinc Oxide Nanoparticles ..... ZnO-NPs

Reactive Oxygen Species..... ROS

Uridine Monophosphate..... UMP

Severe Acute Respiratory Syndrome ..... SARS

Deoxyribonucleic Acid ..... DNA

Corona Virus Disease ..... COVID

Ribonucleic Acid ..... RNA

Methicillin-resistant Staphylococcus aureus..... MRSA

Ultra-Violet..... UV

Tryptic Soy Broth ($_G$ Glucose) ..... TSB_G

Optical Density ..... OD

Nanopyramid..... NPY

Nanosphere ..... NSP

Transmission Electron Microscopy ..... TEM

Selected Area Electron Diffraction ..... SAED

Photoluminescence Spectroscopy ..... PL

Fourier transformed infrared spectroscopy ..... FTIR

Nanoparticle Tracking Analysis ..... NTA

Colony Forming Unit ..... CFU

Aminophenyl Fluorescein ..... APF

Dichlorodihydrofluorescein Diacetate ..... H_2DCFDA

Thiobarbituric Acid Reactive Substances ..... TBARS

Malondialdehyde ..... MDA

N-Acetyl Cysteine ..... NAC

Analysis of Variance ..... ANOVA

Gene Set Enrichment Analysis ..... GSEA

Superoxide Dismutase ..... SOD

Uridine Triphosphate ..... UTP

Cytidine Triphosphate ..... CTP

Nicotinamide Adenine Dinucleotide ..... NAD

Nicotinamide Adenine Dinucleotide Phosphate ..... NADP

Scanning Transmission Electron Microscopy ..... STEM

Synthetic Nasal Medium ..... SNM

Minimum Inhibitory Concentration ..... MIC

Lactate Dehydrogenase ..... LDH

Diethyloxacarbocyanine Iodide ..... $DiOC_2(3)$

Carbonyl cyanide m-chlorophenyl hydrazine ..... CCCP

Adenosine triphosphate ..... ATP

Mean Fluorescence Intensity ..... MFI

Forward Scatter ..... FSC

Red Channel ..... RC

Green Channel ..... GC

Flow Cytometry Software ..... FCS

Oxygen Consumption Rate ..... OCR

Charge-Coupled Device ..... CCD

Field Emission Gun ..... FEG

High-Angle Annular Dark-Field Imaging ..... HAADF

Scanning Electron Microscopy ..... SEM

Through the Lens Detector ..... TLD

Focused Ion Beam ..... FIB

Energy-Dispersive X-Ray ..... EDX

Fluorescein Isothiocyanate ..... FITC

Electron Microscopy ..... EM

Extracellular Vesicle ..... EV

Pulmonary Surfactant..... PS

Endoplasmic reticulum ..... ER

Circular Dichroism..... CD

Deionized Water .....DI Water

Plasmid DNA ..... pDNA

X-Ray Photoelectron Spectrometry ..... XPS

X-Ray Diffractometer ..... XRD

Excitation-Emission Matrix ..... EEM

Stimulated Emission Depletion.....STED

Human Embryonic Kidney ..... HEK

Dulbecco's Modified Eagle's Medium ..... DMEM

Phosphate Buffer Saline..... PBS

3-(4,5-Dimethylthiazol-2-Yl)-2,5-Diphenyl Tetrazolium Bromide ..... MTT

Standard Deviation..... SD

4′,6-Diamidino-2-Phenylindole ..... DAPI

Multiphoton.....MP

Dimethyl Sulfoxide ..... DMSO

Thioglycolic Acid ..... TGA

Ethylenediamine ..... EDA

Powder Diffraction File ..... PDF

Inorganic Crystal Structure Database ..... ICSD

High Resolution Transmission Electron Microscopy ..... HR-TEM

Dynamic Light Scattering ..... DLS

Electrophoresis Mobility Shift Assay ..... EMSA

Supernatant ..... SPN

Atomic Force Microscopy ..... AFM

Differential Interference Contrast ..... DIC

.

Abstract

Biomimetic nanoparticles (NPs) are bio-inspired inorganic nanoscale materials that replicate some biological nanostructures functionalities including self-assembly, catalysis, and enzyme inhibition. These functionalities are being investigated for and, in some cases, are being utilized in optics and electronics such as chemical sensors, superhydrophobic coatings, and antireflective surfaces. This thesis examines the utilization of biomimetic inorganic NPs for various problems in biomedical engineering.

Specifically, the first part of this thesis addresses the problem on controversial explanations of the antibacterial and other biological activity of zinc oxide NPs that are frequently utilized in cosmetics, textiles, and biomedical fields. The second part of the thesis explores the self-organization of NPs into biomimetic supraparticles (SPs) for nucleic acid delivery that can be exploited as drug delivery agents.

NPs have been considered as antimicrobials for a long time; however, their antibacterial mechanism of action against different types of bacteria remains unclear and, in many cases, misinterpreted. Most of the studies on antimicrobial NPs suggest reactive oxygen species (ROS) formation, ion release, and membrane damage as the primary source of antibacterial activity. In Chapter 2, we show that the mechanism of antibacterial activity for *Staphylococcus aureus* is remarkably more complex than generating ROS or the release of Zn^{2+} ions. Gene expression analysis demonstrated that ZnO-NPs significantly affect carbohydrate metabolism and cell energetics, where the uridine monophosphate (UMP) biosynthesis pathway is highly upregulated. In Chapter 3, we explore the ZnO-NP mode of entry into *S. aureus* and the cell metabolism. Here,

we showed that NPs enter the cells within 5 minutes of exposure and induce minimal membrane damage. We note that cells do not depolarize until 60 min post-NPs exposure. Thereby, we highlight that membrane damage is not the primary mechanism of action but rather a downstream effect of ZnO-NPs exposure to bacterial cells. Taken together, causing minimal ROS production and significant changes in carbohydrate metabolism and bioenergetics along with cell entry without immediate membrane damage imply the biomimetic function of these NPs. However, further investigation into the antimicrobial mechanisms of these biomimetic NPs is essential for future clinical translation.

Over the past few decades, there has been considerable interest in developing nanoscale constructs as effective delivery tools for high molecular weight drugs. In chapter 4, we investigate the self-assembly of NPs into compartmentalized SPs, which mimics the structure of a virus to deliver nucleic acid into cells. The time-dependent self-assembly mechanism reveals that these SPs are formed from nanocup intermediates. We found that this intermediate stage is essential for the utilization of SP compartments. Nucleic acid is added to the system at this stage before SP formation, and high encapsulation is achieved. Similar to virus infections, once cells uptake the SP, SP disassociates in endosomes and releases the cargo.

Overall, the work presented in this thesis investigates and highlights the strong potential of biomimetic inorganic NPs use in next-generation biomedical applications.

Chapter 1

Introduction

1.1 Motivation: Biomimetic Nanoparticles

"There's Plenty of Room at the Bottom" is the title of Richard P. Feynman's talk where he put his thoughts on today's technology with the statement "tiny machines " in 1959[1] long before the term nanotechnology was used. He implies that as we go down in scale, we get new properties of materials and would be able to control individual atoms and molecules; and construct tiny machines that behave like biological entities[1]. Since then, research in nanotechnology has been highly active and leads to new knowledge and innovations that were not possible before, from drug delivery to energy-saving technologies, from next-generation antibiotics to surface coatings[2–6]. Among those, biomimetic nanoparticles have become extremely important in many applications.

Biomimetic is the imitation of nature's structures, materials, and functions to solve complex human problems[7–11]. For example, small pillars on the surface of the cicada wings provide self-cleaning properties, or microscopic hair bundles on gecko feet provide wet or dry adhesion[12]. Engineering similar structures from nature provide similar properties that can be utilized in various applications such as optics, electronics, automotive and even buildings. Scientists have followed biomimetic engineering "learning from nature" for a long time, and nanoparticles are the most commonly used material in biomimetic engineering[13–16].

1.2 Background

Nanoparticles (NPs) are a broad class of materials with at least one dimension less than 100nm[17]. Nano is the scientific term meaning one-billionth (1/1,000,000,000), and it comes from a Greek word meaning "dwarf." For better comparison, a fingernail grows one nanometer every second, or a human hair is roughly 50,000 to 100,000 nanometers across[18]. These small structures are engineered for various applications. Specifically, biomimetic nanoparticles become extremely important in biomedical applications since they offer flexibility to materials and behave like complex biological systems similar to tiny machines, as Feynman mentioned decades ago[15,19,20]. These nanoparticles were engineered and designed by imitating the structure and function of nature[21]. For example, lipid-based NPs are commonly used to imitate cell membranes since they have a similar structure, lipid bilayer, and similar function, protecting the internal area from the harsh environment[22]. Similarly, inorganic NPs, another example, are used to mimic the similar function of nature, such as enzyme inhibition[23]; even though the overall shape may not be identical, the size and material of the NP allow imitation of the function. There are a large variety of materials that can be used as the building blocks for the engineering of biomimetic NPs. Based on the material, biomimetic NPs can be categorized into organic NPs, inorganic NPs, and hybrid NPs.

1.2.1 Organic Nanoparticles

Organic NPs are engineered from proteins, carbohydrates, lipids, and other organic compounds. Organic NPs can be exemplified in peptide-based NPs, lipid-based NPs, or polymer-based NPs.

Peptide-Based NPs are self-assembled NPs composed of peptides such as surfactant-like peptides or polypeptides such as viral structural proteins, capsids[24–26]. They can have different morphologies, including nanotubes, nanovesicles, and nanofibers[27]. While there is a remarkable

potential of these NPs, they still have some disadvantages like non-specific immunogenicity to the components of NPs[28,29].

Lipid-Based NPs are self-assembled NPs composed of natural or synthetic phospholipids with one or more bilayers, including lipids, liposomes, or emulsions[22]. Their hydrophilic and hydrophobic compounds allow them to carry various therapeutic substances. Their size may vary with anionic or cationic surfaces[30]. The most common applications of lipid-based NPs are drug/gene delivery[31,32] and vaccine applications[33]. High-production cost is the main disadvantage of lipid-based NPs[34].

Polymer-Based NPs composed of synthetic and natural polymers include poly-l-lysine, poly ethylenimine, dendrimers, chitosan, cyclodextrin, poly (lactic-co-glycolic) NPs. Compared to other organic NPs, they have poor solubility at physiological pH[35]. However, this does not affect their application in various fields.

1.2.2 Inorganic Nanoparticles

Biomimetic NPs engineered from inorganic materials have been widely investigated. These NPs are similar to proteins in size, shape, and, most notably, function, making them biomimetic NPs. Similar to proteins, these nanoparticles can self-assemble, form complex structures, inhibit enzymes and catalyze [36]. Based on the overall shape, inorganic NPs can be 0D, 1D, 2D, or 3D[37], and show unique chemical and physical properties different than the bulk material such as optical, magnetic, thermodynamic, electrochemical, and catalytic [38]. Common inorganic NPs are metal NPs, silica NPs, carbon-based NPs, and metal-oxide NPs.

1.2.2.1 Metal Nanoparticles

Metal NPs are purely made of the metal precursors such as gold, silver, copper[39]. Metal NPs synthesis has great control on the surface properties, facet, size, and shape of the NPs [40,41]. This

controlled synthesis allows NPs to play a crucial role in developing cutting-edge materials for different applications[42–47]. Metal NPs hold unique advanced optical and physicochemical properties due to their surface plasmon resonance properties, making them specifically valuable in imaging, diagnostics, electronics, chemical sensors, and biosensors [45,48–52]. While metal NPs have many advantages, the disadvantages of their use specifically in the biomedical field include lack of biodegradability, poor clearance, the potential for long-term toxicity, and biomolecule adsorption on their surfaces [53,54].

1.2.2.2 Silica Nanoparticles

Silica NPs are inorganic, nonmetallic NPs composed of silicon dioxide and can be found in amorphous, crystalline, poly-crystalline, porous, or hollow forms[39,55]. The most commonly utilized silica NPs are mesoporous silica NPs with honeycomb-like structural features and many empty channels[56–62]. While silica NPs have been used in a wide range of applications such as imaging, and delivery applications[63,64], it has been shown that silica is toxic with showing hemolytic activity[65].

1.2.2.3 Carbon-Based Nanoparticles

Carbon-based NPs are an emerging class of NPs includes fullerenes, carbon nanotubes, graphene and its derivatives, graphene oxide, and carbon-based quantum dots[66]. Carbon-based NPs are unique for the combination of lightweight, chemical resistance, superb mechanical properties[67]. They have been utilized in various applications, including scaffolds in tissue engineering, biosensors, imaging, drug/gene delivery due to their physical, mechanical, electrical, optical, and thermal properties [50–57]. Despite the continued applications, carbon-based NPs carry some drawbacks, including a lack of biodegradability and high in-vivo toxicity[74,75].

1.2.2.4 Metal-Oxide Nanoparticles

Earth's crust consists of many metal oxides; therefore, the most significant advantage among other materials is high availability and low cost. Metal oxide NPs can have semiconducting nature due to the bandgap of the NPs and can be found various shape and size that gives them different properties[23,76–79] Iron oxide NPs, for example, can also carry magnetic, superparamagnetic depending on the crystal type and size[80]. Due to their easy preparation, magnetic susceptibility, and biodegradability, metal-oxide NPs are widely investigated in various applications. These applications can be exemplified in biosensing applications[81], targeted drug delivery [82,83], contrast agents in magnetic resonance imaging (MRI) [78,84], photocatalytic activities[85], antibacterial [86]and antifungal activities[87].

1.2.3 Hybrid Nanoparticles

Hybrid NPs are composed of both organic and inorganic materials. The inorganic part may form the core or the shell of the hybrid NPs[27]. In either case, hybrid NPs have a synergetic effect of both materials for multifunctional properties [88–91]. For example, inorganic NPs can be coated with different types of organic materials to improve the delivery and therapeutic efficacy or increase circulation time in blood [27,92,93]. Gold NPs deposited polystyrene NPs can be utilized for surface-enhanced Raman scattering[94].

1.3 Thesis Overview

Among others, inorganic NPs are specifically become popular for biomimetic approaches because of their outstanding physical and chemical properties and, more importantly, their similarities with proteins [95–98]. Furthermore, their easy preparation, tunable size, charge, and surface functional groups make them suitable for various applications, including but not limited to biosensing,

bioimaging, wound dressing[27,39,99,100]. Specifically, the high potential antimicrobial activity and cargo delivery make inorganic NPs popular for addressing the need for next-generation biomedical challenges.

1.3.1 Biomimetic Inorganic NPs as Antibacterial Agent

The first antibiotic, penicillin, was discovered in 1928. Since then, we have seen a significant improvement in global health and longevity. Unfortunately, emerging antimicrobial resistance is becoming one of the greatest threats to global human health[101]. Less than two decades after discovering penicillin, Alexander Fleming noted that microbes become "educated" to resist penicillin [101,102]. Improper use of antibiotics has led to a widespread increase in the occurrence of drug-resistant and multidrug-resistant bacteria[103]. As more and more pathogenic bacteria develop resistance to multiple classes of antibiotics, previously treatable illnesses will become lethal. [101,102]. Infections caused by antibiotic-resistant bacteria are associated with higher mortality rates and result in prolonged hospital stays and increased healthcare costs[104]. The COVID-19 pandemic has also put a spotlight on the need for new types of antimicrobials, not just specifically against the SARS-CoV-2 coronavirus but against hospital-acquired infections as well. Studies suggest that severe illnesses and death during the pandemics are attributed to secondary bacterial infections by *S. aureus* and *P. aeruginosa*[105–111]. Consequently, there is an imperative need for new antimicrobials with a novel mechanism of action to avoid resistance. Inorganic biomimetic NPs are a viable alternative to antibiotics to solve the problem of multi-drug resistance since nanoscale engineering of surfaces and particles provides new paths for antibacterial drug design [112,113]. Multiple inorganic metals and metal oxide nanomaterials, exemplified by Ag, Cu, Zn, Ni, Ag_2O, CuO, MgO, TiO_2, and ZnO NPs, inhibit bacterial growth [114–129].

Zinc oxide NPs (ZnO-NPs) are one of the most investigated NPs for antibacterial activity[23,130–134]. Zinc is the second most abundant metal on Earth [135]. Therefore, ZnO-NPs have become popular due to their simplicity, eco-friendly, and ability to apply in varied applications [135]. ZnO-NPs are highly used in cosmetics, textiles, and biomedical fields because of prominent antibacterial activity and UV-A & UV-B protection [136–138].

Several factors affect the NPs antibacterial activity, such as size, shape, charge, surface chemistry. Moreover, environmental conditions, the bacterial strain, and the exposure time are other major factors influencing the antibacterial effects of NPs[23,77,131,139–142]. Understanding the NPs' mechanism of action on bacteria is essential for clinical translation.

1.3.1.1 Understanding ZnO-NPs Mechanism of Action on Bacterial Cell for Engineering Next-Generation Antibiotics

ZnO-NPs have extensive documentation of their antimicrobial abilities[121,143,144]. The success of clinical studies of these antibacterial NPs primarily relies on the interaction ability of NPs with the biological environment[145], and therefore there is a tremendous amount of research going on for engineering biomimetic NPs. Understanding the actual mechanism of action is important not just for clinical translations but also for engineering new next-generation antibiotics.

Multiple mechanisms of action of ZnO-NPs are commonly proposed from the action of Zn^{2+} ion release, generation of reactive oxygen species, biomolecules, and membrane damage[121]. It is well documented that ZnO-NPs inhibit enzyme function[66,171,172]; however, the prevailing hypotheses' of the ZnO-NPs mechanism by which this occurs is controversial. One proposed mechanism of action of ZnO-NPs is Zn^{2+} ion release. It is proposed that Zn^{2+} ions released by ZnO-NPs in solution with bacteria interfere with metabolic processes and disturb enzyme function[23,148,149]. However, given the low solubility of ZnO, the concentration of free Zn^{2+} ions is

expected to be low in aqueous suspensions. In Chapter 2, we explore this hypothesis by comparing ZnO-NP conditioned media and $ZnCl_2$ dissolution in media. Another commonly reported mechanism of action is the production of reactive oxygen species (ROS)[101,114,123,150–152]. In Chapter 2, we also look into if ZnO-NP's antimicrobial activity is due to ROS generation by comparing its potency to Hydrogen Peroxide (H_2O_2)[101,121]. The final proposed mechanism of ZnO-NPs involves direct action on the bacterial cell membrane[153–157]as the positively charged surfaces of the NPs interact with the negatively charged bacterial membrane. In Chapter 3, we further explore the mechanism of action of ZnO-NPs on cell membranes and how bacterial metabolism is affected.

1.3.2 Biomimetic NPs as Delivery Tools - Artificial Virus

Over the past few decades, there has been considerable interest in developing biomimetic NPs as effective delivery tools [39,158]. In contrast with small-molecule therapeutics[159], naked nucleic acid itself cannot effectively enter the cell [159–161]. Controlled delivery of nucleic acid to target cells - also known as transfection - is essential for developing next-generation nucleic acid delivery tools [160,162]. The success of transfection largely depends on delivery vectors[163]. These vectors should protect genetic material from nucleases and other environmental agents and facilitate cellular uptake with minimal toxicity[159,164]. Nanoparticles that mimic virus formation and their transfection ability will be the most promising vectors. Vectors in literature are engineered from various materials and divided into two main categories: viral and non-viral vectors [159,160]. Viral vectors such as modified retro and adenoviruses provide efficient delivery [160]; however, they impose serious risks such as the possibility of recombination, strong immunogenicity, carcinogenicity, and inflammation [165–169] Alternative to viral vectors, non-viral vectors such as inorganic NPs [160], lipid-based NPs [147,] and polymer-based NPs [167,171] have been broadly used for nucleic acid delivery

(**Table 1**). However, a low transfection rate is still the most significant limitation when compared to viral vectors [172].

Table 1 Advantages and Disadvantages of Non-Viral Vectors (Table is formatted from [173])

Type of NPs	Advantages	Disadvantages	Ref.
Inorganic NPs	Short time of transfection, easy preparation, wide availability, rich functionality, high transfection efficiency, potential capability for targeted delivery, and controlled release	Most are unstable, toxic and non-biocompatible	[174–176]
Polymer-based NPs	Small size, narrow distribution, more stability, high protection against enzymatic degradation, low toxicity, high cationic potential	Low biodegradability, low efficacy	[24,177,178]
Lipid-based NPs	Safe preparation, low immunogenicity	Toxicity at high dose, difficult preparation, low transfection efficiency	[32,179,180]

1.3.2.1 Challenges in Delivery Systems

The engineering of a non-viral vector requires a rational design for addressing related challenges associated with efficient nucleic acid delivery.

Packaging and Protection of Cargo

The foremost challenge related to vectors is packaging the cargo. Whether it is DNA, RNA, or a drug, the first stage of the effective transfection is packing the cargo in the vector. Here, the cargo and vector should have balanced interactions. The vector must protect the cargo from the environment and release it in ambient conditions. Strong interactions between the cargo and the vector affect the release and transfection capacity similar to cationic polymers[22]. It is essential to understand the packaging capacity and efficiency of a vector.

Cellular Uptake

Once the cargo is packed, the vector needs to penetrate the cells for cargo delivery. NPs can enter cancer cells via different types of endocytosis[181]. Besides cellular level challenges, there is an important barrier to the stability of the vector and targeting issue. The vector must be stable enough for extended plasma circulation and deliver the cargo to the specific target.

Cargo Release

Upon uptake, the vector needs to escape from endocytosis and release the cargo into the cell. If vector enters the cells via endosome, stability in low pH is vital. Releasing efficiency is also another challenge in vector systems[179,182].

1.3.2.2 Self-Assembly of Biomimetic Supraparticles as Delivery Tools

To overcome these challenges, numerous NPs have been studied in nucleic acid delivery. In biological systems, proteins and other biomolecules self-assemble into complex super-structures that efficiently overcome these challenges, such as viral nanoshells formation. Inspired by these structures, scientists developed hierarchical assemblies, namely biomimetic supraparticles (SPs), that present properties and functionalities similar to nature[173,183]. The formation of SPs typically occurs through electrostatic and van der Waals interactions between uniformly shaped NPs and the environment [184,185]. These self-organized NPs can be engineered for obtaining desired physical, chemical, and optical properties [183,186–189]. Even though changing size, shape, and surface chemistry will also change the properties of the NPs, choosing the materials that are highly available, eco-friendly, and biocompatible is vital for engineering NPs for overcoming further challenges. Due to the natural existence of iron and sulfur in the human body [190], virus-like iron sulfide SPs appear promising for efficient and safe nucleic acid delivery. Chapter 4 shows that *L*-cysteine stabilized iron sulfide NPs can self-assemble into multi-compartment supraparticles

(SPs). The transmission electron microscopy results showed that NPs initially produce ~55nm cup-like structures and mature into ~75nm SPs with *ca.*190 interconnected compartments. The color change of the solution from black to yellow suggests the SP formation. The results of selected area electron diffraction and energy dispersive X-ray spectroscopy confirm SPs are formed from FeS_2 and Fe_2O_3 NPs. Elemental mapping showed that Fe_2O_3 NPs are located on the surface of the SP and protecting FeS_2 and compartments from the surroundings. These compartmentalized particles can be used for the successful encapsulation of DNA fragments for gene delivery.

PART I

Chapter 2

Unexpected Insights into Antibacterial Activity of Zinc Oxide Nanoparticles Against Methicillin Resistant *Staphylococcus aureus* (MRSA)

2.1 Abstract

Zinc oxide nanoparticles (ZnO-NPs) are attractive as broad-spectrum antibiotics, however, their further engineering as antimicrobial agents and clinical translation is impeded by controversial data about their mechanism of activity. It is commonly reported that ZnO-NP's antimicrobial activity is associated with the production of reactive oxygen species (ROS). Here we disprove this concept by comparing the antibacterial potency of ZnO-NPs and their capacity to generate ROS with hydrogen peroxide (H_2O_2). Then, using gene transcription microarray analysis, we provide evidence for a novel toxicity mechanism. Exposure to ZnO-NPs resulted in over three-log reduction in colonies of methicillin resistant *S. aureus* with minimal increase in ROS or lipid peroxidation. The amount of ROS required for the same amount of killing by H_2O_2 was much greater than that generated by ZnO-NPs. In contrast to H_2O_2, ZnO-NP mediated killing was not mitigated by the antioxidant, *N*-acetylcysteine. ZnO-NPs caused significant up-regulation of pyrimidine biosynthesis and carbohydrate degradation. Simultaneously, amino acid synthesis in *S. aureus* was significantly downregulated indicating a complex mechanism of antimicrobial action involving multiple metabolic pathways. The results of this study point to the importance of specific experimental controls in the interpretation of antimicrobial mechanistic studies and the need for

targeted molecular mechanism studies. Continued investigation on the antibacterial mechanisms of biomimetic ZnO-NPs is essential for future clinical translation.

2.2 Introduction

Zinc oxide NPs have extensive documentation of their antimicrobial abilities[121,143,144]. Multiple mechanisms of action of ZnO-NPs are commonly proposed. A prevailing hypothesis is that ZnO-NPs spontaneously produce reactive oxygen species (ROS) and enhance intracellular oxidative stress in bacteria leading to their death [114,123,150,151,191–193]. ROS include hydroxyl radicals OH•, superoxide ions $O_2^{-\bullet}$, H_2O_2, and hydroperoxyl radicals [114,151]. ROS are proposed to cause membrane damage by lipid peroxidation[113] triggering cell leakage, loss of energy metabolism, and cell death [129,150,191]. While being plausible and widely reported, this hypothesis requires closer evaluation. The factual support of oxidative stress as the antimicrobial mechanism in case of ZnO-NPs and other nanoscale antimicrobials is controversial. In many studies, ZnO-NPs were first excited by ultraviolet (UV) light and then exposed to bacteria for ROS detection [194,195] . It is well-known that UV excitation creates oxygen vacancies and ROS on the semiconductor surfaces and therefore antibacterial activity can be associated with UV radiation [194]. At the same time, several studies suggested significant antibacterial effects without UV illumination [196,197] however, strong ROS generating positive controls have not been used in parallel to evaluate the respective NP ROS generating capacity. Notably, many of ZnO-NP antibacterial experiments were conducted on nonpathogenic, laboratory strains that are devoid of multiple defense/survival mechanisms (*i.e.*, *E. coli* K12) [151,191] and thus elevated ROS concentrations can originate from their native metabolic state rather than from the NPs. Contrarily, pathogenic strains of *S. aureus* are known to have multiple mechanisms for scavenging ROS [198–200]; they can cope with large amounts of ROS even if NPs can inherently generate them. Finally, spontaneous production of ROS by ZnO-NPs would

act indiscriminately and therefore have significant toxicity for mammalian cells. However, studies have demonstrated that ZnO-NPs have selective toxicity for prokaryotic cells over eukaryotic cells [122,201]. Therefore, we sought to conclusively evaluate the oxidative stress hypothesis for ZnO-NP mediated antibacterial effect.

Despite the poor solubility of ZnO in aqueous media, many studies have attributed antibacterial activity to release of toxic Zn^{2+} ions [202,203]. The basis of this toxicity is related to the specificity of certain essential proteins/enzymes for certain metal cofactors such as zinc [148]. Toxic levels of any of these metal ions lead to mis-metalation of these enzymes leading to loss of function and ultimately lysis. As with ROS, bacteria have evolved complex regulatory processes to maintain intracellular metal ion homeostasis through a wide range of environmental concentrations [148]. Given the low solubility of ZnO, the concentration of free Zn^{2+} ions are expected to be low in aqueous suspensions. However in the growth media, ZnO dissolution is complicated by Zn speciation with various components – amino acids and peptides – in the media [202,204,205]. Since most growth media is undefined soy digest products, it is difficult to predict ZnO dissolution kinetics and resulting complexes. However, studies dedicated to evaluation of ZnO dissolution in a defined bacteria growth media are required for more focused description of the resulting complexes generated from dissolution and beyond the scope of this work. We chose *S. aureus* COL, a methicillin resistant strain, as our model organism because of its prevalence in human infections, virulence, ROS scavenging abilities, and clinical relevance as an antibiotic resistant organism. The ROS generating potential of two ZnO-NP preparations and the resulting effect on *S. aureus* were evaluated. Specifically, we examined a commercially available ZnO-NP previously reported to generate ROS [194] and one synthesized in our laboratory known to inhibit planktonic and biofilm growth of methicillin resistant *S. aureus* (MRSA) [141,206]. Oxidative stress

was evaluated by multiple experimental techniques including fluorescent detection of ROS as well as resulting lipid peroxidation. Comparison was made with an equivalent degree of antibacterial activity by hydrogen peroxide (H_2O_2), which was chosen for its well-studied mechanism of ROS-mediated toxicity [207,208]. The dissolution of Zn^{2+} ions or catalysis of otherwise undefined toxic but soluble species was also considered in this study. Finally, in the abscess of definitive evidence from these specific phenotypic studies, a comprehensive gene transcription microarray analysis was performed to provide new insight into the mechanism of ZnO-NP staphylococcal toxicity.

2.3 Materials and Methods

2.3.1 Bacterial Strain, Media and Growth Conditions

Methicillin-resistant *Staphylococcus aureus* sub-strain COL was used in all experiments due to its strong ROS scavenging abilities [198,200]. A glycerol stock of the strain was maintained at −80°C and was plated on tryptic soy agar. Single colony inoculates were grown in tryptic soy broth + 1% glucose w/v (TSB_G) under shaking conditions at 37°C. Mid-log, optical density of 0.45-0.55 at 600nm (OD_{600}), cultures were used in all experiments.

2.3.2 ZnO Nanoparticles

ZnO nanopyramids with hexagonal base (ZnO-NPYs) synthesized in our laboratory and commercially available ZnO nanospheres (ZnO-NSPs) were investigated. Both of these NPs have been extensively characterized previously[206,209], which predicated our choice of the model nanoscale antimicrobials. ZnO-NPYs were synthesized without the use of surfactants or capping agents as previously described[206,209]. Briefly, pyramids were synthesized by first mixing 0.2 g potassium hydroxide with 5.5 g $Zn(Ac)_2{\cdot}2H_2O$ before adding anhydrous methanol and refluxing for 48h. After synthesis, the white precipitate was purified by washing three times with methanol,

and then frozen in Milli-Q® water to be lyophilized for 24 hours. ZnO-NSP were purchased from Nanostructured & Amorphous Materials, Inc (Houston, Texas) [194]

2.3.3 ZnO-NP Characterization

ZnO-NPs were characterized by transmission electron microscopy (TEM), selected area electron diffraction (SAED), photoluminescence spectroscopy (PL), Fourier transformed infrared spectroscopy (FTIR), and nanoparticle tracking analysis (NTA). A JOEL 2010 transmission electron microscope was used for NP visualization. TEM samples were prepared by adding 10µL of 167µg/ml ZnO-NPs sonicated in Milli-Q® water solution to a carbon TEM grid and drying at room temperature. The nanocrystalline structure of ZnO-NPs was confirmed by SAED from TEM samples on the same microscope. NP surface chemistry was evaluated by PL (Jobin Yvon Horiba Fluoromax-3 instrument) and FTIR (JASCO FT/ IR-4100 instrument). PL samples were prepared by sonicating 167ug/ml ZnO-NPs in Milli-Q® water for 3 mins. PL spectra of the aqueous dispersions were obtained using an excitation wavelength of 320nm at room temperature. Lyophilized ZnO-NP powder was used for FTIR with attenuated total reflection crystals. Particle aggregate distributions were obtained by NTA (Malvern NanoSight NS300) on aqueous dispersions prepared like PL samples.

2.3.4 ZnO-NP Dose Response and Bacterial Killing

To prepare NP dispersions for bacterial killing in planktonic conditions, ZnO-NP powder was sonicated into Milli-Q® water for 3 minutes to ensure a stable dispersion. Concentrations of ZnO-NPs included: 8, 80, 160, 400, and 800µg/ml. H_2O_2 was used as a positive control of a bacterial toxin whose mechanism of action involves the production of ROS. Concentrations of H_2O_2 included: 0.25, 0.50, 0.75, and 1.0 mM. These concentrations were chosen as they generated a similar degree of dose-dependent killing as the ZnO-NPs. Mid-log cultures of *S. aureus* grown

under aerobic conditions were pelleted by centrifugation and resuspended in aqueous dispersions of ZnO-NPs or solutions of H_2O_2. After 30 minutes, samples were serially diluted and plated on tryptic soy agar for colony enumeration (CFUs). Actual exposure times included 30 minutes in planktonic dispersion followed by multiple 10-fold dilutions and 36 hours on agar plate. Therefore, the concentration of dispersed ZnO-NPs and dissolved H_2O_2 were quickly diluted below toxic concentrations after just 30 minutes. It is possible that serial dilutions would not reduce the local concentration of ZnO if the NPs are complexed with the cells. However, this is not dissimilar from H_2O_2 which can readily diffuse through the cell membrane and is immediately reacted to form other ROS (e.g., hydroxyl radicals) which are unable to diffuse back out and remain with the cell despite dilution of the media.

2.3.5 ROS Detection

The presence of ROS was quantified by the fluorescence of 3′-(p-aminophenyl) fluorescein (APF; ThermoFisher Scientific, Waltham, Massachusetts) and 2',7'-dichlorodihydrofluorescein diacetate (H_2DCFDA; ThermoFisher Scientific, Waltham, Massachusetts). Both dyes detect the presence of a variety of ROS including but not limited to peroxyl and hydroxyl radicals, peroxynitrite anion, and hypochlorite anion. The excitation/emission peaks for APF and H_2DCFDA are 490/515 nm and 517/527 nm respectively. To evaluate for potential interactions between these dyes and ZnO-NPs we first evaluated their fluorescence in the presence of ZnO-NP dispersions and H_2O_2 solutions at the concentrations listed above without bacterial cells. Stock solutions of the dyes were made according to manufacturer's instructions and were added to ZnO-NP or H_2O_2 samples and incubated for 30minutes. Samples were then pelleted and fluorescence reading of both the supernatants and resuspended pellets were obtained using Perkin Elmer Enspire Multimode Plate

Reader. Comparing the pellets versus the supernatants provided information regarding interaction between the dye and the NPs which distribute to the pellet fraction.

For bacterial experiments, mid-log cultures grown under aerobic conditions were pelleted and resuspended in water, ZnO-NPs dispersions, or H_2O_2 at the concentrations listed above. Cells with fluorescent ROS detection dyes were exposed to NPs or H_2O_2 at 37°C for 30 minutes. The pellets represent intracellular ROS while the supernatants represent extracellular ROS or ROS spilled from lysed cells. Of note, there were no significant differences in the data trends for pellets or supernatants (see **Figure** S **2.9**). For clarity only the data for the pellets are reported here. All samples were then serially diluted and plated on tryptic soy agar for CFU enumeration to provide a simultaneous measurement of bacterial cell death. This allowed us to correlate the amount of ROS in a sample with the degree of bacterial killing in that same sample.

To confirm that ZnO-NPs dispersions can indeed generate ROS via photocatalysis, APF and H_2DCFDA fluorescence was also measured on ZnO-NP dispersions without bacteria but after UV excitation. These samples were exposed to either ambient light or 2 minutes UV excitation via a UV light box (**Figure S 2.10**).

2.3.6 Lipid Peroxidation

Lipid peroxidation was evaluated using the thiobarbituric acid reactive substances assay (TBARS): OxiSelect™ TBARS Assay Kit (Cell Biolabs, San Diego, California). Mid-log phase cultures grown under aerobic conditions were pelleted and resuspended in ZnO-NPs dispersions or H_2O_2 at the concentrations listed above. After 30minutes, TBARS reagents were added and incubated at 95°C for 50 minutes. Samples were centrifuged and supernatant was collected for fluorescent spectroscopy measurements 540nm excitation and 590nm emission. Just prior to addition of TBARS reagents, an aliquot of each sample was removed for serially dilution and CFU

enumeration to allow for simultaneous measurement of lipid peroxidation and bacterial cell death for each sample. A malondialdehyde (MDA) standard curve (provided by the kit) was used to convert the fluorescence measurements into MDA equivalent concentrations (**Figure S 2.11**).

2.3.7 Bacterial Growth Recovery by Antioxidant

Antioxidant recovery was evaluated by adding increasing concentrations of *N*-acetylcysteine, NAC, to the culture media with H_2O_2 or ZnO-NPs. NAC concentrations between 10mM and 70mM were evaluated to determine the maximum cell growth recovery in the presence of H_2O_2 without toxicity. A concentration of 50mM resulted in maximal recovery with low toxicity (**Figure S 2.12**). Mid-log culture, 10μl, was exposed to 50mM NAC (final concentration) for 15 minutes. Then 1ml of 8, 80, 160, or 400 μg/ml final concentrations of ZnO-NP dispersions or 0.25mM or 0.5mM H_2O_2 was added to the cells. Each sample, ~100μL, were then plated in a 96well plate, and growth curves were measured turbidometrically (OD_{600}) each hour for 10 hours under aerobic shaking conditions. To provide a simultaneous measurement of NP and H_2O_2 mediated killing, a 10μl aliquot of each sample after only 30 minutes exposure were serially diluted and plated on tryptic soy agar for CFU enumeration.

2.3.8 ZnO-NP Supernatant Growth Curves

To evaluate for ZnO dissolution or catalysis of soluble toxic substances on the ZnO-NP surface, we evaluated the toxicity of media conditioned with ZnO-NPs. Briefly, ZnO-NP were sonicated into TSB_G at concentrations of 0, 80, 160, and 400 μg/ml for 3 minutes and then incubated at 37°C for 30min. As a control, $ZnCl_2$ was dissolved into TSB_G at concentrations of 0, 50, 100, 200, and 300 μg/ml and treated similarly with sonication and incubation. The ZnO and $ZnCl_2$ samples were then centrifuged at 14,000*g* for 10 min and the supernatants were removed. Those supernatants

were then inoculated with ~ $5x10^7$ CFU/ml in a 96-well plate, and growth curves were measured turbidometrically (OD_{600}) each hour for 14h under aerobic shaking conditions.

2.3.9 Gene Expression Analysis

To evaluate changes in gene expression by *S. aureus* in response to ZnO-NPs, RNA was isolated from *S. aureus* after exposure to a sub-lethal but growth inhibitory concentration (160 μg/ml) of ZnO-NPYs (**Figure S 2.13**). *S. aureus* grown at the same time but not exposed to ZnO-NPYs were used as a control. A total of 3 ZnO-NP and 3 control samples were obtained and analyzed on independent microarray chips. Mid-log phase cells were lysed with lysostaphin followed by proteinase k digestion. Total RNA was isolated using Trizol (Invitrogen, Carlsbad, CA) followed by RNeasy column cleanup (Qiagen, Valencia, CA). RNA quantity and quality was confirmed on an Agilent 2100 Bioanalyzer before being applied to *S. aureus* whole genome microarray (GeneChip™, Affymetrix, Santa Clara, CA).

Microarray results were validated by performing quantitative RT-PCR on select genes identified to be significantly up or down regulated in the microarray analysis. Briefly, RNA was purified from *S. aureus* COL samples exposed to sub-lethal dose of ZnO-NPs, identical to microarray gene expression experiments. *S. aureus* grown in the same condition while not exposed to ZnO-NPs were used as controls. RNA was isolated through a lysostaphin digestion, TRizol extraction (Invitrogen, Carlsbad, CA), and then elution by RNeasy mini kit (Qiagen, Valencia, CA). RNA quality was checked using NanoDrop 2000 (ThermoFisher Scientific, Kalamazoo, MI) and RT-PCR was performed using QuantiFast SYBR Green RT-PCR Kit (Qiagen, Valencia, CA), and StepOnePlus Real-Time PCR System (Applied Biosystems, ThermoFisher Scientific, Kalamazoo, MI). Primers (Supplemental Table 1) were designed using National Center for

Biotechnology Information database and ordered from Integrated DNA Technologies (Skokie, Illinois).

2.3.10 Statistical Analysis

All data presented in this study are displayed as mean plus or minus standard error of the mean unless otherwise stated. To evaluate the role of oxidative stress on *S. aureus* toxicity we performed simultaneous measurements of ROS generation (by fluorescence of APF and H_2DCFDA) or lipid peroxidation (by TBARS) and quantitative culture. Each measurement was performed in triplicate and at least 5 independent experiments were run on different days. We compared ROS content or lipid peroxidation associated with a greater than two-log reduction in CFUs for the two ZnO-NP preparations and H_2O_2. Hypothesis testing was performed via ANOVA with repeated measures. Post-hoc pairwise testing was performed using the Tukey test with $p < 0.05$ indicating significance. To evaluate the capacity of NAC to mitigate bacterial killing we compared the resulting CFUs after exposure to ZnO-NPs or H_2O_2 with and without the presence of NAC. Again, ANOVA with repeated measures was used for hypothesis testing. To evaluate growth recovery by NAC, individual growth curves were summarized by calculating a growth rate constant using linear regression of the log-transformed optical density data. We then performed linear regression on the growth rate constants as a function of ZnO-NP dose with and without NAC. Hypothesis testing was performed using ANOVA of the resulting regression models.

For the microarray gene expression analysis, weighted linear models specific for microarray analysis [210] were fit to the data to compare ZnO-NP treated samples to control. Specifically, we increased the power to detect differences by pooling information from all probesets to stabilize the variance estimate and samples were weighted on a gene-by-gene update algorithm [211]. We selected probesets with a fold change of 1.5 or greater and an adjusted *p*-value of 0.05 or less. The *p*-values

were adjusted for multiple comparisons using false discovery rate of 5% [212]. Genes were then grouped by biological function. Finally, gene set enrichment analysis (GSEA) was used to organize genes by function, transcriptional regulation, and pathway associations (Biocyc Pathway/Genome database for *S. aureus*, www.biocyc.org) and identify significant biological functions or pathways altered in response to ZnO-NPs. Pathways with enrichment *p*-value of 0.05 or less were identified. The *p*-values were adjusted for multiple comparisons using a Bonferroni correction.

Fold change in gene expression between control and ZnO-NP treated bacteria was determined by quantitative RT-PCR using the delta-delta Ct method. Five separate pairs of control and test samples were performed for each gene of interest with triplicate reactions for each replicate. Student's t-test was used to evaluate each gene for significant change in gene expression with the null hypothesis equal to zero change. Again *p*-values were adjusted for multiple comparisons.

2.4 Results

2.4.1 ZnO-NP Characterization

Although the two NPs are different in size and shape, their electron diffraction patterns were identical and matched the hexagonal crystalline phase of bulk ZnO (**Figure 2.1 a and b**). Their average particle aggregation sizes, under the aqueous conditions used in this study, were also very similar (**Figure S 2.14**). The NPYs and NSPs also had similar FTIR patterns indicating little difference in surface chemistry (**Figure 2.1c**). The photoluminescence spectrum of both NP dispersions shows only one emission peak, located at 390nm (**Figure 2.1d**). There are no other peaks observed, particularly around 520nm, which would indicate the presence of singly ionized oxygen vacancies. The NPY's narrow luminescence peak is consistent with their small size and

high crystallinity. Contrarily, the NSPs had a broader peak, corresponding to their larger size and broader spectrum of light-emitting states.

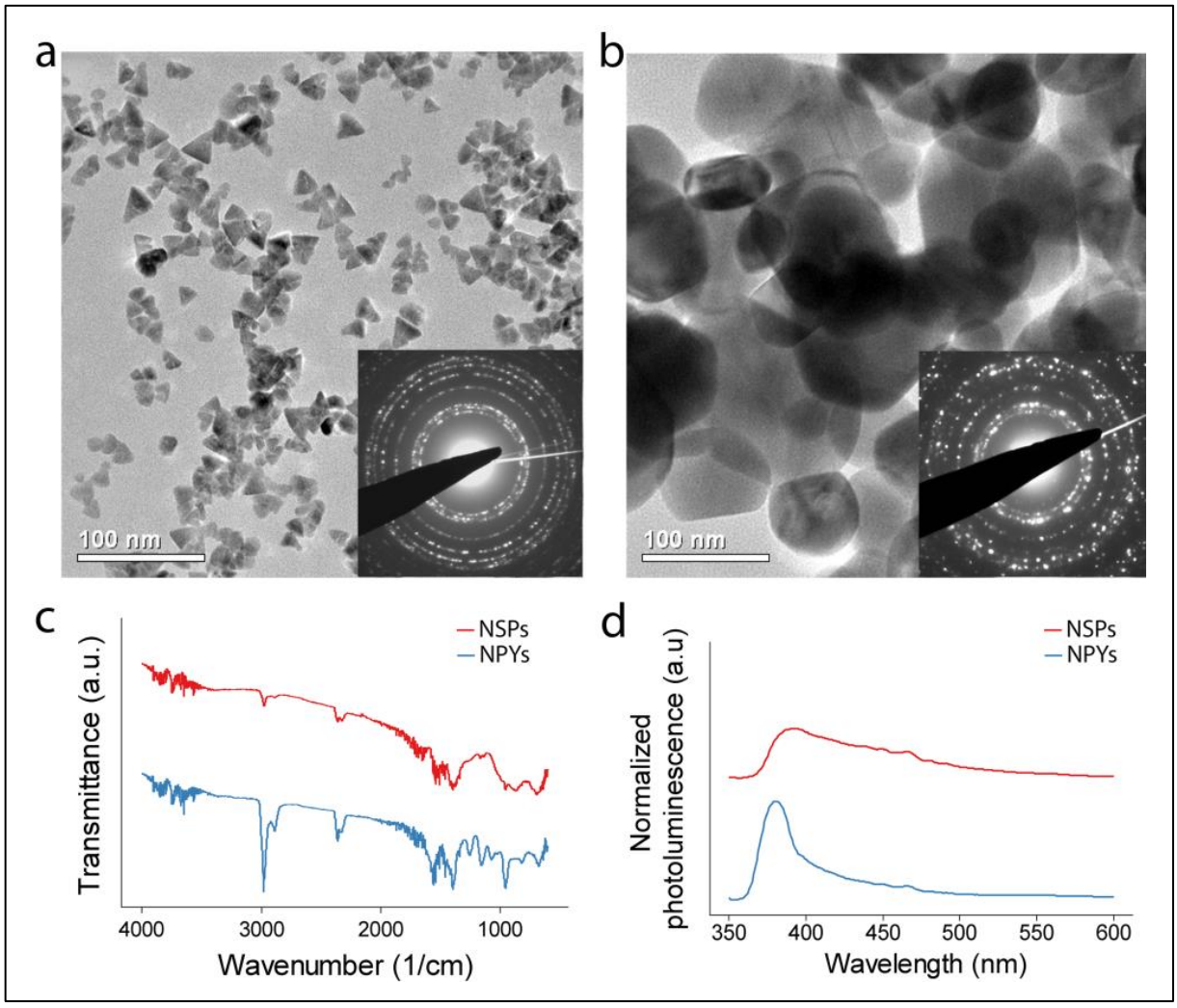

Figure 2.1 Transmission electron micrographs of (a) ZnO-NPYs and (b) ZnO-NSPs. Insets show selected area electron diffraction. (c) Fourier transform infrared spectra and (d) photoluminescence spectra of corresponding ZnO-NPs. The spectra in (c & d) were shifted with respect to the ordinate for clarity

2.4.2 Antimicrobial Properties of ZnO-NPs

Bactericidal activities of both types of NPs and H_2O_2 against *S. aureus* demonstrate dose dependent killing in all cases (**Figure 2.2**). Exposure to ZnO-NP dispersions and H_2O_2 solutions resulted in greater than 1000x reduction in colony forming units (CFU) from control ($5x10^7$ CFUs of *S. aureus* without ZnO-NPs or H_2O_2 grown for 18h) for both shapes at 800µg/ml and H_2O_2 at 0.75mM. CFU

reduction due to increasing H_2O_2 concentrations was similar to the potency of the ZnO-NPs. These concentrations of H_2O_2 were used as a positive control in the subsequent experiments.

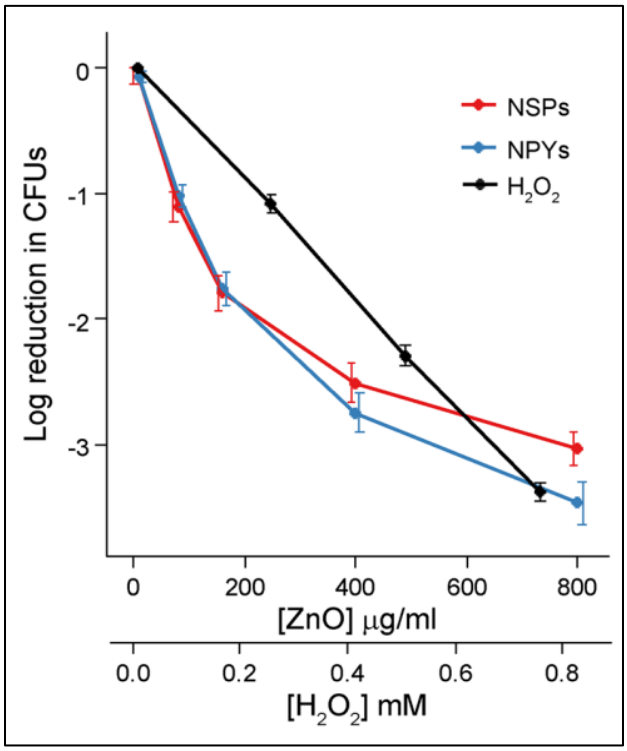

Figure 2.2 Reduction in colony counts (from $5x10^7$) observed after exposure to increasing concentrations of ZnO-NPYs and NSPs as well as H_2O_2. Note the different scales of abscissa for ZnO-NPs and H_2O_2. Error bars represent standard error of five independent experiments run on different days

2.4.3 ROS Production in Presence of ZnO-NPs

Understanding the potential for NPs to interact with a variety of fluorescent probes, we first evaluated the fluorescence of APF and H_2DCFDA in NP dispersions and H_2O_2 solutions without bacterial cells (**Figure S 2.15**). As expected, there is a dose dependent increase in fluorescence of both APF and H_2DCFDA in the presence of H_2O_2. Likewise, we observed dose dependent fluorescence of both ROS indicators in the NP dispersions. However, the absolute fluorescence of APF for low dose ZnO-NPs (80µg/ml) was slightly less than pure water. In addition, a large fraction of APF became bound to the ZnO-NPs as seen by the high fluorescence noted in the pellet fraction. Higher doses of ZnO-NPs (800µg/ml) resulted in only modest elevations in pellet

fluorescence but significant increases in the supernatant. This indicates potential saturation of APF on the NPs. On the other hand, H_2DCFDA appeared to have less affinity for the NPs with significantly less fluorescence in the pellet fraction. There were no significant differences between the NSPs and the NPYs. Although H_2DCFDA appears to be a more reliable ROS indicator with respect to ZnO-NPs, we utilized both indicators in the subsequent studies.

To determine the baseline production of ROS by bacterial cells due to aerobic metabolism we obtained the fluorescence of APF and H_2DCFDA generated by $5x10^7$ *S. aureus* CFUs (the initial inoculum in all future experiments). There is a substantial increase in ROS production as indicated by the increase in APF and H_2DCFDA fluorescence with the addition of bacteria (**Figure S 2.16**). It should be noted that the cells were resuspended in water (not growth media) to remove variation due to rapidly dividing cells. Given the high background ROS production by bacterial cells alone, as well as the significant sample to sample variation (note error bars), all subsequent measurements of ROS fluorescence were expressed as a percent change from a control (bacteria without H_2O_2 or ZnO-NPs) prepared from the same bacterial colony.

S. aureus exposure to H_2O_2 resulted in steady, dose-dependent increase in APF fluorescence (**Figure 2.3a**). For both ZnO-NP preparations, there was also a dose-dependent increase. However, the absolute quantity was always smaller than that of H_2O_2 as well as smaller than the paired controls (*i.e.*, <100%). The difference between the two NP shapes was statistically insignificant. This decrease in APF below controls may indicate that ZnO-NPs reduce cellular metabolism and resulting metabolic ROS, although interaction with APF as seen in **Figure S 2.16** is also possible. As such, the fluorescence of H_2DCFDA was also used to detect small molecule ROS (**Figure 2.3c**). As expected, the presence of H_2O_2 resulted in a large dose-dependent increase in H_2DCFDA fluorescence. Similarly, both ZnO-NPs had a dose-dependent increase in H_2DCFDA

fluorescence above control, with the effect from NPYs being modestly greater than NSPs. These findings alone might appear to confirm the initial ROS hypothesis. Indeed, ZnO-NSPs used in this study were previously shown to produce intracellular ROS[194]. However, these ROS can be produced in a dose-dependent manner as a side product. To be the cause of cell death, ROS from the NPs need to be produced in amounts comparable to a known ROS-based antibacterial agent, for instance H_2O_2, the gold standard in this field. Here, the absolute amount of ROS generated by bacteria exposed to ZnO-NPs was significantly smaller than those exposed to H_2O_2. To quantify the relationship between cell death and ROS production, we correlated the resulting CFU counts with the ROS fluorescence measurements. We then compared the APF and H_2DCFDA fluorescence required for a 2-log or greater reduction in CFUs for H_2O_2 and the two ZnO-NP preparations (**Figure 2.3b and d**). H_2O_2 generated significantly greater amounts of ROS to kill the same amount of *S. aureus* as the ZnO-NPs ($p < 0.001$). This finding leads to different conclusions about the mechanism than one might expect based on superficial evaluation of dose-dependent ROS generation.

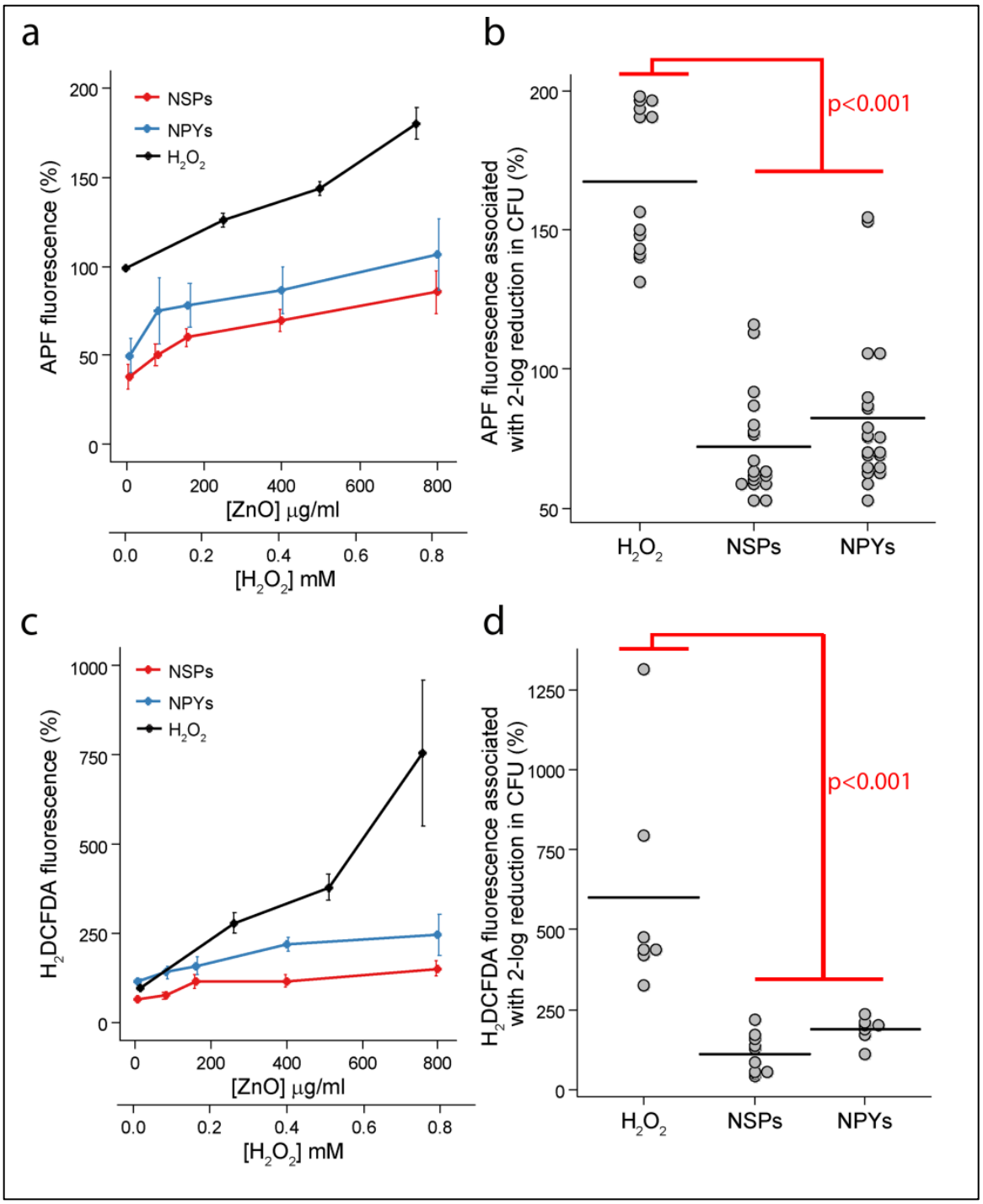

Figure 2.3 Dose and shape-dependent ROS production by (a) APF and (c) H_2DCFDA fluorescence after exposure to ZnO-NPYs and -NSPs as well as H_2O_2. Note the different scales of abscissa for ZnO-NPs. Error bars represent standard error of five independent experiments run on different days. (b) Dot plots of APF and (d) H_2DCFDA fluorescence associated with a two-log reduction in CFUs for each treatment. Black horizontal lines represent the mean value. p-values represent significant difference determine by ANOVA with repeated measures and post-hoc Tukey testing.

2.4.4 Lipid Peroxidation in The Presence of ZnO-NPs

Although APF and H_2DCFDA detect a wide range of small molecule ROS, many ROS are so reactive that their presence is transient and could be difficult to detect. A downstream result of intracellular oxidative stress is lipid peroxidation. To confirm ZnO-NPs were not producing a toxic but undetected ROS, we evaluated downstream lipid peroxidation. There was minimal to no increase in lipid peroxidation for all doses and shapes of ZnO-NPs tested (**Figure 2.4a**). On the other hand, the addition of H_2O_2 resulted in robust dose-dependent lipid peroxidation. Using a similar analysis as for small molecule ROS, we compared the degree of lipid peroxidation required for a greater than 2-log reduction in colonies. As before, we observed that H_2O_2 generated significantly more oxidative stress - lipid peroxidation in this case - for the same degree of bacterial eradication as ZnO-NPs (p<0.001, **Figure 2.4b**). NPYs generated higher levels of lipid peroxidation than NSPs although the absolute difference was small (p<0.001, **Figure 2.4b**).

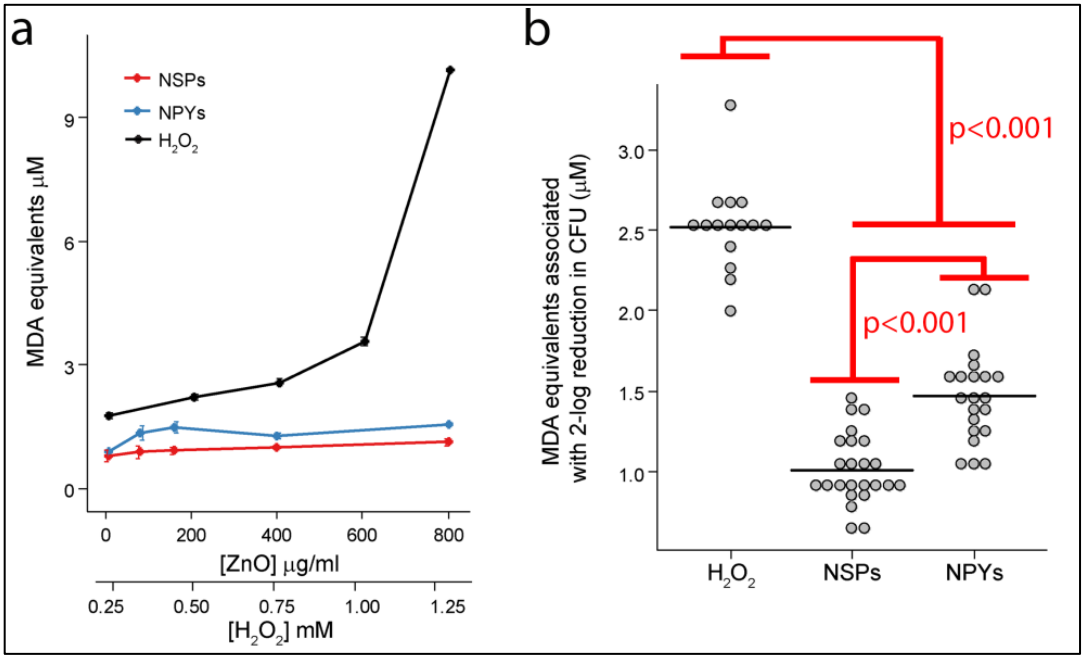

Figure 2.4 (a) Dose-dependent lipid peroxidation by ZnO-NPs and H_2O_2. Error bars represent standard error of five independent experiments run on different days. (b) Dot plots of lipid peroxidation associated with a two-log reduction in CFUs for each treatment. Black horizontal lines represent the mean. p-values denote significant differences determined by ANOVA with repeated measures and post-hoc Tukey testing.

2.4.5 Antioxidant Recovery from Oxidative Stress

As a complementary test, we attempted to mitigate the oxidative stress to bacteria by adding the well-known antioxidant NAC to the culture media prior to the addition of ZnO-NPs or H_2O_2. The addition of NAC resulted in near complete recovery of bacterial colonies whose counts were dramatically reduced by H_2O_2 (**Figure 2.5a**). On the other hand, the addition of NAC did not mitigate the antibacterial activity of either ZnO-NP (**Figure 2.5b and c**). On the contrary, NAC improved the antibacterial effect of ZnO-NPs at 400μg/ml. This could be due to better stability of NPs at high concentrations in the presence of NAC, therefore being more effective. Alternatively, NAC can be toxic at high concentrations (**See Figure S 2.12)** and this particular concentration was synergistic with the ZnO-NPs. However, the key finding was that the presence of NAC did not recover any bacterial growth, as opposed to H_2O_2. The effect of NAC was similar for bacterial growth curves obtained in the presence of H_2O_2 and ZnO-NPs. For H_2O_2 almost 50% recovery was seen in the presence of NAC (**Figure S 2.17**). However, in the case of ZnO-NPs, growth curves and the resulting dose-dependent growth rates were unchanged by NAC (**Figure 2.5 d-i**). The addition of NAC to NP treated cultures did not recover the *S. aureus* growth rate.

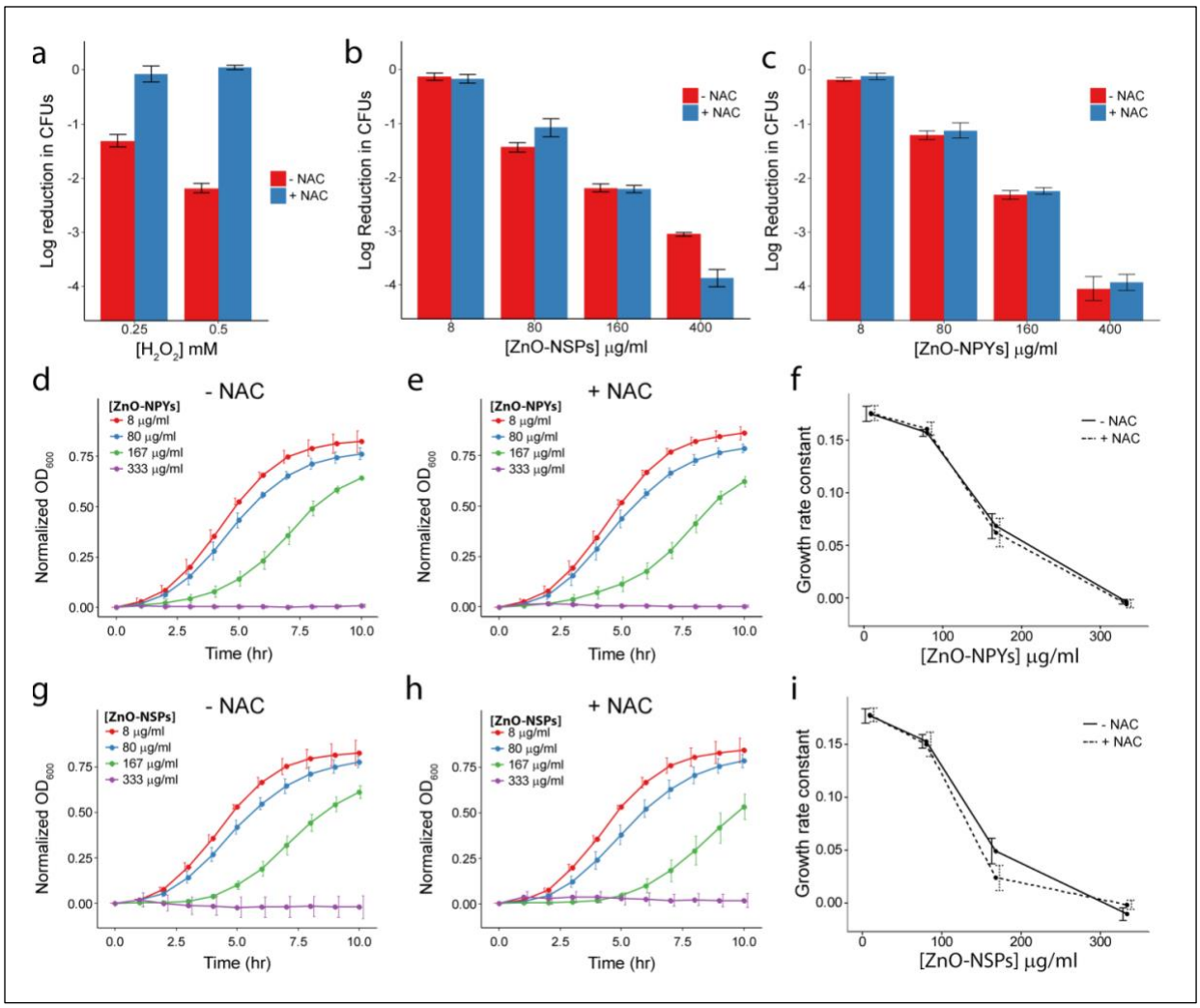

Figure 2.5 Reduction in colony counts (from $5x10^7$) observed after exposure to increasing concentrations of (a) H_2O_2, (b) ZnO-NSPs, or (c) ZnO-NPYs with and without 50 mM NAC. Growth curves of *S. aureus* in ZnO-NPYs dispersions of increasing concentration (d) without and (e) with NAC. Growth curves for *S. aureus* in ZnO-NSP dispersions (g) without and (h) with NAC. Growth rate constants as a function of (f) ZnO-NPY or (i) ZnO-NSP concentration. Error bars represent standard error of five independent experiments run on different days.

2.4.6 Toxicity of ZnO-NP Conditioned Media

The bacterial growth media *(i.e.*, TSB_G) was conditioned with ZnO-NPs as well as $ZnCl_2$ to evaluate for any potential toxicity of dissolved Zn^{2+} ions or other undetermined soluble species catalyzed by the ZnO-NP surface. ZnO-NP conditioned media had minimal to no toxicity compared to $ZnCl_2$ dissolved in media at concentrations consistent with maximum expected dissolution of ZnO (**Figure 2.6**). Although $ZnCl_2$ has a different Zn^{2+} ion release profile at the selected concentrations, we demonstrate that the total amount of Zn ions incorporated into our NPs

at highest concentration of 400ug/ml (which is relative to 300ug/ml $ZnCl_2$) are less toxic to bacteria, thereby challenging the Zn ion toxicity mechanisms of ZnO-NPs against bacteria.

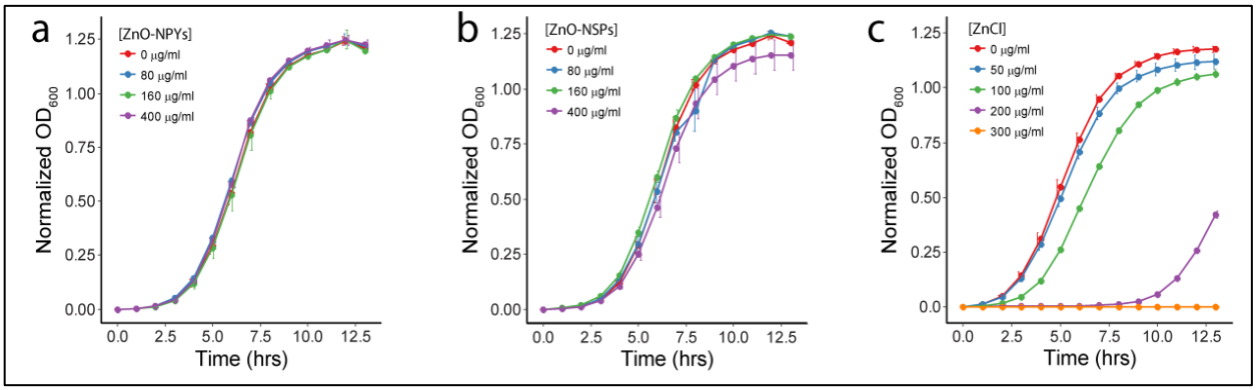

Figure 2.6 Growth curves of *S. aureus* in the media condition with ZnO (a) NPY and (b) NSP dispersions as well as (c) $ZnCl_2$. Error bars represent standard error of three independent experiments run on different days

2.4.7 Gene Expression Changes in Response to ZnO-NPs

Over 800 different gene transcripts were identified as significantly changed in *S. aureus* exposed to ZnO-NPYs compared to controls. Of those, 556 had previously identified function. Of these, 181 genes were up-regulated and 375 were down-regulated (Appendix 1). Functional classification of the genes with a significant change in expression is shown in **Figure 2.7a**. GSEA was performed to identify specific pathways or biological functions whose genes are significantly enriched in the ZnO-NP treated group (**Table 3**). Specifically, ZnO-NPY treated *S. aureus* has up-regulation of pyrimidine biosynthesis and sugar degradation and down-regulation of amino acid synthesis. Most notably, 5 of the 10 most up-regulated genes belong to the uridine monophosphate (UMP) biosynthesis pathway (**Figure 2.7b**), a subpathway of the pyrimidine biosynthesis superpathway. Interestingly 10 of the 13 oxidative stress genes significantly altered in the microarray were down regulated upon ZnO-NPs exposure, and only 3 were upregulated (**Figure 2.7**c;**Table 3**). The upregulated ROS genes experienced an average fold change of 1.91, which is not as strong as the UMP pathway, which experienced average fold changes above 10. To validate the results of the microarray experiments we selected two genes from the UMP biosynthesis pathway (*carB* and

pyrE), two amino acid biosynthesis genes (*lysC* and *leuD*), and one oxidative stress gene (*katA*) for quantitative RT-PCR (**Figure 2.7**d). The results indeed confirm the upregulation of the UMP pathway and downregulation of amino acid synthesis and oxidative stress genes.

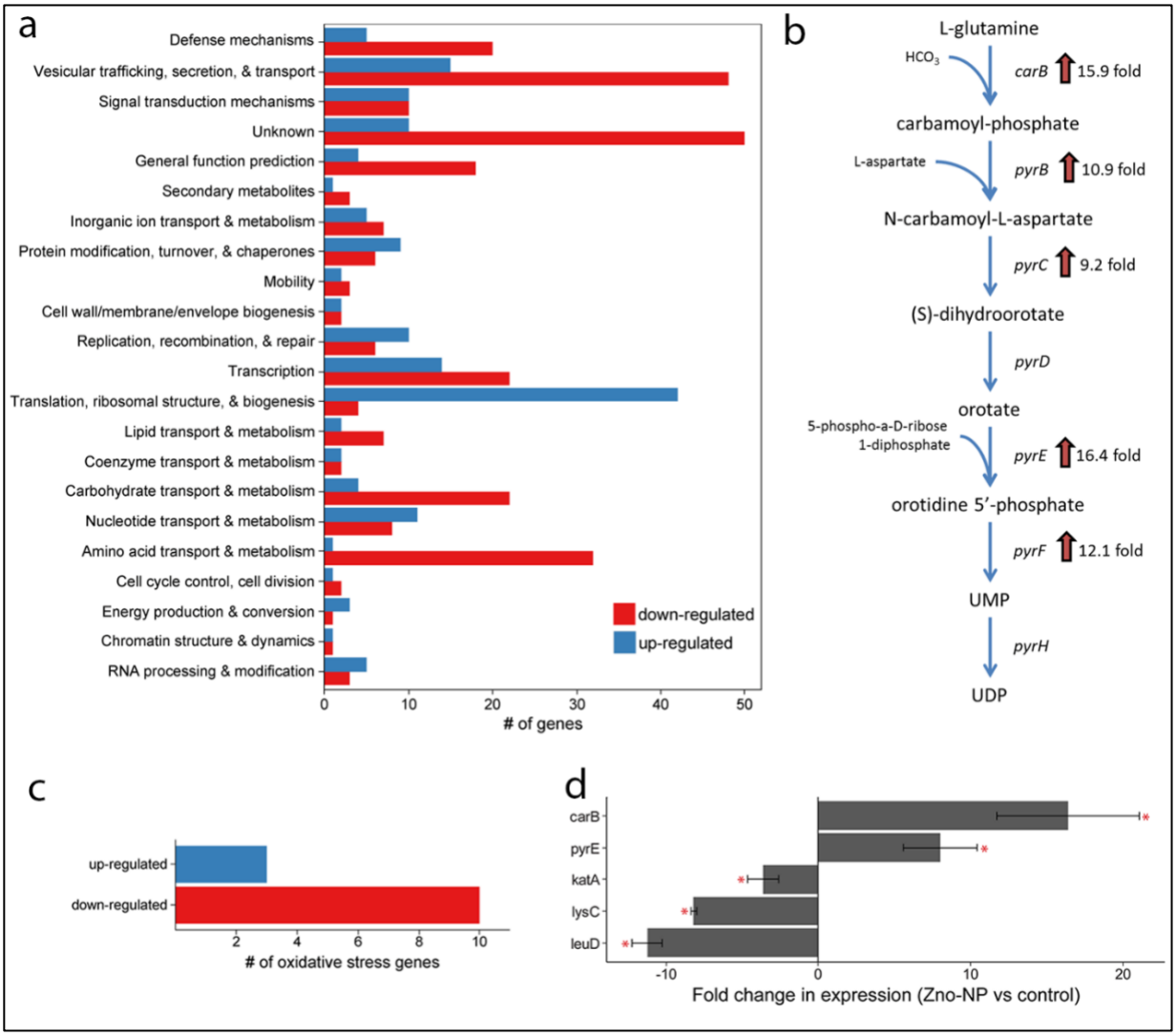

Figure 2.7 (a) Functional classification of genes with significant change in transcription upon exposure to ZnO-NPs (b) UMP biosynthesis pathway with associated enzymes and their fold-change in expression after exposure to ZnO-NPs (c) Oxidative stress genes response to ZnO-NPs exposure (d) Quantitative RT-PCR of selected genes to validate microarray results. Error bars represent standard error for n=5 independent samples with triplicate reactions for each. Red star represents $p < 0.05$.

2.5 Discussion

The work here not only addresses fundamental questions regarding the mechanism of action for ZnO-NP, but it also gives a new rationale for the clinical translation of ZnO-NPs. We demonstrate here that primary antibacterial mode of actions remains undiscovered between ZnO-NPs and bacteria. Literature suggests that the presence of ROS may lead to only sporadic cell death in bacterial biofilms, induce genetic variability, and possibly increase biofilm development[213]. Multiple studies emphasize bacteria's ability to combat excessive ROS and how they incorporate excess ROS into many metabolic and respiratory pathways for survival [193,199,200]. Interestingly, moderate excess ROS may have unexpected consequences and increase the production of extracellular polymeric substances, accelerating the growth of biofilm. For instance, this behavior is noticed in *Acinetobacter oleivorans* [214]. Evolutionary biologists have speculated that microbial biofilm's response to ROS may have evolved in response to increasing oxygen concentration on Earth, resulting in the integration of ROS into several different signaling pathways, including the switch between planktonic and biofilm forms [199]. Therefore, substances causing excessive ROS may not be the best choice to prevent biofilm growth and in particular for combating antibiotic resistant infections of indwelling medical devices. Since ZnO-NPs kill bacteria without inducing high level of oxidative stress, they can obviate ROS-inactivating pathways evolved in bacteria.

Furthermore, the presence of ROS extensively damages mammalian cells, where ROS react with polyunsaturated fatty acids in the lipid bilayer and promoting lipid peroxidation, and inactivate cellular surface proteins leading to loss of cell integrity [215]. NPs that have an ROS mediated bactericidal effect promote mammalian cell death as well. ZnO-NPs present a distinct advantage of broad spectrum antibacterial activity [128,141] similar to H_2O_2 without oxidative stress to mammalian tissues or its rapid decay related to short life time of radicals in biological media.

The data presented here indicates that oxidative stress does not play the central role in antibacterial activity of ZnO-NPs with respect to MRSA. Particularly, taking into account the gene expression results of the oxidative stress genes in response to ZnO-NPs exposure, the down regulation of majority of ROS responsive genes indicates that ROS could not be the primary mode of action for an antibacterial effect. Indeed, comparison of our results with microarray experiments with *S. aureus* exposed to H_2O_2 from the literature showed less than 10% concordance in significantly up- or down- regulated genes between the two studies [216,217]. Other work with ZnO-NPs has also shown down-regulation of oxidative stress genes [218,219]. Some have interpreted that finding as evidence against an oxidative stress mechanism while others have interpreted it as making the cells more susceptible to ROS. These disparate interpretations have continued to fuel the ZnO-NP mechanism controversy. However, the multiple lines of evidence provided here, including gene expression, comparison with H_2O_2 and lack of recovery with an antioxidant, confirm that ROS mediated toxicity is not the mechanism of action for ZnO-NPs. The persistent controversy and multiple experiments required here to investigate it, highlight the complexity in evaluating the mechanism of action of any antimicrobial NP. Specifically, confirmation or rejection of any hypothesized mechanism typically requires multiple lines of evidence including both observed cellular response as well as molecular and 'omics' data.

A consideration of other possible mechanisms with interesting possibilities for molecular and nanoscale engineering is required to further increase and/or tune NP potency [112,220]. Other mechanisms of antibacterial activity of NPs to be considered include toxic ions complexes, bacterial membrane disruption, and enzyme inhibition. In addition, the ability of NPs to suppress amyloid peptide fibrillation essential for biofilm formation may also need to be considered [221].

The ROS production hypothesis for antimicrobial activity is predicated on catalysis of ROS on the ZnO surface. We acknowledge that the techniques described here are certainly not an exhaustive evaluation of toxic species dissolved from or catalyzed by ZnO-NPs. That being said, to evaluate for the production of undetected, soluble, ZnO-NP catalyzed, toxic species, we used the supernatant of ZnO-NP dispersions in growth media to generate growth curves of *S. aureus*. If ZnO-NPs dissolve into toxic Zn^{2+} ions or they catalyze the production of soluble toxic species in media then we would expect *S. aureus* growth to be inhibited by the supernatant of ZnO-NP dispersions, similar to $ZnCl_2$ curves. However, almost no growth inhibition is observed with the supernatants of ZnO-NPs dispersions (Recall **Figure 2.6**). This suggests that the ZnO-NPs must remain dispersed with the cells to have their effect and the experimental conditions of the assays did not contribute to ion dissolution of the NPs. Furthermore, our gene expression data do not identify significant changes in expression of gene pathways related to metal ion transport.

With respect to membrane disruption, although lipid peroxidation results were negative in our study, it is possible that there are other membrane disruption mechanisms present between ZnO-NPs and Gram-positive cells. Previous studies show that NPs with different surface chemistry can differentially attach to various parts of the bacteria's surface[123,150,222,223]. Notably, lipopolysaccharides are attracted to NPs via variety of intermolecular forces including electrostatic interactions, hydrogen bonding, and van der Waals forces, that may cause lipid bilayer rupture, loss of membrane potential and cell death [224]. However, it should be noted that cell membrane compromise and lysis is a common event for most antibacterial agents, including those whose mechanism does not involve the cell membrane (*e.g.*, streptomycin). Therefore, documenting cell membrane damage in the presence of a particular NP is not sufficient. Rather the timing of loss of cell membrane integrity, proton motive force, and lysis in relation to other processes is critical.

Again, we highlight the need for multiple lines of evidence with well-defined controls to test any specific hypothesis. Of note, our gene expression studies do not show significant changes in expression of genes related to cell membrane synthesis/repair.

Considering enzyme inhibition, it was shown recently that ZnO-NPs can enter cells through membrane disruption [114,123] and cause enzyme inhibition [23] exemplified by strongly suppressed activity of β-galactosidase, an essential enzyme in bacterial metabolism. Enzymatic inhibition is not unique to β-galactosidase and may represent a family of biomolecular processes leading to suppression of bacterial growth or cellular death [143]. Ultimately, it is more than likely that several of these mechanisms together impact viability of bacteria. While the exact enzymatic targets for ZnO-NPs remain a question, our gene expression microarray data revealed a metabolic pathway, (*i.e.*, UMP biosynthesis) not previously considered for ZnO-NP mediated bacterial toxicity. Upregulation of the UMP and other pyrimidine biosynthesis pathways have been shown to be critical for continued growth in anaerobic environment [225]. The combined up-regulation of this pathway with sugar catabolism suggests that ZnO-NPs may have a profound effect on carbohydrate metabolism and bioenergetics. This is a fundamentally new mechanism of action for consideration (**Figure 2.8**). Furthermore, when compared to other analyses of staphylococcal transcriptome response to various stressors, we did not find any significant concordance with heat shock, cold shock, stringent response, SOS response, anaerobic response, or oxidative stress [216,217,226,227]. Future work on the antimicrobial effects of ZnO-NPs can now be directed at these pathways and the phenotypic manifestations of altered metabolic state.

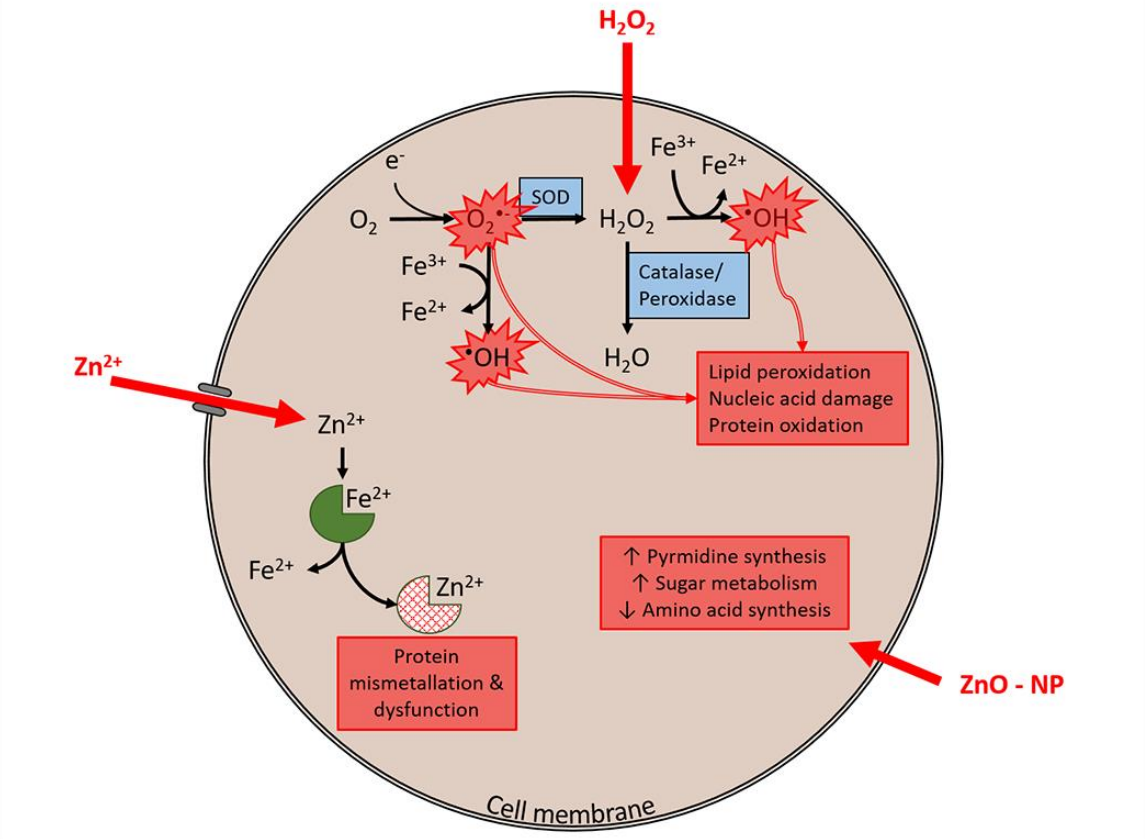

Figure 2.8 H_2O_2 readily diffuses through the cell membrane. High concentrations overwhelm catalase and peroxidase enzymes leading to hydroxyl radical formation via Fenton reaction. In addition, high concentration of H_2O_2 can inhibit superoxide dismutase (SOD) driving Haber-Weiss reaction and additional production of hydroxyl radical. These ROS (hydroxyl radical and superoxide radical) cause toxicity through lipid peroxidation, nucleic acid damage and protein oxidation. Zn^{2+} ions require cell membrane transporters to enter the cell. In high concentrations that exceed normal homeostatic mechanism these ions displace other metal ions cofactors on proteins, causing mis-metalation and resulting protein dysfunction. Evidence here suggests an alternative mechanism for ZnO-NPs. ZnO-NPs result in dramatic increases in pyrimidine biosynthesis, sugar metabolism and decreases in amino acid synthesis. This combination or cellular processes suggests that ZnO-NPs alter energy metabolism within the cell. The precise mechanism by which ZnO-NPs enter the cell and the specific intracellular molecular targets remain unclear.

It is important to note that this work is limited to *S. aureus*. However, the ZnO-NPs used in this study were shown to also be toxic to *Staphylococcus epidermidis* at these concentrations [141]. Others have shown broad antimicrobial spectrum for ZnO-NPs [219,228]. However, the generalizability of this novel potential bioenergetics mechanism involving pyrimidine and amino acid biosynthesis as well as sugar catabolism remains a question. That being said, the UMP biosynthesis pathway is quite similar for *S. aureus* and *E. coli* [225]. Furthermore, enzymes in amino acid synthesis are also quite highly conserved within bacteria [229]. This indicates that the mechanism

may be applicable to both Gram-negative and Gram-positive organisms. Although it does not appear that the UMP pathway is necessary for anaerobic metabolism in *E. coli* as it is in *S. aureus* [225]. This may explain why a higher dose of ZnO-NPs is typically required for *E. coli*. Ultimately, the surface chemistry and crystalline structure of a particular ZnO-NP preparation may have a profound effect on its interaction with the surface of a Gram-positive versus Gram-negative organism and therefore may dictate species selectivity regardless of the final mechanism [230]. Likewise, the three-dimensional shape may be important in accessibility of ZnO-NPs to specific molecular targets [23,231].

2.6 Conclusions

Here we have demonstrated that oxidative stress and toxic ion dissolution are inadequate to cause ZnO-NP mediated killing of methicillin resistant *S. aureus*. By means of gene expression analysis we demonstrate that ZnO-NPs may have a profound effect on anaerobic carbohydrate metabolism and energetics with upregulation of the UMP biosynthesis pathway being a key response. Altogether, the findings about the unexpectedly small role of ROS production and large role of alterations in carbohydrate metabolism and bioenergetics give strong indication of biomimetic mode of action of NPs [96].

2.7 Supplemental Information

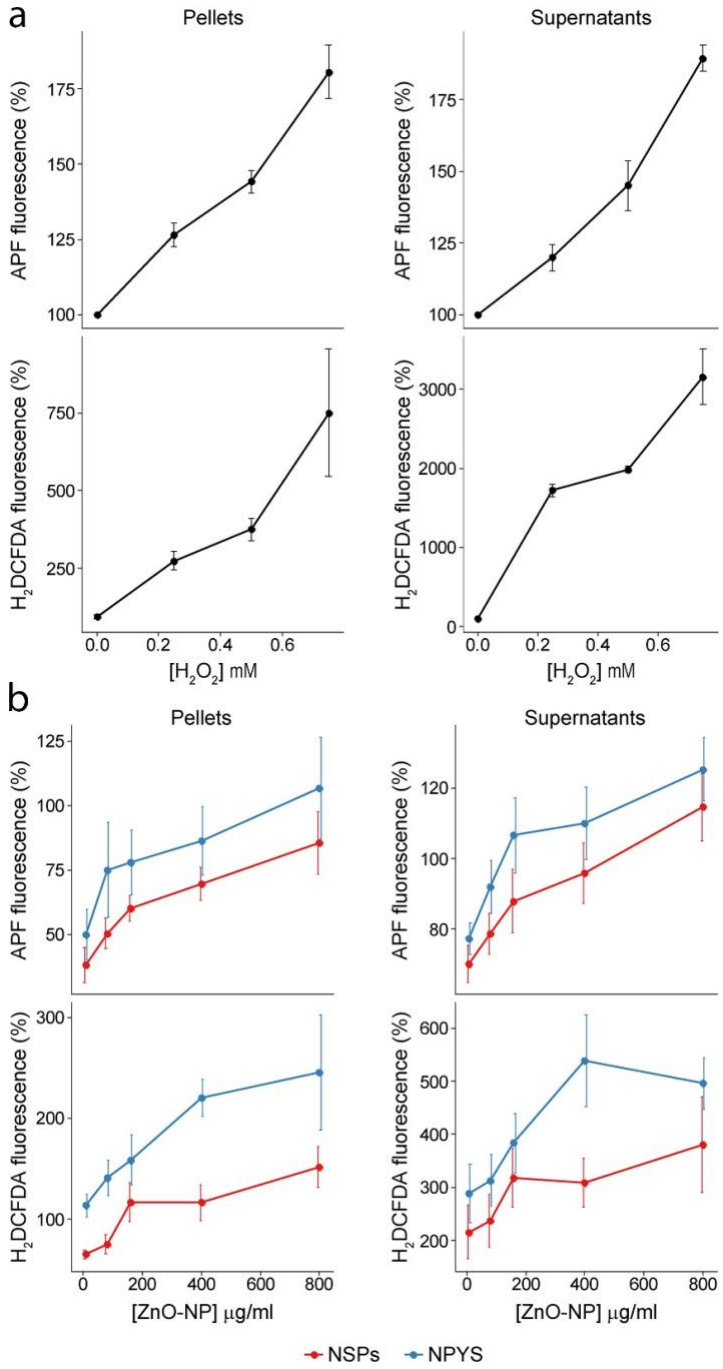

Figure S 2.9 ROS detection in bacterial pellets and supernatants by APF and H2DCFDA fluorescence after 30-minute exposure to increasing concentrations of (a) H2O2 or (b) ZnO-NSPs and -NPYs. Error bars represent standard error of five independent experiments run on different days. Note that the trends for the supernatants and pellets are identical

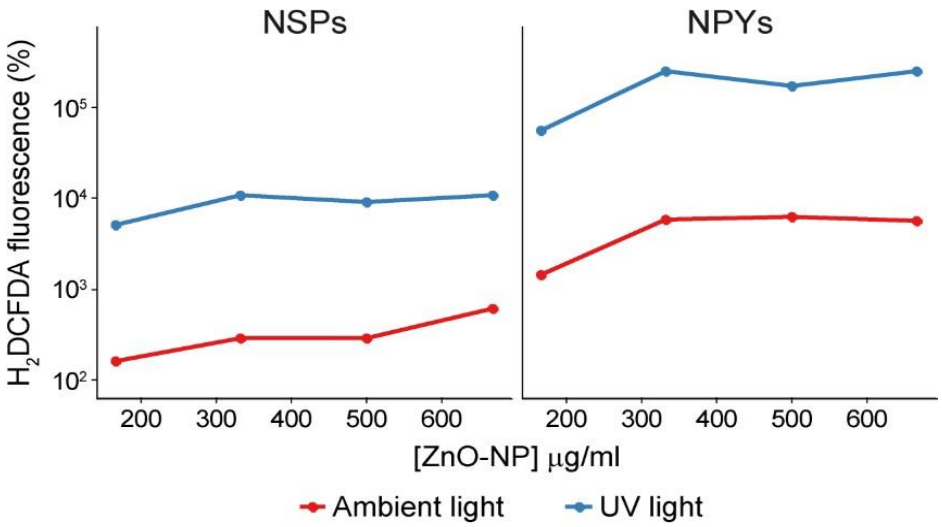

Figure S 2.10 Two minutes of UV light exposure resulted in significant increase in ROS production by ZnO-NPs as measured by H_2DCFDA fluorescence. However, the general dose dependence trend is unchanged.

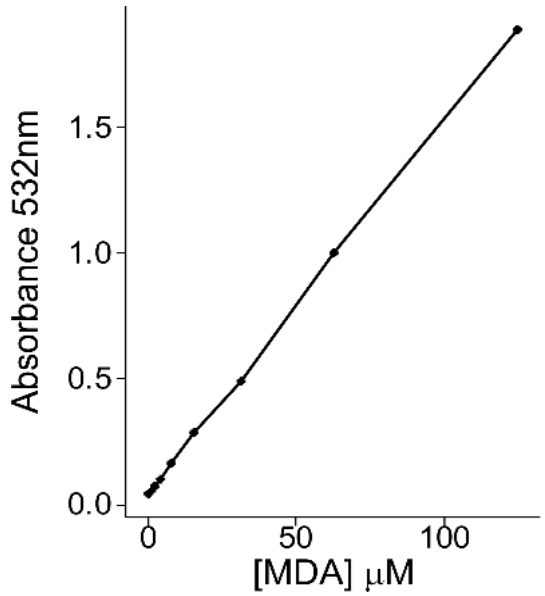

Figure S 2.11 MDA standard curve for TBARS

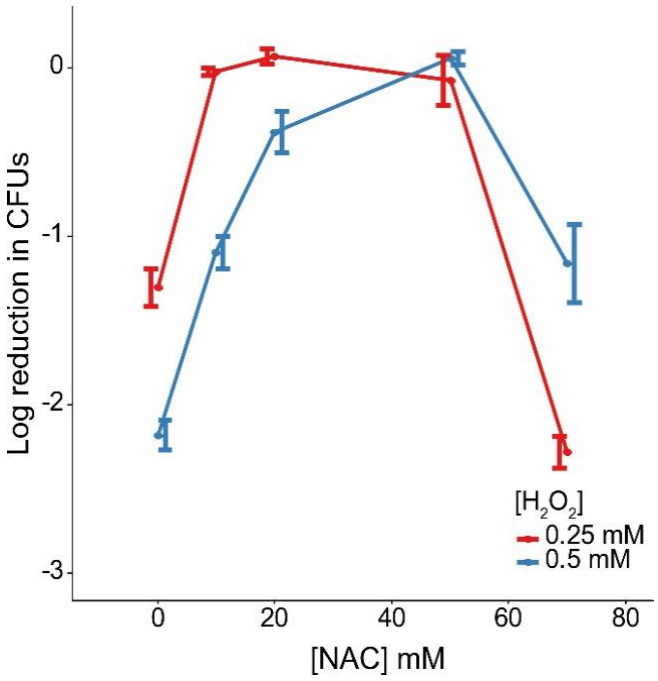

Figure S 2.12 Dose response of bacterial recovery after exposure to 0.25 and 0.5mM H_2O_2 in the presence of increasing doses of N-acetylcysteine (NAC). The initial inoculum was $5x10^7$ CFU. 50mM NAC leads to complete recovery from a >2 log reduction in colonies caused by 0.5mM H_2O_2. Increased doses of NAC beyond 50mM however, lead to toxicity and cell death.

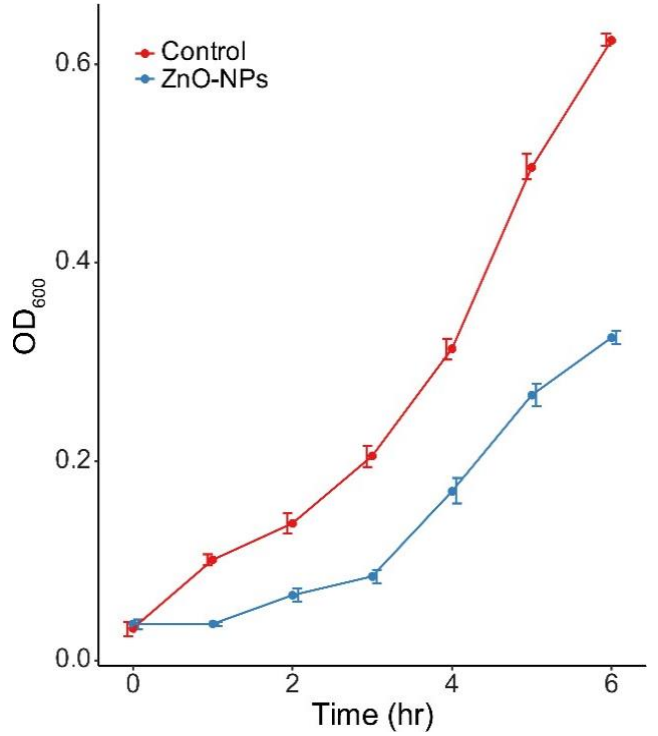

Figure S 2.13 Growth curves of S. aureus with and without 160µg/ml ZnO-NPs used for the gene expression microarray analysis. Each measurement was made in triplicate. Error bars represent standard error.

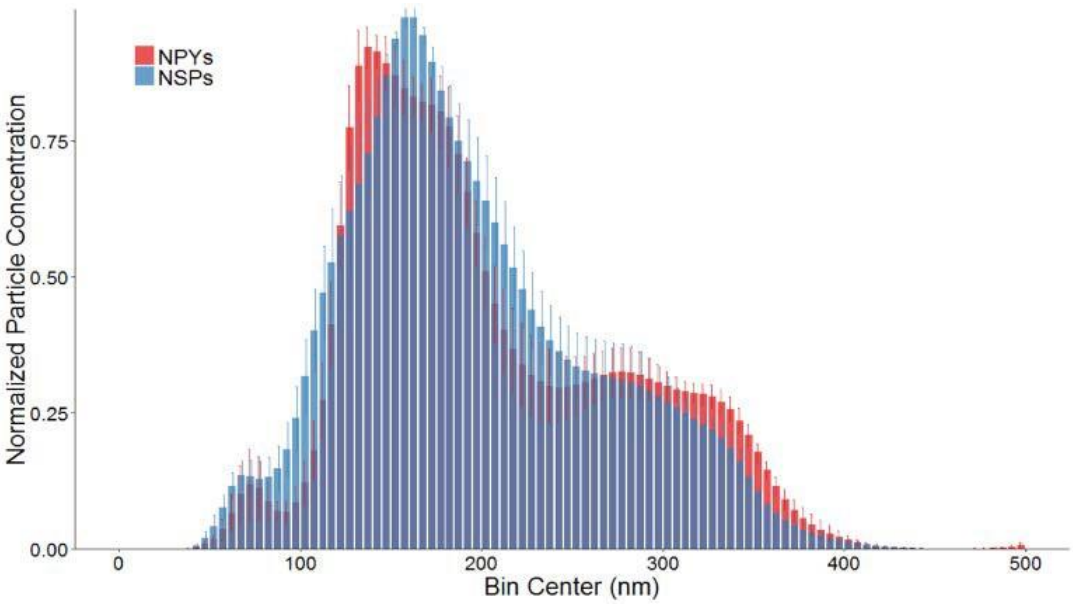

Figure S 2.14 Size distribution of nanoparticle aggregates in aqueous dispersion. Error bars represent standard deviation from 5 independent samples

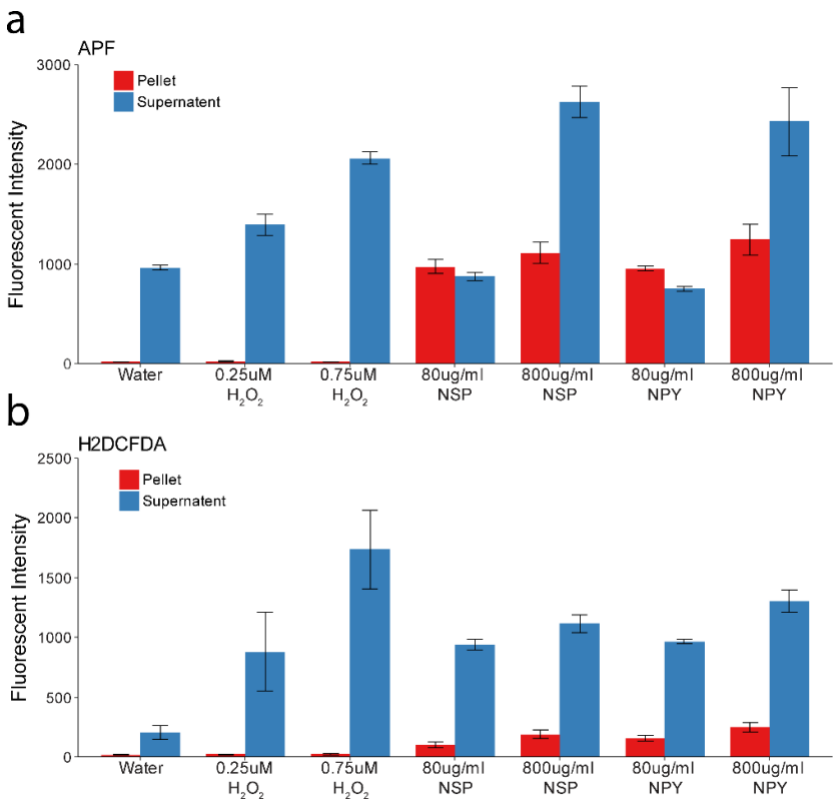

Figure S 2.15 Fluorescence of (a) APF and (b) H2DCFDA in water, H2O2, and ZnO NPs. Each measurement was made in triplicate. Error bars represent standard error of three independent experiments run on different days.

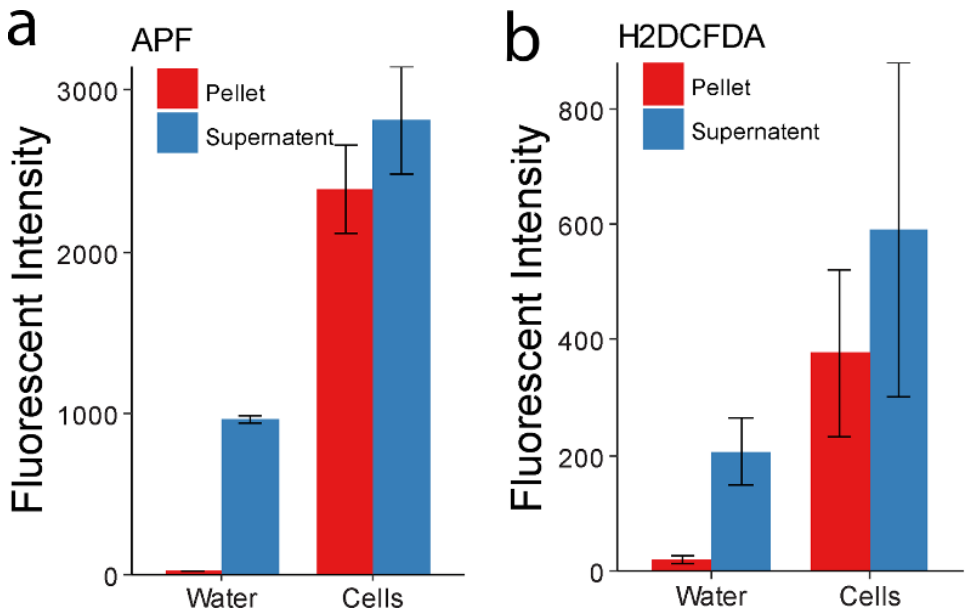

Figure S 2.16 Fluorescence of (a) APF and (b) H2DCFDA due to baseline cellular respiration. Each measurement was made in triplicate. Error bars represent standard error of three independent experiments run on different days.

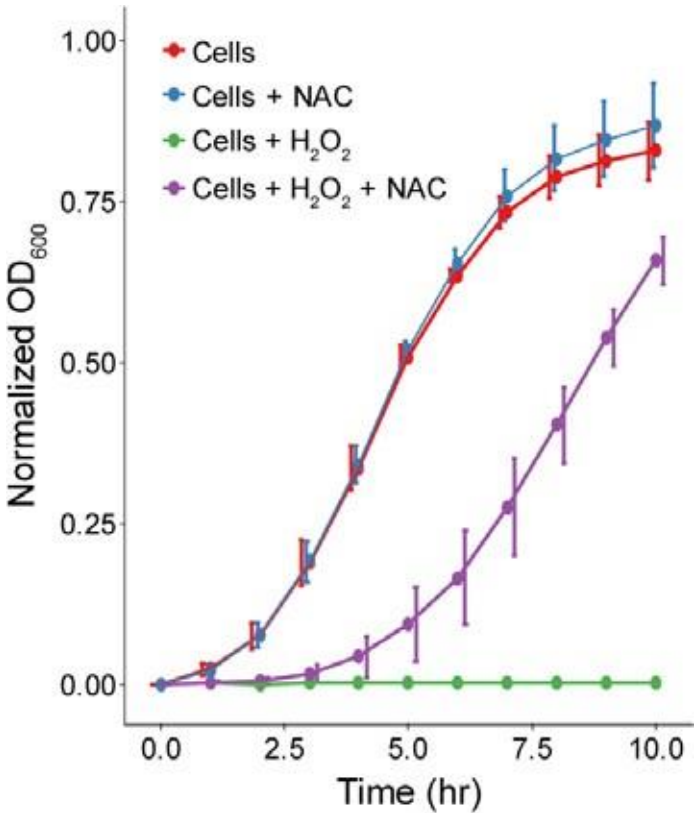

Figure S 2.17 Growth curves of S. aureus with H_2O_2, NAC and H_2O_2 plus NAC. Each measurement was made in triplicate. Error bars represent standard error of five independent experiments run on different days.

Table 2 Primer Pairs for RT-PCR Gene Expression Quantification

Orientation	Gene	Primer Sequence (5'--3')
+	*16s rRNA*	TCGTGTCGTGAGATGTTGGG
-	*16s rRNA*	GTTTGTCACCGGCAGTCAAC
+	*leuD*	GTCGTGAACATGCTGCTTGG
-	*leuD*	TGGAAACGCTTGTCTGGTGA
+	*lycC*	ATCCGCCACGTGGAAATGTA
-	*lycC*	CTGACGTCCCACAAGAAGCA
+	*katA*	GGAGCGTGACATTCGAGGAT
-	*katA*	GACCCGTCCAGAAATCCCAG
+	*pyrE*	GCTGGTATTCCACATGCAGC
-	*pyrE*	GACTGAAGATCCCCCTGTCG

Table 3 Pathways with Genes Significantly Enriched (Up or Downregulated) by ZnO-NPs

Pathways	p-values	Genes	Sub-Pathways
Downregulated			
Amino acids synthesis	0.016945	aroK ilvH ilvE rocF rocD proC rocA ilvB budB ilvC ilvD pth lysC asd dapA dapD lysA leuC leuD leuA leuB gltB arcB1 ilvA1 ilvA2 hom metX thrC thrB acsA	This class contains the pathways of biosynthesis of each of the 21 amino acids present normally in proteins.
Upregulated			
Superpathway of pyrimidine de novo biosynthesis	0.002223	pyrF pyrE pyrC pyrB carB carA dut	UTP and CTP *de novo* biosynthesis; UMP biosynthesis; Superpathway of pyrimidine ribonucleotides de novo biosynthesis; Pyrimidine deoxyribonucleotides *de novo* biosynthesis
Lactose and galactose degradation	0.02163352	lacD lacB Lac A lacC	

Table 4 Oxidation/Reduction Gene Expression Altered by ZnO-NPs

Gene	ID	Fold Change
Downrelgulated		
Nitrate reductase gamma chain (narL)	SACOL2392	-2.56
Thioredoxin	SACOL2550	-2.16
NAD dehydrogenase	SACOL0941	-2.11
Acyl carrier protein phosphodiesterase (acpD)	SACOL0190	-1.80
Succinate dehydrogenase (sdhA)	SACOL1159	-1.74
Catalase (katA)	SACOL1368	-1.72
NADP flavin oxidoreductase (frpP)	SACOL2534	-1.69
Luciferase	SACOL0394	-1.62
Thioredoxin reductase	SACOL2369	-1.59
Upregulated		
Oxidoreductase	SACOL0763	1.60
Cytochrome d ubiquinol oxidase subunit I (cydA)	SACOL1094	2.00
Cytochrome d ubiquinol oxidase subunit II (cydB)	SACOL1095	2.13

Chapter 3

Membrane Dynamics of ZnO Nanoparticles in Methicillin-Resistant *Staphylococcus aureus* and Subsequent Effects on Cell Respiration

3.1 Abstract

Zinc oxide NPs are noted to be an attractive broad-spectrum alternative to traditional small molecule antibiotics. The most commonly reported mechanism of actions are oxidative stress, Zn^{2+} ion dissolution and membrane damage. Previously we showed that ZnO-NPs induce cell death in methicillin resistant *Staphylococcus aureus* by means beyond the commonly reported mechanisms of oxidative stress and the generation of toxic ions. We identified that ZnO-NPs strongly affect specific pathways: particularly pyrimidine biosynthesis, carbohydrate degradation and amino acid synthesis. Therefore, in this chapter, we further explore how ZnO-NPs affect pathways and study their interaction with cell membrane. We show that within 60 minutes of exposure, ZnO-NPs reduce bacterial growth with minimal disruption to the cell membrane. More thorough investigation utilizing scanning transmission electron microscopy (STEM) shows that ZnO-NPs penetrate bacterial cells as early as 5 minutes post-exposure without causing observable cell damage. Immediately after exposure, ZnO-NPs exhibit a dose dependent reduction of cellular respiration, as measured through oxygen consumption rate. With prolonged NPs exposure, cells switch from aerobic to anaerobic respiration, and eventually to cell death. Our data suggest that a time sensitive antimicrobial mechanism of action exists for ZnO-NPs, whereby cell metabolism is immediately affected upon NPs exposure and membrane damage is a downstream response to

bacterial cell death. The ZnO-NPs' interaction with metabolic pathways within *S.aureus* indicates a unique mechanism that has previously not been identified.

3.2 Introduction

Among other metal oxide NPs, ZnO appears to be one of the most promising for clinical translation due to its high potency against antibiotic resistant bacterial strains [232], low toxicity to mammalian cells [122,201,233], and low cost. Apart from antimicrobial activity induced by dispersions, surfaces coated with ZnO-NPs, [128,150] for instance layer-by-layer assembled (LbL) coatings, [234,235] suppress biofilm formation of common bacterial pathogens[141] as well. Staphylococcal adhesion and biofilm growth can be reduced by as much as 95% for NPs of specific shapes [141]. These findings motivate an in-depth look into the fundamental mechanism of action for ZnO-NPs.

In Chapter 2 we have shown that Zn^{2+} ion release cannot be the only mechanism of action via comparison of growth curves of ZnO-NP conditioned media and $ZnCl_2$ dissolution. Furthermore, there is no change in gene expression for metal ion transport [144]. We also disproved the notion that ZnO-NPs antimicrobial activity is due to ROS generation by comparing its potency to Hydrogen Peroxide (H_2O_2)[121,101]. The amount of ROS required was much greater than what was generated by ZnO-NPs compared to H_2O_2 and was not mitigated by the administration of antioxidant *N*-acetylcysteine. Additionally, gene expression data indicated the downregulation of oxidative stress genes, and thus ROS could not be the primary mode of action[141]. We showed evidence pointing to multiple metabolic pathways being involved in the antimicrobial activity of ZnO NPs.

The final commonly reported mechanism of action of ZnO-NP's antibacterial activity suggests that ZnO-NPs damage the bacterial cell membrane[153–157]. Since most ZnO-NPs are positively charged, it is expected that they can interact with the negatively charged bacterial membrane.

However, membrane interaction is complex and may provide the opportunity for many downstream and consequential effects of ZnO-NPs on bacterial cells. This interaction can cause lysis and loss of structural integrity which can be identified through changes in metabolism and cell entry. The order and causality of the NPs and membrane interaction are unknown.

In this chapter, we explore the antibacterial mechanism of ZnO-NYPs by focusing on the membrane and metabolism of Methicillin-resistant *Staphylococcus aureus*. We present a time course of bacterial response to ZnO-NPYs exposure and the cellular location of ZnO-NPYs through multiple microscopy methods.

3.3 Materials and Methods

3.3.1 Bacterial Strain, Media and Growth Conditions

Methicillin-resistant *Staphylococcus aureus* strain USA300 was used in all experiments since it is a well characterized strain of *S. aureus*. A glycerol stock of the strain was maintained at −80°C and was plated on tryptic soy agar. Single colony inoculates were grown in synthetic nasal medium (SNM)[146] under shaking conditions at 37°C. SNM is reported to mimic human nasal conditions[146]. Krismer, B. *et al.* analyzed human nasal secretions by metabolomics and found potential nutrients in low concentrations. We chose to study *S. aureus* and ZnO-NPYs interactions in this media as it represents a suitable *in vivo* surrogate environment for *in vitro* studies. The simplicity and complete understanding of each component of SNM allowed us to control for our NP surface chemistry and stability within the media. Bacterial growth for experiments first required the growth of an overnight culture, which was then diluted 1:10 into SNM for mid-log culture-optical density of 0.55-0.64 at 600nm (OD600). Mid-log reached after 18 hr of incubation (slow growth due to the minimal nutrient content of the media), and this culture was used for all experiments.

3.3.2 ZnO NPYs Synthesis and Characterization

ZnO nanopyramids with hexagonal base (ZnO-NPYs) were synthesized and characterized in our laboratory[206]. These ZnO-NPYs were synthesized without capping agents or surfactants and have previously shown strong antibacterial activity towards *S. aureus*[101,141]. Briefly, ZnO-NPYs were synthesized by mixing 0.2 g potassium hydroxide with 5.5 g $Zn(Ac)_2 \cdot 2H_2O$ and adding anhydrous methanol and refluxing for 48h. After synthesis, the white precipitate was purified by washing three times with methanol (centrifuging at 8,000g) and then frozen in Milli-Q® water (-80°C) to be lyophilized for 24 hours. The dry powder was extensively characterized as reported in Chapter 2.

3.3.3 ZnO-NPYs Solution Preparation and Dose-Response

Dry ZnO-NPYs powder was measured and reconstituted into SNM and sonicated for 5 minutes for bacterial experiments. Minimum inhibitory concentration (MIC) for 1.0 $x10^6$ bacterial cells was optimized using various concentrations of ZnO-NPYs. The MIC for the ZnO-NPYs was determined to be 10µg/ml. Which is drastically lower from MIC of ZnO-NPYs (660µg/ml) in a tryptic soy broth as demonstrated before[141] and Chapter 2. Concentrations of ZnO-NPYs include 2.5, 5.0, and 10.0µg/ml. All antibiotics and enzymes were purchased from Sigma. Growth curves were generated by adding $1.0x10^6$ bacterial cells (10µL of SNM mid-log culture, 0.55-0.64 at OD600) to various ZnO-NPYs concentrations and controls. Each sample, 100µL, was then plated in a 96well plate, and growth curves were measured turbidometrically (OD600) each hour for 15 hours under aerobic shaking conditions (BioTEK Synergy 2 Plate Reader, Vermont, USA).

3.3.4 Lactate Dehydrogenase Detection

Lactate dehydrogenase (LDH) was quantified by using Cell Biolabs' CytoSelect™ LDH Cytotoxicity Assay Kit. Sonicated ZnO-NPYs solutions and antibiotics were mixed with 1.0

x10^6/ml mid-log USA300 culture in SNM and exposed to the LDH cytotoxicity assay reagent. Antibiotics, chloramphenicol, and streptomycin were used as controls, and lysostaphin used as positive control. Their MIC was identified to be 4µg/ml, 2µg/ml, and 1 unit, respectively. Cells were exposed to the NPYs and controls for 10, 20, 30, 60, 120, and 180 minutes. OD was collected at 490nm. SNM with cells was used as the negative control. The relative cytotoxicity percentage was calculated by equation

Equation 1 $OD_{experimental} - OD_{negative\ control}) / (OD_{positive\ control} - OD_{negative\ control}) * 100$

in where negative control is cells in SNM and positive control is lysostaphin.

3.3.5 Membrane Depolarization

BacLight™ Bacterial Membrane Potential Kit (ThermoFisher) was used to quantify bacterial membrane depolarization. The fluorescent membrane potential indicator -3,3'-Diethyloxacarbocyanine Iodide ($DiOC_2(3)$) was used to detect membrane depolarization. $DiOC_2(3)$ is a fluorescence dye which exhibits red fluorescence in cell with intact membrane potential and shifts toward green emission in compromised cells. The red to green fluorescence shift in the bacterial populations were distinguished using a flow cytometer (Bio-Rad ZE5 Cell Analyzer). Samples were prepared by exposing 1.0 x 10^6 mid-log-cultured cells to 2.5, 5, 10, 15µg/ml ZnO-NYPs for 15, 30, 60, 120, and 180 minutes at 37°C in shaking conditions (200rpm). Samples were stained with $DiOC_2(3)$ prior to inject into the instrument, the final concentration of 30uM for 10 minutes at room temperature. Carbonyl cyanide m-chlorophenyl hydrazine (CCCP) is a proton ionophore and causes membrane depolarization as it reduces ATP production by efflux pump inhibition and increases membrane permeability in bacteria[236,237]. CCCP was used as a positive control for membrane depolarization, and cells were exposed to this ionophore for 20 minutes before measurement.

Excitation/emission used for DiOC2(3) was 482/497, with a flow cytometer laser line of 488. Fluorescein and Texas Red dye filters were used. The forward scatter, side scatter, and fluorescence was collected with logarithmic signal amplification. An unstained control sample was used to locate bacterial populations in the forward and side scatter channels. Side scatter was used as the parameter for setting acquisition triggers. The threshold level was set to minimize electronic noise appearing on the instrument. Forward versus side scatter was used to gate bacteria, and fluorescence photomultiplier tube voltages were adjusted such that the green and red MFI values were approximately equal without compensation. The acquisition was performed with washing between each sample and thresholding on FSC at a value of 1,000. Using the ratiometric parameter, calculated as follows

Equation 2 (RC mean) – (GC mean) + 1.5(# of channels per decade).

The 1.5-decade offset assures that the ratiometric values are positive. The number of channels per decade*1.5 in our system was 384. Therefore, our ratiometric parameter was calculated as

Equation 3 [(red value) – (green value) +384].

Data analysis was compiled using DenovoFCS software. On a ratiometric histogram, markers were set around positive control peak (+CCCP) and negative control (-CCCP), cell in SNM) peaks to record the mean ratio values. Membrane depolarization was determined as the percentage for ZnO-NPYs exposed cells and controls that fell within the +CCCP marker.

3.3.6 Oxygen Consumption

The Seahorse XFe96 Analyzer (Agilent) was used to quantitate live-cell oxygen consumption rates (OCR). Mid-log *S. aureus* cells, grown to an OD600 of ~0.5, were plated into the XF Cell Culture Microplates at a cell density of 1.0 x 10^6/well and were centrifuged for 10 min at 1,400 × g in a Heraeus Multifuge ×1R (M-20 rotor) to attach them to the plates. After centrifugation, fresh SNM

media was added to each well for a final volume of 180µL. To assure uniform cellular seeding, initial OCR was calibrated for ten cycles (30 min) before the injection of ZnO-NPYs (2.5, 5, 10 µg/ml). Measurement was taken for 100 minutes. Maximal OCR read on the SeaHorse is ~700–800 pmol/min, after which point the consumption rate exceeds the replenishment of the system and curves show a false declination in OCR; we did not notice this in our system.

3.3.7 Electron Microscopy

Mid-log-cultured *S. aureus* cells were exposed to 10µg/ml ZnO-NPYs in MilliQ water for certain minutes (1, 5, 10, 15 and 30 min) and fixed in 2.5% glutaraldehyde (microscopy grade) for 24h at 4°C. Samples were placed onto cupper-based carbon TEM grids (TedPella), washed twice with MilliQ water, and serially dehydrated with ethanol (30-100%) within the incubation period of 10 minutes at room temperature between each concentration switch.

Transmission electron microscopy (TEM) images of ZnO-NPYs were obtained with JEOL 3011 high-resolution electron microscope equipped with a CCD camera and a field emission gun (FEG) operating at 300 kV. Scanning electron microscopy (SEM-TLD) imaging, high-angle annular dark-field scanning transmission electron microscopy (HAADF-STEM) imaging, and focused ion beam slicing (FIB) were done with FEI Helios 650 Nanolab SEM/FIB. SEM images of cells were obtained with a through-the-lens detector (TLD) at 30kV and 0.16nA; only vesicles were imaged at 24kV with 0.20nA current. HAADF-STEM images were obtained with the STEM detector under 30 kV with a current of 0.40nA. FIB was done with deposition of platinum (first) and carbon (second), and then sliced with ion beam and imaged at 10kV and 0.20nA. Elemental mapping and energy-dispersive X-ray (EDX) along with HAADF-STEM images were obtained with Thermo Fisher Talos F200X G2, a 200 kV FEG scanning transmission electron microscope

(S/TEM) equipped with Super-X window-less detector consists of four equal crystals with an active area of 4 × 30 mm2 and a solid angle of 0.9 srad.

3.3.8 Nanolive Microscopy

Mid-log cultures *S. aureus* cells were again exposed to 10µg/ml ZnO-NPYs in a flow channel slide with a #1.5H glass bottom (Ibidi) and channel height of 450µm. After exposing cells to ZnO-NPY solution, the cells were filled to the channel and let them settle at the bottom of the slide for 10 minutes. Samples were imaged under a 10x objective on a Nanolive 3D Cell Explorer-fluo label-free imaging of live cells.

3.3.9 Statistical Analysis

All data presented in this study are displayed as mean plus or minus standard error of the mean unless otherwise stated. To evaluate the role of ZnO-NPYs on *S. aureus* membrane and cellular respiration, simultaneous measurements are made for membrane depolarization (fluorescence of $DiOC_2(3)$), membrane damage (LDH release assay), and cell respiration inhibition (OCR) measurements. Each measurement was performed in triplicates, and at least 5 independent experiments were run on different days.

3.4 Results

3.4.1 ZnO-NPYs Effect on *S. aureus* Aerobic Metabolism

3.4.1.1 LDH Release Assay

Lactate dehydrogenase (LDH) release assay was used to indicate membrane damage or cytotoxicity in response to ZnO-NPYs and antibiotics. No immediate membrane damage was noticed until 60 min expose time (**Figure 3.1**). LDH release (% Lysis) increases after 60 min of

exposure to ZnO-NPYs. During the first 30-minute of ZnO-NPYs exposure, cells release little to no LDH from the cells comparing to control, indicating no significant membrane damage. However, with an increased incubation period of 60-180 minutes, membrane damage is evident (% lysis increases up to 50 %) in a NP dose dependent manner. Streptomycin, a bactericidal, and chloramphenicol, a bacteriostatic, antibiotics were used as controls for this assay as they are known for having membrane damage as a downstream effect of their mechanism of action. Both antibiotics' mechanism of action is the inhibition of protein synthesis through binding to ribosomal subunits[238–240]. Streptomycin inhibits polypeptide synthesis and forces misreads[240]. It has been proposed that these polypeptides can still incorporate with the membrane causing them to be leaky to small molecules which is important for our work because we are expecting membrane damage as a downstream effect of the mechanism[241]. Chloramphenicol stops mRNA translation as well and causes jamming of translocation complexes on the cell membrane, which results in unfolded proteins accumulation in cytoplasm.[242,243]. As a downstream of effect of this action, cell membrane loses its integrity and LDH release increases. As expected, both antibiotic samples demonstrate strong membrane damage within 30 min exposure to cells. Lysostaphin, on the other hand, directly targets crosslinking in the peptidoglycan of *Staphylococci*. Therefore, it has a strong immediate membrane damage action, and LDH releases immediately after exposure to cells. For this reason, lysostaphin is used to set 100% lysis point and the percentage calculations of other samples are made based on lysostaphin's LDH release at each time point (**Figure S 3.8**).

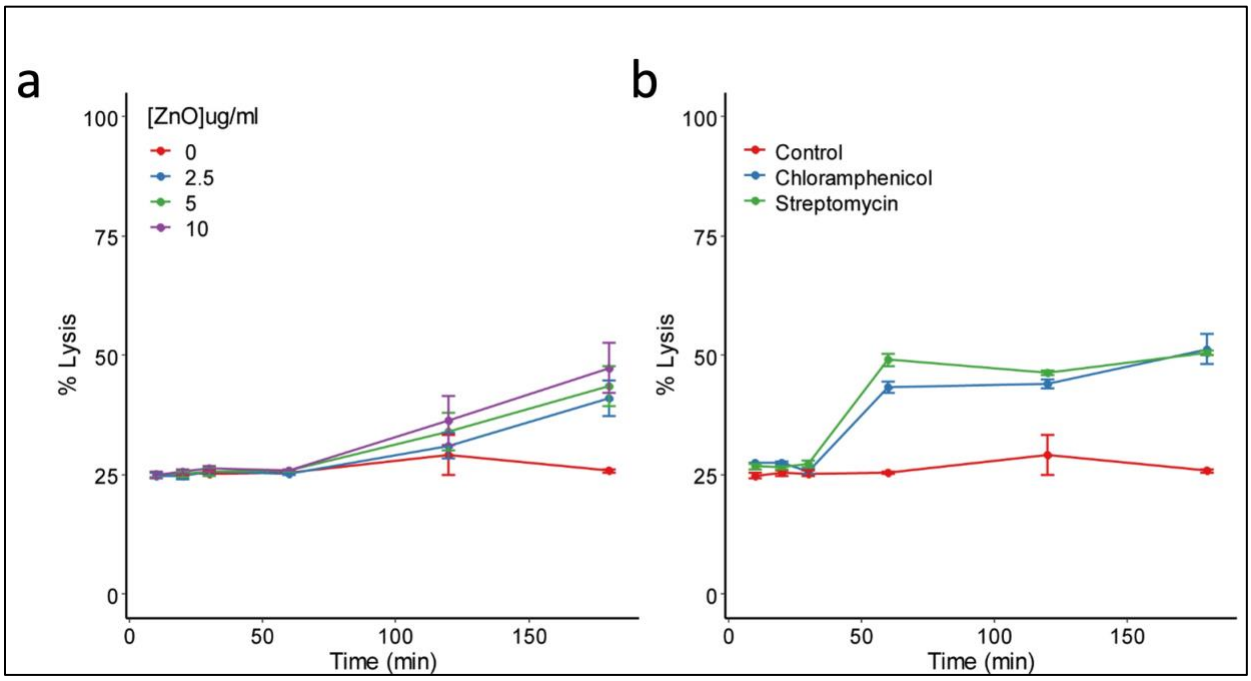

Figure 3.1 LDH release assay for cells exposed to ZnO-NPYs and antibiotics. % Lysis of cells (a) exposed to ZnO-NPYs in concentration of 2.5, 5 and 10 µg/ml, (b) treated with chloramphenicol and streptomycin antibiotics. Control for each experiment is cells in SNM media. Lysostaphin results in Figure S1 are used for percentage calculations. Error bars represent standard error of five independent experiments run on different days.

3.4.1.2 Oxygen Consumption

Extracellular measurement of oxygen consumption is a simple and powerful way to monitor respiration rates and a good assessment for total energy metabolism[244]. Oxygen consumption rate as the result of cellular respiration is determined by a measurement of the amount of dissolved oxygen in the medium. There is an observed dose-dependent decrease in oxygen consumption rate with increased concentrations of ZnO-NPY (**Figure 3.2a**), whereas no significant change is observed for antibiotics (**Figure 3.2b**). The system is calibrated with 10 cycles for 30 minutes before adding ZnO-NPYs or antibiotics at time 0. Data collected over the calibration (30 min) are averaged to yield the basal OCR (**Figure 3.2b**). OCR change over time (ΔOCR/ΔTime) is calculated by subtracting the basal values from the values at maximum incubation time (100 min). ΔOCR/ΔTime clearly decreases as ZnO-NPYs concentration increases.

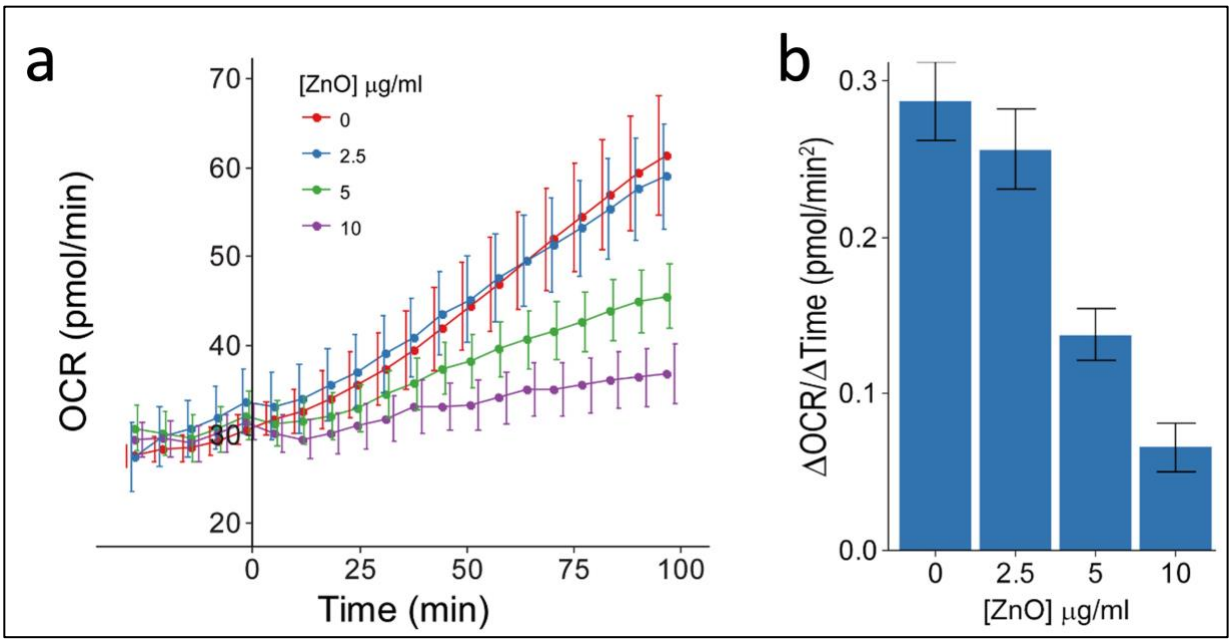

Figure 3.2 Oxygen consumption rate (OCR) of the cells exposed to (a) different concentration of ZnO-NPYs. ZnO-NPYs are added to cells at time 0, after 10 calibration cycles (30min) (c) OCR change over time for ZnO-NPYs exposed cells; and is calculated based on basal data calculated the average OCR during calibration time. Control is cells in SNM media. Error bars represent standard error of five independent experiments run on different days.

3.4.1.3 Membrane Depolarization

CCCP is a proton ionophore and causes membrane depolarization as it reduces ATP production by efflux pump inhibition and increases membrane permeability in bacteria[236,237]. CCCP, positive control for membrane depolarization, was used to calculate % membrane depolarization of ZnO-NPYs exposed cells and controls (**Figure 3.3a**). The ratio of red to green fluorescence intensity was plotted and used as a size-independent indicator of membrane potential (**Figure 3.3b**). Based on the % depolarization data, ZnO-NPYs do not cause any significant membrane depolarization up until 180 min compared to control (**Figure 3.3c**).

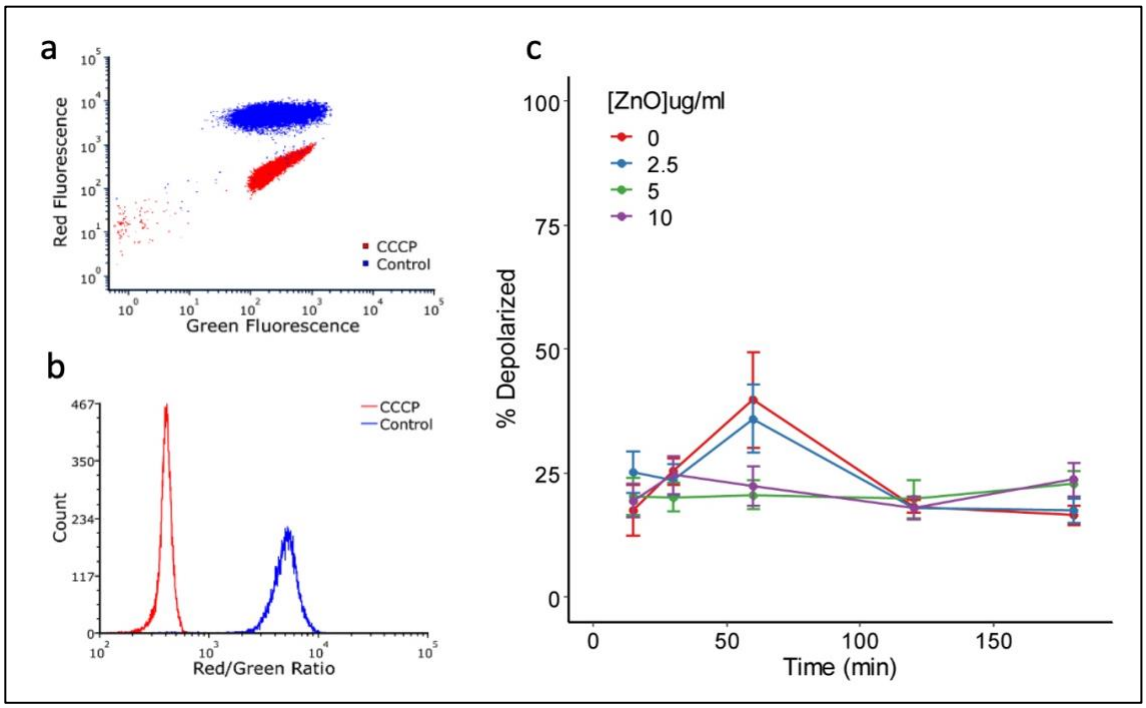

Figure 3.3 Membrane depolarization of cells exposed to ZnO-NPYs and antibiotics. (a) % depolarization of cells exposed to different concentration of ZnO-NPYs (b) Flow cytometer results for positive (CCCP) and negative controls. (c) The ratio of red to green fluorescence intensity was used as a size-independent indicator of membrane potential. Control in graph is cells in SNM media. Error bars represent standard error of five independent experiments run on different days.

3.4.2 Microscopy Analysis

ZnO NPYs are positively charged NP, therefore their interaction with cell membrane is expected. However, this electrostatic interaction cannot simply explain the mechanism of action or cell entry. Here, we will further investigate the NP- membrane interaction via different imaging method. Each method has limitations and disadvantages, for example, in FIB imaging NP on the surface can be dragged into cytoplasm and cause misleading results. Therefore, we utilized several imaging techniques and analysis method to confirm ZnO-NPYs membrane interaction and cell entry.

3.4.2.1 ZnO-NPYs

ZnO-NPYs are characterized under TEM microscopy (**Figure 3.4**). TEM images confirm ZnO-NPYs are within 15 nm range and are crystalline hexagonal based-pyramid NPs.

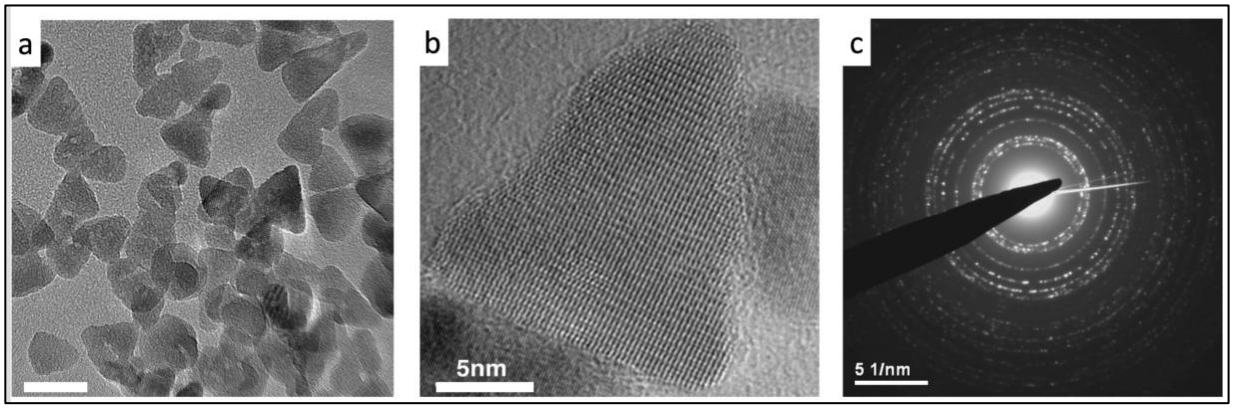

Figure 3.4 (a-b) TEM images of ZnO-NPYs. (b) High-resolution TEM (HR-TEM) image at high magnification (c) SAED pattern of ZnO-NPYs. Scale bar: (a) 20nm, (b) 5nm

3.4.2.2 ZnO-NPYs Entry to Cells

There is an observed time-dependent ZnO-NPYs accumulation on the cell surface, cell entry, and aggregation inside the cells (**Figure 3.5**). In TEM images, we started to see ZnO-NPYs accumulate on the cell surface within 1 minute after exposure (**Figure 3.5 a-b**). ZnO-NPYs, dark spots, accumulate inside the cells after 5 min of exposure (**Figure 3.5c**), and after 30 min of exposure, the cell lysis (**Figure 3.5 f-red circle**). This data led us to hypothesize that ZnO are entering cells.

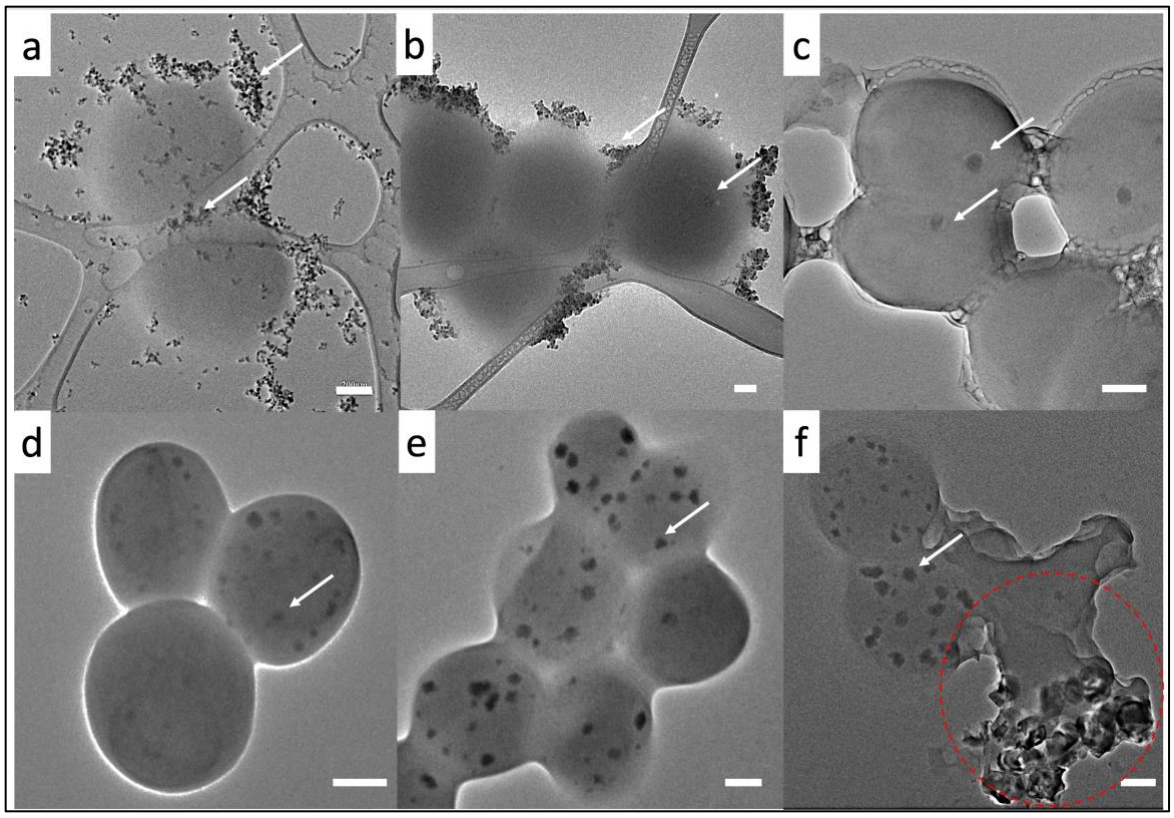

Figure 3.5 TEM images ZnO-NPYs exposed cells in time dependent experiment. Cells are exposed to ZnO-NPYs for (a) 1 minute without wash (b) 1 minute (c) 5 min (d) 10 min (e) 15 min (f) 30 min. All samples are washed before fixation unless otherwise differently stated. ZnO-NPYs or their accumulations in cells are marked with arrow in each image. Dotted red circle in (f) shows cell lysis after 30min exposure. Scale bar: 200nm

We also performed HAADF-STEM and SEM-TLD imaging to confirm these dark spots are inside the cells but not on the surface (**Figure S 3.9**). SEM-TLD images show secondary electrons coming from the just the cell surface. HAADF-STEM images, on the other hand, show an annular dark field image formed by very high angle, incoherently scattered electrons. HAADF is highly sensitive to variations in the atomic number of atoms in the sample and the detector senses a greater signal from elements with a higher atomic number (heavier elements). This cause the ZnO-NPYs to appear brighter in the resulting image as opposed to TEM images (See Chapter 3.7.2). We further performed elemental mapping to confirm whether the spots contains ZnO-NPYs (**Figure 3.6**). Co-localization of Zn and O on the bright spots confirms ZnO-NPYs entry (**Figure 3.6a)**. The intensity of Zn and O increase within these spots (**Figure 3.6b**). On the other hand, we do not

observe any Zn signal in cell only samples (See Chapter 3.7.3). We therefore believe that ZnO-NPYs enter and start aggregating inside the cells. As the number of NPs increase in the cells, the number of bright spots increase in the HAADF-STEM images (See Chapter 3.7.4). We visualized ZnO containing spots localizing inside cells via Focused ion beam (FIB) slicing on ZnO-NPYs exposed cells. The sliced images show that the Zn containing spots are located inside the NP exposed cells (**Figure S 3.17**).

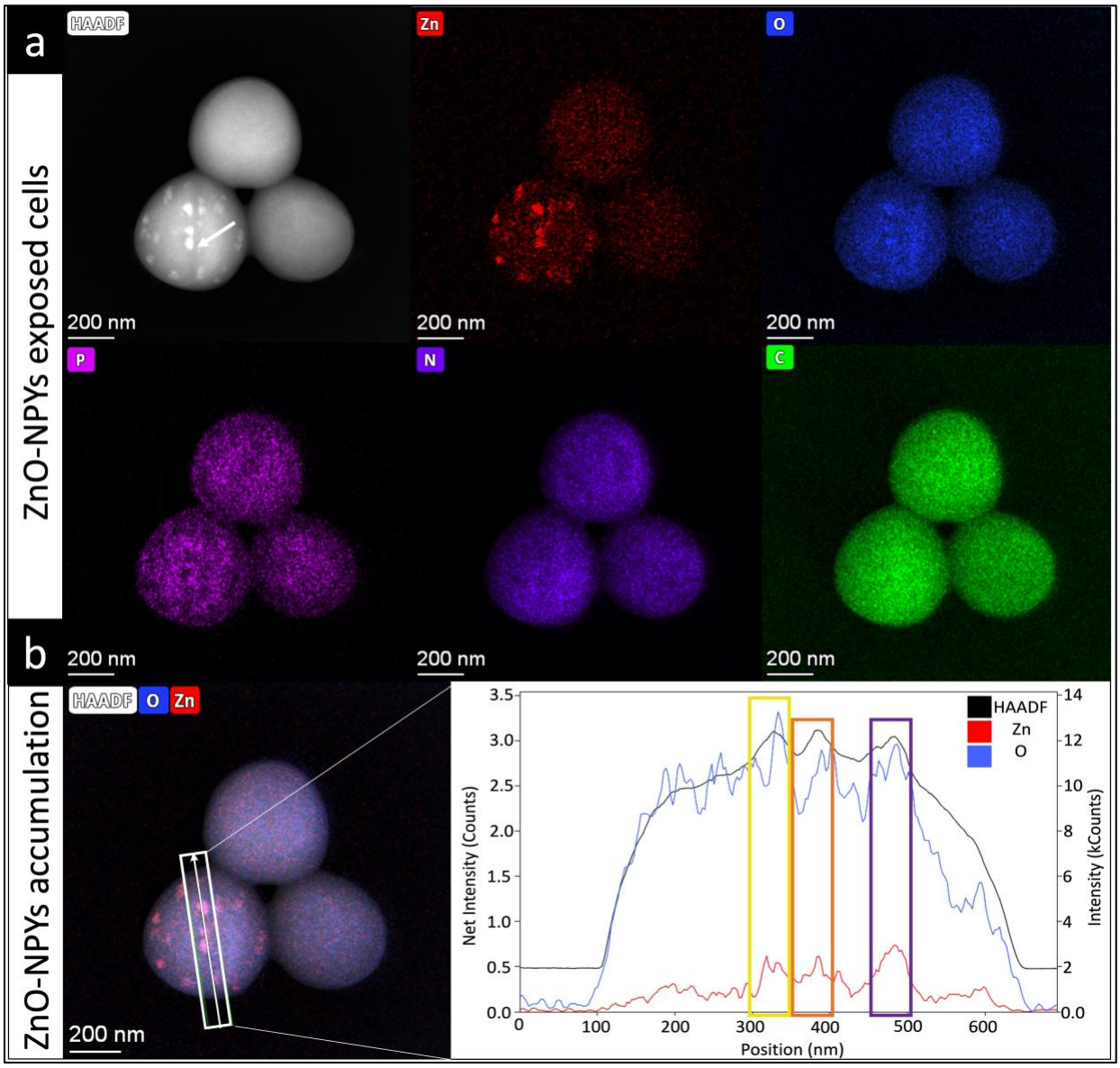

Figure 3.6 (a) Elemental analysis of ZnO-NPYs exposed cells after 10 min of exposure along with HAADF-STEM image (b) Intensity profile of ZnO-NPY accumulation in cells. (Zn-zinc, O-oxygen, P-phosphorus, N-nitrogen, and C-carbon). Bright spots (one of them is marked with an arrow) in HAADF are an accumulation of ZnO-NPYs in cells. (b) An overlay image of HAADF, Zn and O. White box in this image specifies an area for intensity profile. The graph shows intensity profile for each image HAADF (black line), Zn (red line) and O (blue line). Yellow, orange and purple boxes show 3 different ZnO-NPYs accumulated spots. Zn and O signal to background (cell) ratio is higher in these spots. These spots are measured ~50nm in diameter based on this graph's x-axes. Scale bar: 200nm

3.4.2.3 Nanolive Imaging

Further alternative confirmation of ZnO-NPYs entry was obtained by the Nanolive 3D Cell Explorer in which different cell components and NPs can be distinguished based on the distinctive refractive index (See Chapter 3.7.6). ZnO-NPYs in media and cell only samples were used as a control to determine the digital stain of each component (membrane, cytoplasm and NPs) based on their distinguished refractive index for analysis. We used red digital stain for cell membrane, green digital stain for cytoplasm and blue digital stain for ZnO-NPYs. The blue color in ZnO-NPYs exposed cells can be clearly seen in **Figure 3.7**. We also confirmed the digital stain of NPs with FITC-labeled ZnO-NPYs (**Figure S 3.19**).

$ZnCl_2$ is also used as a control for eliminating the possibility of Zn^{2+} ions release from ZnO-NPYs and aggregate in cells. We did not observe any spots in cells or Zn signal in elemental mapping or in Nanolive imaging. Data not shown but similar data obtain with cell only sample (**Figure 3.7** and Chapter 3.7.3)

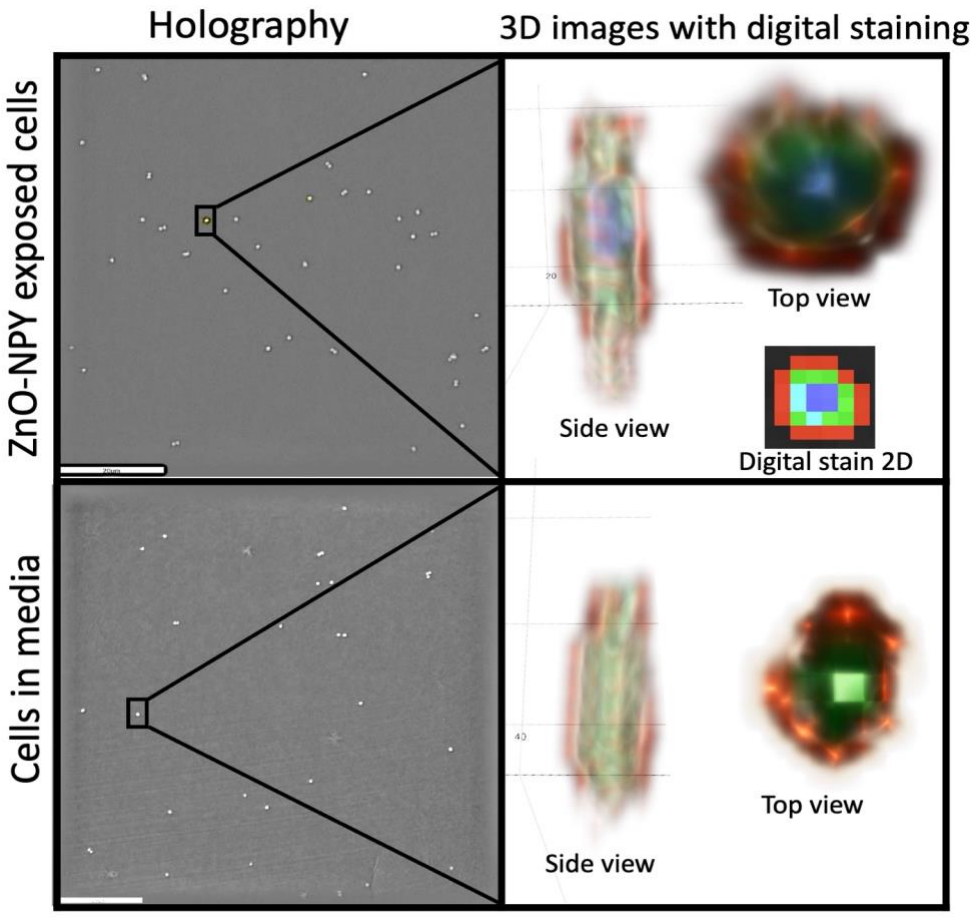

Figure 3.7 Nanolive images of ZnO-NPYs exposed cells and cell in media. 3D images with digital staining on the right panel. Here we digitally labeled cell membrane with red color, cytoplasm with green (anything inside of the cell surface), and ZnO-NPYs with blue color. In top panel we can observe blue color within the cell.

We observe three different features in EM imaging of ZnO-NPYs exposed cells (**Figure S 3.9**): ZnO-NPYs aggregation (See Chapter 3.4.2.2), polyphosphate granule formulation (See Chapter 3.4.3) and vesicle formulation (See Chapter 3.4.4)

3.4.3 Polyphosphate Granule Formation

As a downstream effect of ZnO-NPY entry, we observed polyphosphate granules in ZnO-NPYs exposed cells. It is well known that polyphosphate is a primordial energy source and an active metabolic regulator[245]. Polyphosphate granule formation started to form within 10 min of exposure the ZnO-NPYs. It can be seen with (**Figure S 3.23**) or without ZnO-NPYs aggregations (**Figure**

S 3.20 and **Figure S 3.21**) and the size of the granule is about 250nm. As time progresses, we observe more ZnO-NPYs aggregations along with polyphosphate granules (**Figure S 3.22**).

3.4.4 Extracellular Membrane Vesicle formation

S. aureus develops extracellular membrane vesicles (EV) when the cells are placed under stress. Disrupting the cytoplasmic membrane or altering the peptidoglycan crosslinking can modulate EV production by altering the permeability of the cell wall[246]. *S. aureus* exposed to ZnO-NPYs exhibited the release of membrane vesicles the size of 0.1 µm in diameter within 30min (See Chapter 3.7.8) which would indicate some damage to or disruption of the cell membrane.

3.5 Discussion

It is known that positively charged NPs interact and are stuck on the negatively charged cell membrane[153–157]. In this study, we observed ZnO-NPYs accumulate on the cell surface within a minute (**Figure 3.5 a-b**). This shows the bacterial membrane is a likely target of these NPs. Our results indicate ZnO-NPYs cause delayed membrane damage without interfering with the proton motive force for the first 60 min (**Figure 3.1**a) and is confirmed by a lack of membrane depolarization via $DiOC_2(3)$ (**Figure 3.3**). This data suggests that ZnO-NPYs cause significant membrane damage occurs as a downstream effect similar to streptomycin and chloramphenicol (**Figure 3.1b)**. One of the foremost functions of the cell membrane is in the respiratory activity of bacteria. Studies have reported that NPs disrupt the respiratory activity of the bacterial cell membrane, which can be analyzed by detecting the uptake of O_2[247]. Immediate decrease in OCR (**Figure 3.2**) without significant change in membrane depolarization confirms t ZnO-NPYs - cell membrane interaction. However, a dose-dependent decrease in O_2 consumption rate cannot be explained with this interaction itself. This can be the direct or downstream effect of ZnO-NPYs

entry to the cell. ZnO-NPYs interact with biomolecules inside the cell upon entry and cause change of metabolism to anaerobic which can be confirmed by gene expression data as we previously uncovered in chapter 2.4.7 for the up-regulation of pyrimidine synthesis pathway of UMP that plays role in cell energetics, is critical for the shift from aerobic to anaerobic. Localization of NPs in the ZnO-NPYs exposed cells can provide further information into mechanism of action. We are well aware that artifacts of electron microscopy are well documented and pose a major issue for understanding the effect of metal oxide NPs[248,249]. A misrepresentation of location could indicate a much different mechanism. Internalization of NPs is often indicated by one method but not another. Artifacts due to fixation, staining, or anomalous deposits can complicate our understanding of NPs. Singular methods alone may give a misrepresentation of true localization. For example, looking at Focused Ion Beam Slicing (**Figure S 3.17**) alone may give the impression of direct NP entry without accounting for the possibility of transplantation of NP during the processing of the sample. To combat artifacts of electron microscopy and ensure accurate representation, ZnO-NPYs entry is confirmed with multiple different nondestructive methods. To ensure reliability of bright spots observed in FIB data we ventured to confirm localization. We observe consistently bright spots in HAADF-STEM (See Chapter 3.7.4). Elemental analysis reveals that those spots are ZnO-NPYs aggregation (**Figure 3.6**). Using both SEM-TLD and HAADF-STEM images we were able to show that the bright spots are not on the surface but inside the cells (**Figure S 3.9**). Please note, in order to simplify the EM image analysis, we prepared EM samples in water. However, we further confirm the observation was not due to artifact in the sample preparation process for electron microscopy, so we performed NanoLive microscopy, a live cell imaging method that can be used to observe living cells actively being exposed to ZnO-NPY in media (**Figure 3.7**). This removes any potential damage to the cell outside of ZnO-NPY

exposure without stains, fixation or photobleaching. Utilizing the refractive index, we digitally label cells and ZnO. This was further confirmed by FITC labeled ZnO to ensure our digital labeling of refractive index was accurate (See Chapter3.7.6). Via this multi-method approach we ensure that the localization of ZnO-NPY in bacterial cells.

The shape of the ZnO-NPYs is important to note here for not causing membrane damage until 60 min exposure time, even though NPs entry is evident within 5min. We think that the pointed apex of ZnO-NPYs (**Figure 3.4**) allows particle entry without damaging membrane integrity. Similar to the studies that showed NPs with tetrahedral, cuboid, and cylindrical NPs, which have at least one sharp corner or a needle-like shape, they readily penetrated through the pulmonary surfactant (PS) layer with slight PS perturbation[245]. Similarly, we think sharp apex of ZnO-NPYs allow cell penetration without membrane damage or depolarization.

We observed different features in EM images in between the time 0 to 60min: polyphosphate granule and vesicle formation (**Figure S 3.9**). We have previously shown that ZnO-NPYs interact with proteins and enzymes[101]. Therefore, we believe that once ZnO-NPYs enters the cells, they start interacting with biomolecules in the cells, cause cells switch from aerobic to anaerobic respiration, and eventually to cell death. Within 10 min, cell starts to form polyphosphate granules that are synthesized for both energy and phosphate storage energy. The energy released from these energetic carriers used to produce all vital molecules such as amino acids, nucleobases, sugars, and lipids. Upon entry, NPs interact with biomolecules in different pathways to further interfere aerobic metabolism and start forming polyphosphate granules for later use in anerobic state (See Chapter 3.7.7). Another feature we observed in EM images is EV formation. Even though we did not observe time dependent formation for these EVs, it is known that

Staphylococcus aureus develops extracellular membrane vesicles (EV) when their membrane is placed under some sort of stress[246] .

We propose that the direct mechanism of action of ZnO NPY is still complex and unknown. However, it was recently shown that ZnO-NPs can cause enzyme inhibition exemplified by strongly suppressed activity of β-galactosidase[23], an essential enzyme in bacterial metabolism, therefore the complexity of the mechanism can be explained with ZnO NPs inhibits proteins involved in metabolic pathways, by formation of NP-protein adduct. Moreover, the selection of cell membrane transporter mutants from a mutant library indicates different responses to NP exposure (work that has been completed but not submitted for publication). This could indicate multiple mechanisms may be in play simultaneously in the antimicrobial properties of ZnO NPYs. A combination of many factors including sequestering of nutrients, membrane damage, and NP entry are responsible for the bacterial killing observed.

3.6 Conclusions

In this chapter, we studied ZnO-NPs interaction with cell membrane and explored how this affect metabolomics. The mechanism of action employed by ZnO-NPYs much more complex than previously understood. Immediately after exposure, ZnO-NPs exhibit a dose dependent reduction of cellular respiration as measured through OCR without showing any cell membrane damage. With prolonged NPs exposure, cells switch from aerobic to anaerobic respiration, and eventually to cell death. Our work highlights the importance of studying the dynamics of NPs and bacterial cell interactions to better understand the underlying antibacterial mechanism of action. The results of this study point to the importance of specific experimental controls in the interpretation of antimicrobial mechanistic studies and the need for targeted molecular mechanism studies.

3.7 Supplemental Information

3.7.1 LDH Assay for Lysostaphin

LDH release of lysostaphin treated cells used to set 100% lysis point for the percentage lysis calculation of the samples in **Figure 3.1**.

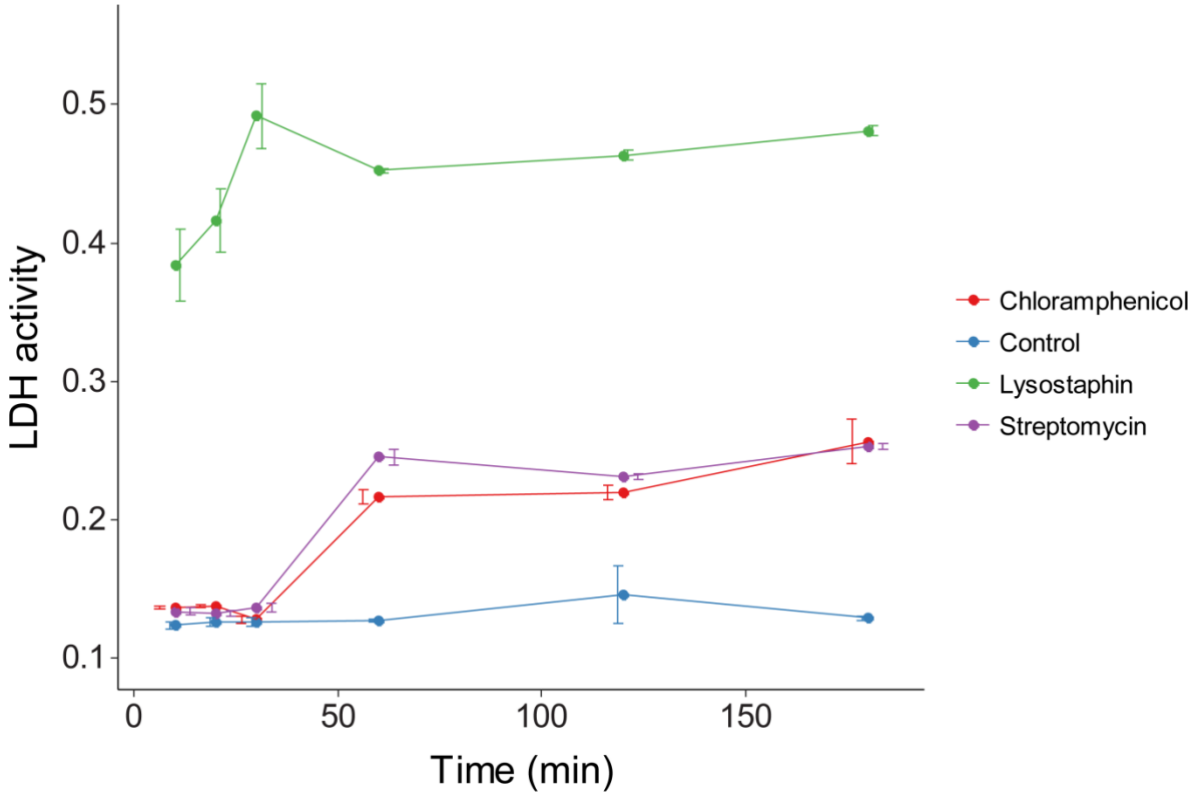

Figure S 3.8 LDH release assay for chloramphenicol, streptomycin, lysostaphin and control (cell in SNM media). Lysostaphin has a strong membrane damage effect on cells and immediate LDH released is observed. For percentage lysis calculations in Figure 1, lysostaphin data is used to set 100% lysis point. Error bars represent standard error of five independent experiments run on different days.

3.7.2 Cell Only Sample *vs*. Features Observed in ZnO-NPYs Exposed Cells

We use SEM-TLD images to observe the surface features and HAADF-STEM images to observe the internal features. In **Figure S 3.9**, we observed different features in ZnO-NPYs exposed cells: ZnO-NPYs accumulation in cells, polyphosphate granule formation and vesicle formation.

Whereas we do not observe any internal feature or vesicle formation in cell only samples (**Figure S 3.9**).

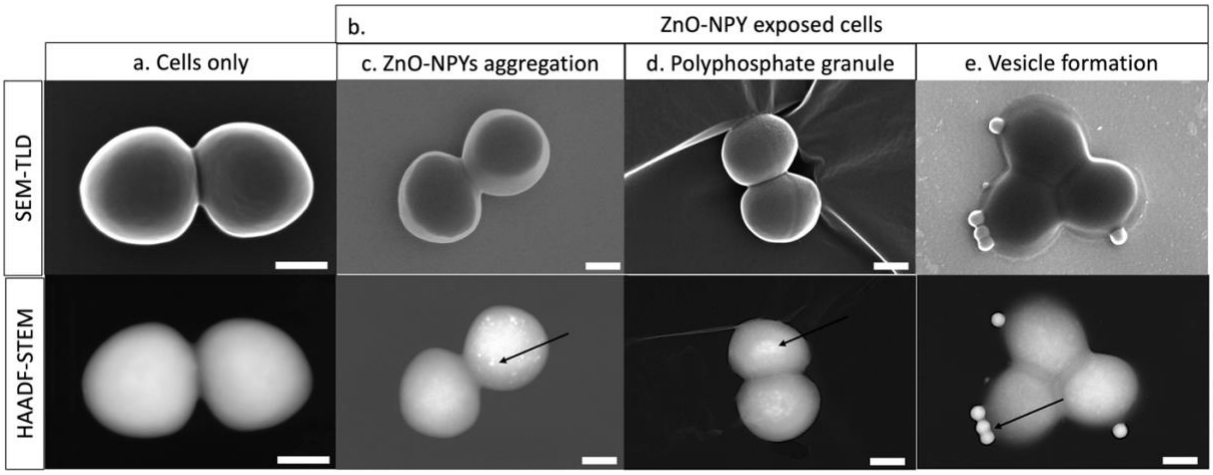

Figure S 3.9 SEM-TLD and HAADF-STEM images of (a) cell only and (b) ZnO-NPYs exposed cells. These two imaging is compared to show that features are inside of the not the surface features. (a) in cell only images no features are observed at all. (b) Arrow in each panel in ZnO-NPYs exposed cells showing a feature in cells. (c) ZnO-NPYs accumulation, (d) polyphosphate granule formation and (e) vesicle formation. Scale bar: 200nm

3.7.3 Cell Only Sample

We wanted to look more into cell only samples and performed qualitative and quantitative elemental analysis. As expected, we did not observe any Zn signal within cell only samples. Because of the background signal in elemental mapping we observe very weak signal in Zn panel in **Figure S 3.10**, however once we investigate the image intensity profile (**Figure S 3.11)** and EDX analysis **(Figure S 3.12)**, no significant signal (noise background ratio is almost zero) observed as opposed to ZnO-NPYs exposed cells. In addition, the quantified elemental analysis **Table 5** shows only 0.04 % Zn in cell only sample that confirms no significant Zn signal detected in cell only samples or any other special feature similar to ZnO-NPYs exposed cells.

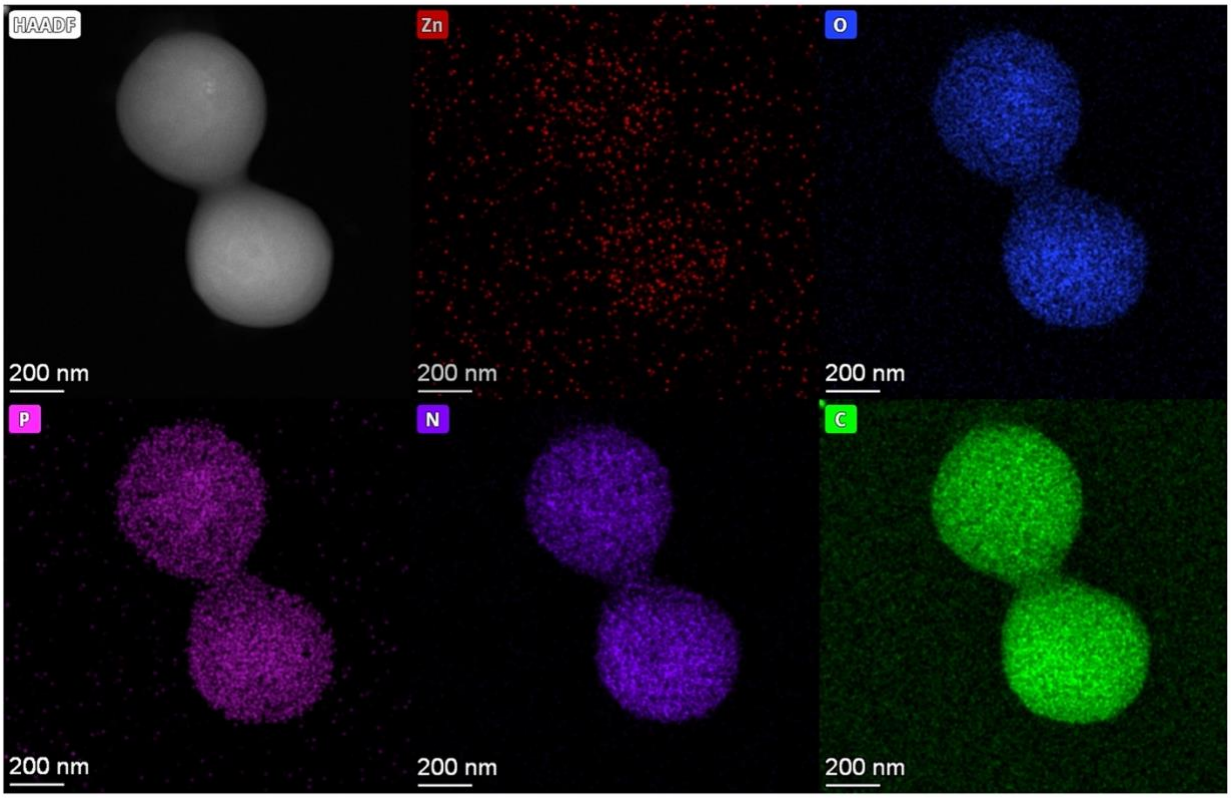

Figure S 3.10 Elemental mapping of ell only sample (Zn-zinc, O-oxygen, P-phosphorus, N-nitrogen and C-carbon). Scale bar: 200nm

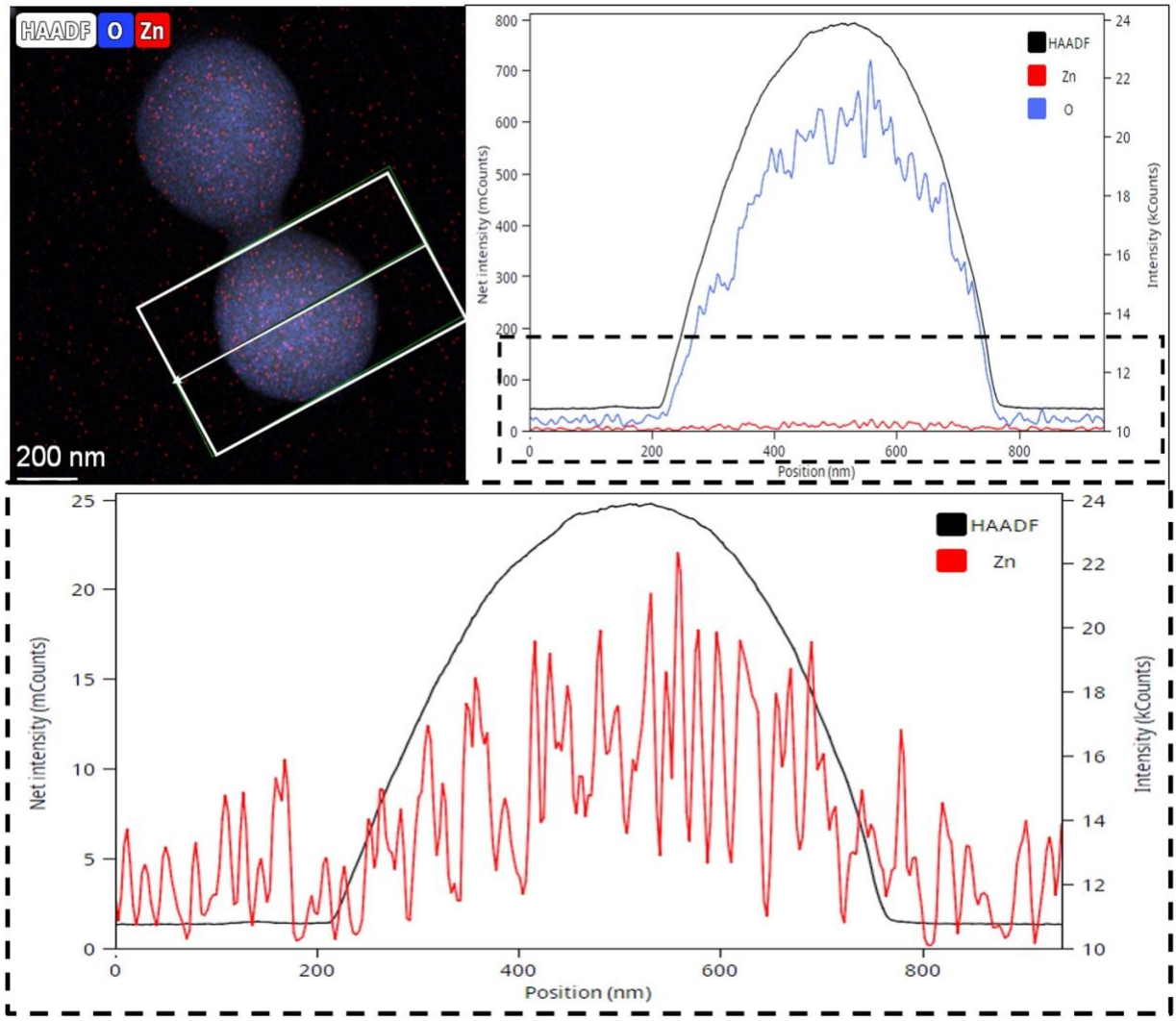

Figure S 3.11 An overlay image of HAADF, Zn and O of cell only sample. White box in this image specifies an area for intensity profile. The graph shows intensity profile for each image HAADF, Zn and O on top. Zoomed area of the graph at the bottom shows Zn signal intensity. Scale bar: 200nm

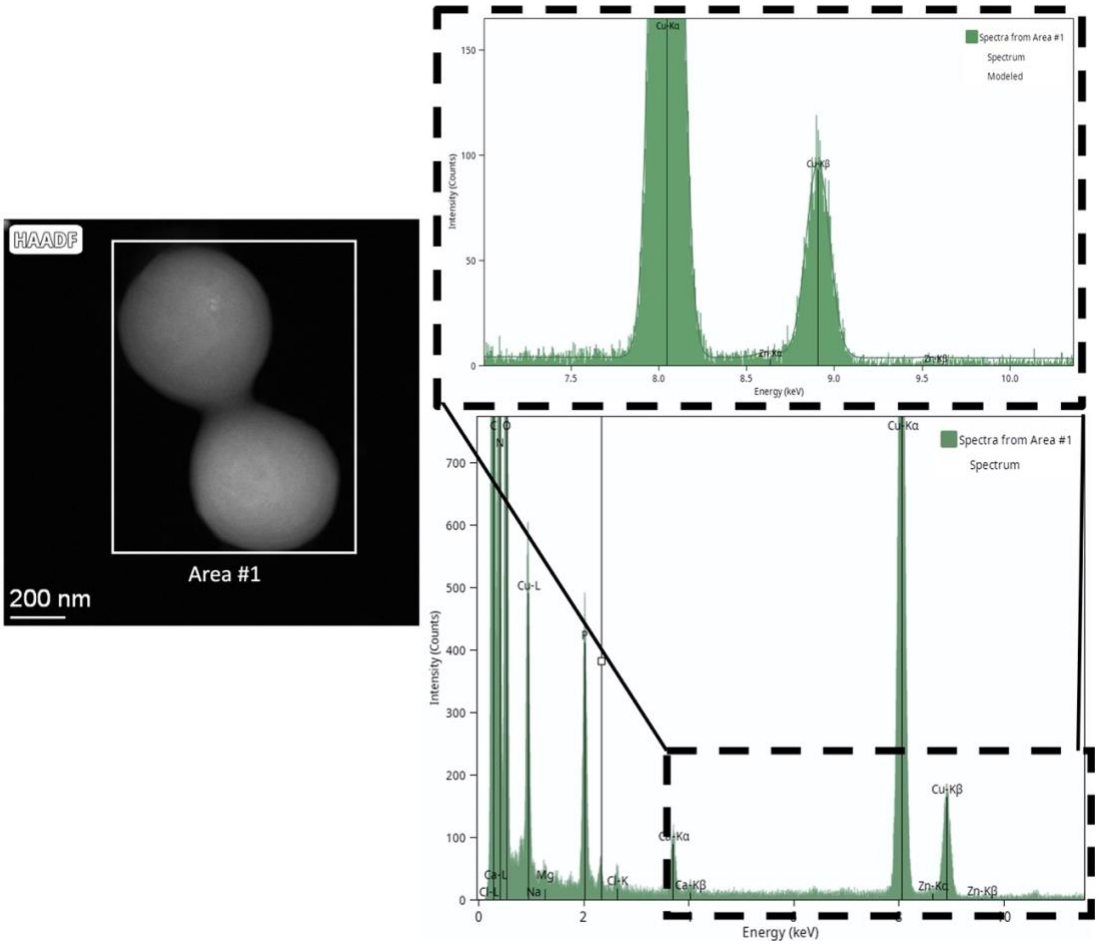

Figure S 3.12 EDX analysis of cell only sample within area 1(white box). Zoomed area (top panel) of EDX analysis does not show any Zn signal (almost 0 compared to background noise).

Table 5 Quantitative EDX Analysis of Cell Only Sample

Element	Atomic Fraction (%)	Mass Fraction (%)
C	73.92	67.99
N	13.75	3.04
O	10.59	12.97
Na	0.0	0.0
P	1.48	3.50
S	0.12	0.30
Cl	0.10	0.28
Zn	0.04	0.21

3.7.4 ZnO-NPYs Aggregation in Exposed Cells

Once ZnO-NPYs started to enter cells, they start aggregating in cells and create bright spots in HAADF-STEM images due to the heavier atoms (**Figure S 3.13**). Even though we do not observe aggregated spots in every cell, we can still observe Zn signals (**Figure S 3.14**). These data suggest that smaller or non-aggregated NPs in cells cannot be detectable in EM at this magnification. But not necessarily means they do not enter each cell. To see the individual ZnO-NPYs we need to utilize microtome to prepare EM samples. On the other hand, Zn signal in cells without bright spots is a confirmation of their presence in the cells (**Figure S 3.14 and Table 6**). However, intensity of Zn signal still much higher than Zn signal within the cells in bright spots (**Figure S 3.15**), confirming ZnO-NPYs aggregation in those spots. As time progress we see more and more cells have bright spots and they start to lyse **(Figure S 3.16).**

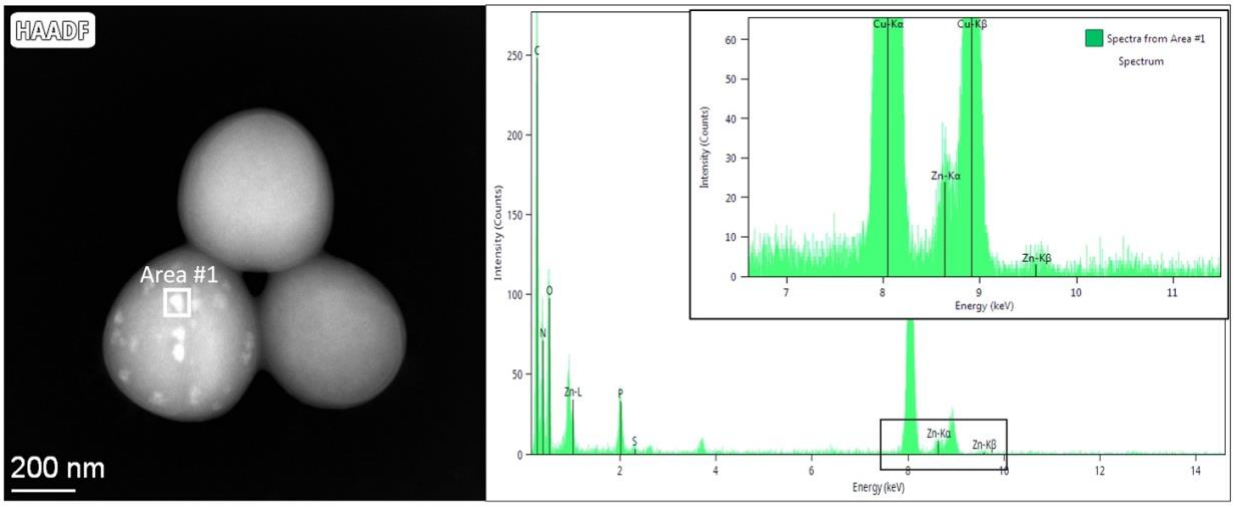

Figure S 3.13 HAADF-STEM image of ZnO-NPYs accumulation in cells after 10min (bright spots) and EDX analysis of a spot in cells. Small window on top-right is the zoom area of black box. As this spot is inside of the cell, signals from the other elements can be seen in EDX such as C, S, N.

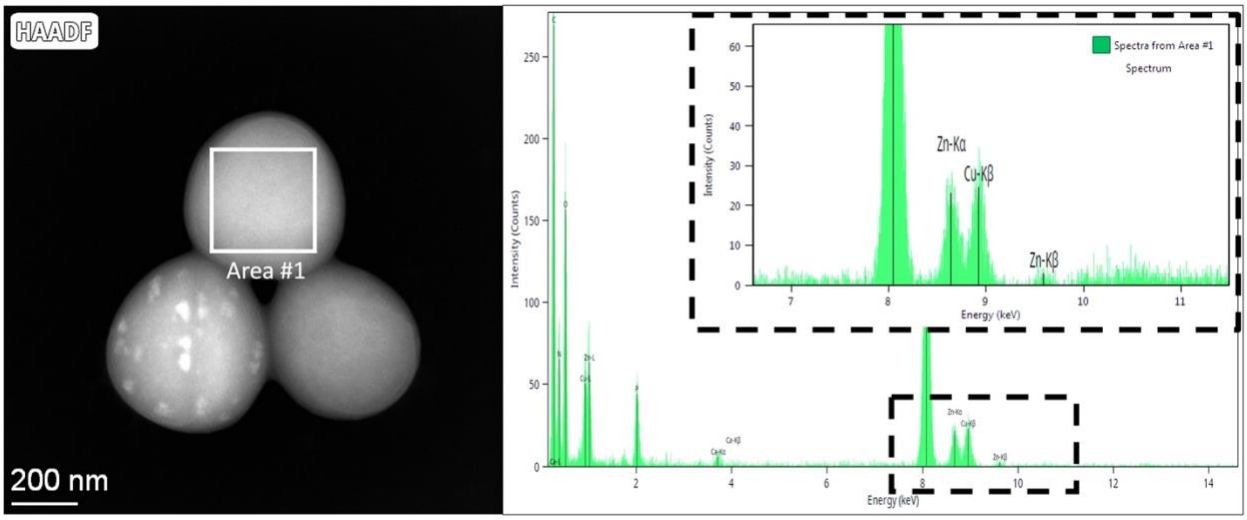

Figure S 3.14 HAADF-STEM image of ZnO-NPYs exposed cells without bright spots and EDX analysis of a cell. Small window on top-right is the zoom area of black box

Table 6 Quantitative EDX Analysis of ZnO-NPYs Exposed Cells in **Figure S 3.14**Error! Reference source not found.

Element	Atomic Fraction (%)	Mass Fraction (%)
C	67.68	56.81
N	10.85	10.62
O	16.86	18.86
P	2.73	5.91
S	0.14	0.31
Cl	0.21	0.52
Zn	1.53	6.97

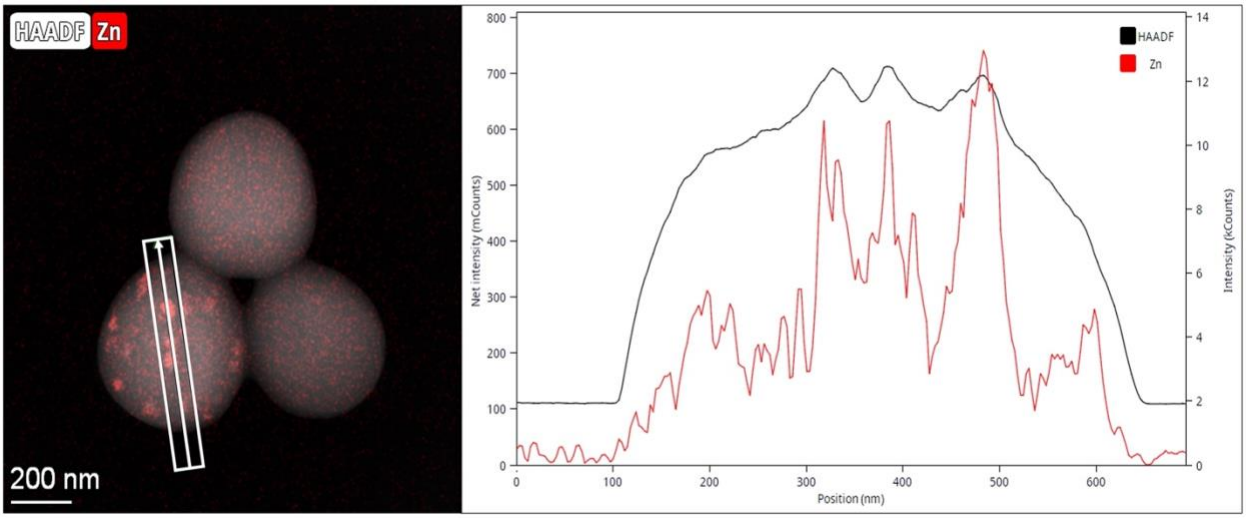

Figure S 3.15 Overlay of HAADF-STEM image and Zn elemental mapping, and Intensity profile on bright spots (white box) in ZnO-NPYs exposed cells.

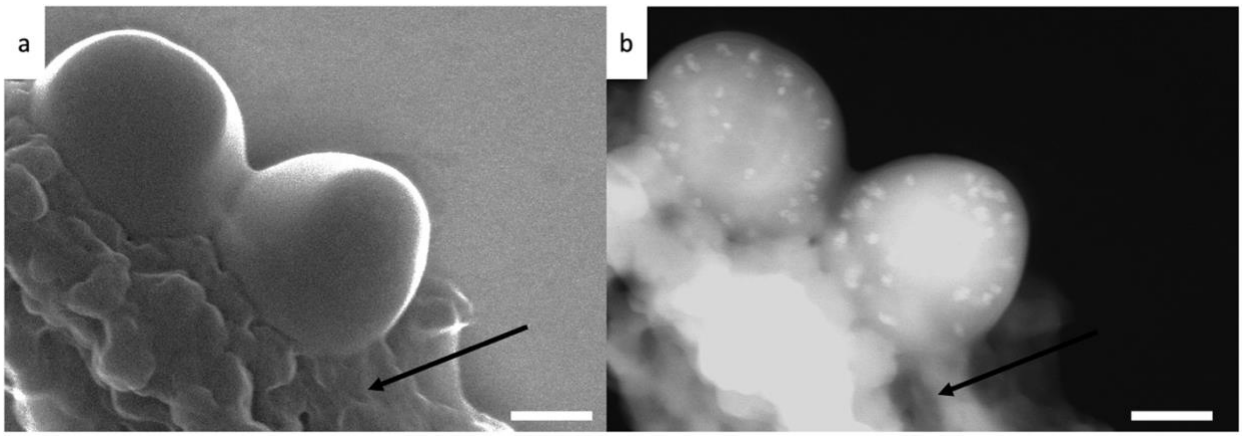

Figure S 3.16 EM images of ZnO-NPYs exposed cells at 30min. (a) SEM-TLD image (b) HAADF-STEM image Arrow indicates ZnO NP aggregation and death cell residue mixture. Scale bar: 200nm

3.7.5 ZnO Accumulated Spots in FIB Sliced Image

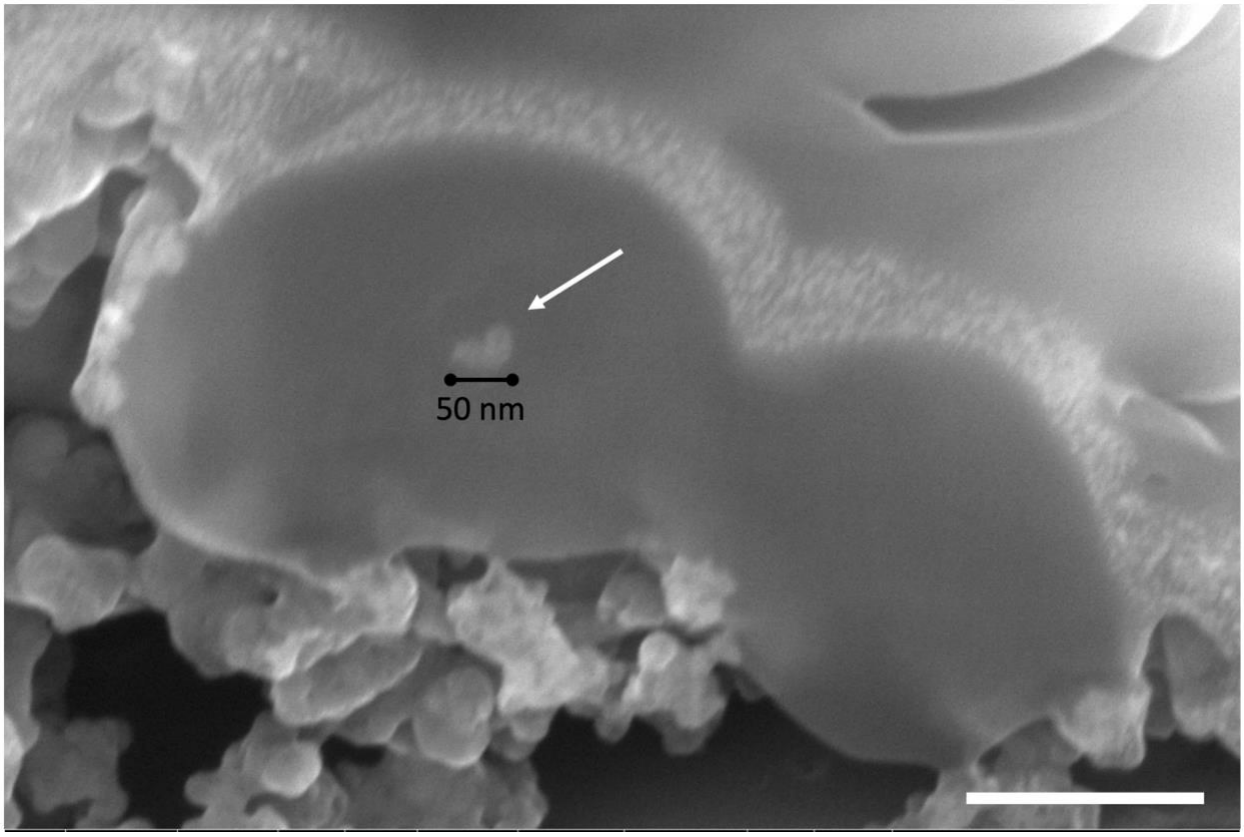

Figure S 3.17 SEM-TLD image of FIB sliced ZnO-NPYs exposed cells. This image clearly shows ZnO-NPYs aggregation are in the cells and size is around 50nm.

3.7.6 Nanolive Imaging

3.7.6.1 Nanolive image of ZnO samples

We utilized Nanolive for ZnO-NPYs sample only to find out NPYs digital staining. We used digital blue color for ZnO-NPYs make it visible in cells.

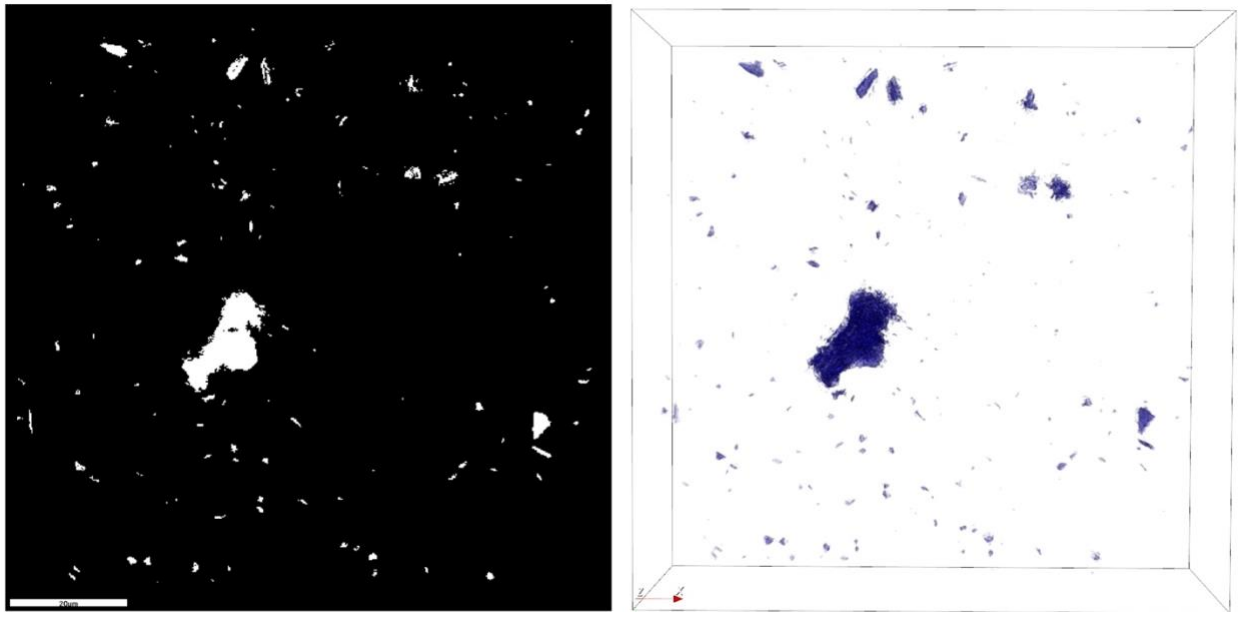

Figure S 3.18 Nanolive image of ZnO-NPYs for deciding the refractive index digital stain. Left panel holographic image after digital processing. Right panel 3D image with blue digital stain.

3.7.6.2 Fluorescent image of labeled ZnO-NPYs exposed cells.

To confirm the digital stain of ZnO-NPYs we labeled the particles with FITC utilizing Thermo Scientific™ Pierce™ FITC Antibody Labeling Kit. This data confirms digital staining is coming from ZnO NPYs (**Figure S 3.19**). The area of the digital stain adjusted based on these labeled NPYs.

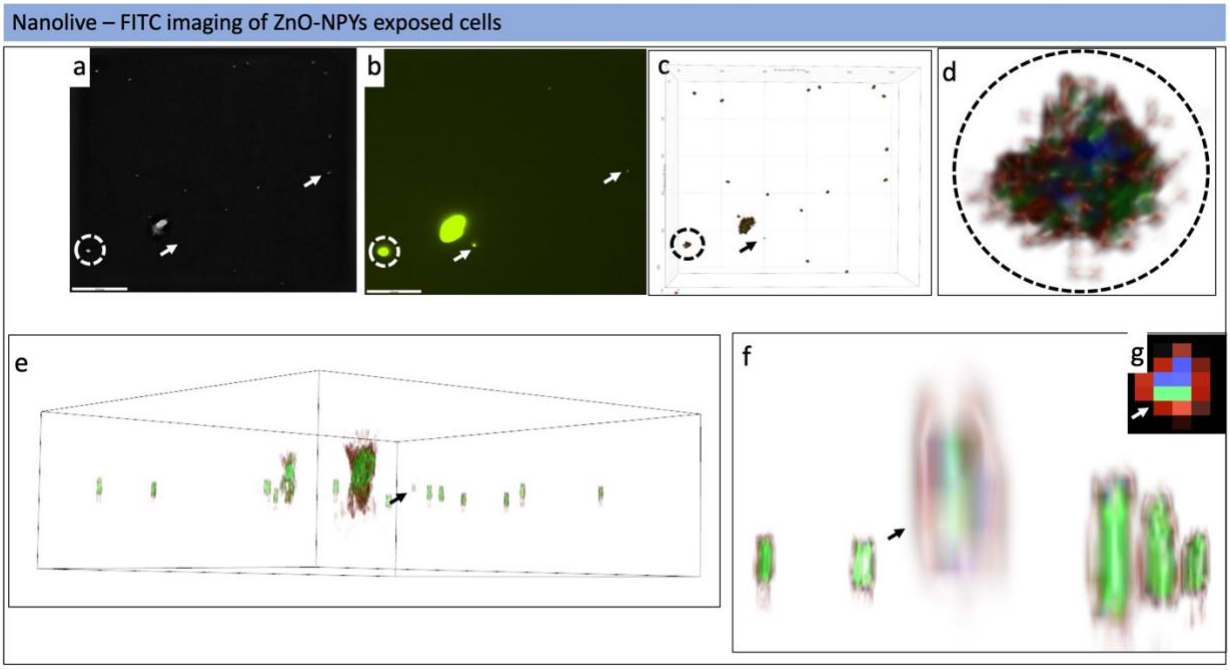

Figure S 3.19 Nanolive image of FITC-Labeled ZnO-NYPs exposed cells. (a) Holography image (b)FITC image (c)3D image with digital staining. We can see both cells (marked with arrow) and cell-ZnO aggregation (circled). (d) Cell-ZnO-NPYs aggregation. (e)Side of 3D image with digital staining in (c). (f)Zoom area of side image (f), here we can see fluorescence coming from ZnO-NPYs inside the cell, rest of the cells around marked cell do not show any blue color (no ZnO-NPYs inside them). (g) digital stain of marked cell in (f). Arrow shows the same cell along the panels. Scale bar :20um

3.7.7 Polyphosphate Granules in ZnO-NPYs Exposed Cells

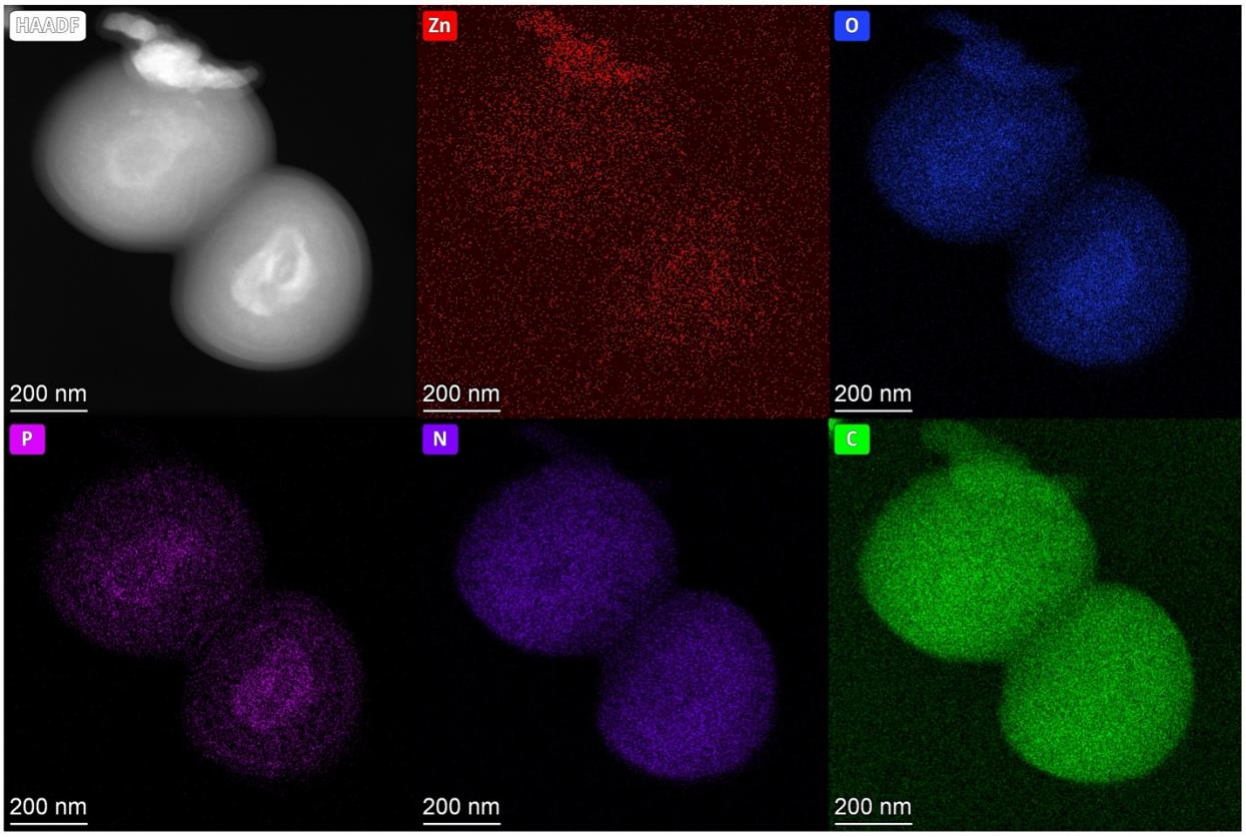

Figure S 3.20 HAADF-STEM image and elemental mapping of ZnO-NPYs exposed cells. Zn-zinc, O-oxygen, P-phosphorus, N-nitrogen, and C-carbon). Scale bar: 200nm

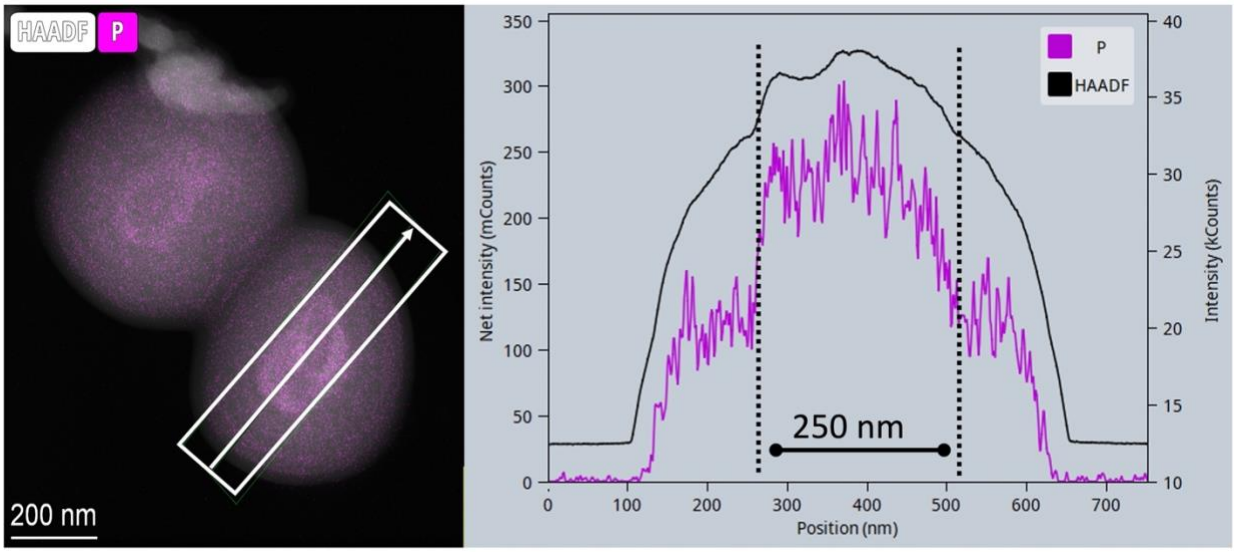

Figure S 3.21 Overlay image and HAADF-STEM image and phosphorus elemental mapping. White box in overlay image indicates the area on the right graph signal intensity analysis. The size of the measured polyphosphate granule is about 250nm. Scale bar 200nm.

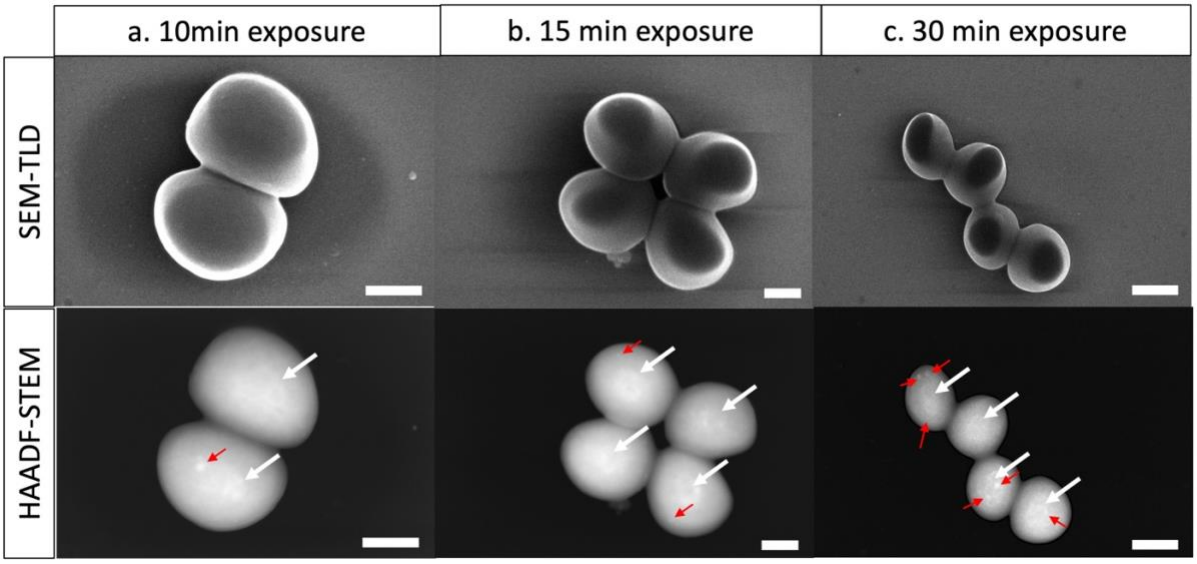

Figure S 3.22 Time course of ZnO-NPYs exposed cell for polyphosphate granule formation (marked with white big arrows) and ZnO-NPYs aggregation (marked with red small arrows). As time progress we observe bigger and higher number of ZnO-NPYs aggregated bright spots, each cell shows some degree of polyphosphate granule formation within each time point.

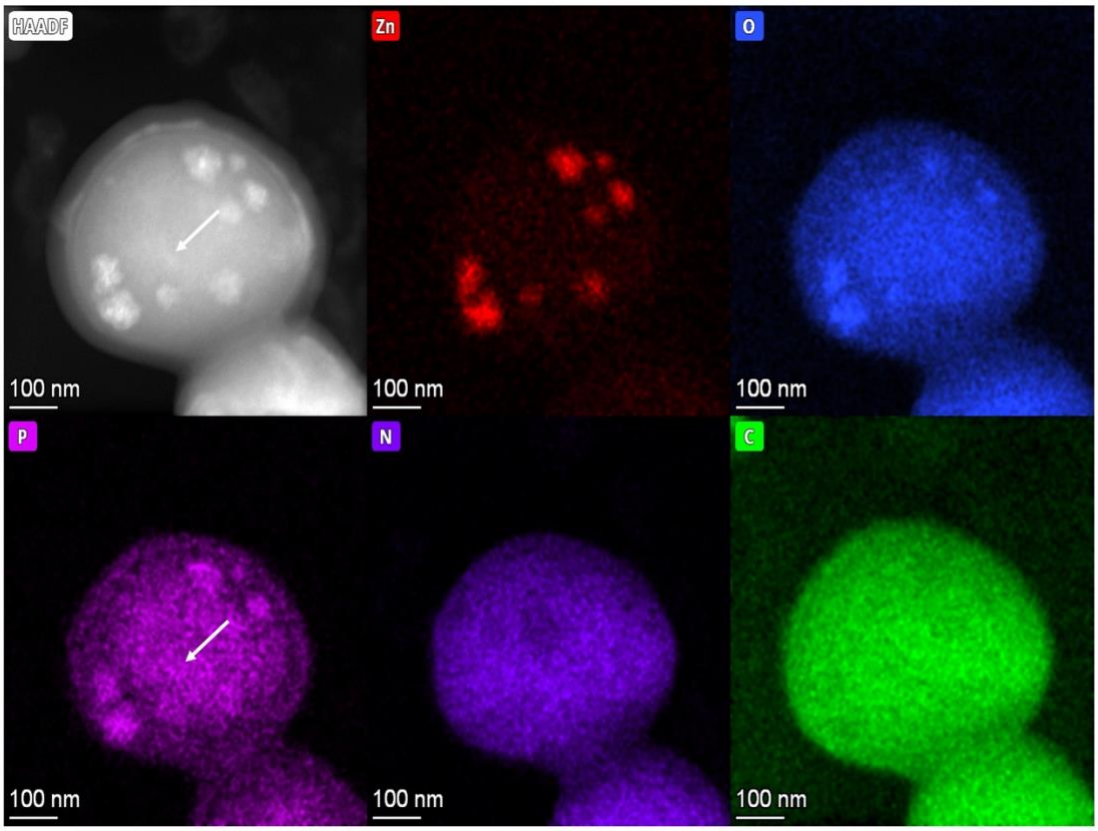

Figure S 3.23 Polyphosphate granule (marked with arrow) and ZnO-NPYs accumulation together. Phosphorus signal increase on the ZnO-NPYs accumulated spots as they are getting bigger and entangled with polyphosphate granules.

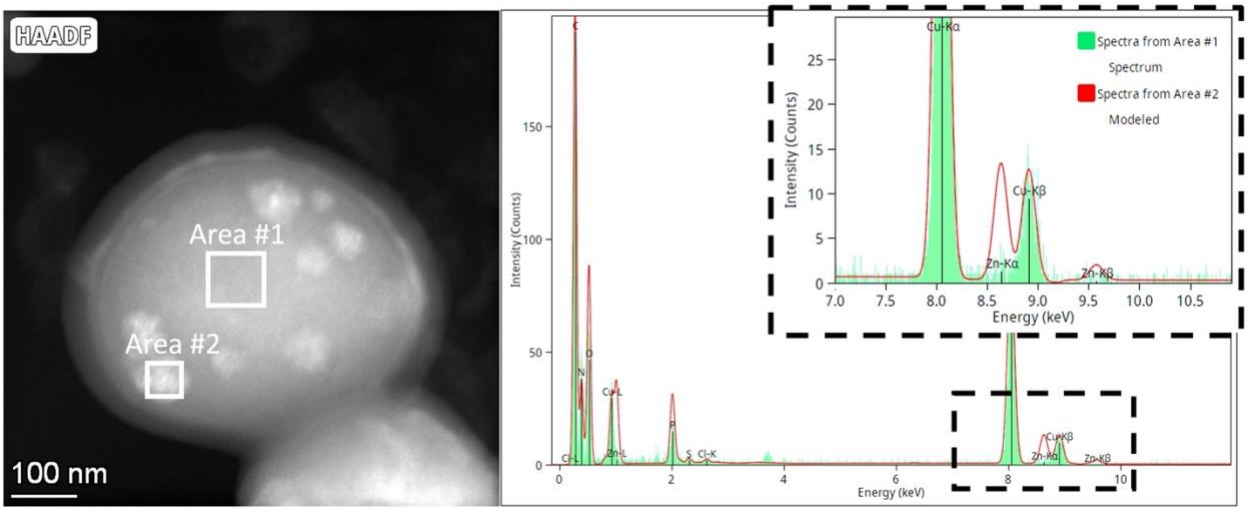

Figure S 3.24 Zn signal differences between in polyphosphate granule formations (Area #1- green on the EDX graph) and ZnO-NPYs aggregations (Area #2- red on the EDX graph)

3.7.8 Vesicle Formation in ZnO-NPYs Exposed Cells

The feature we observed in ZnO-NPYs exposed cells is vesicle formation. Even though it is not clear why cells form these vesicles when they exposed to ZnO-NPYs, they excrete these vesicles and they require further investigation.

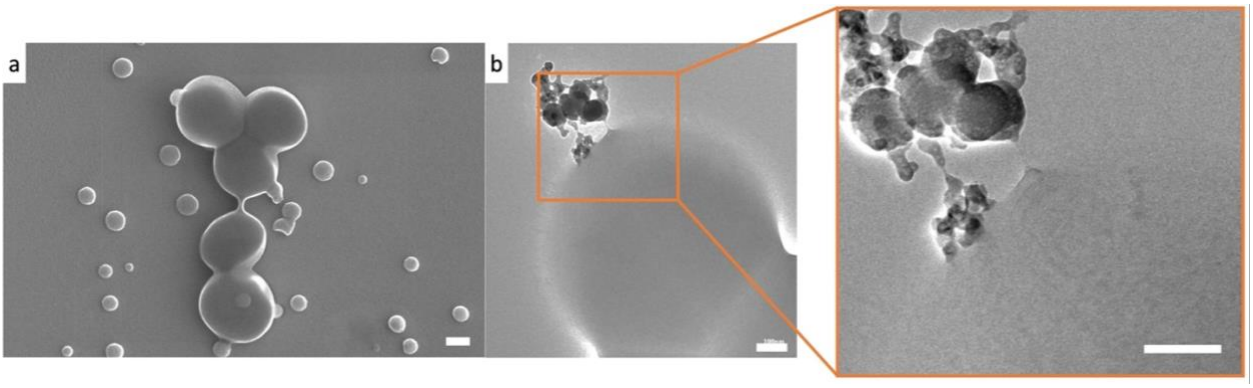

Figure S 3.25 EM images of vesicle formations in ZnO-NPYs exposed cells after 10min. (a) SEM-TLD image, (b) TEM image of cells with vesicles around. Orange boxed zoom image reveals some cell-vesicle connection. Scale bar 100nm

Part II

Chapter 4

Self-organization of *Iron Sulfide* Nanoparticles into Multi-compartment Supraparticles as Artificial Viruses for DNA Delivery

4.1 Abstract

Compartments are essential for any life. Besides fundamental importance, their realization from technologically friendly inorganic nanomaterials is essential for multiplicity of biomedical and biochemical technologies. The practical engineering of such biomimetic structures is, however, complex multistep process and often involves biologically unfriendly components. Here we show that that amino acid-stabilized iron sulfide NPs can spontaneously self-assemble into multi-compartment supraparticles (SPs). The transmission electron microscopy showed that NPs initially produce ~55nm cup-like structures and mature into ~75nm SPs with *ca.*190 interconnected compartments. The results of selected area electron diffraction and energy dispersive X-ray spectroscopy confirm SPs are formed from FeS_2 and Fe_2O_3 NPs. Elemental mapping showed that Fe_2O_3 NPs are located on the surface of the SP and protecting FeS_2 and compartments from the surroundings. These compartmentalized particles can be used for the successful encapsulation of DNA and mRNA fragments for gene delivery and vaccines.

4.2 Introduction

Compartmentalization is one of the key architectural components in nature. [250–253] Examples of shell-like biological structures of nanoscale dimensions include viruses, cellular vesicles[254], bacterial micro-compartments,[255–257] carboxysomes,[258] and some organelles of various sizes ranging from 10 nm to 500 nm such as endosomes and lysosomes.[253,259] While these shell-like particles are essential to provide selective transport, increase the reaction rate by keeping the volume small, and protect the molecules from the surroundings; they are serving only one specific function at a time. Interconnected compartmentalization, on the other hand, allows communication between its multiple compartments[260] for multifunctionality and providing a large surface area within a particular volume for further increased reaction rate. Some of the biological particles having multiple interconnected compartments can be exemplified by the endoplasmic reticulum, Golgi apparatus, mitochondria, and chloroplast.

Endoplasmic reticulum (ER), for example, is one of the biggest organelles in eukaryotic cells and responsible for multifunctionality such as protein synthesis, folding and modification as well as lipid, carbohydrate metabolism and calcium storage. These different functions take place in distinct structural domains of ER in close proximity and a parallel manner without the endangering of degradation and interfering[261]. This multifunctionality is achieved by interconnected multi-compartments.

Synthetic particles with single or multi- compartments made from organic amphiphilic compounds[253,262,263], such as nucleic acids [264,265], lipids[266–268], polymers[269] that form liposomes[270,271], polymersomes[250,272,273], capsosomes[274–276], and protocells[250,266,277] have been extensively utilized for multiple research and technological purposes. In contrast to other structures, compartmentalized biomimetic particles made from inorganic components bring novel

optical,[278,279] mechanical[280], and catalytic characteristics,[281,282] but are less common and more challenging to make. They are typically synthesized using the organic structures as templates.[283–288]

Compartmentalized self-assembled particles from inorganic components are a much less investigated research area. The use of inorganic NPs is favorable also because some aspects of their self-organization behavior replicate those of nanoscale biological components,[96,289–292] while possessing robustness of inorganic materials, for example, metals, semiconductors, or ceramics. From the fundamental perspective, it will also be essential to trace the pathway to increase the complexity of self-assembled structures from nanoscale components. There are diverse examples of self-organization of NPs that forms a new, high order nanostructure including, but not limited to nanoshells,[183,252] helices,[293–295] ribbons,[296] nanostars,[297] chains,[290,298] rings[299], sheets,[187] superlattices,[300] hybrid supraparticles (SPs),[301] and SPs [189,301–304]. In this paper, we show self-organization of iron sulfide NPs into multi-compartment SPs, which has ability to encapsulate more than one biological cargo. However, for this paper we utilized SPs for encapsulating and delivering one cargo, plasmid deoxyribonucleic acid (pDNA), similar to viruses.

4.3 Materials and Methods

All materials except plasmids were purchased from commercial sources: Iron III Chloride ($FeCl_3$), sodium sulfide nonahydrate ($NaS_2.9H_2O$) and L/D-cysteine and N-Acetyl cysteine were purchased from Sigma-Aldrich (St. Louis, MO, USA); absolute ethanol from Fisher-Scientific (Hampton, NH, USA); grids with ultra-thin carbon film on holey carbon film support for transmission electron microscope (TEM) and carbon film only for scanning transmission electron microscope (STEM) analysis purchased from Ted Pella (Redding, CA, USA); disposable folded capillary cells for dynamic light scattering measurements were purchased from Malvern Instrument (Worcestershire,

UK). Hellma fluorescence cuvettes were purchased from Sigma Aldrich for UV-Vis, Fluorescence, and CD measurements. All cell culture materials were purchased from Gibco-BRL Inc. (Gaithersburg, MD, USA) unless otherwise stated differently. The pEBB-mchery plasmid is used to transform *Escherichia coli* and amplified plasmid extracted with plasmid isolation kit (Invitrogen™ PureLink™ HiPure Plasmid Filter Maxiprep Kit).

4.3.1 Constituent NPs Synthesis

0.5 x 10^{-3} M L-cysteine and 10^{-2}M iron III chloride in 100 ml DI water under magnetic stirring at 3 ^{o}C temperature under air. 10 ml of 5 x 10^{-1} M sodium sulfate nano-hydrate was then dropwise added to the solution under constant magnetic stirring. Once color changed to black, reaction stopped, and NPs were collected by centrifugation at 14K for 1h, washed three times with absolute ethanol. We dried the particles entirely at room temperature to make sure no trace of ethanol. Particles then dissolved in Milli Q water for further experiments.

4.3.2 Compartmentalized SPs Synthesis

SPs obtained by increasing the reaction temperature to room temperature. After 30 min, the color changed from black to yellow and the reaction is stopped. SPs are collected by centrifugation 10k for 15min, and subsequently washed three times with absolute ethanol. For the time-dependent experiment, the reaction stopped at specific time points. We dried the particles entirely at room temperature to make sure no trace of ethanol. Particles then dissolved in Milli Q water for further experiments.

4.3.3 Cup-like Intermediate Structure Synthesis

The time-dependent experiment showed that intermediate structures form between time 0 (right after the sulfur source added to reaction) and 15min when the reaction is at room temperature. For collecting cup-like intermediates, the SP reaction stopped at 15min and washed three times as SPs.

4.3.4 SP-pDNA Synthesis

The system was slowed down by stopping the SP reaction at 15 min to utilize the compartments of the SPs. At this point, 150 μg plasmid (pEEB cherry – 6073bp) is added dropwise to the system, and the reaction was allowed to complete the SP formation under magnetic stirring. After 30 min, SPs containing DNA (SP-pDNA) were collected and washed as usual.

4.3.5 Calculating Amount of DNA Molecule in SP

This calculation is based on the assumption that the average weight of a base pair (bp) is 650 Daltons.

Equation 4: number of DNA copies = (amount in g* 6.022×10^{23}) / (length* 650)

150μg pDNA = $2.29 * 10^{13}$ pDNA molecule per sytem

4.3.6 Particle Characterization

UV-Vis measurements are acquired by an 8453 UV-vis Chem Station spectrophotometer produced by Agilent Technologies. Zeta potential of SPs was measured at 25°C using a Zetasizer Nano ZSP (Dynamic Light Scattering (DLS)) instrument (Malvern Instruments Ltd, Malvern, Worcestershire, UK). Circular Dichroism (CD) spectra were obtained by a JASCO J-815. TEM images obtained by utilizing JEOL 3011 high-resolution electron microscope equipped with a CCD camera and a field emission gun (FEG) operating at 300 kV. SEM images were obtained with FEI Helios 650 Nanolab SEM/FIB. STEM images obtained with JEOL 2100 Probe-Corrected

Analytical electron microscope equipped with a Gatan Ultrascan 1000 CCD TV camera and a field emission gun (FEG) operating at 200kV. The Fourier transform infrared spectroscopy (FTIR, Thermo-Nicolet IS-50); energy dispersive X-ray spectrometry (EDX, FEI Helios 650 Nanolab SEM/FIB and JEOL 2100F) and X-ray photoelectron spectrometry (XPS, Kratos Analytical AXIS Ultra) and X-Ray diffractometer (XRD, Rigaku Rotating Anode with Cu Kα radiation generated at 40 kV and 100 mA) were used to exam the composition of particles. Fluorescence data is obtained by a Jobin Yvon Horiba FluoroMax-3 instrument.

4.3.7 Particle Size

Particle size is calculated with image J analysis with number of TEM images. The total number of particle (n) is measured for calculatios. n for SP is 1276, n for 300 cup-like structures and n for 150 NP. NP Tracking Analysis (NTA) was also conducted for confirming size of SP in aqueous environment. NTA data were obtained by Malvern NanoSight NS300 on aqueous dispersions.

4.3.8 Phase Identification

Multiple diffraction rings of SPs are obtained, and d-spacing of each diffraction rings calculated with image-J. All results are recorded and sorted with decreasing d-spacing, here ± 0.1 Å is considered as a measurement error. The list of d-spacing of SPs is compared with known samples containing iron, sulfur, and any combination of these three elements.

4.3.9 Excitation-Emission Matrix

Excitation-emission matrix (EEM) is a 3D landscape with a z-axis measuring the intensity where red color shows the highest intensity, and purple color displays the lowest intensity. If the material is fluorescent, emission peaks of different excitation wavelengths should be stable in the scanning. Likewise, we excited SP suspension from 200 nm to 600 nm with 10 nm increments.

4.3.10 Electron Tomography

The electron tomography studies at room temperature were carried out on two different systems:

1) JEOL 2100 Probe-Corrected Analytical electron microscope equipped with a Gatan Ultrascan 1000 CCD TV camera and a field emission gun (FEG) operating at 200kV and

2) FEI Helios 650 Nanolab SEM/FIB with slice and view software.

For JEOL 2100, a series of 2D projection images were recorded by tilting the specimen from -65º to 70º for increments of 1º. A tomography reconstruction software package Etomo was used to align the tilt series manually. The surface and volume rendering were generated also using the Avizo software.

For Helios, slice, and view software employed. The particle cluster on a silicon wafer was coated with first carbon and then platinum to protect the particles from ion beam damage. The area is milled with an ion beam every 3 nm, and images are saved. As the specimen was not tilted with this method, there is no need to create the tomogram with Etomo. The images taken with Helios were aligned within Avizo software. The surface and volume rendering was generated also using the Avizo software.

4.3.11 Surface Area and Volume Calculation

The surface of the grid searched for SP aggregations that include different size of particles. 17 polydisperse SPs were grouped based on location in the cluster and color-coded. Number of SP, each SP size in diameter, average volume, and surface area of each color-coded area were calculated within Avizo software.

4.3.12 Calculation of the Number of Compartments in a SP

If we consider the shape of the individual compartments and whole compartments unit structure are sphere, we can calculate the number of compartments in SP in a way that a volume of a sphere

is highly packed with smaller spheres. Based on our tomography analysis, the volume of compartments is 0.15 ± 0.048 *10^6 nm^3, and Kepler conjecture the highest packing density of same-sized spheres in the three-dimensional space is$\frac{\pi}{3\sqrt{2}}$ ≈ 74.048%. We also know the sphere volume is

Equation 5: $\frac{4}{3}\pi r^3$.

Using the diameter of compartments (r=5.2nm- tomography analysis) number of compartments per SP can be calculated to be ~190.

Equation 6: $V_{SC} * 0.74048 / V_{IC} \approx 190$

In where V_{SC} is 0.15 *10^6 nm^3, and V_{IC} is 0.58*10^3 nm^3, V_{SC}: Volume of compartments in SP, V_{IC}: Volume of individual compartments (**Fig. S22**)

4.3.13 The Number of NPs in a SP

The densest packing of circles in the plane is the Steinhaus's hexagonal lattice packing is $\frac{\sqrt{3}\pi}{6}$ ≈ 90.689%. We consider the packing density of NP in an SP is ≈ 90% and we know the volume of a cylinder is $\pi r^2 h$, where r=4.5nm and h=1.5nm. Therefore, number of ind NPs per SP can be calculated to be ~6100.

V_{IN} = 0.127 πr^3.*10^3 nm^3

Equation 7: $(V_{SP}-V_{SC})/V_{IC}$ = ~6100NPs

Where $V_{SP}-V_{SC}$ = 0.86 *10^6 nm^3

0.86 *10^6 nm^3 * 0.9 = 0.774*10^6 nm^3

The top two layers (~8.9nm) of SPs are Fe_2O_3 NPs, therefore number of Fe_2O_3 NPs in SP can be calculated ~2975. ~48% of ind NPs are Fe_2O_3 NPs.

4.3.14 Lambda Scanning in Confocal Microscopy

Super-resolution Leica SP8 MP Confocal STED microscope is utilized for lambda scanning. A lambda scan is an acquisition of an emission spectrum using spectral detectors, and it records a series of individual images of the sample within a defined wavelength range. Lambda scan is performed between 470-570 nm excitation range with a white light laser to find the best excitation wavelength. The size of the emission window is kept 50 nm long, and it is shifted 20 nm further along with excitation wavelength for the sake of the detector. The intensity of each image is quantified and graphed with Las X software. As the white light laser range is 470-670 nm, we performed the lambda scanning starting from 470 nm and ending at 570 nm (no emission after 570nm).

4.3.15 Cell Culture

HEK293T cells were purchased from ATCC (#CRL-11268). Cells were maintained at 37°C with 5% CO_2 in Dulbecco's Modified Eagle's Medium (DMEM) media supplemented with 10% fetal bovine serum and 1% penicillin/streptomycin (Thermo Fisher Scientific, Waltham, MA) and passaged every 3-4 days at 80% confluency.

4.3.16 Cell Viability Assay

100µl HEK 293T cells were seeded on cell culture treated 96 well-plate (in the concentration of from 100.000 cells/ml serial dilution to 82 cells/ml and incubated at 37C^o for 24 hours Then, medium discarded and cells were washed with PBS 2 times to remove non-attached cells. 90µl fresh media added along with 10µl SPs in the concentration of 10x and 1000x, and incubated for 24h or 48h. Promega™ CellTiter 96™ Nonradioactive Cell Proliferation Assay (MTT) was conducted as described in the protocol. Shortly, 15µl dye solution added to cells and incubated for 4 h, then 100µl stop/solubilization solution is added, and then sealed and incubated at 37C^o

overnight to allow complete formazan product solubilization. Tetrazolium salt in the dye solution converted into the formazan by living cells, and the solubilization solution solubilizes the formazan product. The next day, plate reader (BioTek Synergy 2 Plate Reader, BioTek Instruments, Inc., Winooski, Vermont, USA) utilized to record absorbance at 570nm. As a blank absorbance of SP solutions in media used and subtracted from all samples. All experiments were repeated three times. The results were expressed as mean ± SD (n = 5).

4.3.17 Cellular Uptake and Transfection

The Hek293T cells were seeded in a Lab-Tek® chambered coverglass system at 4.8×10^4 cells per well (8 wells per chamber) and cultured for 24 h to achieve 70% confluence. The media is discarded, and cells washed two times to remove unattached cells. 20 μL of SP and SP-pDNA dissolved in media were added for cellular uptake and transfection, respectively. Wells are completed to 200 μL with media. Treated cells were incubated for 30min to 48h. The cells were washed two times with PBS and fixed by 4% paraformaldehyde for 1h, and fixative was aspirated, and the cells washed with PBS three times. Nuclei were labeled by Prolong® Gold Antifade Reagent with DAPI and store in the dark until imaging. Cells were imaged using Leica SP8 MP Confocal STED microscope. Fifteen different confocal images were taken from different locations of a plate in a matrix of 3 by 5 at 475 and 500 nm excitation wavelength for cellular uptake experiment and texas red filter for transfection experiments. Mean fluorescence intensity quantified by using FIJI software. Instead of threshold apply, we subtracted an empty area of an image of cells without particles taken by exact same conditions. The results were graphed based on each time point in origin, and data were normalized. This imaging was repeated on three different experiment sets for each time slot.

4.3.18 Mobility Shift Assay

1% agarose gel was prepared with gel red, and 10 μL samples (SP, SP-pDNA, pDNA) mixed with 10x loading dye (Thermo Scientific™ 6X TriTrack DNA Loading Dye). Samples were then loaded to wells along with 2 μL 1K ladder (Thermo Scientific™ GeneRuler 1 kb DNA Ladder) . Gel run in gel apparatus (Bio-Rad) at 35V for 2h. Gel imaged with a gel imaging instrument (Bio-Rad).

4.3.19 DNA Release Assay

SP-pDNA incubated in two different pH (5.5 and 7.4) in two different solvents (water and PBS buffer) for 0-48h every 20 min for the first 2 hours and for 6, 12, 24 and 48h, each time intervals absorbance was taken with nanodrop. SP in water or PBS used as a reference, and relative absorbances recorded for percentage calculation.

4.3.20 Statistical Analysis

The data were summarized as means ± standard deviation based on experimental values obtained in multiple measurements. Where necessary, the statistical variations (*p* values) between the group means were evaluated by one-way ANOVA.

4.4 Results and Discussion

Iron sulfide (FeS_2) is the most abundant mineral on the Earth and includes sulfur, an essential element to life. While there is little research on iron sulfide NPs, potential advantages include low price, non-toxicity, biocompatibility, high availability and potential biodegradability. Biodegradability is anticipated since it has been reported that FeS_2 can be oxidized to form soluble iron sulfide under biologically relevant conditions involving redox enzymes[305]. Therefore, we aim to synthesized iron sulfide-based SPs as an artificial virus for packing and delivery of DNA. Synthesis of iron sulfide NP in the literature involves toxic reagents such as dimethyl sulfoxide (DMSO), thioglycolic acid (TGA), and ethylenediamine (EDA) [306,307] and include only high boiling point organic solvents as a function of long-chain surfactants.[306] In this study, we investigate the possibility of a simple method that produces iron sulfide NPs, in aqueous media, with amino acid surface ligands in ambient conditions. Aqueous media is used to mimic nature to perceive the self-assembly; as aqueous media can provide a variety of forces to initiate NP self-assembly, and a greater variety of superstructures expected to form with water-soluble NPs.[292] A short stabilizer, amino acid, is chosen to increase the anisotropy of the NP interactions for self-assembly. The choice of an aqueous media and amino acid stabilizer (cysteine, Cys) is also made to reduce the toxicity of the solvent and surfactant.

Careful selection and optimization of the reaction conditions such as precursor concentrations, temperature, pH level, reaction time and temperature allowed us to find a condition where iron sulfide NPs self-assemble into compartmentalized, positively charged SPs (**Figure 4.1**).

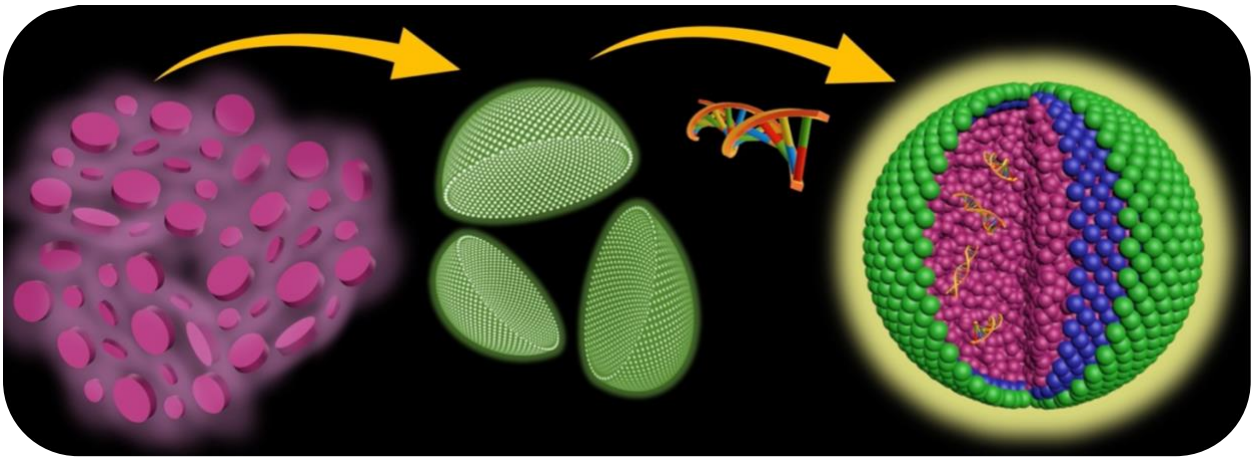

Figure 4.1 Graphical Abstract: Nanoparticles can form compartmentalized supraparticles with cup-like structure intermediates

4.4.1 Constituent Nanoparticles

Constituent NPs are synthesized at low temperature (in ice), and they are plate-like particles with a diameter of 4.5±1.6 nm and a height of ~1.5nm. **(Figure 4.2 a, b, i and Figure S 4.7)**. Zeta potential measured for NPs is ζ 20.5±1.5mV (**Figure S 4.8, NP**). X-Ray diffraction (XRD) gives a weak broad peak (**Figure S 4.9a**). This broad peak may suggest short-range order of NPs.[308] Therefore, we utilized selected area electron diffraction (SAED) analysis (**Figure S 4.9b**) for particle phase identification. SAED analysis reveals that NPs are not just with FeS_2 (Pnnm and Pa-3 space groups, PDF 37-475 and PDF 06-710, respectively) and but also Fe_2O_3 (Aba-2 space group ICSD 430557) NPs (**Table 7**). Energy dispersion X-Ray spectrometry (EDX) also confirms the presence of oxygen (O) along with iron (Fe), sulfur (S) in NPs (**Figure S 4.9c**). During the reaction, some of the NPs oxidized and partially transform to iron oxide NPs. Even though we aimed for iron sulfide NPs, iron oxide NPs incorporation will not change the value of the formed SPs and will actually provide even higher complexity to SPs.

After obtaining constituent NPs, we increased the reaction temperature (room temperature) and conducted a time-dependent experiment. The samples are collected at time 0, after 5, 10, 15, 30, 45, 60, 90, 120, 180, 360 minutes. TEM images show the particle formation during 0-30 min

(**Figure 4.2** a-f), and 0-360 min (**Figure S 4.10**). Based on TEM images, we obtained terminal SPs at 30min (**Figure 4.2**f). UV-Vis spectroscopy gives peaks at 225nm, 270nm, and 365nm for SPs (**Figure 4.2l -blue line**). As can be seen, there is a red-shift in the spectrum from NP (**Figure 4.2l -black line)** to SP at 30 min. For semiconductors, this is a common phenomenon that absorption has a red shift as particle size grows. The color change of black (iron sulfide NPs) to yellow during the reaction also suggests the SP formation (**Figure 4.2l insert**).

4.4.2 Intermediate Structure Between NP and SPs

At the time within 15min an intermediate (cup-like structure) formation is observed in between individual NP and SP. The terminal SP (**Figure 4.2g**) has a solid surface with spherical structures, whereas the intermediate (**Figure 4.2 c-d**). has a translucent and more formless structure. Intermediate structures and terminal SPs can be seen together during synthesis (**Figure 4.2e**), and broken SP pieces reveals similar translucent structures in TEM images (**Figure 4.2d** and **Figure S 4.11**). These indicate that intermediate structures have a role in SP formation. Based on the image analysis of TEM images, the size of the intermediate structure is measured as 55.2±23.1 nm (**Figure 4.2j**).

4.4.3 Supraparticles

Under high-resolution transmission electron microscopy (HR-TEM) at higher magnification, different direction of crystal lattices in the SPs (**Figure 4.2g and h**) indicates SPs formed from individual NPs (*ca.* 6100 ind NPs per SP). Based on the image analysis of TEM images, the diameter of SPs is 72.4±27.3 nm at 30min (**Figure 4.2k**) and it does not change much after this time point (**Figure S 4.10)**. Even though the larger aggregations present after 6 hours, structure and the size of the SPs remain the same (**Figure 4.2f insert**). NTA data of SPs at 360 min also shows aggregation formation as the optimal reaction time (30-minute) passes (Figure S **4.12**,

360min). This data suggests that SPs are self-limiting terminals when optimal time is reached. A system composed of finite sizes and shapes is defined by self-limiting self-assemblies.

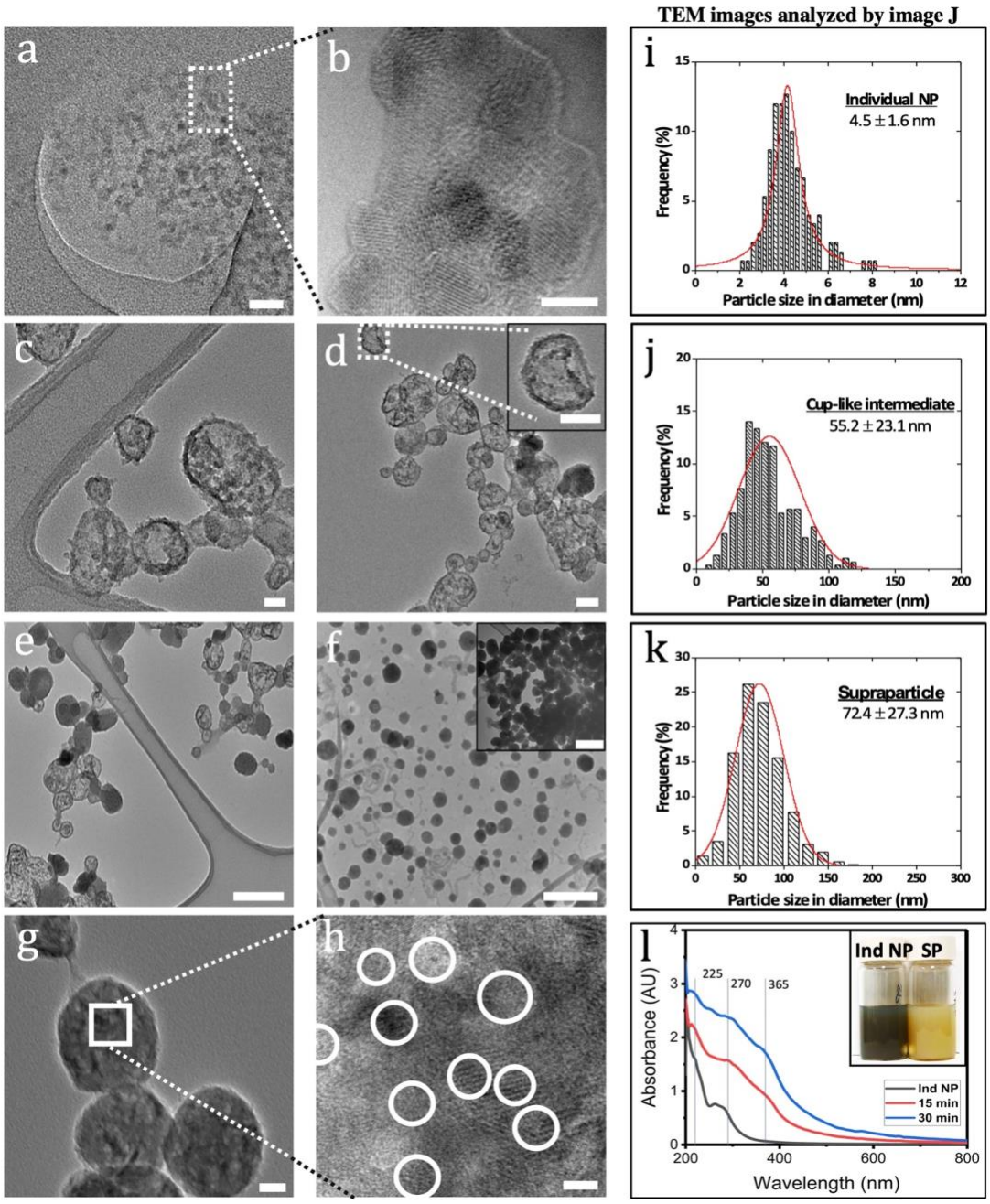

Figure 4.2 Representative high-resolution TEM images (a-h) and image J analysis (i-k) of the SP assembly. (a-b) TEM images of individual NPs. (c-d) Cup-like intermediate structures at 0-15 min. (e) Cup like intermediate structures and mature SPs together at 15min. (f-g) Mature polydisperse SPs (30 min). (f-insert) SP after 6 hours reaction. (h) Individual NP in the SP (g). Based on image J analysis of EM images (i) NP are 4.5± 1.6 nm in diameter, (j) Cup-like intermediate structures are 55.2 ± 23.1 nm in diameter and (k) Mature SPs are 72.4 ±27.3 nm in diameter. (l) UV-Vis spectrum of NP, cup-like structures (15min), and SP (30min). (l-insert) Reaction color of NP and SP at 30 min. Scale bars: (a, c and g) 20nm, (b and h)5nm, (d and insert in d)50nm, (e, f and insert in f) 200nm.

4.4.4 Topological Analysis of Intermediate Structure and SPs

SEM was utilized to understand the surface topography of the intermediate structures and SPs (**Figure 4.3 a-f**). SEM-TLD images show that the intermediate structure is cup-like with open rim area and closed bottom (**Figure 4.3a, 3D model**). Additional images acquired with high angle annular dark-field (HAADF) in scanning transmission electron microscopy (STEM) mode. HAADF images revel the organization of individual NPs in the cup-like intermediate structure **(Figure 4.3b-arrow**).

SEM images show SPs are closed spheres are polydisperse in terms of size (**Figure 4.3**e), similar to image analysis of TEM images and NP tracking analysis measurements SPs (**Figure 4.2k and Figure S 4.12, 30min**). HAADF images reveal some internal structures, as HAADF provides high contrast between heavy atoms and light atoms or empty (void) areas. Therefore, HAADF images show the void area (compartments) in terminal SPs (**Figure 4.3f-arrow**).

4.4.5 Multicompartment in Supraparticle

For further analysis of the 3D structure of the SP and its compartmental organization, STEM tomography (**Figure 4.3 g-i**), and SEM-FIB ion milling (**Figure 4.3 j-l)** was utilized. Two different instrumentations (SEM and TEM) utilized to confirm void area (compartment) formation is not an artifact of the electron beam of the instrument, and both methods show similar continuous compartmentation. Transparent tomographic volume and computational slices reveal that SP has multiple continuous compartments within the shell-like structure (**Figure 4.3h-k**). The measured size of SP is 78.04 ± 37.2 nm (**See 4.6.3**) which is consistent with the TEM image analysis (**Fig. 1k**). The measured volume of SP is $1.01*10^6 \pm 0.832 *10^6$ nm^3, and the size of the compartments is 5.2 ± 1.9nm (**Table 9**). The total volume of the compartments in an SP is $0.15*10^6 \pm 0.048*10^6$ nm^3. This data indicates that approximately 17 ± 5 % of SP's volume is compartments (**Table 9**).

These analyses are especially necessary for calculating possibility as well as the number of cargos that can be packed in an SP.

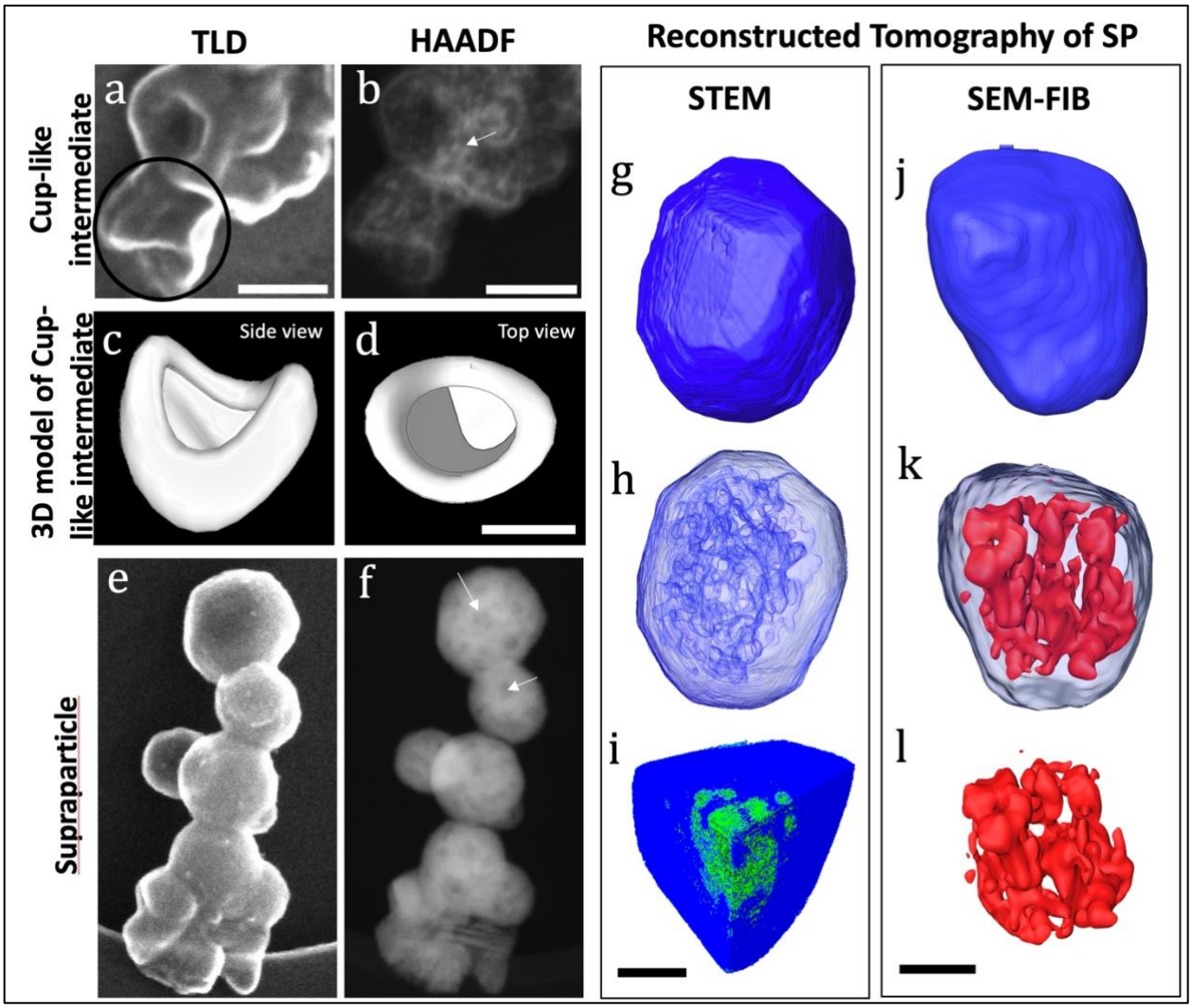

Figure 4.3 SEM and STEM images of supraparticles and cup-like intermediates (a-d) acquired with default Through the Lens Detector (TLD) and High-angle annular dark field (HAADF) in STEM mode. (b) HAADF shows compartments in supraparticles with darker color (pointed with arrow) and (d) Nanoparticle in cup-like intermediate with bright color (pointed with arrow). (e-f) 3D Model of cup-like structures highlighted with black circle in (c). Reconstructed tomography images of SPs (g-l). 3D images of supraparticles acquired by STEM tomography (g-i) and SEM-FIB slice and view (j-l) reconstructed with Avizo software. (g and j) Surface rendering of supraparticles. (h and k) transparent surface of supraparticles showing continues compartments in the supraparticles, red color in (k). (i) x-y-z cross-section of the supraparticle with compartments (green). (l) compartments itself. Scale bars: 50nm, 3D model 20nm.

We conducted elemental mapping analysis to understand how these compartments are formed via localization the elements therefore, different type of NPs in the SPs (**Figure 4.4 a-e**).

These results indicate that Fe and S are located inside of the SP, and they are protected from the outside by 9.86 ± 1.85 nm thick Fe and O layer (**Figure 4.4e**). We can then conclude that FeS_2 NPs located inside of the SP are surrounding the continuous internal compartments and forming the compartments under layers of Fe_2O_3 NPs (**Figure 4.4 f-i**). Based on the calculations, approximately 48% of NPs are Fe_2O_3 and located on the surface of the SPs.

To investigate surface composition, we performed X-ray photoelectron spectroscopy (XPS), and Fourier transform infrared spectroscopy (FTIR) analyses (**See 4.6.4**), and found out cysteine binds to iron in NPs on the surface from its thiol group, and the positive charge is explained by the NH_3^+ groups of the surface ligand (**Figure 4.4 j**).

FeS_2 has an indirect bandgap energy of 0.95 eV [309,310], and Fe_2O_3 has a bandgap energy of 2.1 eV.[311] These two factors combined with the different morphology, various bandgap due to nanoconfinement, crystal size and different intercalation chemistry make SPs almost ideal semiconductor for absorbing broad spectrum of light with wavelengths as long as 700 nm.[312–314] Such energy level structures of FeS_2 and Fe_2O_3 are the main reason of broad absorption (refer back to **Figure 4.2l**). A possibility for photoluminescence from energy states higher than the band edge should also be considered. Based on emission scanning and 3D fluorescence spectroscopy (EEM), we confirmed photoluminescence of SPs (**See Chapter 4.6.5**). Having fluorescence property is an advantage for SPs tracking and localization in cell cultures.

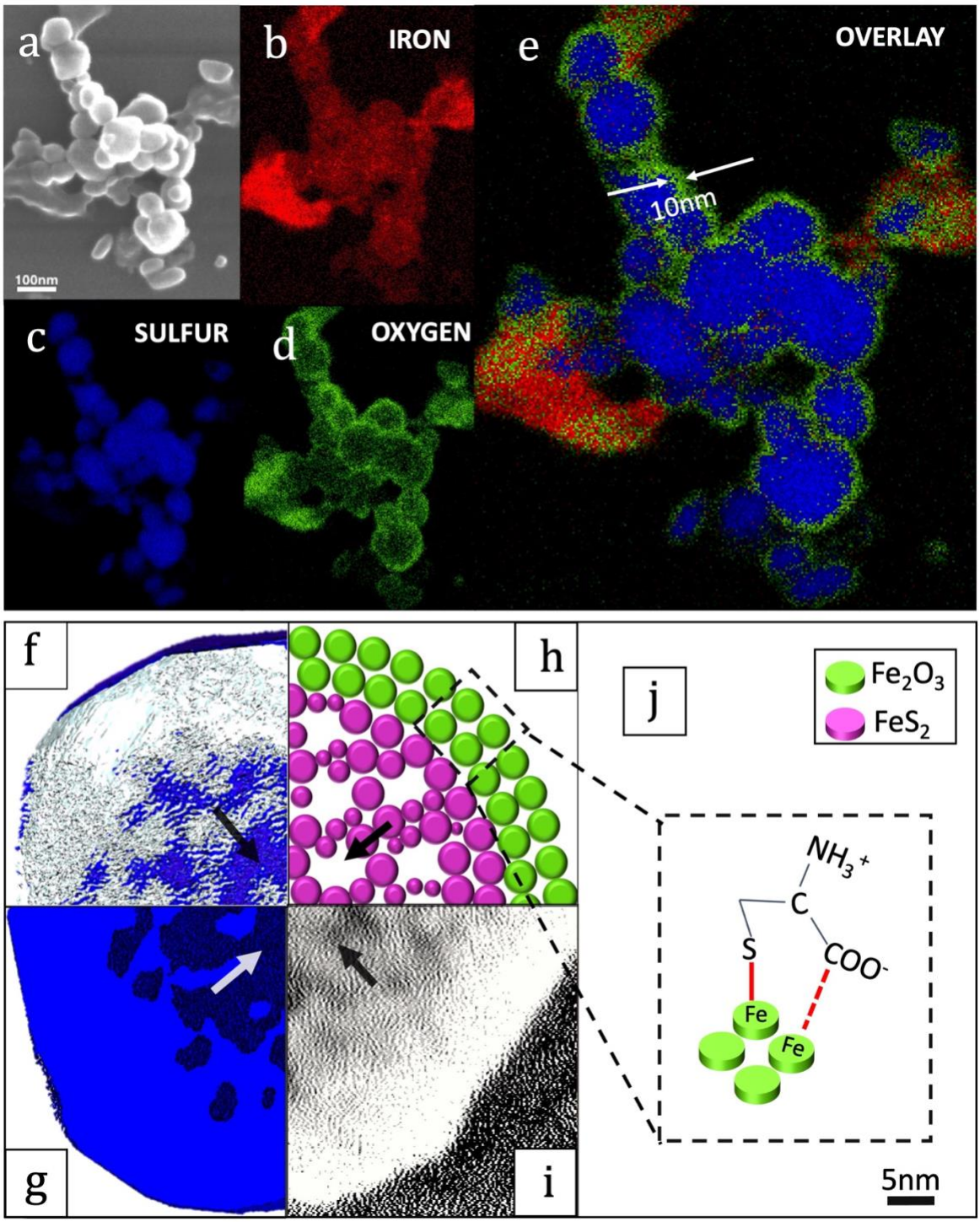

Figure 4.4 Elemental analysis and cross section of SPs (a) An SEM image of SPs (b-d) Elemental analysis of the SPs and location of iron, sulfur and oxygen elements in SPs. (e) overlay image of three element. This image shows that iron oxide NPs are at the surface of the supraparticle and create a shell on the supraparticle. Supraparticles contain internal continuous compartments protected from the outside by Fe_2O_3 NP membrane 9.86 ± 1.85 nm thick. Scale bar in (e) 100nm. Cross-section of reconstructed supraparticle (f) surface and (g) volume acquired by STEM tomography. (h) Scheme of cross section where GREEN spheres show 2 layers of Fe_2O_3 and RED spheres show FeS_2 NPs. (i) orthogonal slice of STEM tomography. Black arrows in each image (f-i) shows compartments.

4.4.6 Assembly Mechanism

Let us now describe the formation mechanisms. The self-assembly of NP into terminal SPs relies on attractive short-range forces: van der Waals, hydrophobic, dipolar interactions, hydrogen bonds and entropic forces, coordination and long-range repulsive interactions; primarily intermolecular electrostatic interactions. [183,187,302,315–317] Anisotropy is also quite critical for SP formation. Anisotropy of the force fields can result from both disk-like shaped NPs and the "patchy" distribution of electron density. [292] Also, type and amount of stabilizer play a critical role in SP formation. Short stabilizer, cysteine, provides a thinner shell on the surface and allows attraction forces to play their roles for SP assembly since short stabilizers increase electronic interactions between the NP core.[292] Plus that, similar to CdS nanoshell formation, the amount of stabilizer is very little[252] that may cause the patchy distribution of electron to increase the anisotropy and also may increase repulsions inside of the nanoshell to form compartments.

NP with thin shells starts to assemble first into cup-like structures and then SPs. The cup-like formation is a very unusual structure for self-assembly. We saw chains,[290,298] rings[299], and sheets[187] assembly, but what causing concave structure. So, we think that once oxidation starts on NPs, it increases the anisotropy for self-assembly. The repulsion electrostatic forces on the big lateral surface of the nanodisk must help them to assemble side by side instead of vertical stackings. Once intermediate cup-like structure are formed, couple of them come together and form SPs. Size distribution and anisotropy on these intermediates may cause compartment formation during the reactions.

It is worthwhile to say that these SPs are very similar to virus capsids. Typical structural capsid protein, having a mean diameter of 5 nm and a mean thickness of couple nm[318] similar to

NP size and thickness. The way of SPs formation helped us to utilize the compartments for cargo packing.

4.4.7 Compartment Utilization - DNA Encapsulation

To utilize the compartments within SPs, we captured cup-like structures before they matured into SPs with decreasing the temperature at 15min; and add condensed pEEB cherry plasmid DNA (pDNA) as a reporter gene to the system dropwise. SP maturation is then allowed for another 15min. SPs containing plasmid DNA (SP-pDNA) are analyzed for DNA presence. UV-Vis and circular dichroism data do not show any differences in the spectra between SP and SP-pDNA (**Figure 4.5a-b**). DLS data of SP-pDNA also provides the same zeta potential with SP (**Figure 4.5**c). STEM and TEM (**Figure S 4.22**) do not show any significant differences. Only in HAADF STEM images show some difference (**Figure S 4.22 d vs. h**), and it looks like the compartments are filled in SP-pDNA (**Figure S 4.22, arrow**). This could be due to the organization of compartments are different with DNA or DNA is filling the compartments. All these data suggest that there is no evidence of DNA is on the surface of the SPs. The supernatant of SP-pDNA is also measured to make sure DNA does not remain in the solution after centrifugation (**Figure 4.5a SPN SP-pDNA**). However, these data also do not prove any DNA present in the system. Therefore, we utilized electrophoresis mobility shift assay (EMSA) in where naked DNA moves freely in the gel, but if it attached to anything becoming heavier and stays behind.

EMSA proves the DNA present in the system by first showing a band in the gel (**Figure 4.5d**-**SP only**, SP does not show any band in); second, it stays behind in well. (**Figure 4.5d**) Also, the DNase assay indicates that DNA is protected in SPs (**Figure 4.5d SP-pDNA-DNase I**). The absence of a free pDNA band in the SP-pDNA line, along with no DNA in the supernatant of the reaction, may also suggest that SPs show approximately 100% encapsulation and protection of

pDNA. Final prove of the DNA encapsulation is elemental mapping in where phosphate signal specific to DNA stays inside of the iron oxide layer of SP (**Figure 4.5e**). All these data confirm DNA is successfully encapsulated in the SP.

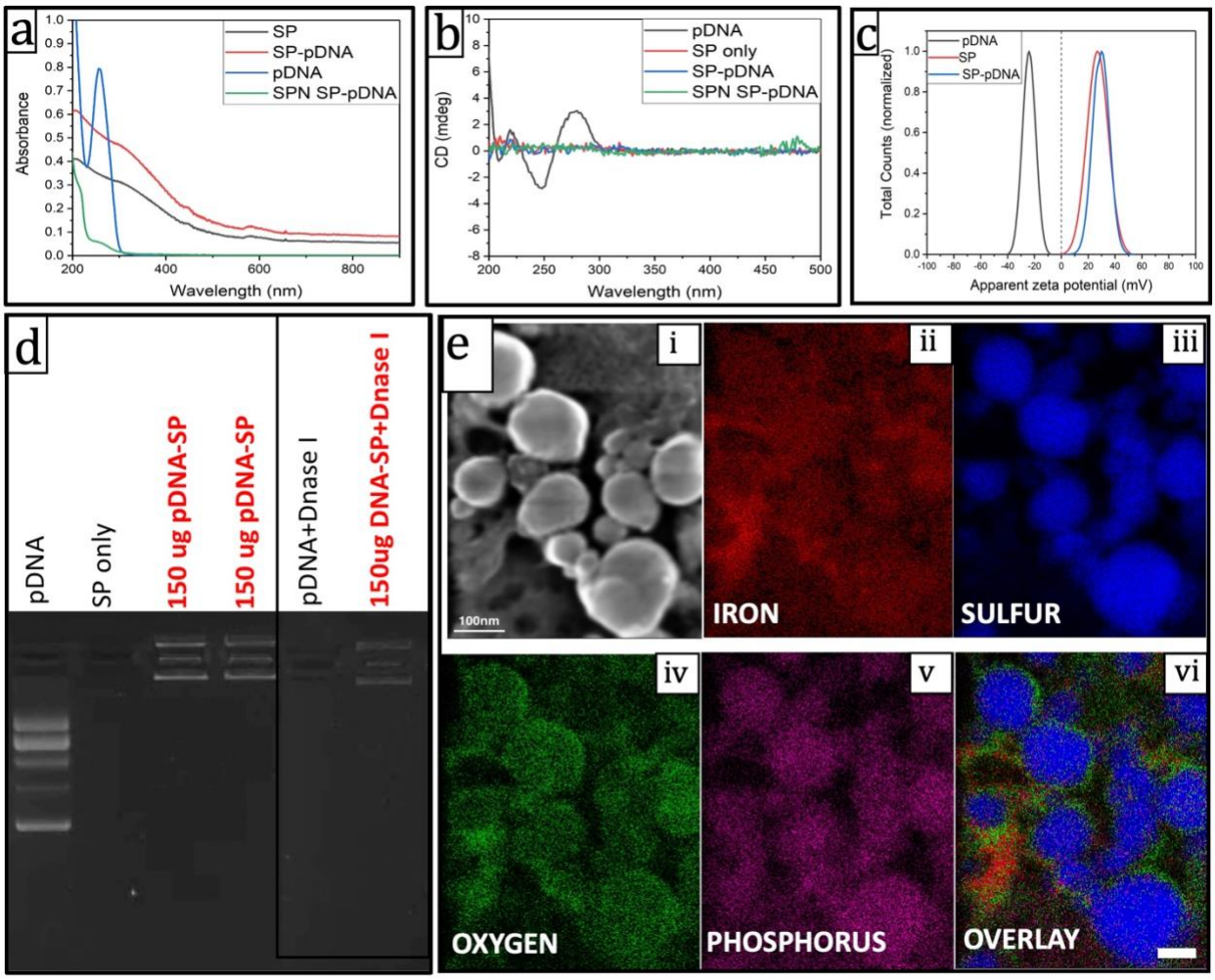

Figure 4.5 DNA encapsulation: (a) UV-Vis spectra (b) Circular dichroism and (c) Zeta potential comparison of SP, DNA encapsulated SP (SP-DNA) and pDNA. (d) Electromobility shift assay (EMSA). SP bounded DNA stays behind of naked pDNA. SP can protect DNA from DNase I degradation. (e)Elemental analysis of SP-DNA (i) An SEM image of SP-DNA (ii-v) Elemental analysis of the SPs and location of iron, sulfur, oxygen and phosphorus (DNA specific signal) elements in SP-DNA. (vi) overlay image of four element. This image shows that DNA stays under the iron oxide NPs shell in the supraparticle. Abbreviations: SP: Supraparticle, SPN: Supernatant, pDNA: Plasmid DNA

4.4.8 Cellular Uptake, Cytotoxicity, and Transfection

For cellular experiments the number of particles per cell must be controlled. We want to provide as much particle as possible to overcome the drawbacks and increase the transfection but also do not want to cause any cytotoxicity. Based on cytotoxicity assay, we calculated particle concentration of SP that is ~1000 SPs per cell (10X) gives the high enough particles without creating cytotoxicity (**See 4.6.9**). For cellular uptake analysis we use the advantage of auto fluorescent of SPs and calculate mean fluorescent intensity of SPs under confocal images. SPs gave the highest emission intensity when they excited at 475 nm and 500 nm in the window of 520-700nm emission wavelengths (**See 4.6.5**). Thus, confocal images of SP treated cells are observed at 475 nm (**Figure 4.6 a**) and 500 nm (**Figure 4.6b**). We are using two different excitation wavelengths to confirm the signal is coming from SPs, and it is not an artifact of the other cell compound. With increasing incubation time, the mean fluorescence intensity per area of an image is increased gradually, representing cellular uptake increases. For the first 2 hours, the cellular uptake was much faster; after 2 h, the cellular uptake started to slow down, and in 6 h, the cellular uptake gradually reached saturation where is the percentage of fluorescence positive cells no longer increased (**Figure 4.6e**). SPs are started to attach to cells in 1h; even after 3x washing, we can see particle attachment on the cell surface (**Figure S 4.25**). Fluorescence intensity of particle in cells does not change between 4h-12h (**Figure S 4.26 a-b**), and untreated cells do not show any fluorescence at the same laser intensity **(Figure S 4.26 c**).

For transfection experiments, we imaged HEK293T cells treated with SP-pDNA for specific time intervals starting from 6h to 24h. Transfection is also expressed as mean fluorescent intensity of confocal images of reporter protein (pEBB cherry-red color). Even though cellular uptake reaches saturation at 6h, releasing and transcription of pDNA takes time. Therefore, we started to see red-

colored cells after 9 hours (**Figure 4.6f- See 4.6.11 for release assay**). Confocal images of SP-pDNA transfection can be seen in **Figure 4.6h-j**. The results comparison between SP and lipofectamine is not statistically significant (**Figure 4.6g, Figure S 4.28**). However, improving these SPs are very promising; as SPs can condense DNA, protect it against degradation, enter through cellular membranes, and facilitate endolysosomal escape in gene therapy. Here it worth the mention that there are possibilities that not all DNA will be packed and not all vectors will enter the cell and not all uptaken vectors will release the cargo. All these challenges lower the transfection efficiency.

A fine balance between extracellular protection, intracellular release, and biodegradation is crucial. The presence of iron in SPs may facilitate cellular uptake due to van der Waals interactions of the SPs and cellular membrane. This feature may decrease the excessive membrane potential change occur with liposomes. The release of cargo after transmembrane transport is facilitated by the spontaneous disassembly of SPs in the cells. Attractive-repulsive forces between constituent NPs control SPs stability. The low dielectric constant of cytosol will result in increased inter-NP repulsion and, thus, SP disassembly. Therefore, the development of these particles can be used as an effective delivery tool for gene therapy. These SPs can be used for imaging too since they can be observed under confocal microscopy such as cadmium and selenium based quantum dots [319]. However, iron sulfide NP does not carry the potential of carcinogenicity.

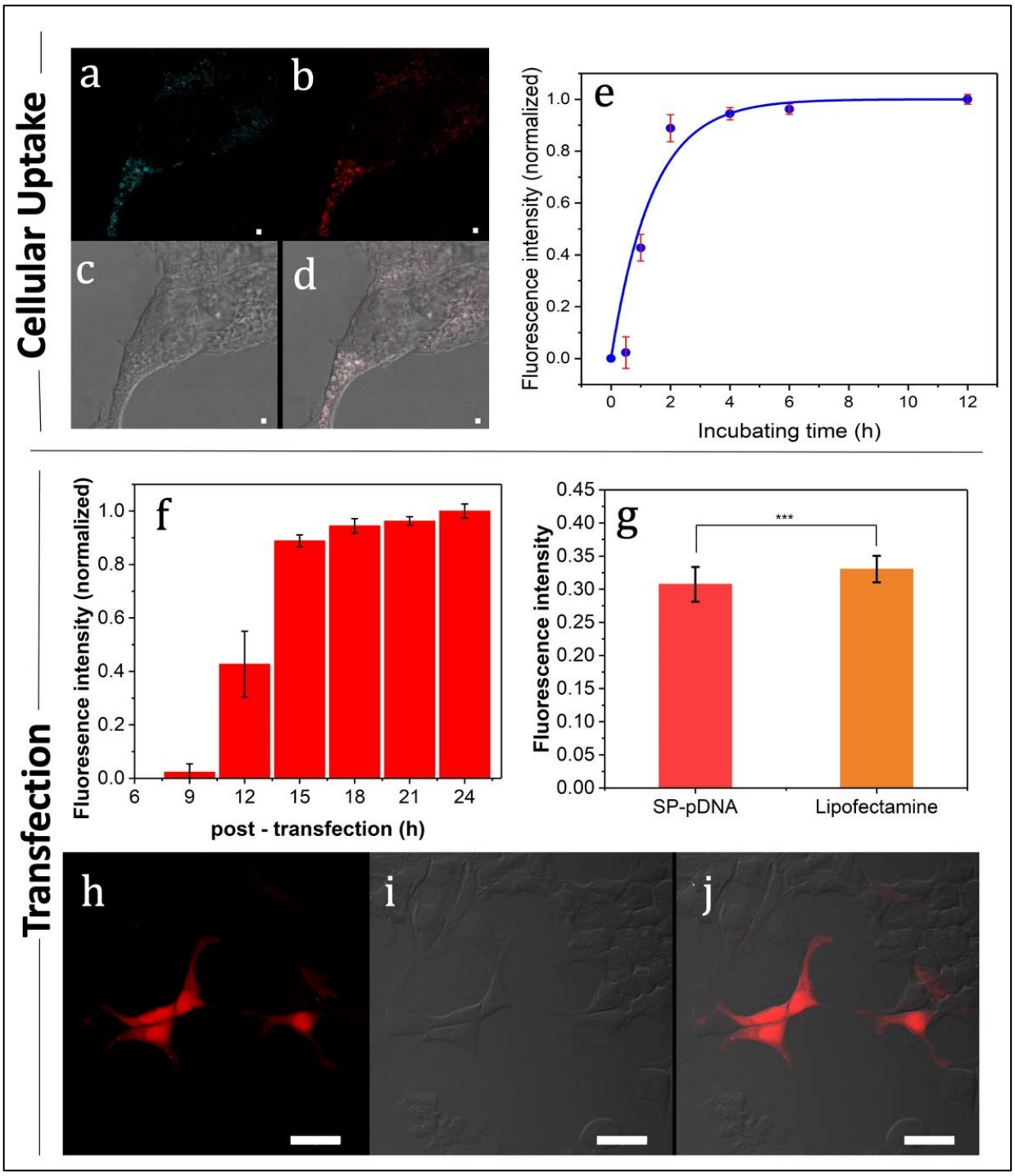

Figure 4.6 Cellular uptake and transfection data. (a-d) A confocal image of cellular uptake of SP after 12h. SP in cell in (b) is excited at 475 nm and in (c) is excited at 500 nm emission for both excitation is 520-570nm. (d) SP aggregations can be seen in a cell. (e) Average fluorescence intensity of confocal images of SP treated cells. (f) Average fluorescence intensity of confocal images of SP-DNA treated cells post-transfection 6-24h. At 24 h it reaches the highest transfections efficiency. (g) Transfection capability comparison of SP and lipofectamine. ****p* value: (h-j) Confocal images of cells post-transfection 24h. Cheery protein gives the red color to the cells. Scale bars: (b-e) 0.5µm, (h-j)25µm

4.5 Conclusions

In this paper, we showed that inorganic NPs could self-assemble to SPs with compartments within a stable shell. Self-organization of these SPs origins from very unusual shape, cup-like, intermediate structures. Couple of cup-like structures assembles in a way that arranges into a multi-compartment within a shell. These self-organized compartments can be used for multiple functions such as biomacromolecules packing and delivery. Hence, the development of these particles can be used as an effective delivery tool for DNA or mRNA as artificial viruses for next generation theranostic applications.

4.6 Supplemental Information

4.6.1 Constituent Nanoparticles

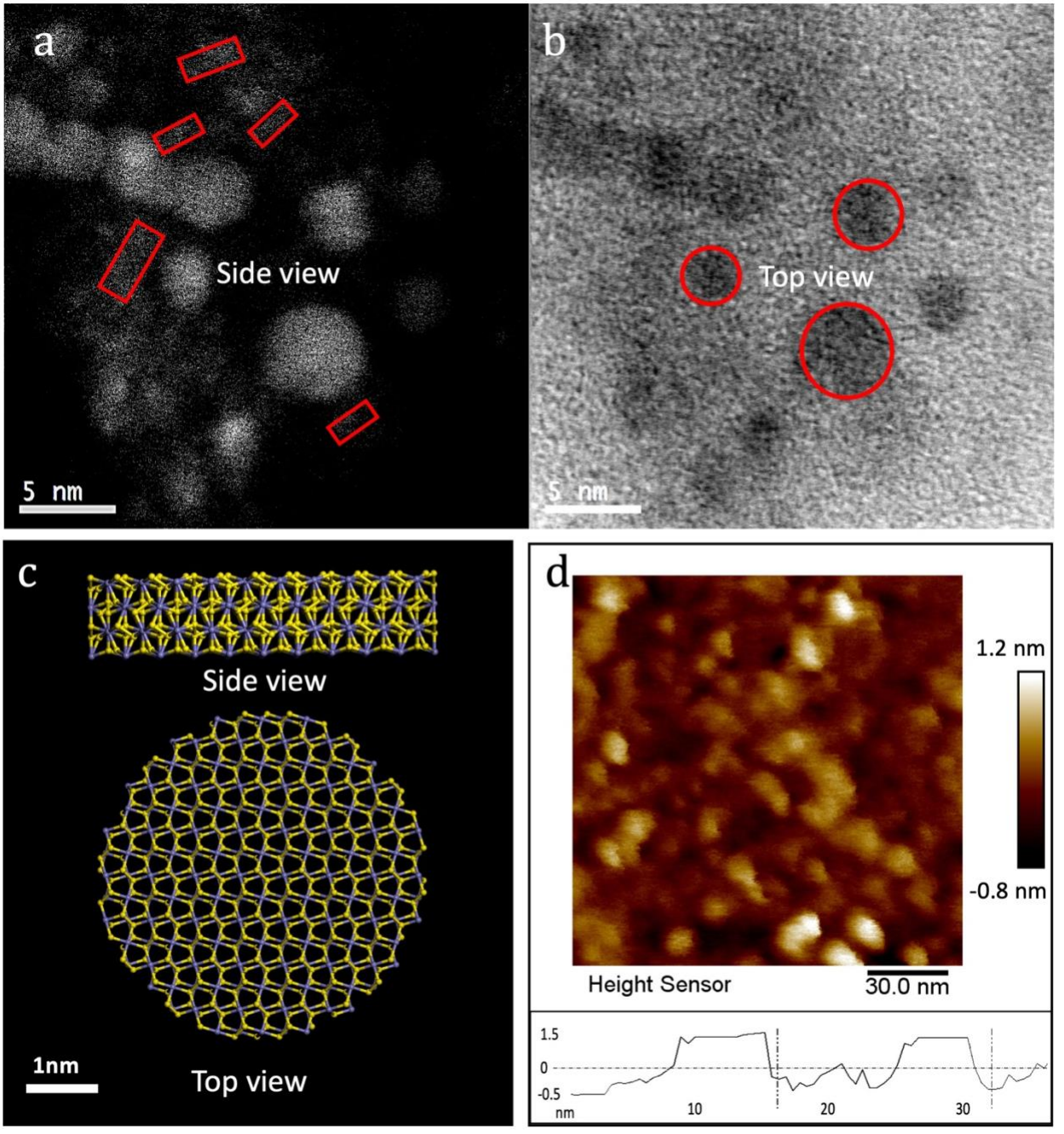

Figure S 4.7 STEM images of nanoparticles that are seen from various angles. (a) Dark Field (b) Bright Field (c) Scheme of ind NP - represents 45 different images and shows plate-like particles. (d) AFM data of NP. Scale bar (a,b) 5nm, (c) 1nm.

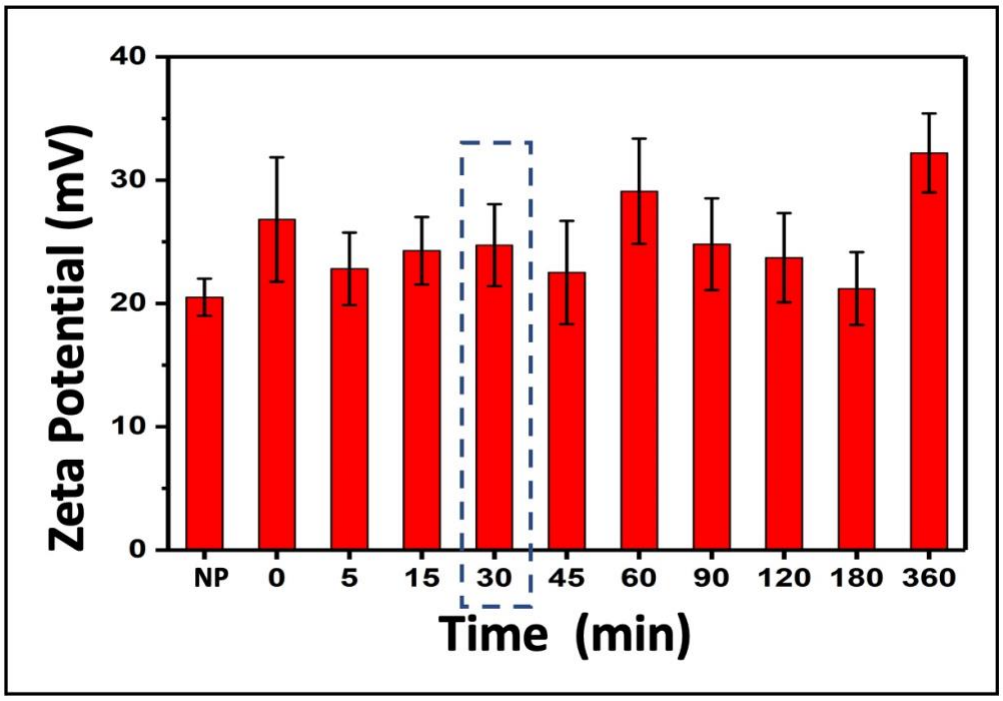

Figure S 4.8 Zeta potential of synthesis reaction time points at NP, 0, 5, 15, 30, 60, 90, 120, 180 and 360min.

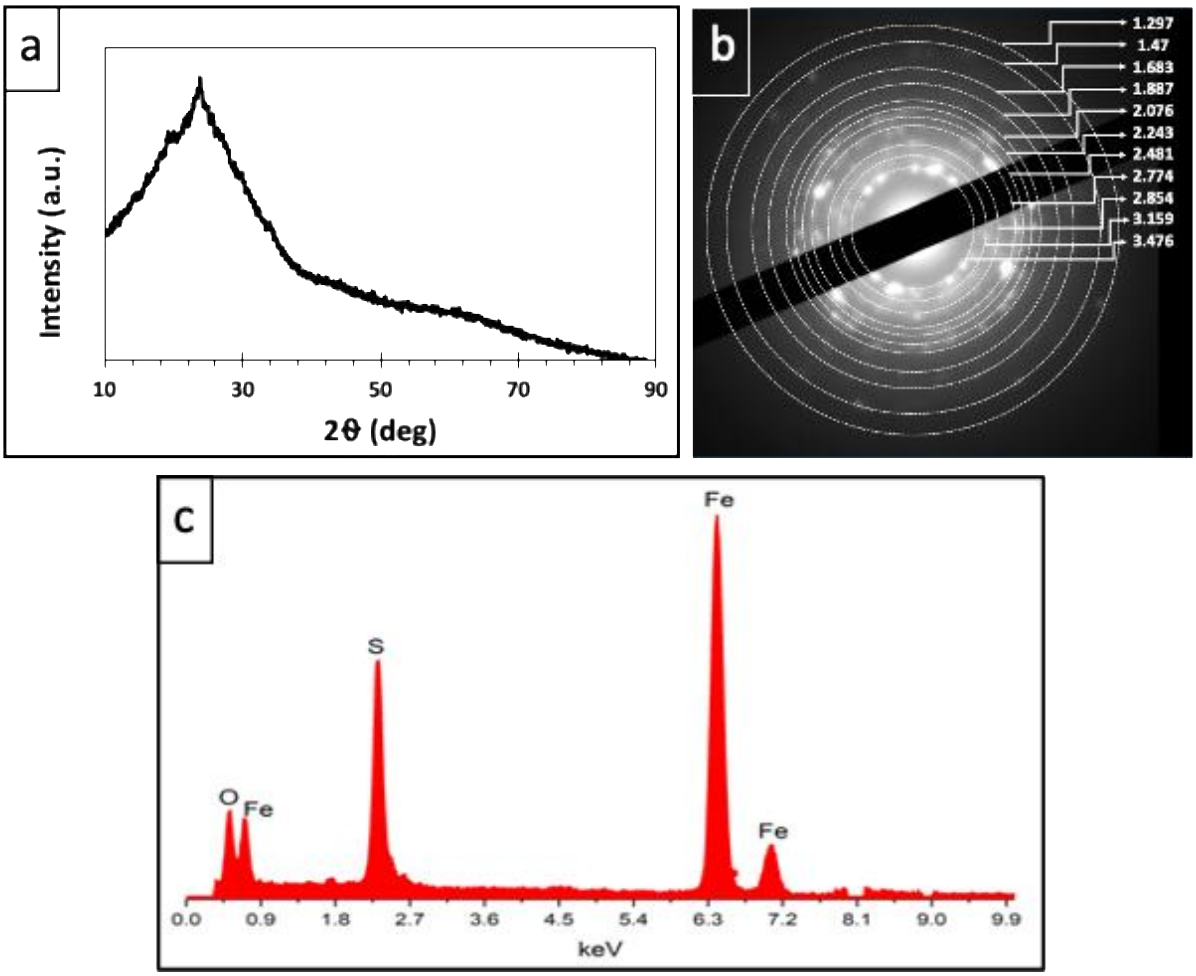

Figure S 4.9 (a) XRD data of constituent NPs. (b) SAED of constituent NPs and corresponding d-spacing of each diffraction ring. (c) EDX analysis data of constituent NPs, background subtracted.

Table 7 Comparison of d-spacing of NPs *vs*. FeS_2 and Fe_2O_3

NP	**FeS_2 (Pnnm)**		**FeS_2 (Pa-3)**		**Fe_2O_3 (Aba2)**	
d-spacing	d(hkl)	hkl	d(hkl)	hkl	d(hkl)	hkl
3.476	3.4313	110				
3.159			3.1339	111	3.262	200
2.854	2.8677	011			2.9371	111
2.774	2.689	101	2.7141	200		
2.481	2.4083	111	2.4275	210	2.351	020
2.243	2.218	200	2.216	211	2.2118	120
2.076	2.0524	210	1.9191	220	1.9073	220
1.887	1.7545	211	1.8094	221	1.8805	202
1.683	1.5921	031	1.6366	311	1.6446	022
1.47	1.3998	230	1.4507	321	1.4685	222
1.297	1.2977	320	1.2794	411	1.2256	331

Components of this table is chosen based on selected area electron diffraction (SAED) analysis

4.6.2 Time Dependent Experiment During SP Formation

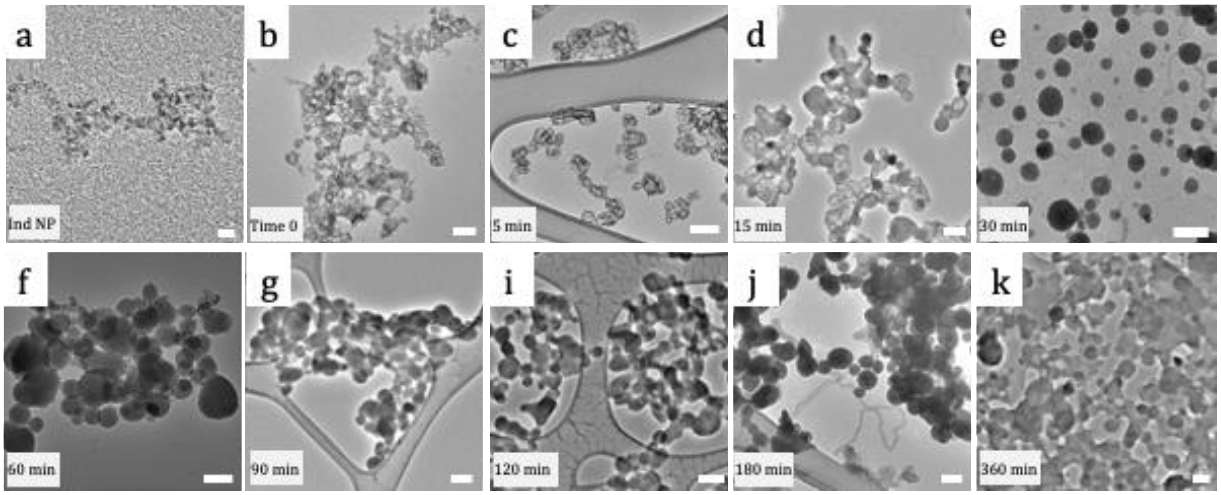

Figure S 4.10 TEM images of ind NPs and synthesis reaction time points at, 0, 5, 15, 30, 60, 90, 120, 180 and 360min. Scale bars: (a) 5nm, (b-k) 100nm

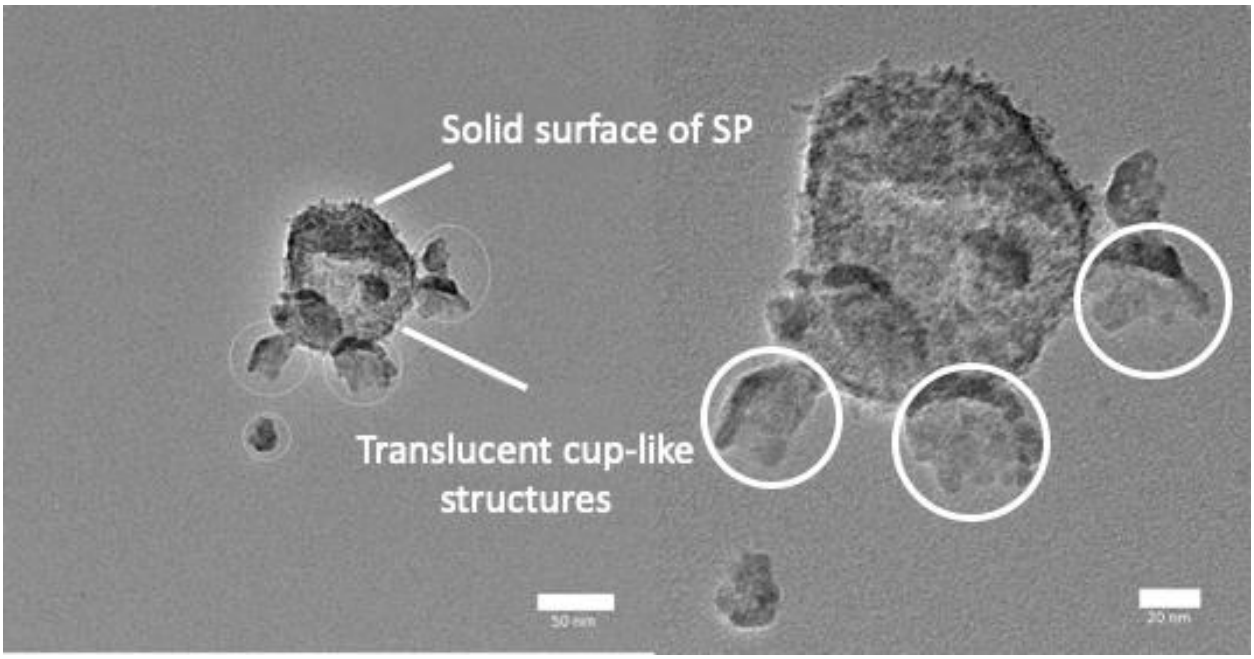

Figure S 4.11 TEM images broken SP pieces.

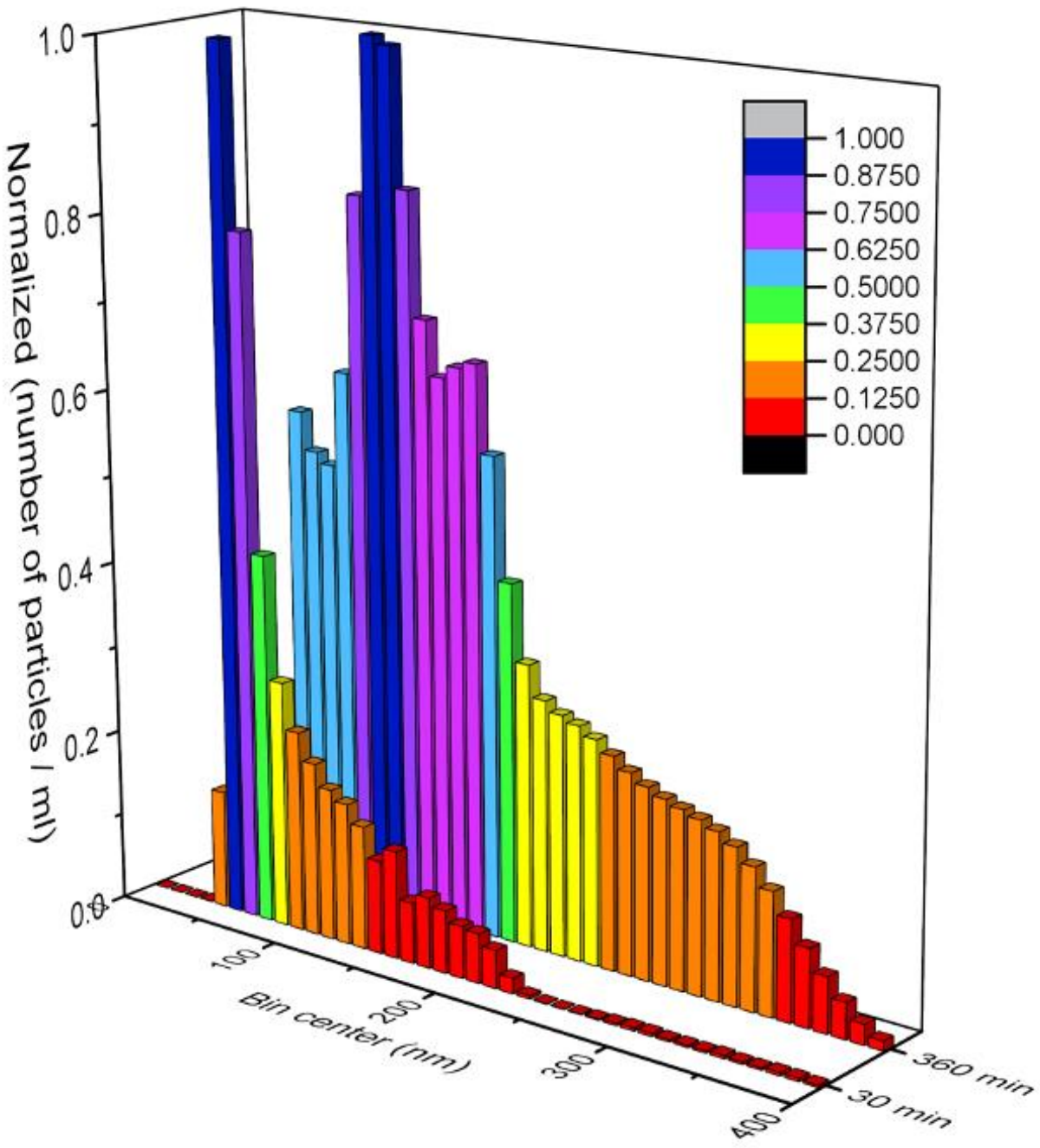

Figure S 4.12 Nanoparticle tracking analysis of SP at 30 min and 360min.

4.6.3 Statistical Analysis of SP and Compartments Volume

For the statistical analysis of the compartments, SEM-FIB ion milling (slice and view) was utilized since STEM tomography is not quite feasible for a cluster imaging and requires excess tomography data. SEM-FIB uses only the sliced particle images instead of tilted imaging; it is quite useful for multiple particle analyses at once. We, therefore, chose an area that has a cluster with polydisperse SPs for further investigation under SEM. Polydispersity is crucial to represent the entire SP population (**Figure S 4.13**). Seventeen SPs in this cluster are first grouped based on location in the cluster and color-coded. Number of SPs, each SP size in diameter, average volume, and surface area of each color-coded area (blue, green, red, yellow, gray, and light blue) are measured (**Table 8).** We used

Figure S 4.14 for calculation of the volume. As SPs are not perfect spheres, volume measurements ($1.01*10^6 \pm 0.832 *10^6$ nm^3) are slightly different than the calculation based on the average radius of a sphere with R=72.4 ($1.59 \pm 0.0853*10^6$ nm^3) **(Table 9)**.

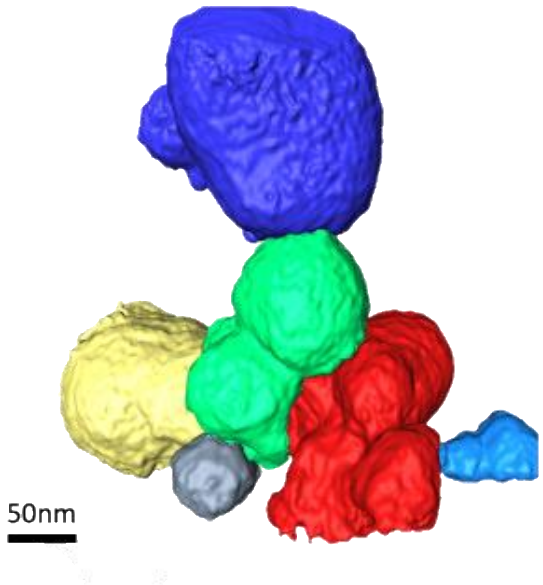

Figure S 4.13 3D reconstruction images of supraparticles acquired by SEM-FIB slice and view. Scale bars: 50nm.

Table 8 Summary of Volume and Surface Area of SPs in Figure (a) Based on 3D Reconstruction Analysis

Color area of SPs	Number of SP in each color area	Diameter of each SP in each color (nm)	Total Volume ($106\ nm^3$)	Total Surface Area ($105\ nm^2$)
Blue	3	174.61, 74.98, 58.21	2.29	1.03
Green	5	95.84, 71.35, 47.58, 58.63, 53.26	1.12	0.69
Red	5	138.24, 68.07, 40.74, 68.97, 97.52	1.3	0.83
Yellow	1	124.29	1.15	0.67
Gray	1	60.29	0.10	0.12
Light Blue	2	57.5, 36.74	0.72	0.10

Table 9 Measured Average Diameter and Volume of SPs and Compartments

	Diameter (nm)	Volume (*106 nm3)	Calculated volume (*106 nm3) (R=72.4nm)
Supraparticle	78.05± 37.22	1.01 ± 0.0832	1.59 ± 0.0853
Compartment	5.2± 1.9	0.15± 0.048	* Volume is calculated based on average sized SP from image J.
17 ± 5 % of the volume of supraparticles is compartments			

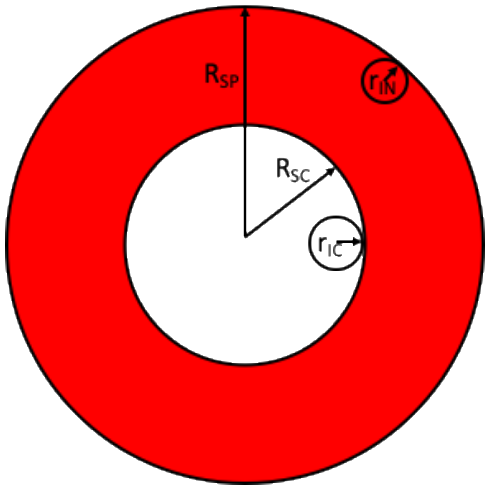

Figure S 4.14 Geometrical model for ind NP calculation in a SP. SP with radius R_{SP}, ind NP with radius r_{IN}, compartments of SP with radius R_{SC}, individual compartments with radius r_{IC}.

4.6.4 Surface Composition of SPs

We performed X-ray photoelectron spectroscopy (XPS), and Fourier transform infrared spectroscopy (FTIR) analyses to investigate surface composition (

Figure S 4.15 a-b). High-resolution XPS data **(Figure S 4.16)** suggests that cysteine binds to iron from the thiol group with the presence of Fe-S bond on FeS_2 surface and O-Fe-S bond on the Fe_2O_3 surface. S_{2p} spectra were fitted with several doublets corresponding to the $S_{2p\ 3/2\ -\ 1/2}$ components with a 1.2 eV spin-orbit splitting and area ratio of 0.5.[320] The S_{2p} binding energy at 162.30 eV and 163.50 eV should be assigned to FeS_2 $S2p_{3/2}$ and $S2p_{1/2}$ respectively. On the other hand, the S_{2p} binding energy at 167.20 eV and 168.40 eV should be assigned the sulfur from cysteine binds to Fe_2O_3 (S-Fe-O) $S2p_{3/2}$ and $S2p_{1/2}$ respectively. The peak at 167.20eV (5 eV shift of typical S-H peak 162.20eV) is indicating the chemisorption of cysteine via a sulfur group on Fe_2O_3 [321,322] (**Figure S 4.16 a**). Fe_{2p} spectra of high-spin compounds exhibit multiple complex splitting and have satellite features. Therefore, five peaks are observed under Fe_{2p}. Two peaks for Fe_2O_3 $2p_{3/2}$ and $2p_{1/2}$, and two peaks for their satellite peaks. The fifth peak is $2p_{3/2}$ for FeS_2. Fe_{2p} in FeS_2 has low spin compounds; therefore, no split or satellite features observed (**Figure S 4.16 b**). O_{1s} binding energy at 529.80 eV should be assigned to Fe_2O_3, and 531.5 eV should be assigned to O-C=O from L-cysteine (**Figure S 4.16 c**). The cysteine binding on the NP confirmed with FT-IR (

Figure S 4.15 a). Amino acids generally show IR spectra specific to both carboxylate and primary amine salts since they exist as zwitterions[52]. Therefore, *L*-cysteine showed very broad peak for NH_3^+ stretch ($\nu(NH_3^+)$) at 3000-3500 cm^{-1} and COO^- stretch ($\nu(COO^-)$) at 1350-1700 cm^{-1} all are very typical amino acid IR spectra.[323] The weak S–H bend at 2550 cm^{-1} specifies a cysteine molecule (

Figure S 4.15 a). Asymmetric COO- and NH_3^+ stretching can cause a shift in the position in the IR spectra due to dipole moment change as when cysteine binds on the metal surface with high electron density. Weak S-H peak disappears in SPs' IR spectra, and this verifies the covalent interaction of sulfur and iron (

Figure S 4.15 a). Therefore, cysteine binding to iron from the thiol group is confirmed, and the positive charge is explained by the NH_3^+ groups of the surface ligand (**Fig. 3j and**

Figure S 4.17).

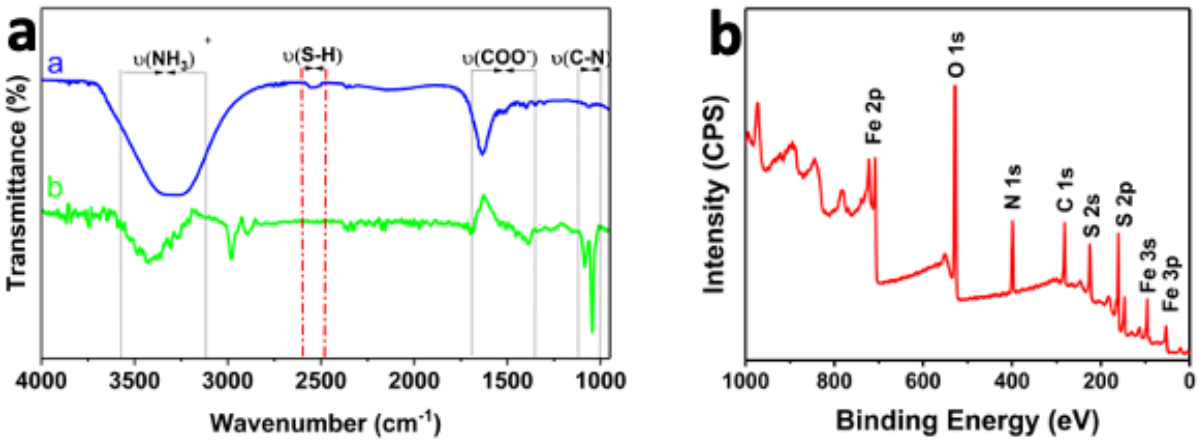

Figure S 4.15 (a) FT-IR spectra of L-cysteine (a-blue) and SP (b-green). (b) XPS survey spectrum of SPs.

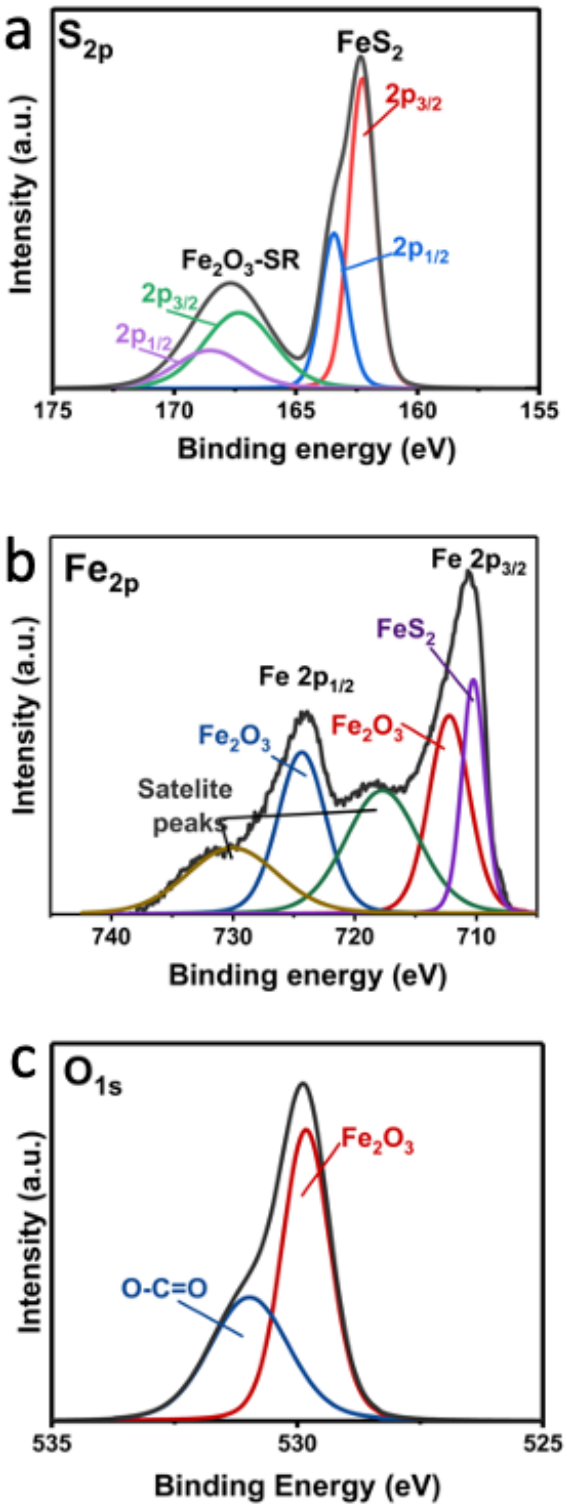

Figure S 4.16 High resolution XPS spectra of (a) S_{2p} (b) Fe_{2p} and (c) O_{1s} of SPs.

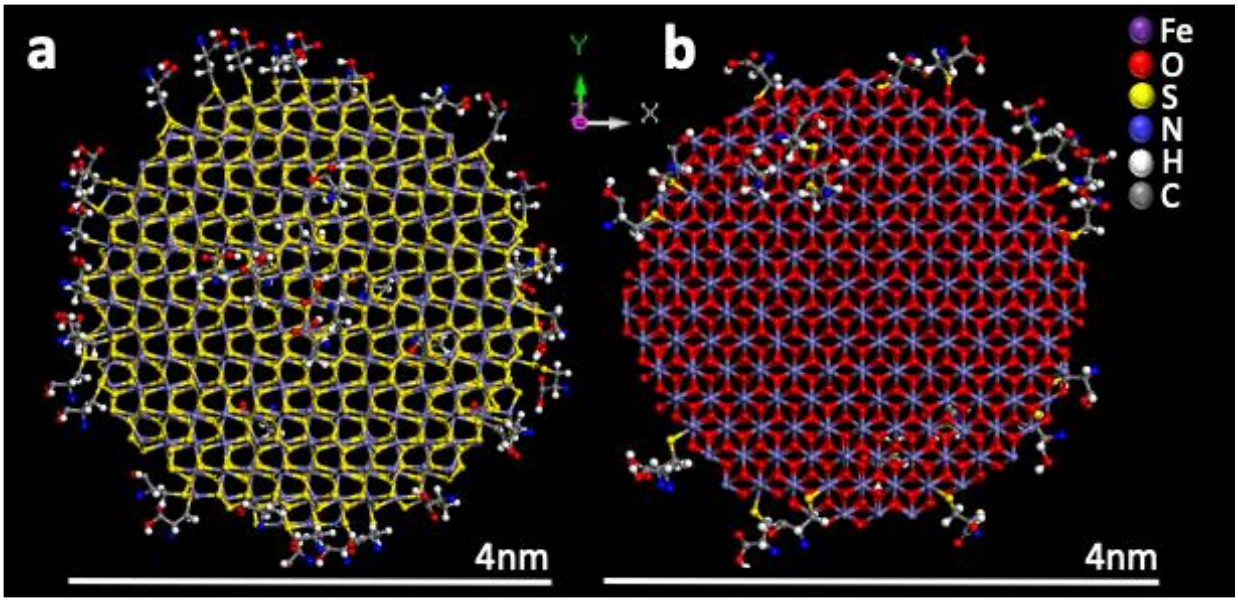

Figure S 4.17 An atomic representative of iron sulfide NP (c) and iron oxide NP with L-cysteine on the surface. L-cysteine bind s to iron from thiol group.

4.6.5 Photoluminescence Analysis of SP

We performed an emission scanning and 3D fluorescence spectroscopy (EEM) to confirm photoluminescence. The stable emission peaks are seen at between 320 nm - 650 nm confirms the autofluorescence of SPs **(Figure S 4.18a and Figure S 4.19**). Emission picks at 350-550nm (**Figure S 4.19b**-solid lined box) with broad range excitations (200-600nm) sources large stokes shift (~50nm). We also performed lambda scanning under Leica SP8 confocal microscope to find the best excitation and corresponding emission wavelengths for future confocal imaging. Fluorescence intensity data from lambda scanning is entirely consistent with our fluorescence data and stays in the highest excitation range (**Figure S 4.18).** This data also shows the highest emission can be obtained when SP suspension excited at 475nm and 500nm under confocal microscopy. Further imaging is continued with 475nm and 500 nm excitation with a 520-570 nm emission window. The resolution of the light microscopy is not enough to observe individual SP; however, around 200nm aggregations of SPs can be easily seen (**Figure S 4.18b-e)**

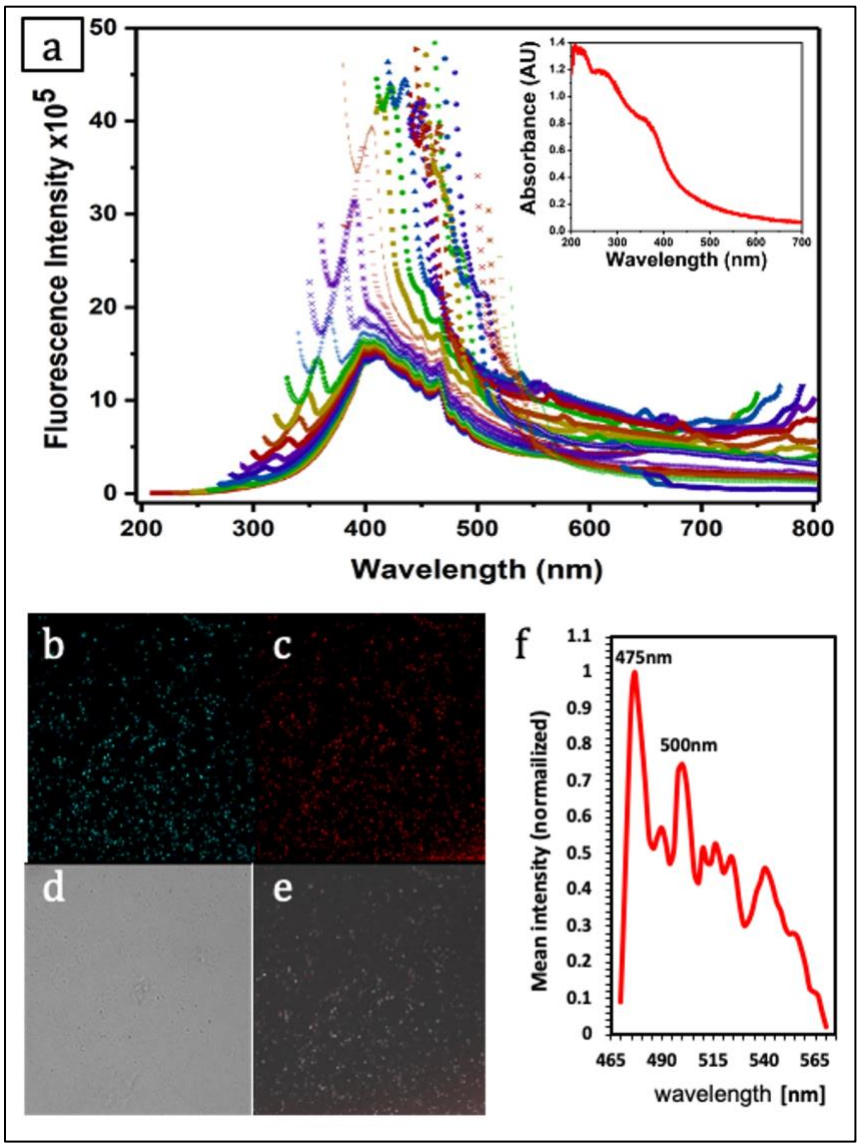

Figure S 4.18 (a) Fluorescence emission of the SP. The graph shows SP emission at the excitation wavelengths from 200 to 600 every 10 nm increments. The graph in the insert shows UV-Vis spectrum of the SP. b-e) SP suspension under confocal microscopy. b is excited at 475 nm and c is excited at 500 nm emission for both emission is 520-570nm. d) DIC image e) overlay image. Scale bar : 2 μm f)Excitation spectrum in confocal microscopy shows 475nm and 500nm gives the highest emission intensity.

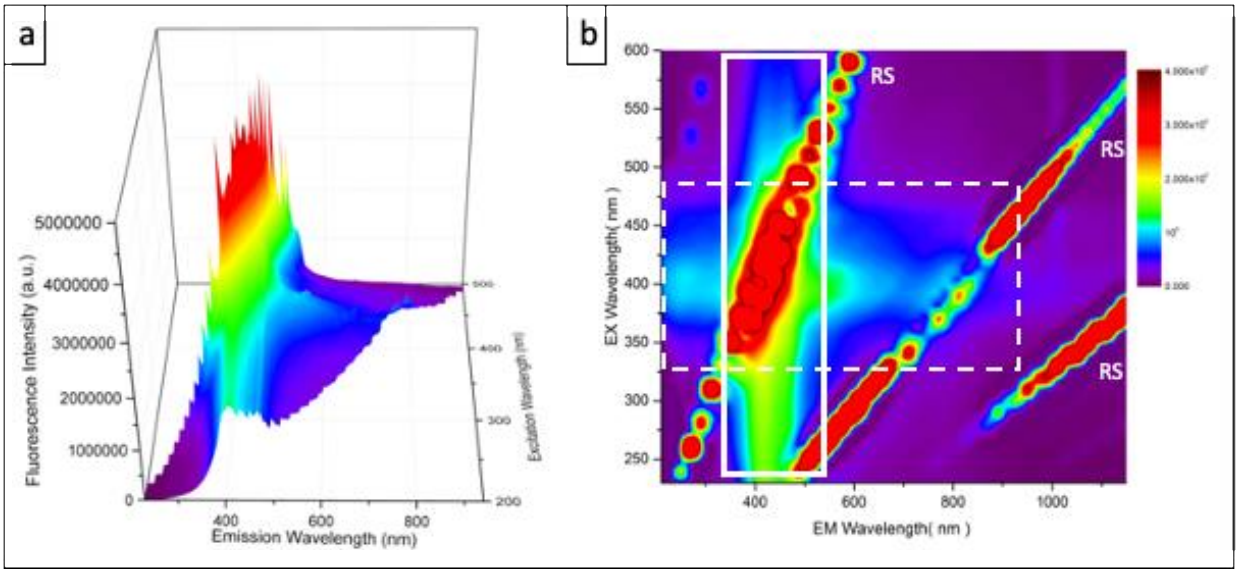

Figure S 4.19 (a) 3D waterfall of Figure S10a fluorescence spectra and (b) contour map Excitation-emission matrix (EEM) spectra of the SP suspension. RS is Rayleigh scattering peak, $\lambda_{ex} = \lambda_{em}$. Solid lined box in (b) shows stable picks (350-550nm) with broad range excitations (200-600nm). Dashed box in (b) shows the excitation range gives highest emission.

4.6.6 Chemical Composition of Cup-Like Structures

To understand the mechanism of cup-like structure formation, we checked the composition of cup-like structures. Cup like structures are also composed of Fe, S, and O (**Figure S 4.20**); the amount of Fe_2O_3 NP is higher than FeS_2 NPs (**Table 10**). However, the amount of FeS_2 NP is higher in SP. Not packed FeS_2 NPs must be washed through washing steps while we collect cup-like structures from the reaction. Color change during the reaction shows that individual NPs are self-assembled into first cup-like structures (15min) and then SPs (30 min) with the effect of oxidation.

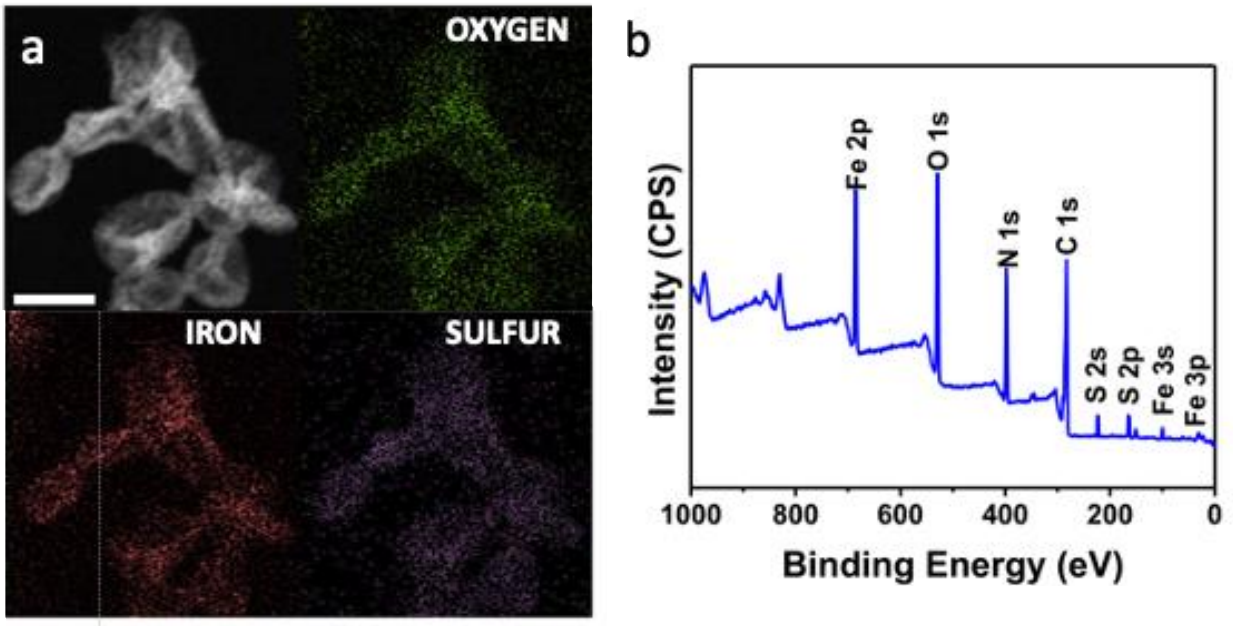

Figure S 4.20 (a) Elemental analysis of the SPs and location of iron, sulfur and oxygen elements in cup-like structures, (b) XPS survey spectrum of cup-like structures. Scale bar: (a)50nm

Table 10 Atomic Percentage of Elements in Cup-Like Intermediate Obtained By EDX

Element	Atomic Percentage, %
Fe	42.8
S	13
O	44.2

4.6.7 SPs with Different Amino Acids

Different handed or derivative of cysteine such that *L*-cysteine, *D*-cysteine, and N-Acetyl cysteine (NAC) are used to synthesize SPs. Nevertheless, the type of stabilizer did not change the SPs formation and their structures (**Figure S 4.21**). Only with NAC mostly cup-like intermediate structures are observed at the same reaction time (30min) (**Figure S 4.21c**); since the solubility of NAC is different than cysteine, and it takes a longer time to complete the reaction for forming terminal SPs.

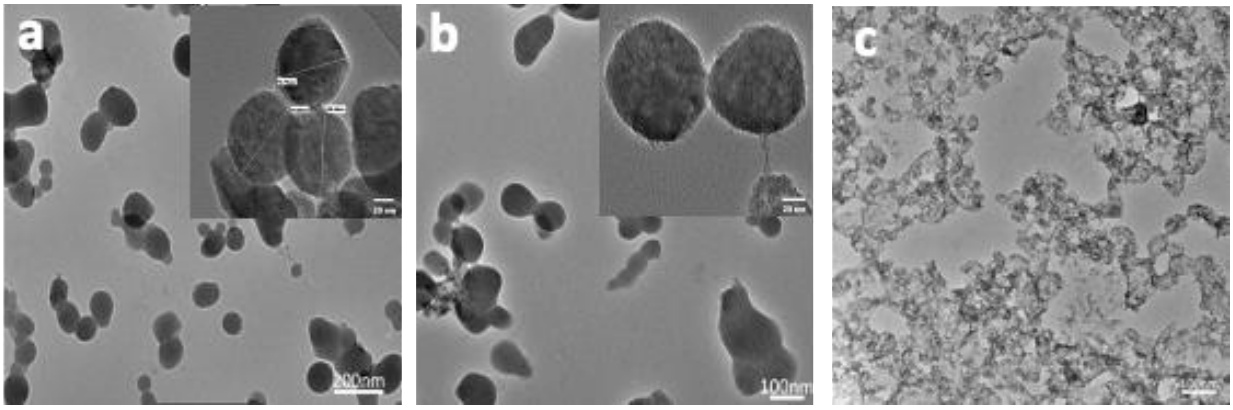

Figure S 4.21 Same reaction condition with different stabilizer. L-cysteine (a), D-cysteine (b) and N-Acetyl-Cysteine (NAC) (c) Scale bar: (a) 200nm (insert 20nm) (b) 100nm (insert 20nm) (c) 100nm

4.6.8 SP *vs.* SP-pDNA Comparison

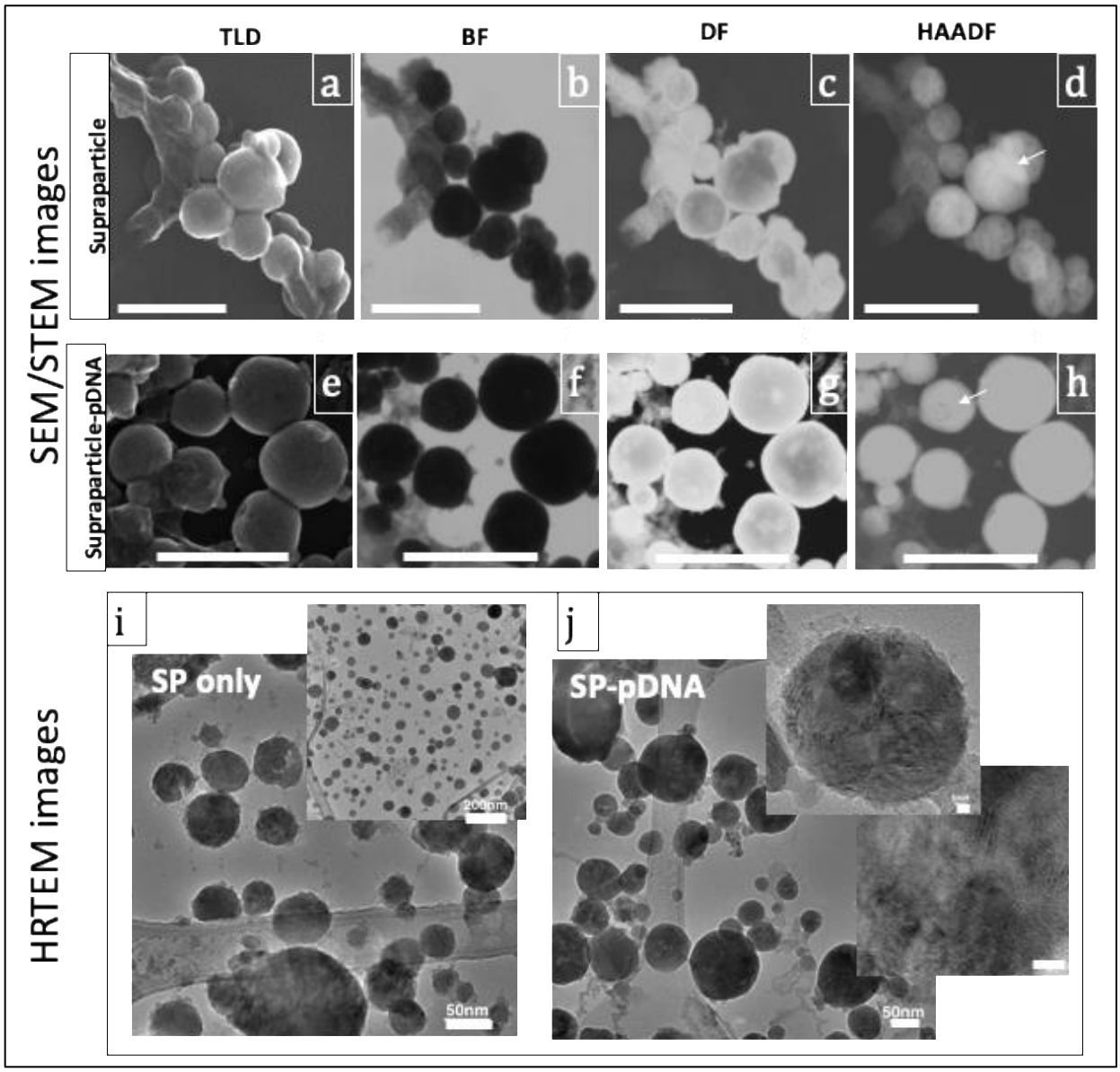

Figure S 4.22 Comparison of SP and SP-DNA. STEM images of supraparticle (a-d) and SP-pDNA (e-h) acquired with default Through the Lens Detector (TLD), Bright field (BF), Dark Field (DF) and High-angle annular dark field (HAADF) (STEM mode) detectors. HAADF shows compartments in supraparticles with darker color (pointed with arrow) in (d). In SP-pDNA HAADF filled compartment. TEM images of SP (i) and SP-pDNA (j). Scale bar: (a-h) is 200nm, (i-J) is 50 nm, insert in (i) is 200nm, insert in (j) is 5nm.

4.6.9 SP Concentration and Cytotoxicity

We calculated particle concentration before cellular experiments via nanosight what gives the number of particles per ml. Particles are prepared in different concentration: 10^{11} particles/ml (1000x) and 10^{9} particles/ml (10x) (**Figure S 4.23**). The cellular uptake is also a critical step for transfection. Hence, we performed cellular uptake before transfection to make time progress data of the uptake of SPs. For this experiment, we used 10X concentration of SP (~1000 SPs per cell) and HEK293T cell, as this cell line is prominent for transfection experiments. The uptake is expressed as mean fluorescent intensity of SPs under confocal images. As we discovered previously, SPs gave the highest emission intensity when they excited at 475 nm and 500 nm (**Figure S 4.18**) in the window of 520-700nm emission wavelengths. Further analysis made based on these two excitation wavelengths.

Even though toxicity is not expected with these SPs, the cytotoxicity may still originate from the nature of NPs. So, we tested how SP-pDNA affect the viability of human cells (HEK293T) for different exposure times, concentrations, and cell numbers (**Figure S 4.24**). The toxicity of SP-pDNA on cells compared to the control group is insignificant if the particle: cell ratio kept 4000 or low for 24h (**Figure S 4.24**)., dashed lines show the thresholds for both treatment times). It is noticeable that 1000x concentration is decreasing cell viability significantly since particle: cell ratio is $4*10^{5}$ or higher (**Figure S 4.24** blue color). One can even easily see particle aggregations by the naked eye in cell culture plates for these concentrations. After 48h of incubation in the presence of 10x SP-pDNA, cell viability decreased by *ca*.22% if particle: cell ratio is higher than 2000 (**Figure S 4.24 b,** dashed lines show the threshold).

For transfection experiments, HEK293T cells treated with SP-pDNA with 1000 particle: cell ratio for specific time intervals starting from 6h to 24h.

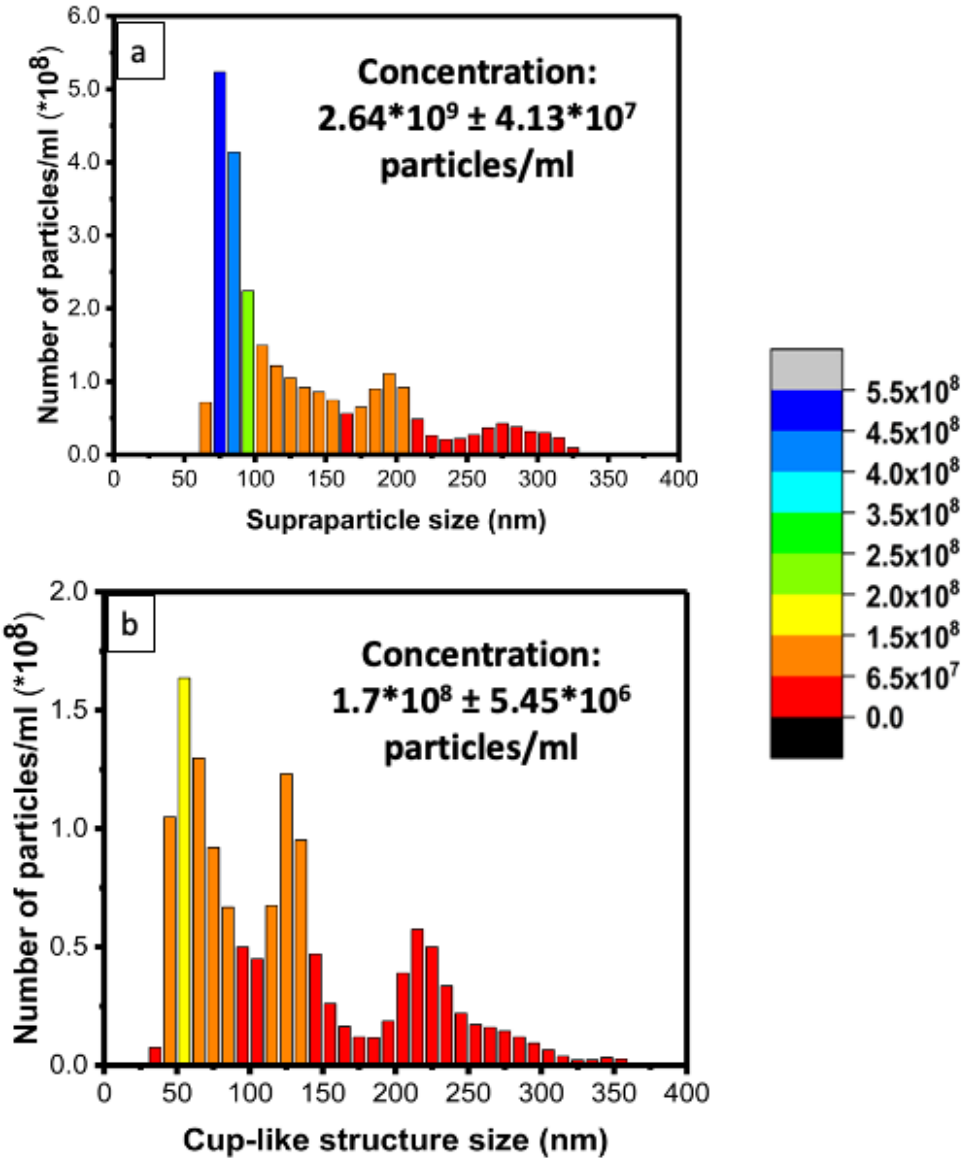

Figure S 4.23 (a) Nanosight data for SP (10x) and (b) cup-like structures (1x) concentration.

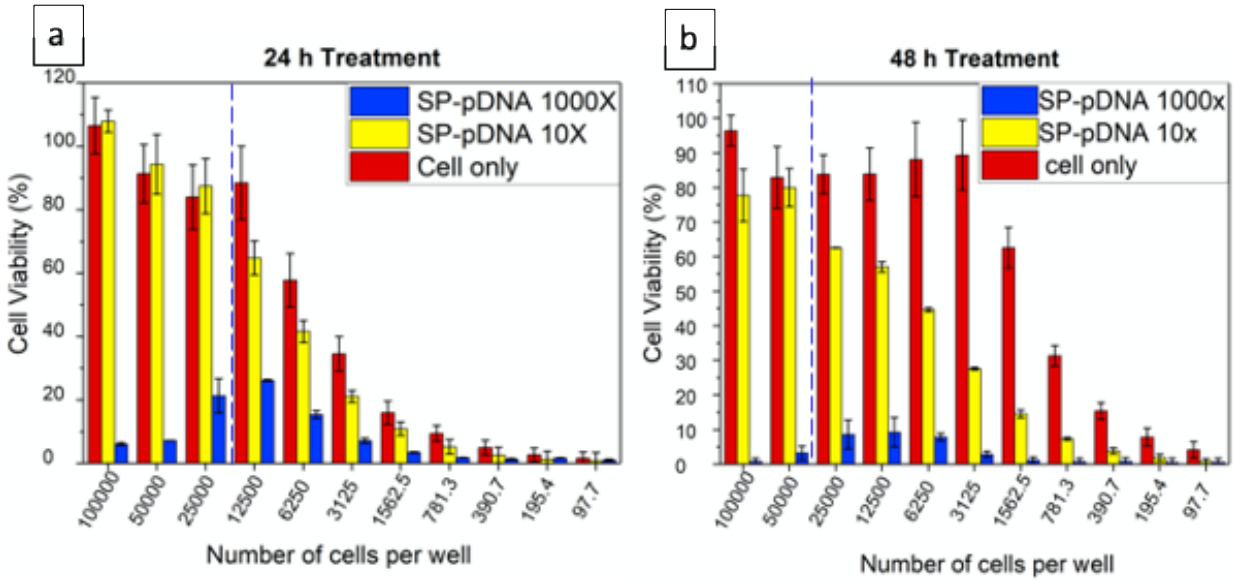

Figure S 4.24 Cell viability assay for SP-DNA 10 times concentrated (10X) and 1000 times concentrated (1000X) along with cell only. (a) 24h treatment (b) 48h treatment. Dashed lines show threshold of cell: particle ratio for significant cell viability reduction

4.6.10 Cellular Uptake

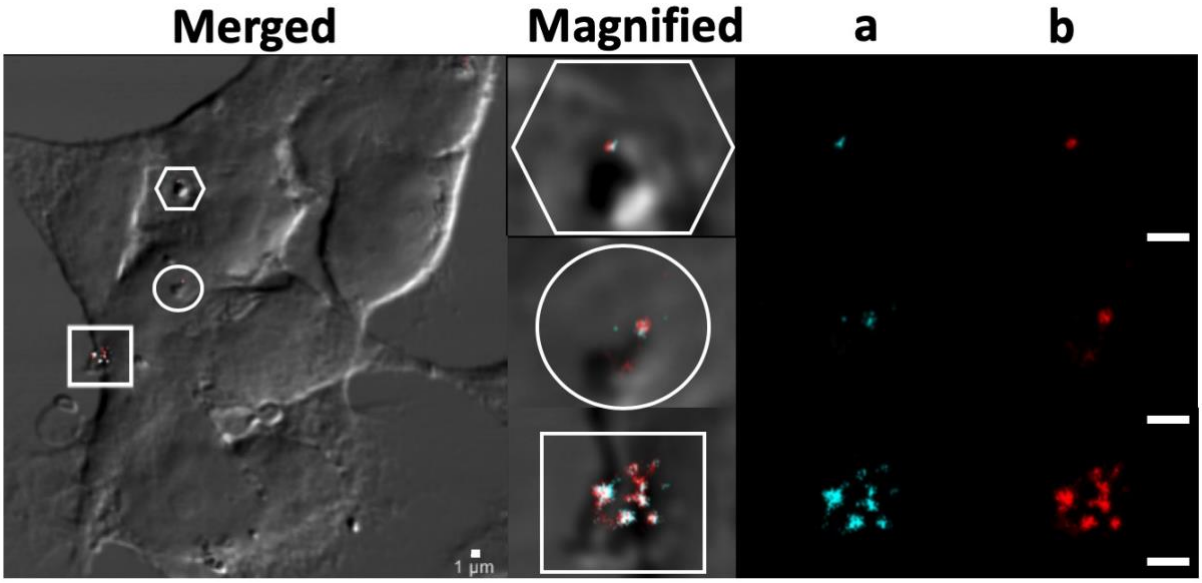

Figure S 4.25 HEK cells treated with SP for 1 hour. (a) is excited at 475 nm and (b) is excited at 500 nm emission for both emissions is 520-570nm. Scale bars: 1µm

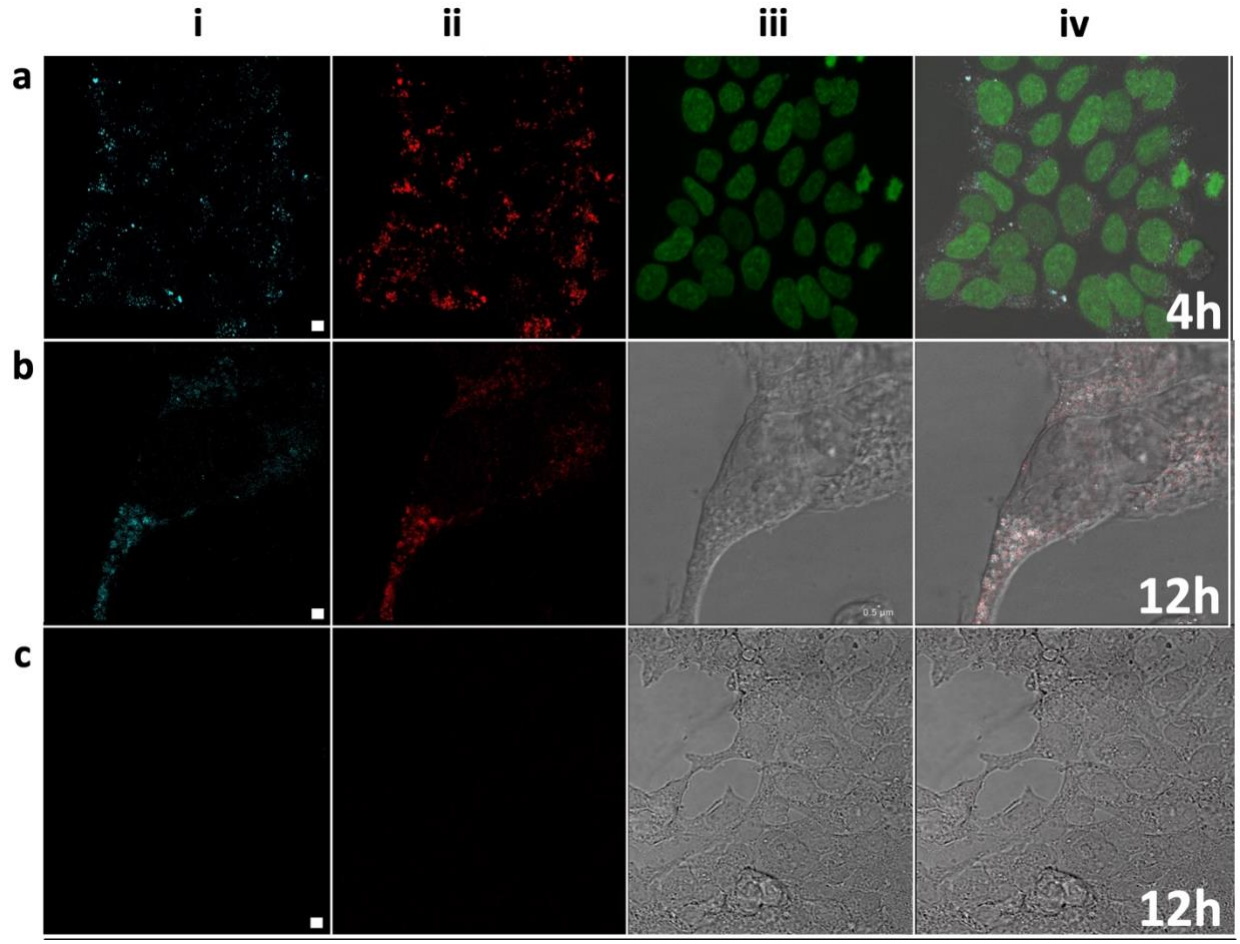

Figure S 4.26 Cellular uptake confocal images. (a-b) HEK cells treated with SPs. (c) HEK cells are not treated with SP. (a) Cell treatment with SP after 4h, (b-c) Cell treatment with SP after 12h. All images are taken under same conditions, laser power, intensity and brightness are all same. (A) is excited at 475 nm and (B) is excited at 500 nm; emission window for both excitations are 520-570 nm. (C) DIC or DAPI images (D) Merged image. Scale bar: (a) 4µm (b) 2 µm (c) 4 µm.

4.6.11 DNA Release and Degradation Assay of SP-pDNA

DNA release assay performed to find out in what conditions and how long it takes to release the DNA from the SP-pDNA complex. pDNA release assay of SP-pDNA was conducted at two different pH (5.5 and 7.4) in two different solvents (water and PBS buffer). pH 7.4 and PBS buffer is used as the model of biological fluids such as blood and intracellular fluid. pH 5.5 and water are used to model the early/late endosome environment and to make TEM imaging easier, respectively. The relative pDNA release was quantified by nanodrop at 260nm (***Figure* S 4.27a**). Encapsulated pDNA released at acidic conditions (pH 5.5 in water and pH 5.8 in PBS) within 2hours (**Figure S 4.27b**) as SP started to degrade as seen in TEM images (**Fig. S16d -**shows only samples in water). TEM images show increasing ind NPs content as time progress after 30min (blue box), 1h (red box), and 2h (black box) (**Figure S 4.27d**). SP-pDNA stays stable even after 50h in water and PBS at pH 7.4 (**Figure S 4.27d a green and red lines**). Electrophoresis is also utilized as proof of intact pDNA release (**Figure S 4.27d c**).

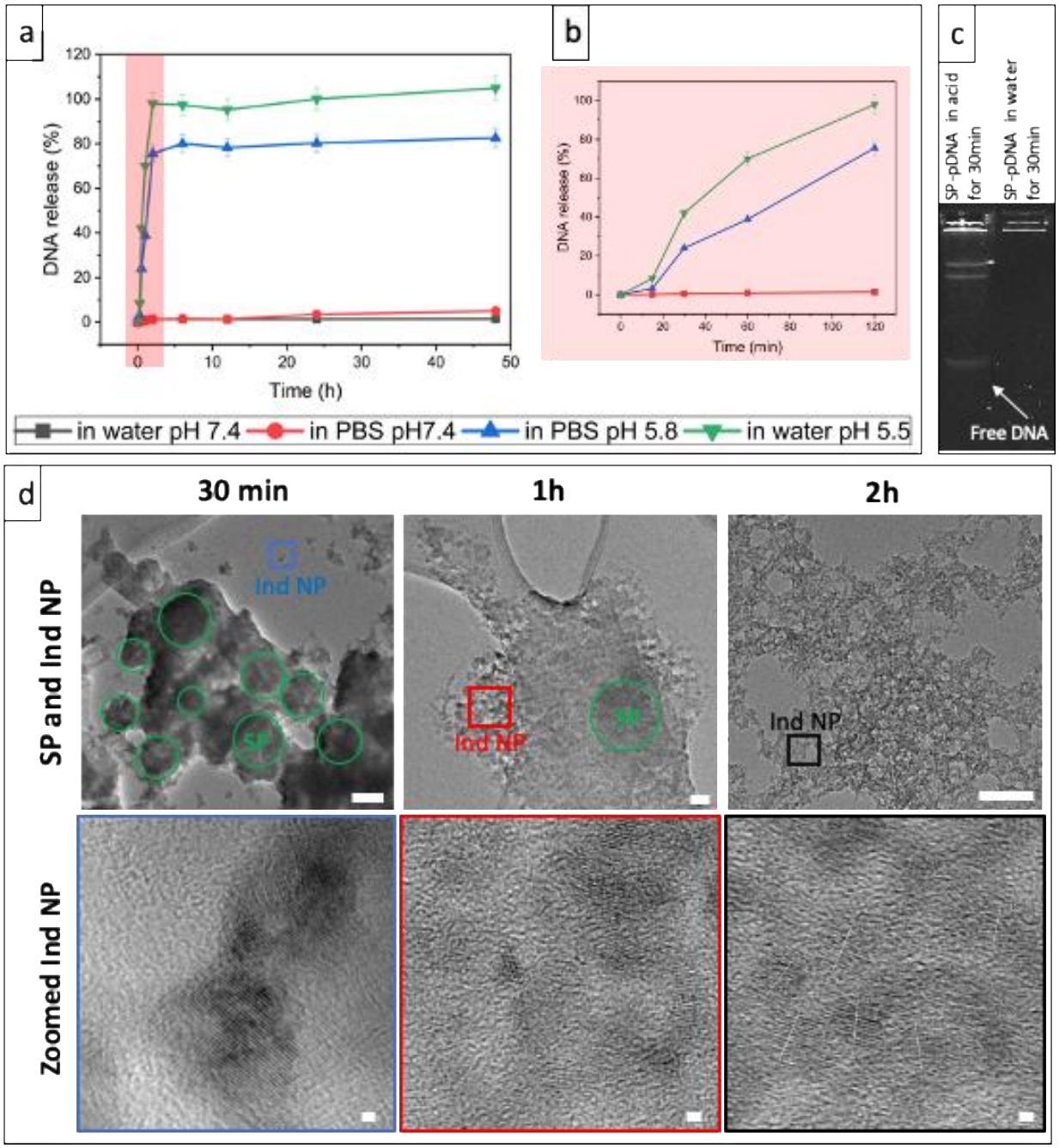

Figure S 4.27 DNA release and degradation of SP-pDNA under biologically relevant conditions. Graph shows relative DNA release percentage during acid incubation time of SP-pDNA for 48h (a). Red box zoomed graph shows DNA release percentage for 2h (b). Gel electrophoresis shows free DNA after 30 min acid incubation along with intact SP-pDNA (c). TEM images shows number of ind NPs increase and SPs decrease over acid incubation time for 2 h. (d) Each image zoomed on colored boxes for high resolution images. Scale bars: top panel 50nm, bottom panel 1nm.

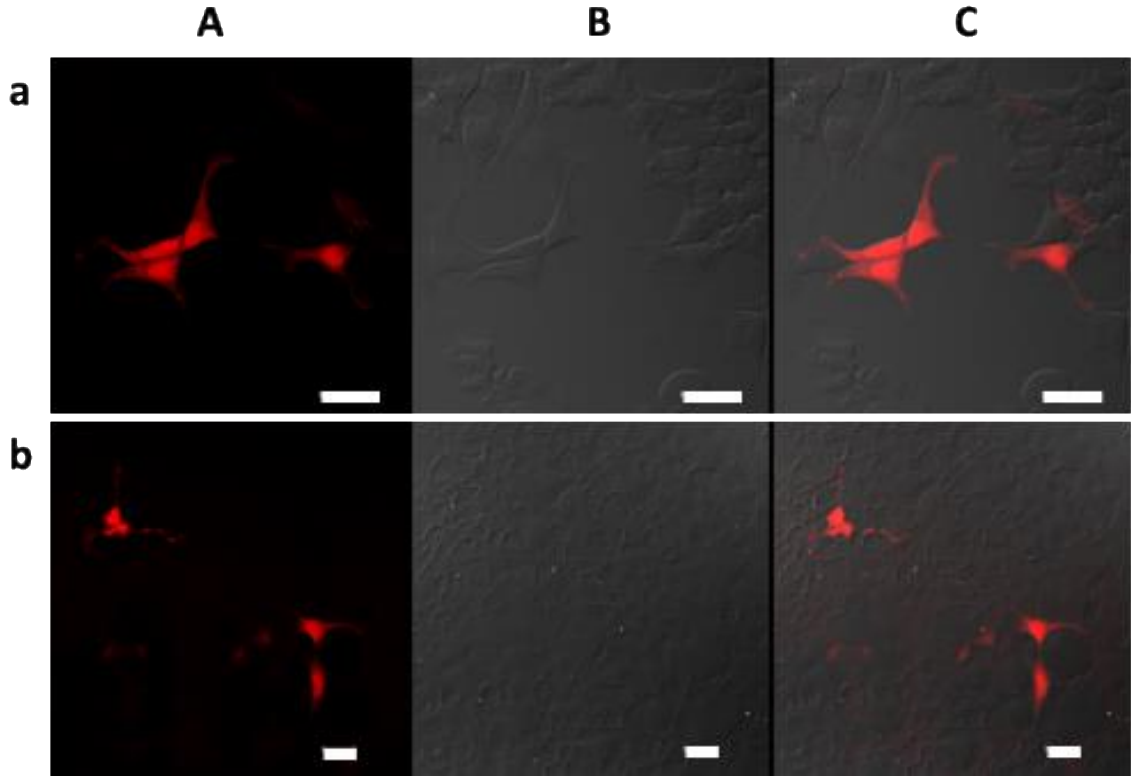

Figure S 4.28 24h Post-transfection comparison of SP-pDNA and Lipofectamine. Supraparticle with DNA and lipofectamine. (a) SP-pDNA (b) Lipocfectamine after 24 transfection. (A) Texas red filter for cherry red (B) DIC (C) Merge image. Scale bar: 25µm.

Chapter 5

Conclusions

5.1 Scientific Contribution

The work in this thesis provides two main contributions to the field of engineered biomimetic NPs in biomedical applications. The first contribution directly impacts preclinical research on engineering antibacterial NPs, which is critical to advancing our understanding of the molecular mechanism of NPs as next-generation antibiotics (Part I: Chapter 2 and 3). The second contribution is indirectly impacting the next-generation vaccine development field. A vector that is biocompatible, stable at room temperature, and can carry any nucleic acid with high transfection efficiency, similar to viruses, is what the field is looking for [324] (Part II: Chapter 4).

5.1.1 Understanding the Mechanism of Antibacterial Activity of NPs

Understanding the molecular mechanism of the antibacterial activity of NPs will help in engineering next-generation antibiotics that combat emerging drug resistance. The work presented in part I of this thesis (chapters 2 and 3) contributes to the potential clinical translation of ZnO-NPs since it shows that the mechanism of action is much more complex than previously reported. Therefore, it would be challenging for *S. aureus* to develop resistance against these ZnO-NPs.

In addition, a well-defined description of the antimicrobial molecular mechanism is necessary to guide the engineering of NPs toward a specific mechanism of antibacterial activity. Fine-tuning the NP activity using biomimetic concepts [96] opens the possibilities of improving both potency and selectivity of NPs as antimicrobials.

5.1.1.1 The Effect of ROS Formation and Ion Release on Engineered ZnO-NPs Toxicity

In chapter 2, as opposed to popular belief, we demonstrated that oxidative stress and ion dissolution from ZnO-NPYs are not sufficient to kill methicillin-resistant *S. aureus*. We found that ZnO-NPYs profoundly affect aerobic carbohydrate metabolism and energetics via upregulation of the UMP biosynthesis pathway in gene expression analysis. Altogether, the findings of the unexpectedly small role of ROS production and extensive role of alterations in carbohydrate metabolism and bioenergetics suggest that the mechanism of action of ZnO-NPYs are much more complex than previously reported and further exploration is needed.

5.1.1.2 Engineered NP and Bacterial Cell Membrane Interaction

In chapter 3, we have demonstrated that ZnO-NPYs interact with the bacterial cell membrane and enter cells without causing significant membrane damage and membrane depolarization. Localization of ZnO-NPYs helps to understand the kinetics of the time-sensitive antibacterial mechanism of action. Cell metabolism is immediately affected upon NP-membrane interaction. The collective analysis of the dynamics of NPs and bacterial cell interactions helped us better understand the underlying antibacterial mechanism of action. We think that NPs are simultaneously interacting with many biomolecules in different metabolic pathways that do not allow *S.aureus* to develop resistance. The downstream effect of NP entry can cause polyphosphate granule and vesicle formation, and response to bacterial cell death.

5.1.2 Engineering New Iron-Based Artificial Virus for Nucleic Acid Delivery

In part II (chapter 4), we engineered a biomimetic SP self-assembled with multi-compartments similar to intracellular organelles or viruses that can be utilized as a vector for nucleic acid delivery. Self-assembly of iron-based NPs forms an intermediate structure, nano cups before assembling into SPs. This progressive self-assembly generates multi-compartments within a shell

that can be utilized for multiple functions such as biomacromolecules packing and delivery. The tight structural integration of NP components in supraparticles presents the capacity to protect the nucleic acid from degradation and deliver it to cells. These SPs, artificial viruses, display similarities to viruses: they self-assemble, have relatively high uniformity, have a modular core-shell structure with around 100 nm dimensions, and can carry biological cargo. In addition to biocompatibility and easy preparation, these SPs are stable at room temperature for a long time. Therefore, the development of these SPs can help to expand the window of the next-generation vaccine development strategies.

5.2 Future Directions

We found that the choice of media is used for the bacterial studies affects the MIC of ZnO-NPYs; however, we did not have a chance to investigate the specific media-NP interactions. In Chapter 2, we investigated the antibacterial activity of ZnO-NPYs in TSB_G in where MIC is ten times higher than the MIC in SNM used in Chapter 3. TSB_G is the most commonly used, nutritionally rich media for bacterial studies; however, the ingredients are not well defined, and do not provide physiologically relevant conditions. SNM, on the other hand, is reported to mimic human nasal conditions[146] that represents a suitable *in vivo* surrogate environment for *in vitro* studies. We think, in addition of interactions of biomolecules in cells, ZnO-NPYs may interact with essential amino acids in media that allow much lower (10x) MIC in SNM. The simplicity and complete understanding of each component of SNM can allow us additional investigation on NP-media interactions that can further help clinical implications.

Continued investigation and engineering of biomimetic NPs are essential for future biomedical applications. However, detailed exploration of every engineered NP is not practical, is labor-intensive, and costly in terms of time and money. Therefore, the work on a machine-learning

algorithm to continue to explore NP and biomacromolecule interactions would accelerate studies. And this algorithm may help better engineer antibacterial NPs and contribute to selecting appropriate cargo for engineered SPs. As Feynman mentioned decades ago, there is still plenty of room at the bottom to make new technologies, and ML algorithms can accelerate the development of these technologies.

5.3 Translations Potential

Next-generation antimicrobials: Metal oxide NPs can be used as an antibacterial agent since they have a complex mechanism of action on bacteria. It will be challenging for bacteria to develop resistance to these complex mechanisms. ZnO-NPs, in particular, can be used as next-generation antibacterial agents since it has been shown that they are selectively killing bacteria over the mammalian cells.[325] This selectivity will allow ZnO-NPs to be translated into clinics such as antibacterial coatings on catheters and implants prone to biofilm formation. In the spotlight of the recent pandemic, the engineering of new types, probably smaller NPs, can also be translated as anti-viral agents into clinics.

Supraparticles as next-generation vaccines: During the recent COVID-19 pandemic, nucleic acid vaccines have become popular since these vaccines are capable of scalable manufacturing within a short period of time. This success relies on a vector that is biocompatible, easy to prepare, and can carry any nucleic acid with high efficiency. Specifically, the vector that is thermostable will gain more importance over the next years. Accessibility was one of the most significant issues for COVID-vaccines. Many developing countries, just because they do not have appropriate systems for transferring and storing the vaccines, cannot access the vaccines, which affects the controlling the spread[326]. Thus, the vectors that are stable at room temperature are highly preferred for next-generation vaccines. The SPs presented in this thesis are engineered from inorganic nanoparticles

that have stability at room temperature for a long time. Therefore, the development of these kinds of SPs can be translated into clinics as an accessible vector in next-generation vaccines for controlling and treating many different diseases.

Bibliography

1. Feynman, R. P. There's plenty of room at the bottom. *Micromechanics MEMS Class. Semin. Pap. to 1990* **XXIII**, 2–9 (1997).

2. Qu, A. *et al.* Quantitative zeptomolar imaging of miRNA cancer markers with nanoparticle assemblies. *Proc. Natl. Acad. Sci.* **116**, 3391–3400 (2019).

3. Andres, C. M., Zhu, J., Shyu, T., Flynn, C. & Kotov, N. A. Shape-Morphing Nanocomposite Origami. *Langmuir* **30**, 5378–5385 (2014).

4. Wang, Y. *et al.* Anti-Biofilm Activity of Graphene Quantum Dots via Self-Assembly with Bacterial Amyloid Proteins. *ACS Nano* **13**, 4278–4289 (2019).

5. Zhao, S. *et al.* The Future of Layer-by-Layer Assembly: A Tribute to ACS Nano Associate Editor Helmuth Möhwald. *ACS Nano* **13**, 6151–6169 (2019).

6. Huang, T. *et al.* Enhanced Antibacterial Activity of Se Nanoparticles Upon Coating with Recombinant Spider Silk Protein eADF4(kappa16). *Int. J. Nanomedicine* **15**, 4275–4288 (2020).

7. Ahmed, F. *et al.* Novel Biomimatic Synthesis of ZnO Nanorods Using Egg White (Albumen) and Their Antibacterial Studies. *J. Nanosci. Nanotechnol.* **16**, 5959–5965 (2016).

8. Nie, C. *et al.* Bioinspired and biocompatible carbon nanotube-Ag nanohybrid coatings for robust antibacterial applications. *Acta Biomater.* **51**, 479–494 (2017).

9. Mainwaring, D. E. *et al.* The nature of inherent bactericidal activity: insights from the nanotopology of three species of dragonfly. *Nanoscale* **8**, 6527–6534 (2016).

10. Xu, L., Zhao, X., Xu, C. & Kotov, N. A. Water-Rich Biomimetic Composites with Abiotic Self-Organizing Nanofiber Network. *Adv. Mater.* **30**, (2018).

11. Zhang, Z., Zhang, J., Zhang, B. & Tang, J. Mussel-inspired functionalization of graphene for synthesizing Ag-polydopamine-graphene nanosheets as antibacterial materials. *Nanoscale* **5**, 118–123 (2013).

12. Liu, M., Wang, S. & Jiang, L. Nature-inspired superwettability systems. *Nat. Rev. Mater. 2017 27* **2**, 1–17 (2017).

13. Mukherjee, A. Biomimetics Learning from Nature. *Biomimetics Learn. from Nat.* (2010). doi:10.5772/198

14. Wang, M. *et al.* Biomimetic Solid-State Zn2+ Electrolyte for Corrugated Structural Batteries. *ACS Nano* **13**, 1107–1115 (2019).

15. Fang, R. H., Jiang, Y., Fang, J. C. & Zhang, L. Cell membrane-derived nanomaterials for biomedical applications. *Biomaterials* **128**, 69–83 (2017).

16. Turlybekuly, A. *et al.* Synthesis, characterization, in vitro biocompatibility and antibacterial properties study of nanocomposite materials based on hydroxyapatite-biphasic ZnO micro- and nanoparticles embedded in Alginate matrix. *Mater. Sci. Eng. C. Mater. Biol. Appl.* **104**, 109965 (2019).

17. Mahmoudi, M., Sant, S., Wang, B., Laurent, S. & Sen, T. Superparamagnetic iron oxide nanoparticles (SPIONs): Development, surface modification and applications in chemotherapy. *Adv. Drug Deliv. Rev.* **63**, 24–46 (2011).

18. Wei, G., Bhushan, B. & Torgerson, P. M. Nanomechanical characterization of human hair using nanoindentation and SEM. *Ultramicroscopy* **105**, 248–266 (2005).

19. Parodi, A. *et al.* Synthetic nanoparticles functionalized with biomimetic leukocyte membranes possess cell-like functions. *Nat. Nanotechnol. 2012 81* **8**, 61–68 (2012).

20. Jin, K., Luo, Z., Zhang, B. & Pang, Z. Biomimetic nanoparticles for inflammation targeting. *Acta Pharm. Sin. B* **8**, 23–33 (2018).

21. Wang, W. *et al.* Bioinspired Pollen-Like Hierarchical Surface for Efficient Recognition of Target Cancer Cells. *Adv. Healthc. Mater.* **6**, 1700003 (2017).

22. Li, W. & Szoka, F. C. Lipid-based nanoparticles for nucleic acid delivery. *Pharm. Res.* **24**, 438–449 (2007).

23. Cha, S. H. *et al.* Shape-Dependent Biomimetic Inhibition of Enzyme by Nanoparticles and Their Antibacterial Activity. *ACS Nano* **9**, 9097–9105 (2015).

24. Nitta, S. K. & Numata, K. *Biopolymer-based nanoparticles for drug/gene delivery and tissue engineering*. *International Journal of Molecular Sciences* **14**, 1629–1654 (Multidisciplinary Digital Publishing Institute, 2013).

25. W. Hamley, I. Self-assembly of amphiphilic peptides. *Soft Matter* **7**, 4122–4138 (2011).

26. A, Z. Construction and characterization of virus-like particles: a review. *Mol. Biotechnol.* **53**, 92–107 (2013).

27. Moeinzadeh, S. & Jabbari, E. Nanoparticles and Their Applications. *Springer Handbooks* **11**, 335–361 (2017).

28. B, D., Z, L., GF, W., SL, Y. & VK, W. Virus-like particle vaccines: immunology and formulation for clinical translation. *Expert Rev. Vaccines* **17**, 833–849 (2018).

29. Komla, E. *et al.* Effect of Preexisting Immunity to Tetanus Toxoid on the Efficacy of Tetanus Toxoid-Conjugated Heroin Vaccine in Mice. *Vaccines* **9**, (2021).

30. Akbarzadeh, A. *et al.* Liposome: classification, preparation, and applications. *Nanoscale Res. Lett. 2013 81* **8**, 1–9 (2013).

31. A, P. *et al.* Lipid-based nanoparticles as pharmaceutical drug carriers: from concepts to clinic. *Crit. Rev. Ther. Drug Carrier Syst.* **26**, 523–580 (2009).

32. Fan, Y. & Moon, J. J. Nanoparticle Drug Delivery Systems Designed to Improve Cancer Vaccines and Immunotherapy. *Vaccines* **3**, 662–85 (2015).

33. Kuai, R., Ochyl, L. J., Schwendeman, A. & Moon, J. J. Lipid-Based Nanoparticles for Vaccine Applications. *Biomed. Eng. Front. Res. Converging Technol.* **9**, 177–197 (2016).

34. Sharma, V. K. & Agrawal, M. K. A historical perspective of liposomes-a bio nanomaterial. *Mater. Today Proc.* **45**, 2963–2966 (2021).

35. Cowen, T., Karim, K. & Piletsky, S. A. Solubility and size of polymer nanoparticles. *Polym. Chem.* **9**, 4566–4573 (2018).

36. Kotov, N. A. Inorganic Nanoparticles as Protein Mimics as Protein Mimics.

37. Tiwari, J. N., Tiwari, R. N. & Kim, K. S. Zero-dimensional, one-dimensional, two-dimensional and three-dimensional nanostructured materials for advanced electrochemical energy devices. *Prog. Mater. Sci.* **57**, 724–803 (2012).

38. Huang, C., Chen, X., Xue, Z. & Wang, T. Effect of structure: A new insight into nanoparticle assemblies from inanimate to animate. *Sci. Adv.* **6**, eaba1321 (2020).

39. Khan, I., Saeed, K. & Khan, I. Nanoparticles: Properties, applications and toxicities. *Arab. J. Chem.* **12**, 908–931 (2019).

40. Saha, K., Agasti, S. S., Kim, C., Li, X. & Rotello, V. M. Gold Nanoparticles in Chemical and Biological Sensing. (2012). doi:10.1021/cr2001178

41. Geethalakshmi, R. & Sarada, D. Gold and silver nanoparticles from Trianthema decandra: synthesis, characterization, and antimicrobial properties. *Int. J. Nanomedicine* **7**, 5375 (2012).

42. Kavaz, D., Umar, H. & Shehu, S. Synthesis, characterization, antimicrobial and antimetastatic activity of silver nanoparticles synthesized from Ficus ingens leaf. *Artif. cells, nanomedicine, Biotechnol.* **46**, S1193–S1203 (2018).

43. Munchow, E. A. *et al.* Synthesis and characterization of CaO-loaded electrospun matrices for bone tissue engineering. *Clin. Oral Investig.* **20**, 1921–1933 (2016).

44. Rajeshkumar, S. & Naik, P. Synthesis and biomedical applications of Cerium oxide

nanoparticles – A Review. *Biotechnol. Reports* **17**, 1–5 (2018).

45. Gao, Y. *et al.* Size-tunable Au@Ag nanoparticles for colorimetric and SERS dual-mode sensing of palmatine in traditional Chinese medicine. *J. Pharm. Biomed. Anal.* **174**, 123–133 (2019).

46. Velmurugan, P. *et al.* Antibacterial activity of silver nanoparticle-coated fabric and leather against odor and skin infection causing bacteria. *Appl. Microbiol. Biotechnol.* **98**, 8179–8189 (2014).

47. Dreaden, E. C., Alkilany, A. M., Huang, X., Murphy, C. J. & El-Sayed, M. A. The golden age: gold nanoparticles for biomedicine. *Chem. Soc. Rev.* **41**, 2740–2779 (2012).

48. Unser, S., Bruzas, I., He, J. & Sagle, L. Localized Surface Plasmon Resonance Biosensing: Current Challenges and Approaches. *Sensors 2015, Vol. 15, Pages 15684-15716* **15**, 15684–15716 (2015).

49. Mohan, S. *et al.* Completely green synthesis of dextrose reduced silver nanoparticles, its antimicrobial and sensing properties. *Carbohydr. Polym.* **106**, 469–474 (2014).

50. Makwana, B. A., Vyas, D. J., Bhatt, K. D., Jain, V. K. & Agrawal, Y. K. Highly stable antibacterial silver nanoparticles as selective fluorescent sensor for Fe3+ ions. *Spectrochim. Acta. A. Mol. Biomol. Spectrosc.* **134**, 73–80 (2015).

51. Yu, M. *et al.* Antibiotics mediated facile one-pot synthesis of gold nanoclusters as fluorescent sensor for ferric ions. *Biosens. Bioelectron.* **91**, 143–148 (2017).

52. Soomro, R. A. *et al.* L-cysteine protected copper nanoparticles as colorimetric sensor for mercuric ions. *Talanta* **130**, 415–422 (2014).

53. Ronavari, A. *et al.* Biological activity of green-synthesized silver nanoparticles depends on the applied natural extracts: a comprehensive study. *Int. J. Nanomedicine* **12**, 871–883 (2017).

54. Alkilany, A. M. & Murphy, C. J. Toxicity and cellular uptake of gold nanoparticles: what we have learned so far? *J. Nanoparticle Res. 2010 127* **12**, 2313–2333 (2010).

55. Sigmund, W. *et al.* Processing and Structure Relationships in Electrospinning of Ceramic Fiber Systems. *J. Am. Ceram. Soc.* **89**, 395–407 (2006).

56. Liong, M. *et al.* Multifunctional inorganic nanoparticles for imaging, targeting, and drug delivery. *ACS Nano* **2**, 889–96 (2008).

57. Chang, C., Wang, X., Bai, Y. & Liu, H. Applications of nanomaterials in enantioseparation and related techniques. *TrAC - Trends Anal. Chem.* **39**, 195–206 (2012).

58. Gounani, Z. *et al.* Mesoporous silica nanoparticles carrying multiple antibiotics provide enhanced synergistic effect and improved biocompatibility. *Colloids Surf. B. Biointerfaces*

175, 498–508 (2019).

59. Qi, G., Li, L., Yu, F. & Wang, H. Vancomycin-modified mesoporous silica nanoparticles for selective recognition and killing of pathogenic gram-positive bacteria over macrophage-like cells. *ACS Appl. Mater. Interfaces* **5**, 10874–10881 (2013).

60. Sattary, M., Amini, J. & Hallaj, R. Antifungal activity of the lemongrass and clove oil encapsulated in mesoporous silica nanoparticles against wheat's take-all disease. *Pestic. Biochem. Physiol.* **170**, 104696 (2020).

61. Xu, G. *et al.* Reduced bacteria adhesion on octenidine loaded mesoporous silica nanoparticles coating on titanium substrates. *Mater. Sci. Eng. C. Mater. Biol. Appl.* **70**, 386–395 (2017).

62. Safi, S., Karimzadeh, F. & Labbaf, S. Mesoporous and hollow hydroxyapatite nanostructured particles as a drug delivery vehicle for the local release of ibuprofen. *Mater. Sci. Eng. C. Mater. Biol. Appl.* **92**, 712–719 (2018).

63. Thomas, S., Harshita, B. S. P., Mishra, P. & Talegaonkar, S. Ceramic Nanoparticles: Fabrication Methods and Applications in Drug Delivery. *Curr. Pharm. Des.* **21**, 6165–6188 (2015).

64. Narayan, R., Nayak, U. Y., Raichur, A. M. & Garg, S. Mesoporous Silica Nanoparticles: A Comprehensive Review on Synthesis and Recent Advances. *Pharm. 2018, Vol. 10, Page 118* **10**, 118 (2018).

65. Lin, Y.-S. & Haynes, C. L. Impacts of Mesoporous Silica Nanoparticle Size, Pore Ordering, and Pore Integrity on Hemolytic Activity. *J. Am. Chem. Soc.* **132**, 4834–4842 (2010).

66. Patel, K. D., Singh, R. K. & Kim, H.-W. Carbon-based nanomaterials as an emerging platform for theranostics. *Mater. Horizons* **6**, 434–469 (2019).

67. Zhang, M. (Assistant professor of biomedical engineering), Naik, R. (Rajesh) & Dai, L. *Carbon nanomaterials for biomedical applications*.

68. Astefanei, A., Núñez, O. & Galceran, M. T. Characterisation and determination of fullerenes: A critical review. *Anal. Chim. Acta* **882**, 1–21 (2015).

69. Pandiyan, R., Mahalingam, S. & Ahn, Y.-H. Antibacterial and photocatalytic activity of hydrothermally synthesized SnO2 doped GO and CNT under visible light irradiation. *J. Photochem. Photobiol. B.* **191**, 18–25 (2019).

70. Brahmachari, S., Mandal, S. K. & Das, P. K. Fabrication of SWCNT-Ag nanoparticle hybrid included self-assemblies for antibacterial applications. *PLoS One* **9**, e106775 (2014).

71. Maiti, D., Tong, X., Mou, X. & Yang, K. Carbon-Based Nanomaterials for Biomedical Applications: A Recent Study. *Front. Pharmacol.* **0**, 1401 (2019).

72. Fan, X., Liu, Y., Wang, X., Quan, X. & Chen, S. Improvement of Antifouling and Antimicrobial Abilities on Silver-Carbon Nanotube Based Membranes under Electrochemical Assistance. *Environ. Sci. Technol.* **53**, 5292–5300 (2019).

73. Chan, T. S. Y. *et al.* Carbon nanotube compared with carbon black: effects on bacterial survival against grazing by ciliates and antimicrobial treatments. *Nanotoxicology* **7**, 251–258 (2013).

74. Yang, S.-T., Luo, J., Zhou, Q. & Wang, H. Pharmacokinetics, Metabolism and Toxicity of Carbon Nanotubes for Biomedical Purposes. *Theranostics* **2**, 271 (2012).

75. Du, J., Wang, S., You, H. & Zhao, X. Understanding the toxicity of carbon nanotubes in the environment is crucial to the control of nanomaterials in producing and processing and the assessment of health risk for human: A review. *Environ. Toxicol. Pharmacol.* **36**, 451–462 (2013).

76. Girigoswami, K. Toxicity of Metal Oxide Nanoparticles. *Adv. Exp. Med. Biol.* **1048**, 99–122 (2018).

77. Esfandiari, N., Simchi, A. & Bagheri, R. Size tuning of Ag-decorated TiO2 nanotube arrays for improved bactericidal capacity of orthopedic implants. *J. Biomed. Mater. Res. A* **102**, 2625–2635 (2014).

78. Geng, S. *et al.* Anisotropic Magnetite Nanorods for Enhanced Magnetic Hyperthermia. *Chem. – An Asian J.* **11**, 2996–3000 (2016).

79. Roca, A. G. *et al.* Design strategies for shape-controlled magnetic iron oxide nanoparticles. *Adv. Drug Deliv. Rev.* **138**, 68–104 (2019).

80. Ittrich, H., Peldschus, K., Raabe, N., Kaul, M. & Adam, G. Superparamagnetic Iron Oxide Nanoparticles in Biomedicine: Applications and Developments in Diagnostics and Therapy. *RöFo - Fortschritte auf dem Gebiet der Röntgenstrahlen und der Bildgeb. Verfahren* **185**, 1149–1166 (2013).

81. Miller, M. M., Prinz, G. A., Cheng, S.-F. & Bounnak, S. Detection of a micron-sized magnetic sphere using a ring-shaped anisotropic magnetoresistance-based sensor: A model for a magnetoresistance-based biosensor. *Appl. Phys. Lett.* **81**, 2211 (2002).

82. Laurent, S. *et al.* Magnetic Iron Oxide Nanoparticles: Synthesis, Stabilization, Vectorization, Physicochemical Characterizations, and Biological Applications. *Chem. Rev.* **108**, 2064–2110 (2008).

83. Margarethe Hofmann-Amtenbrink1, B. von R. & Hofmann, and H. New forms of superparamagnetic nanoparticles for biomedical applications. *Superparamagnetic nanoparticles Biomed. Appl. Margarethe* **65**, 119–147 (2009).

84. Ling, D., Lee, N. & Hyeon, T. Chemical Synthesis and Assembly of Uniformly Sized Iron Oxide Nanoparticles for Medical Applications. *Acc. Chem. Res.* **48**, 1276–1285 (2015).

85. Arularasu, M. V., Devakumar, J. & Rajendran, T. V. An innovative approach for green synthesis of iron oxide nanoparticles: Characterization and its photocatalytic activity. *Polyhedron* **156**, 279–290 (2018).

86. Ismail, R. A., Sulaiman, G. M., Abdulrahman, S. A. & Marzoog, T. R. Antibacterial activity of magnetic iron oxide nanoparticles synthesized by laser ablation in liquid. *Mater. Sci. Eng. C. Mater. Biol. Appl.* **53**, 286–297 (2015).

87. Nehra, P., Chauhan, R. P., Garg, N. & Verma, K. Antibacterial and antifungal activity of chitosan coated iron oxide nanoparticles. *Br. J. Biomed. Sci.* **75**, 13–18 (2018).

88. de Rancourt, Y., Couturaud, B., Mas, A. & Robin, J. J. Synthesis of antibacterial surfaces by plasma grafting of zinc oxide based nanocomposites onto polypropylene. *J. Colloid Interface Sci.* **402**, 320–326 (2013).

89. Ke, Y. *et al.* Polypseudorotaxane functionalized magnetic nanoparticles as a dual responsive carrier for roxithromycin delivery. *Mater. Sci. Eng. C. Mater. Biol. Appl.* **99**, 159–170 (2019).

90. Liu, Z. *et al.* Synthesis of polyethylenimine (PEI) functionalized silver nanoparticles by a hydrothermal method and their antibacterial activity study. *Mater. Sci. Eng. C. Mater. Biol. Appl.* **42**, 31–37 (2014).

91. Gu, Y. *et al.* Vitamin B2 functionalized iron oxide nanozymes for mouth ulcer healing. *Sci. China. Life Sci.* **63**, 68–79 (2020).

92. Cheng, Z., Zaki, A. Al, Hui, J. Z., Muzykantov, V. R. & Tsourkas, A. Multifunctional Nanoparticles: Cost Versus Benefit of Adding Targeting and Imaging Capabilities. *Science (80-.).* **338**, 903–910 (2012).

93. Hong, S. *et al.* The Binding Avidity of a Nanoparticle-Based Multivalent Targeted Drug Delivery Platform. *Chem. Biol.* **14**, 107–115 (2007).

94. Wagner, C. S., Shehata, S., Henzler, K., Yuan, J. & Wittemann, A. Towards nanoscale composite particles of dual complexity. *J. Colloid Interface Sci.* **355**, 115–123 (2011).

95. Dizaj, S. M., Jafari, S. & Khosroushahi, A. Y. A sight on the current nanoparticle-based gene delivery vectors. *Nanoscale Res. Lett.* **9**, 252 (2014).

96. Kotov, N. A. Inorganic Nanoparticles as Protein Mimics. *Science* **330**, 188–189 (2010).

97. Tian, H., Chen, J. & Chen, X. Nanoparticles for gene delivery. *Small* **9**, 2034–2044 (2013).

98. Xu, Z. P., Zeng, Q. H., Lu, G. Q. & Yu, A. B. Inorganic nanoparticles as carriers for efficient cellular delivery. *Chem. Eng. Sci.* **61**, 1027–1040 (2006).

99. Loureiro, A., G. Azoia, N., C. Gomes, A. & Cavaco-Paulo, A. Albumin-Based Nanodevices as Drug Carriers. *Curr. Pharm. Des.* **22**, 1371–1390 (2016).

100. Martis, E., Badve, R. & Degwekar, M. Nanotechnology based devices and applications in medicine: An overview. *Chronicles Young Sci.* **3**, 68 (2012).

101. Kadiyala, U. *et al.* Unexpected insights into antibacterial activity of zinc oxide nanoparticles against methicillin resistant Staphylococcus aureus (MRSA). *Nanoscale* **10**, 4927–4939 (2018).

102. Conly, J. M. Antimicrobial resistance - Judicious use is the key. *Canadian Journal of Infectious Diseases* **15**, 249–251 (2004).

103. Alqahtani, F. *et al.* Antibacterial Activity of Chitosan Nanoparticles Against Pathogenic N. gonorrhoea. *Int. J. Nanomedicine* **15**, 7877–7887 (2020).

104. Dadgostar, P. Antimicrobial Resistance: Implications and Costs. *Infect. Drug Resist.* **12**, 3903 (2019).

105. Wat, D. & Doull, I. Respiratory virus infections in cystic fibrosis. *Paediatric Respiratory Reviews* **4**, 172–177 (2003).

106. Smyth, R. L., Smyth, A. R., Tong, C. Y. W., Hart, C. A. & Heaf, D. P. Effect of respiratory virus infections including rhinovirus on clinical status in cystic fibrosis. *Arch. Dis. Child.* **73**, 117–120 (1995).

107. Hiatt, P. W. *et al.* Effects of viral lower respiratory tract infection on lung function in infants with cystic fibrosis. *Pediatrics* **103**, 619–626 (1999).

108. Collinson, J. *et al.* Effects of upper respiratory tract infections in patients with cystic fibrosis. *Thorax* **51**, 1115–1122 (1996).

109. Villeret, B. *et al.* Influenza A Virus Pre-Infection Exacerbates Pseudomonas aeruginosa-Mediated Lung Damage Through Increased MMP-9 Expression, Decreased Elafin Production and Tissue Resilience. *Front. Immunol.* **11**, 117 (2020).

110. Morens, D. M., Taubenberger, J. K. & Fauci, A. S. Predominant Role of Bacterial Pneumonia as a Cause of Death in Pandemic Influenza: Implications for Pandemic Influenza Preparedness. *J. Infect. Dis.* **198**, 962–970 (2008).

111. Shafran, N. *et al.* Secondary bacterial infection in COVID-19 patients is a stronger predictor for death compared to influenza patients. *Sci. Reports 2021 111* **11**, 1–8 (2021).

112. Djurisic, A. B. *et al.* Toxicity of metal oxide nanoparticles: mechanisms, characterization, and avoiding experimental artefacts. *Small* **11**, 26–44 (2015).

113. Jiang, W., Mashayekhi, H. & Xing, B. Bacterial toxicity comparison between nano- and micro-scaled oxide particles. *Environ. Pollut.* **157**, 1619–1625 (2009).

114. Kumar, A., Pandey, A. K., Singh, S. S., Shanker, R. & Dhawan, A. Engineered ZnO and TiO(2) nanoparticles induce oxidative stress and DNA damage leading to reduced viability

of Escherichia coli. *Free Radic Biol Med* **51**, 1872–1881 (2011).

115. Liu, J. L., Luo, Z. & Bashir, S. A progressive approach on inactivation of bacteria using silver-titania nanoparticles. *Biomater. Sci.* **1**, 194–201 (2013).

116. Romero-Urbina, D. G. *et al.* Ultrastructural changes in methicillin-resistant Staphylococcus aureus induced by positively charged silver nanoparticles. *Beilstein J. Nanotechnol.* **6**, 2396–2405 (2015).

117. Setyawati, M. I., Fang, W., Chia, S. L. & Leong, D. T. Nanotoxicology of common metal oxide based nanomaterials: their ROS-y and non-ROS-y consequences. *Asia-Pacific J. Chem. Eng.* **8**, 205–217 (2013).

118. Zhang, L., Ding, Y., Povey, M. & York, D. ZnO nanofluids – A potential antibacterial agent. *Prog. Nat. Sci.* **18**, 939–944 (2008).

119. Zhang, L., Wu, L., Mi, Y. & Si, Y. Silver Nanoparticles Induced Cell Apoptosis, Membrane Damage of Azotobacter vinelandii and Nitrosomonas europaea via Generation of Reactive Oxygen Species. *Bull. Environ. Contam. Toxicol.* **103**, 181–186 (2019).

120. Nabraska Transposon Mutant Library.

121. Jin, S. E. & Jin, H. E. Antimicrobial activity of zinc oxide nano/microparticles and their combinations against pathogenic microorganisms for biomedical applications: From physicochemical characteristics to pharmacological aspects. *Nanomaterials* **11**, 1–35 (2021).

122. Premanathan, M., Karthikeyan, K., Jeyasubramanian, K. & Manivannan, G. Selective toxicity of ZnO nanoparticles toward Gram-positive bacteria and cancer cells by apoptosis through lipid peroxidation. *Nanomedicine* **7**, 184–192 (2011).

123. Xie, Y., He, Y., Irwin, P. L., Jin, T. & Shi, X. Antibacterial activity and mechanism of action of zinc oxide nanoparticles against Campylobacter jejuni. *Appl Env. Microbiol* **77**, 2325–2331 (2011).

124. Zhang, L. *et al.* Mechanistic investigation into antibacterial behaviour of suspensions of ZnO nanoparticles against E. coli. *J. Nanoparticle Res.* **12**, 1625–1636 (2009).

125. Du, J. *et al.* Antibacterial activity of a novel Forsythia suspensa fruit mediated green silver nanoparticles against food-borne pathogens and mechanisms investigation. *Mater. Sci. Eng. C. Mater. Biol. Appl.* **102**, 247–253 (2019).

126. Padmavathi, A. R. *et al.* Copper oxide nanoparticles as an effective anti-biofilm agent against a copper tolerant marine bacterium, Staphylococcus lentus. *Biofouling* **35**, 1007–1025 (2019).

127. Garza-Cervantes, J. A. *et al.* Antimicrobial and antibiofilm activity of biopolymer-Ni, Zn nanoparticle biocomposites synthesized using R. mucilaginosa UANL-001L

exopolysaccharide as a capping agent. *Int. J. Nanomedicine* **14**, 2557–2571 (2019).

128. Applerot, G. *et al.* ZnO nanoparticle-coated surfaces inhibit bacterial biofilm formation and increase antibiotic susceptibility. *RSC Adv.* **2**, 2314–2321 (2012).

129. Krishnamoorthy, K., Manivannan, G., Kim, S. J., Jeyasubramanian, K. & Premanathan, M. Antibacterial activity of MgO nanoparticles based on lipid peroxidation by oxygen vacancy. *J. Nanoparticle Res.* **14**, 1–10 (2012).

130. Yazhini, K. B. & Prabu, H. G. Antibacterial activity of cotton coated with ZnO and ZnO-CNT composites. *Appl. Biochem. Biotechnol.* **175**, 85–92 (2015).

131. Lallo da Silva, B., Caetano, B. L., Chiari-Andreo, B. G., Pietro, R. C. L. R. & Chiavacci, L. A. Increased antibacterial activity of ZnO nanoparticles: Influence of size and surface modification. *Colloids Surf. B. Biointerfaces* **177**, 440–447 (2019).

132. Shao, F. *et al.* Bio-synthesis of Barleria gibsoni leaf extract mediated zinc oxide nanoparticles and their formulation gel for wound therapy in nursing care of infants and children. *J. Photochem. Photobiol. B.* **189**, 267–273 (2018).

133. Balaure, P. C. *et al.* In vitro and in vivo studies of novel fabricated bioactive dressings based on collagen and zinc oxide 3D scaffolds. *Int. J. Pharm.* **557**, 199–207 (2019).

134. Venkatasubbu, G. D., Baskar, R., Anusuya, T., Seshan, C. A. & Chelliah, R. Toxicity mechanism of titanium dioxide and zinc oxide nanoparticles against food pathogens. *Colloids Surf. B. Biointerfaces* **148**, 600–606 (2016).

135. Kalpana, V. N. *et al.* Biosynthesis of zinc oxide nanoparticles using culture filtrates of Aspergillus niger: Antimicrobial textiles and dye degradation studies. *OpenNano* **3**, 48–55 (2018).

136. Fouda, A., El-Din Hassan, S., Salem, S. S. & Shaheen, T. I. In-Vitro cytotoxicity, antibacterial, and UV protection properties of the biosynthesized Zinc oxide nanoparticles for medical textile applications. *Microb. Pathog.* **125**, 252–261 (2018).

137. Pandimurugan, R. & Thambidurai, S. UV protection and antibacterial properties of seaweed capped ZnO nanoparticles coated cotton fabrics. *Int. J. Biol. Macromol.* **105**, 788–795 (2017).

138. Sasani Ghamsari, M., Alamdari, S., Han, W. & Park, H.-H. Impact of nanostructured thin ZnO film in ultraviolet protection. *Int. J. Nanomedicine* **12**, 207–216 (2017).

139. Mohseni, S., Aghayan, M., Ghorani-Azam, A., Behdani, M. & Asoodeh, A. Evaluation of antibacterial properties of Barium Zirconate Titanate (BZT) nanoparticle. *Braz. J. Microbiol.* **45**, 1393–1399 (2014).

140. Kujda, M. *et al.* Charge Stabilized Silver Nanoparticles Applied as Antibacterial Agents. *J. Nanosci. Nanotechnol.* **15**, 3574–3583 (2015).

141. McGuffie, M. J. *et al.* Zinc oxide nanoparticle suspensions and layer-by-layer coatings inhibit staphylococcal growth. *Nanomedicine Nanotechnology, Biol. Med.* **12**, 33–42 (2016).

142. M, A. *et al.* Antimicrobial activity of iron oxide nanoparticle upon modulation of nanoparticle-bacteria interface. *Sci. Rep.* **5**, 14813 (2015).

143. Saptarshi, S. R., Duschl, A. & Lopata, A. L. Interaction of nanoparticles with proteins: relation to bio-reactivity of the nanoparticle. *J Nanobiotechnology* **11**, 26 (2013).

144. Kadiyala, U., Kotov, N. A. & VanEpps, J. S. Antibacterial Metal Oxide Nanoparticles: Challenges in Interpreting the Literature. *Curr. Pharm. Des.* **24**, 896–903 (2018).

145. Sushnitha, M., Evangelopoulos, M., Tasciotti, E. & Taraballi, F. Cell Membrane-Based Biomimetic Nanoparticles and the Immune System: Immunomodulatory Interactions to Therapeutic Applications. *Front. Bioeng. Biotechnol.* **0**, 627 (2020).

146. Krismer, B. *et al.* Nutrient Limitation Governs Staphylococcus aureus Metabolism and Niche Adaptation in the Human Nose. *PLoS Pathog.* **10**, (2014).

147. Padmavathy, N. & Vijayaraghavan, R. Enhanced bioactivity of ZnO nanoparticles - An antimicrobial study. *Sci. Technol. Adv. Mater.* **9**, (2008).

148. Lemire, J. A. *et al.* Antimicrobial activity of metals: mechanisms, molecular targets and applications. *Nat Rev Microbiol* **11**, 371–384 (2013).

149. Pasquet, J. *et al.* The contribution of zinc ions to the antimicrobial activity of zinc oxide. *Colloids Surfaces A Physicochem. Eng. Asp.* **457**, 263–274 (2014).

150. Dutta, R. K., Nenavathu, B. P., Gangishetty, M. K. & Reddy, A. V. Studies on antibacterial activity of ZnO nanoparticles by ROS induced lipid peroxidation. *Colloids Surf B Biointerfaces* **94**, 143–150 (2012).

151. Horie, M. *et al.* Association of the physical and chemical properties and the cytotoxicity of metal oxide nanoparticles: metal ion release, adsorption ability and specific surface area. *Metallomics* **4**, 350–360 (2012).

152. Soni, D. *et al.* Oxidative Stress and Genotoxicity of Zinc Oxide Nanoparticles to Pseudomonas Species, Human Promyelocytic Leukemic (HL-60), and Blood Cells. *Biol. Trace Elem. Res.* **178**, 218–227 (2017).

153. Gutiérrez, C., Plessing, C. Von & García, A. Metal nanostructures as antibacterial agents. *Sci. against Microb. Pathog. Commun. Curr. Res. Technol. Adv.* 210–218 (2011).

154. Zhang, L., Ding, Y., Povey, M. & York, D. ZnO nanofluids-A potential antibacterial agent. *Prog. Nat. Sci.* **18**, 939–944 (2008).

155. Zhang, L., Jiang, Y., Ding, Y., Povey, M. & York, D. Investigation into the antibacterial

behaviour of suspensions of ZnO nanoparticles (ZnO nanofluids). *J. Nanoparticle Res.* **9**, 479–489 (2007).

156. Stanković, A. *et al.* Influence of size scale and morphology on antibacterial properties of ZnO powders hydrothemally synthesized using different surface stabilizing agents. *Colloids Surf. B. Biointerfaces* **102**, 21–28 (2013).

157. Stoimenov, P. K., Klinger, R. L., Marchin, G. L. & Klabunde, K. J. Metal oxide nanoparticles as bactericidal agents. *Langmuir* **18**, 6679–6686 (2002).

158. Zhang, J. & Saltzman, M. Engineering biodegradable nanoparticles for drug and gene delivery. *Chem. Eng. Prog.* **109**, 25 (2013).

159. Ding, Y. *et al.* Gold nanoparticles for nucleic acid delivery. *Mol. Ther.* **22**, 1075–83 (2014).

160. Sokolova, V. & Epple, M. Inorganic nanoparticles as carriers of nucleic acids into cells. *Angew. Chemie - Int. Ed.* **47**, 1382–1395 (2008).

161. Li, S. & Huang, L. Nonviral gene therapy: promises and challenges. *Gene Ther.* **7**, 31–34 (2000).

162. Cross, D. & Burmester, J. K. Gene Therapy for Cancer Treatment : Past , Present and Future. **4**, 218–227 (2006).

163. Pranatharthiharan, S., Patel, M. D., D'Souza, A. A. & Devarajan, P. V. Inorganic nanovectors for nucleic acid delivery. *Drug Deliv. Transl. Res.* **3**, 446–470 (2013).

164. Wolff, J. A. & Budker, V. The Mechanism of Naked DNA Uptake and Expression. *Advances in Genetics* **54**, 1–20 (2005).

165. Kay, M. A., Glorioso, J. C. & Naldini, L. Viral vectors for gene therapy: the art of turning infectious agents into vehicles of therapeutics. *Nat. Med.* **7**, 33–40 (2001).

166. Gao, K. & Huang, L. Nonviral methods for siRNA delivery. *Molecular Pharmaceutics* **6**, 651–658 (2009).

167. Yamanouchi, D. *et al.* Biodegradable arginine-based poly(ester-amide)s as non-viral gene delivery reagents. *Biomaterials* **29**, 3269–3277 (2008).

168. Dufès, C., Uchegbu, I. F. & Schätzlein, A. G. Dendrimers in gene delivery. *Advanced Drug Delivery Reviews* **57**, 2177–2202 (2005).

169. Choi, Y. & Chang, J. Viral vectors for vaccine applications. *Clin. Exp. Vaccine Res.* **2**, 97–105 (2013).

170. Semple, S. C. *et al.* Rational design of cationic lipids for siRNA delivery. *Nat. Biotechnol.* **28**, 172–6 (2010).

171. Wu, J., Yamanouchi, D., Liu, B. & Chu, C.-C. Biodegradable arginine-based poly(ether

ester amide)s as a non-viral DNA delivery vector and their structure–function study. *J. Mater. Chem.* **22**, 18983–18991 (2012).

172. Alhakamy, N. A., Dhar, P. & Berkland, C. J. Charge Type, Charge Spacing, and Hydrophobicity of Arginine-Rich Cell-Penetrating Peptides Dictate Gene Transfection. **al**, (2016).

173. Piccinini, E., Pallarola, D., Battaglini, F. & Azzaroni, O. Recognition-driven assembly of self-limiting supramolecular protein nanoparticles displaying enzymatic activity. *Chem. Commun. (Camb).* **51**, 14754–7 (2015).

174. Lee, J.-M., Yoon, T.-J. & Cho, Y.-S. Recent developments in nanoparticle-based siRNA delivery for cancer therapy. *Biomed Res. Int.* **2013**, 782041 (2013).

175. Ramos-Perez, V., Cifuentes, A., Coronas, N., de Pablo, A. & Borrós, S. Modification of carbon nanotubes for gene delivery vectors. *Methods Mol. Biol.* **1025**, 261–8 (2013).

176. Lu, A. H., Salabas, E. L. & Sch??th, F. Magnetic nanoparticles: Synthesis, protection, functionalization, and application. *Angewandte Chemie - International Edition* **46**, 1222–1244 (2007).

177. Fishbein, I., Chorny, M. & Levy, R. J. Site-specific gene therapy for cardiovascular disease. *Curr. Opin. Drug Discov. Devel.* **13**, 203–13 (2010).

178. Karimi, M., Avci, P., Mobasseri, R., Hamblin, M. R. & Naderi-Manesh, H. The novel albumin-chitosan core-shell nanoparticles for gene delivery: Preparation, optimization and cell uptake investigation. *J. Nanoparticle Res.* **15**, (2013).

179. Liu, C. & Zhang, N. *Nanoparticles in gene therapy: Principles, prospects, and challenges*. *Progress in Molecular Biology and Translational Science* **104**, 509–562 (Academic Press, 2011).

180. Guevara, M. L., Persano, F. & Persano, S. Advances in Lipid Nanoparticles for mRNA-Based Cancer Immunotherapy. *Front. Chem.* **0**, 963 (2020).

181. B. Devika Chithrani, †,‡, Arezou A. Ghazani, †,‡ and & Warren C. W. Chan*, †,‡,§. Determining the Size and Shape Dependence of Gold Nanoparticle Uptake into Mammalian Cells. *Nano Lett.* **6**, 662–668 (2006).

182. Read, M. L., Logan, A. & Seymour, L. W. Barriers to Gene Delivery Using Synthetic Vectors. *Adv. Genet.* **53**, 19–46 (2005).

183. Xia, Y. *et al.* Self-assembly of self-limiting monodisperse supraparticles from polydisperse nanoparticles. *Nat. Nanotechnol.* **6**, 580–587 (2011).

184. Banin, U. & Sitt, A. Colloidal self-assembly: Superparticles get complex. *Nat. Mater.* **11**, 1009–11 (2012).

185. Li, F., Josephson, D. P. & Stein, A. Colloidal assembly: The road from particles to colloidal molecules and crystals. *Angewandte Chemie - International Edition* **50**, 360–388 (2011).

186. Tang, Z. Spontaneous Organization of Single CdTe Nanoparticles into Luminescent Nanowires. *Science (80-.).* **297**, 237–240 (2002).

187. Tang, Z., Zhang, Z., Wang, Y., Glotzer, S. C. & Kotov, N. A. Self-assembly of CdTe nanocrystals into free-floating sheets. *Science* **314**, 274–8 (2006).

188. Xia, Y. *et al.* supraparticles from polydisperse nanoparticles. *Nat. Nanotechnol.* **6**, 580–587 (2011).

189. Xia, Y. & Tang, Z. Monodisperse inorganic supraparticles: formation mechanism, properties and applications. *Chem. Commun. (Camb).* **48**, 6320–6336 (2012).

190. Schlachter, E. K. *et al.* Metabolic pathway and distribution of superparamagnetic iron oxide nanoparticles: in vivo study. *Int. J. Nanomedicine* **6**, 1793–1800 (2011).

191. Applerot, G. *et al.* Understanding the antibacterial mechanism of CuO nanoparticles: revealing the route of induced oxidative stress. *Small* **8**, 3326–3337 (2012).

192. Cui, Y. *et al.* The molecular mechanism of action of bactericidal gold nanoparticles on Escherichia coli. *Biomaterials* **33**, 2327–2333 (2012).

193. von Moos, N. & Slaveykova, V. I. Oxidative stress induced by inorganic nanoparticles in bacteria and aquatic microalgae--state of the art and knowledge gaps. *Nanotoxicology* **8**, 605–630 (2014).

194. Leung, Y. H. *et al.* Antibacterial activity of ZnO nanoparticles with a modified surface under ambient illumination. *Nanotechnology* **23**, 475703 (2012).

195. Thill, A. *et al.* Cytotoxicity of CeO2 Nanoparticles for Escherichia coli. Physico-Chemical Insight of the Cytotoxicity Mechanism. *Environ. Sci. Technol.* **40**, 6151–6156 (2006).

196. Leung, Y. H. *et al.* Mechanisms of antibacterial activity of MgO: non-ROS mediated toxicity of MgO nanoparticles towards Escherichia coli. *Small* **10**, 1171–1183 (2014).

197. Lyon, D. Y., Brunet, L., Hinkal, G. W., Wiesner, M. R. & Alvarez, P. J. Antibacterial activity of fullerene water suspensions (nC60) is not due to ROS-mediated damage. *Nano Lett* **8**, 1539–1543 (2008).

198. Gaupp, R., Ledala, N. & Somerville, G. A. Staphylococcal response to oxidative stress. *Front. Cell. Infect. Microbiol.* **2**, 33 (2012).

199. Gambino, M. & Cappitelli, F. Mini-review: Biofilm responses to oxidative stress. *Biofouling* **32**, 167–178 (2016).

200. Painter, K. L. *et al.* Staphylococcus aureus Adapts to Oxidative Stress by Producing

H(2)O(2)-Resistant Small-Colony Variants via the SOS Response. *Infect. Immun.* **83**, 1830–1844 (2015).

201. Reddy, K. M. *et al.* Selective toxicity of zinc oxide nanoparticles to prokaryotic and eukaryotic systems. *Appl. Phys. Lett.* **90**, 213902–213903 (2007).

202. Li, M., Zhu, L. & Lin, D. Toxicity of ZnO Nanoparticles to Escherichia coli: Mechanism and the Influence of Medium Components. *Environ. Sci. Technol.* **45**, 1977–1983 (2011).

203. McDevitt, C. A. *et al.* A Molecular Mechanism for Bacterial Susceptibility to Zinc. *PLOS Pathog.* **7**, e1002357 (2011).

204. Reed, R. B., Ladner, D. A., Higgins, C. P., Westerhoff, P. & Ranville, J. F. Solubility of nano-zinc oxide in environmentally and biologically important matrices. *Environ. Toxicol. Chem.* **31**, 93–99 (2012).

205. Wang, N., Tong, T., Xie, M. & Gaillard, J. F. Lifetime and dissolution kinetics of zinc oxide nanoparticles in aqueous media. *Nanotechnology* **27**, 324001 (2016).

206. Yang, M., Sun, K. & Kotov, N. A. Formation and assembly-disassembly processes of ZnO hexagonal pyramids driven by dipolar and excluded volume interactions. *J. Am. Chem. Soc.* **132**, 1860–1872 (2010).

207. Repine, J. E., Fox, R. B. & Berger, E. M. Hydrogen peroxide kills Staphylococcus aureus by reacting with staphylococcal iron to form hydroxyl radical. *J Biol Chem* **256**, 7094–7096 (1981).

208. Thomas, E. L., Milligan, T. W., Joyner, R. E. & Jefferson, M. M. Antibacterial activity of hydrogen peroxide and the lactoperoxidase-hydrogen peroxide-thiocyanate system against oral streptococci. *Infect Immun* **62**, 529–535 (1994).

209. Yan, W. *et al.* Self-assembly of chiral nanoparticle pyramids with strong R/S optical activity. *J. Am. Chem. Soc.* **134**, 15114–15121 (2012).

210. Smyth, G. K. Linear models and empirical bayes methods for assessing differential expression in microarray experiments. *Stat Appl Genet Mol Biol* **3**, Article3 (2004).

211. Ritchie, M. E. *et al.* Empirical array quality weights in the analysis of microarray data. *BMC Bioinformatics* **7**, 261 (2006).

212. Benjamini, Y. & Hochberg, Y. Controlling the False Discovery Rate: A Practical and Powerful Approach to Multiple Testing. *J. R. Stat. Soc. Ser. B* **57**, 289–300 (1995).

213. Čáp, M., Váchová, L. & Palková, Z. Reactive Oxygen Species in the Signaling and Adaptation of Multicellular Microbial Communities. *Oxid. Med. Cell. Longev.* **2012**, 13 (2012).

214. Jang, I.-A., Kim, J. & Park, W. Endogenous hydrogen peroxide increases biofilm formation

by inducing exopolysaccharide production in Acinetobacter oleivorans DR1. *Sci. Rep.* **6**, 21121 (2016).

215. Stark, G. Functional Consequences of Oxidative Membrane Damage. *J. Membr. Biol.* **205**, 1–16 (2005).

216. Chang, W., Small, D. A., Toghrol, F. & Bentley, W. E. Global Transcriptome Analysis of Staphylococcus aureus Response to Hydrogen Peroxide. *J. Bacteriol.* **188**, 1648–1659 (2006).

217. Nobre, L. S. & Saraiva, L. M. Effect of combined oxidative and nitrosative stresses on Staphylococcus aureus transcriptome. *Appl Microbiol Biotechnol* **97**, 2563–2573 (2013).

218. Pati, R. *et al.* Topical application of zinc oxide nanoparticles reduces bacterial skin infection in mice and exhibits antibacterial activity by inducing oxidative stress response and cell membrane disintegration in macrophages. *Nanomedicine* **10**, 1195–1208 (2014).

219. Raghupathi, K. R., Koodali, R. T. & Manna, A. C. Size-Dependent Bacterial Growth Inhibition and Mechanism of Antibacterial Activity of Zinc Oxide Nanoparticles. *Langmuir* **27**, 4020–4028 (2011).

220. Amna, S. *et al.* Review on Zinc Oxide Nanoparticles: Antibacterial Activity and Toxicity Mechanism. *Nano-Micro Lett.* **7**, 219–242 (2015).

221. Yoo, S. Il *et al.* Inhibition of amyloid peptide fibrillation by inorganic nanoparticles: functional similarities with proteins. *Angew. Chemie* **50**, 5110–5 (2011).

222. Arakha, M., Saleem, M., Mallick, B. C. & Jha, S. The effects of interfacial potential on antimicrobial propensity of ZnO nanoparticle. *Sci. Rep.* **5**, 9578 (2015).

223. de Planque, M. R. R., Aghdaei, S., Roose, T. & Morgan, H. Electrophysiological Characterization of Membrane Disruption by Nanoparticles. *ACS Nano* **5**, 3599–3606 (2011).

224. Jacobson, K. H. *et al.* Lipopolysaccharide Density and Structure Govern the Extent and Distance of Nanoparticle Interaction with Actual and Model Bacterial Outer Membranes. *Environ. Sci. Technol.* **49**, 10642–10650 (2015).

225. McIllMurray, M. B. & Lascelles, J. Anaerobiosis and the Activity of Enzymes of Pyrimidine Biosynthesis in Staphylococcus aureus. *Microbiology* **64**, 269–277 (1970).

226. Anderson, K. L. *et al.* Characterization of the Staphylococcus aureus heat shock, cold shock, stringent, and SOS responses and their effects on log-phase mRNA turnover. *J Bacteriol* **188**, 6739–6756 (2006).

227. Fuchs, S., Pané-Farré, J., Kohler, C., Hecker, M. & Engelmann, S. Anaerobic Gene Expression in Staphylococcus aureus. *J. Bacteriol.* **189**, 4275–4289 (2007).

228. Jones, N., Ray, B., Ranjit, K. T. & Manna, A. C. Antibacterial activity of ZnO nanoparticle suspensions on a broad spectrum of microorganisms. *FEMS Microbiol Lett* **279**, 71–76 (2008).

229. Hernandez-Montes, G., Diaz-Mejia, J. J., Perez-Rueda, E. & Segovia, L. The hidden universal distribution of amino acid biosynthetic networks: a genomic perspective on their origins and evolution. *Genome Biol* **9**, R95 (2008).

230. Yu, F. *et al.* Zn or O? An Atomic Level Comparison on Antibacterial Activities of Zinc Oxides. *Chemistry* **22**, 8053–8058 (2016).

231. Liao, H. *et al.* Falling Leaves Inspired ZnO Nanorods–Nanoslices Hierarchical Structure for Implant Surface Modification with Two Stage Releasing Features. *ACS Appl. Mater. Interfaces* **9**, 13009–13015 (2017).

232. Zhang, Y., Nayak, T. R., Hong, H. & Cai, W. Biomedical Applications of Zinc Oxide Nanomaterials. *Curr Mol Med* **13**, 1633–1645 (2013).

233. Cory, H. *et al.* Preferential killing of cancer cells and activated human T cells using ZnO nanoparticles. *Nanotechnology* **19**, 295103 (2008).

234. Pastoriza-Santos, I. *et al.* One-Pot Synthesis of Ag@TiO2 Core−Shell Nanoparticles and Their Layer-by-Layer Assembly. *Langmuir* **16**, 2731–2735 (2000).

235. Podsiadlo, P. *et al.* Layer-by-Layer Assembly of Nacre-like Nanostructured Composites with Antimicrobial Properties. *Langmuir* **21**, 11915–11921 (2005).

236. Sekyere, J. O. & Amoako, D. G. Carbonyl cyanide m-chlorophenylhydrazine (CCCP) reverses resistance to colistin, but not to Carbapenems and tigecycline in multidrug-resistant Enterobacteriaceae. *Front. Microbiol.* **8**, (2017).

237. Park, Y. K. & Ko, K. S. Effect of carbonyl cyanide 3-chlorophenylhydrazone (CCCP) on killing Acinetobacter baumannii by colistin. *J. Microbiol.* **53**, 53–59 (2015).

238. GALE, E. F. & FOLKES, J. P. The assimilation of amino-acids by bacteria. XV. Actions of antibiotics on nucleic acid and protein synthesis in Staphylococcus aureus. *Biochem. J.* **53**, (1953).

239. HANCOCK, R. The bactericidal action of streptomycin on Staphylococcus aureus and some accompanying biochemical changes. *J. Gen. Microbiol.* **23**, (1960).

240. Luzzatto, L., Apirion, D. & Schlessinger, D. Mechanism of action of streptomycin in E. coli: interruption of the ribosome cycle at the initiation of protein synthesis. *Proc. Natl. Acad. Sci. U. S. A.* **60**, 873–880 (1968).

241. Davis, B. D. *Mechanism of Bactericidal Action of Aminoglycosides*. (1987).

242. Van Stelten, J., Silva, F., Belin, D. & Silhavy, T. J. Effects of antibiotics and a proto-

oncogene homolog on destruction of protein translocator SecY. *Science (80-.).* **325**, (2009).

243. Segers, K. & Anné, J. *Traffic Jam at the Bacterial Sec Translocase: Targeting the SecA Nanomotor by Small-Molecule Inhibitors*. *Chemistry & Biology* **18**, 685–698 (Cell Press, 2011).

244. Mookerjee, S. A., Gerencser, A. A., Nicholls, D. G. & Brand, M. D. Quantifying intracellular rates of glycolytic and oxidative ATP production and consumption using extracellular flux measurements. *J. Biol. Chem.* **292**, 7189 (2017).

245. Luo, Z. *et al.* The role of nanoparticle shape in translocation across the pulmonary surfactant layer revealed by molecular dynamics simulations. *Environ. Sci. Nano* **5**, 1921–1932 (2018).

246. Wang, X., Thompson, C. D., Weidenmaier, C. & Lee, J. C. Release of Staphylococcus aureus extracellular vesicles and their application as a vaccine platform. *Nat. Commun.* **9**, 1–13 (2018).

247. A, E., D, M., DK, C. & CP, H. The short-term toxic effects of TiO_2nanoparticles toward bacteria through viability, cellular respiration, and lipid peroxidation. *Environ. Sci. Pollut. Res. Int.* **22**, 17917–17924 (2015).

248. Leung, Y. H. *et al.* Transmission electron microscopy artifacts in characterization of the nanomaterial-cell interactions. *Appl. Microbiol. Biotechnol. 2017 10113* **101**, 5469–5479 (2017).

249. Chen, S. *et al.* Avoiding artefacts during electron microscopy of silver nanomaterials exposed to biological environments. *J. Microsc.* **261**, 157 (2016).

250. Bayoumi, M., Bayley, H., Maglia, G. & Sapra, K. T. Multi-compartment encapsulation of communicating droplets and droplet networks in hydrogel as a model for artificial cells. *Sci. Rep.* **7**, 1–11 (2017).

251. Kushner, D. J. Self-assembly of biological structures. *Bacteriol. Rev.* **33**, 302–45 (1969).

252. Yang, M. *et al.* Self-assembly of nanoparticles into biomimetic capsid-like nanoshells. *Nat Chem* **9**, 287–294 (2017).

253. Mitragotri, S. & Lahann, J. Physical approaches to biomaterial design. *Nat. Mater.* **8**, 15–23 (2009).

254. Settembre, C., Fraldi, A., Medina, D. L. & Ballabio, A. Signals from the lysosome: a control centre for cellular clearance and energy metabolism. *Nat. Rev. Mol. Cell Biol.* **14**, 283–96 (2013).

255. Kerfeld, C. A., Heinhorst, S. & Cannon, G. C. Bacterial Microcompartments. *Annu. Rev. Microbiol.* **64**, 391–408 (2010).

256. Kerfeld, C. A. *et al.* Protein Structures Forming the Shell of Primitive Bacterial Organelles. *Science (80-.).* **309**, 936–938 (2005).

257. Yeates, T. O., Kerfeld, C. A., Heinhorst, S., Cannon, G. C. & Shively, J. M. Protein-based organelles in bacteria: carboxysomes and related microcompartments. *Nat. Rev. Microbiol.* **6**, 681–691 (2008).

258. Tanaka, S. *et al.* Atomic-level models of the bacterial carboxysome shell. *Science (80-.).* **319**, 1083–1086 (2008).

259. Martin, W. Evolutionary origins of metabolic compartmentalization in eukaryotes. *Philos. Trans. R. Soc. B Biol. Sci.* **365**, 847–855 (2010).

260. Lentini, R., Yeh Martín, N. & Mansy, S. S. Communicating artificial cells. *Current Opinion in Chemical Biology* **34**, 53–61 (2016).

261. Voeltz, G. K., Rolls, M. M. & Rapoport, T. A. Structural organization of the endoplasmic reticulum. *EMBO Rep.* **3**, 944–950 (2002).

262. Chen, A. H. & Silver, P. A. Designing biological compartmentalization. *Trends Cell Biol.* **22**, 662–70 (2012).

263. Tawfik, D. S. & Griffiths, A. D. Man-made cell-like compartments for molecular evolution. *Nat. Biotechnol.* **16**, 652–656 (1998).

264. Aldaye, F. A., Palmer, A. L. & Sleiman, H. F. Assembling Materials with DNA as the Guide. *Science (80-.).* **321**, 1795–1799 (2008).

265. Wei, B., Dai, M. & Yin, P. Complex shapes self-assembled from single-stranded DNA tiles. *Nature* **485**, 623–626 (2012).

266. Zhu, T. F. & Szostak, J. W. Coupled Growth and Division of Model Protocell Membranes. *J. Am. Chem. Soc.* **131**, 5705–5713 (2009).

267. Balakumaran, A. *et al.* Superparamagnetic iron oxide nanoparticles labeling of bone marrow stromal (mesenchymal) cells does not affect their 'stemness'. *PLoS One* **5**, e11462 (2010).

268. Channon, K., Bromley, E. H. & Woolfson, D. N. Synthetic biology through biomolecular design and engineering. *Current Opinion in Structural Biology* **18**, 491–498 (2008).

269. Belluati, A. *et al.* Multicompartment Polymer Vesicles with Artificial Organelles for Signal-Triggered Cascade Reactions Including Cytoskeleton Formation. *Adv. Funct. Mater.* 2002949 (2020). doi:10.1002/adfm.202002949

270. Paleos, C. M., Tsiourvas, D., Sideratou, Z. & Pantos, A. Formation of artificial multicompartment vesosome and dendrosome as prospected drug and gene delivery carriers. *Journal of Controlled Release* **170**, 141–152 (2013).

271. Bolinger, P.-Y., Stamou, D. & Vogel, H. An Integrated Self-Assembled Nanofluidic System for Controlled Biological Chemistries. *Angew. Chemie* **120**, 5626–5631 (2008).

272. Peters, R. J. R. W. *et al.* Cascade reactions in multicompartmentalized polymersomes. *Angew. Chemie - Int. Ed.* **53**, 146–150 (2014).

273. Marguet, M., Edembe, L. & Lecommandoux, S. Polymersomes in polymersomes: Multiple loading and permeability control. *Angew. Chemie - Int. Ed.* **51**, 1173–1176 (2012).

274. Godoy-Gallardo, M. *et al.* Multicompartment Artificial Organelles Conducting Enzymatic Cascade Reactions inside Cells. *ACS Appl. Mater. Interfaces* **9**, 15907–15921 (2017).

275. Hosta-Rigau, L., York-Duran, M. J., Zhang, Y., Goldie, K. N. & Städler, B. Confined multiple enzymatic (cascade) reactions within poly(dopamine)-based capsosomes. *ACS Appl. Mater. Interfaces* **6**, 12771–12779 (2014).

276. Chandrawati, R. *et al.* Triggered cargo release by encapsulated enzymatic catalysis in capsosomes. *Nano Lett.* **11**, 4958–4963 (2011).

277. Engelhart, A. E., Adamala, K. P. & Szostak, J. W. A simple physical mechanism enables homeostasis in primitive cells. *Nat. Chem.* **8**, 448–453 (2016).

278. Huang, Y. *et al.* Impact of MoS₂ supporting interface on the photothermal-induced deformation of gold nanoshells: tracked through an optical microfiber. *2D Mater.* (2019). doi:10.1088/2053-1583/ab2c22

279. Khalid, M., Ciracì, C., Khalid, M. & Ciracì, C. Numerical Analysis of Nonlocal Optical Response of Metallic Nanoshells. *Photonics* **6**, 39 (2019).

280. Liu, Y. F., Wang, Y. Q., Liu, Y. F. & Wang, Y. Q. Thermo-Electro-Mechanical Vibrations of Porous Functionally Graded Piezoelectric Nanoshells. *Nanomaterials* **9**, 301 (2019).

281. Pampalakis, G. From Chemical Gardens to Quasibiological Inorganic Cells. *ChemistrySelect* **4**, 2802–2805 (2019).

282. Barge, L. M. *et al.* From Chemical Gardens to Chemobrionics. *Chem. Rev.* **115**, 8652–8703 (2015).

283. Caruso, F., Spasova, M., Susha, A., Giersig, M. & Caruso, R. A. Magnetic nanocomposite particles and hollow spheres constructed by a sequential layering approach. *Chem. Mater.* **13**, 109–116 (2001).

284. Iskandar, F., Mikrajuddin & Okuyama, K. In Situ Production of Spherical Silica Particles Containing Self-Organized Mesopores. *Nano Lett.* **1**, 231–234 (2001).

285. Walsh, D., Lebeau, B. & Mann, S. Morphosynthesis of Calcium Carbonate (Vaterite) Microsponges. *Adv. Mater.* **11**, 324–328 (1999).

286. Jung, J. H., Ono, Y. & Shinkai, S. Novel preparation method for multi-layered, tubular silica using an azacrown-appended cholesterol as template and metal-deposition into the interlayer space. *J. Chem. Soc. Perkin Trans. 2* **0**, 1289–1291 (1999).

287. Ono, Y. *et al.* Preparation of novel hollow fiber silica using collagen fibers as a template. *Chem. Lett.* 475–476 (1999). doi:10.1246/cl.1999.475

288. Van Bommel, K. J. C., Friggeri, A. & Shinkai, S. Organic templates for the generation of inorganic materials. *Angewandte Chemie - International Edition* **42**, 980–999 (2003).

289. Glotzer, S. C. & Solomon, M. J. Anisotropy of building blocks and their assembly into complex structures. *Nat. Mater.* **6**, 557–562 (2007).

290. Tang, Z., Kotov, N. A. & Giersig, M. Spontaneous Organization of Single CdTe Nanoparticles into Luminescent Nanowires. *Science (80-.).* **297**, 237–240 (2002).

291. Ariga, K. *et al.* Challenges and breakthroughs in recent research on self-assembly. *Sci. Technol. Adv. Mater.* **9**, 014109 (2008).

292. Kotov, N. A. N. A. *Practical aspects of self-organization of nanoparticles: Experimental guide and future applications*. *Journal of Materials Chemistry* **21**, 16673–16674 (2011).

293. Feng, W. *et al.* Assembly of mesoscale helices with near-unity enantiomeric excess and light-matter interactions for chiral semiconductors. *Sci. Adv.* **3**, e1601159 (2017).

294. Yang, M. & Kotov, N. A. N. A. Nanoscale helices from inorganic materials. *J. Mater. Chem.* **21**, 6775–6792 (2011).

295. Yan, J. *et al.* Self-Assembly of Chiral Nanoparticles into Semiconductor Helices with Tunable near-Infrared Optical Activity. *Chem. Mater.* **32**, 476–488 (2020).

296. Srivastava, S. *et al.* Light-controlled self-assembly of semiconductor nanoparticles into twisted ribbons. *Science (80-.).* **327**, 1355–9 (2010).

297. Zhou, H., Kim, J.-P., Bahng, J. H., Kotov, N. A. & Lee, J. Self-Assembly Mechanism of Spiky Magnetoplasmonic Supraparticles. *Adv. Funct. Mater.* **24**, 1439–1448 (2014).

298. Gao, M. R. *et al.* One-pot synthesis of hierarchical magnetite nanochain assemblies with complex building units and their application for water treatment. *J. Mater. Chem.* **21**, 16888–16892 (2011).

299. Wei, A., Kasama, T. & Dunin-Borkowski, R. E. Self-assembly and flux closure studies of magnetic nanoparticle rings. *J. Mater. Chem.* **21**, 16686–16693 (2011).

300. Shevchenko, E. V *et al.* Structural characterization of self-assembled multifunctional binary nanoparticle superlattices. *J. Am. Chem. Soc.* **128**, 3620–37 (2006).

301. de Q. Silveira, G. *et al.* Supraparticle Nanoassemblies with Enzymes. *Chem. Mater.* **31**,

(2019).

302. Park, J. Il *et al.* Terminal supraparticle assemblies from similarly charged protein molecules and nanoparticles. *Nat. Commun.* **5**, 3593 (2014).

303. Zhou, Y. *et al.* Biomimetic Hierarchical Assembly of Helical Supraparticles from Chiral Nanoparticles. *ACS Nano* 3248–56 (2016). doi:10.1021/acsnano.5b05983

304. Piccinini, E., Pallarola, D., Battaglini, F. & Azzaroni, O. Self-limited self-assembly of nanoparticles into supraparticles: towards supramolecular colloidal materials by design. *Mol. Syst. Des. Eng.* **1**, 155–162 (2016).

305. Lowson, R. T. R. T. Aqueous Oxidation of Pyrite by Molecular Oxygen. *Chem. Rev.* **82**, 461–497 (1982).

306. Bai, Y. *et al.* Universal synthesis of single-phase pyrite FeS2 nanoparticles, nanowires, and nanosheets. *J. Phys. Chem. C* **117**, 2567–2573 (2013).

307. Chen, G., Zhu, Z. & Qin, Y. Synthesis of Pure Micro- and Nanopyrite and Their Application for As (III) Removal from Aqueous Solution. *Adv. Mater. Sci. Eng.* **2016**, 1–6 (2016).

308. Holder, C. F. & Schaak, R. E. Tutorial on Powder X-ray Diffraction for Characterizing Nanoscale Materials. *ACS Nano* **13**, 7359–7365 (2019).

309. Ennaoui, A., Fiechter, S., Goslowsky, H. & Tributsch, H. Photoactive Synthetic Polycrystalline Pyrite (FeS2). *J. Electrochem. Soc.* **132**, 1579–1582 (1985).

310. Ennaoui, A., Fiechter, S., Jaegermann, W. & Tributsch, H. Photoelectrochemistry of Highly Quantum Efficient Single-Crystalline n-FeS[sub 2] (Pyrite). *J. Electrochem. Soc.* **133**, 97 (1986).

311. Zangeneh Kamali, K., Alagarsamy, P., Huang, N. M., Ong, B. H. & Lim, H. N. Hematite Nanoparticles-Modified Electrode Based Electrochemical Sensing Platform for Dopamine. *Sci. World J.* **2014**, 1–13 (2014).

312. Ennaoui, A. *et al.* Iron disulfide for solar energy conversion. *Sol. Energy Mater. Sol. Cells* **29**, 289–370 (1993).

313. Chatzitheodorou, G. *et al.* Thin photoactive FeS2 (pyrite) films. *Mater. Res. Bull.* **21**, 1481–1487 (1986).

314. Chen, K.-L. *et al.* Influence of magnetoplasmonic γ-Fe2O3/Au core/shell nanoparticles on low-field nuclear magnetic resonance. *Sci. Rep.* **6**, 35477 (2016).

315. Kotov, N. A. *Nanoparticle assemblies and superstructures*. (Dekker/CRC Press, 2006).

316. Wu, Z. *et al.* Self-Assembly of Nanoclusters into Mono-, Few-, and Multilayered Sheets via Dipole-Induced Asymmetric van der Waals Attraction. *ACS Nano* **9**, 6315–23 (2015).

317. Hirai, K. *et al.* Coordination Assembly of Discoid Nanoparticles. *Angew. Chemie Int. Ed.* **54**, 8966–8970 (2015).

318. Lidmar, J., Mirny, L. & Nelson, D. R. Virus shapes and buckling transitions in spherical shells. *Phys. Rev. E. Stat. Nonlin. Soft Matter Phys.* **68**, 051910 (2003).

319. Boschi, F. & De Sanctis, F. Overview of the optical properties of fluorescent nanoparticles for optical imaging. *Eur. J. Histochem.* **61**, 2830 (2017).

320. Alarcón, L. S. *et al.* Adsorption and thermal stability of 1,4 benzenedimethanethiol on InP(110). *Surf. Sci.* **664**, 101–109 (2017).

321. E. Mateo Marti, †, Ch. Methivier, and & Pradier*, C. M. (S)-Cysteine Chemisorption on Cu(110), from the Gas or Liquid Phase: An FT-RAIRS and XPS Study. (2004). doi:10.1021/LA048952W

322. Ma, Z. & Han, H. One-step synthesis of cystine-coated gold nanoparticles in aqueous solution. *Colloids Surfaces A Physicochem. Eng. Asp.* **317**, 229–233 (2008).

323. Aryal, S. *et al.* Spectroscopic identification of SAu interaction in cysteine capped gold nanoparticles. *Spectrochim. Acta Part A Mol. Biomol. Spectrosc.* **63**, 160–163 (2006).

324. Riel, D. van & Wit, E. de. Next-generation vaccine platforms for COVID-19. *Nat. Mater. 2020 198* **19**, 810–812 (2020).

325. de Oliveira, J. F. A. *et al.* Defeating Bacterial Resistance and Preventing Mammalian Cells Toxicity Through Rational Design of Antibiotic-Functionalized Nanoparticles. *Sci. Rep.* **7**, 1326 (2017).

326. Zhang, N. N. *et al.* A Thermostable mRNA Vaccine against COVID-19. *Cell* **182**, 1271-1283.e16 (2020).

Apendix 1

Table 11 Genes with Significantly Altered Expression in Response to ZnO-NPs

Accession	Common Name	Fold Change	Gene products	Summary
Downregulated				
SACOL0200	uhpT	31.92	sugar phosphate antiporter	cytoplasmic membrane protein that functions as a monomer; catalyzes the active transport of sugar-phosphates such as glucose-6-phosphate with the obligatory exchange of inorganic phosphate or organophosphate
SACOL1173	hlY	11.68	alpha-hemolysin precursor	identified by similarity to SP:P09616; match to protein family HMM PF01117; match to protein family HMM TIGR01002
SACOL2022	hld	8.13	delta-hemolysin	Lyses erythrocytes and other mammalian cells
SACOL1083	purD	7.45	phosphoribosylamine--glycine ligase	catalyzes the formation of N(1)-(5-phospho-D-ribosyl)glycinamide from 5-phospho-D-ribosylamine and glycine in purine biosynthesis
SACOL1082	purH	6.30	bifunctional phosphoribosylaminoimidazole carboxamide formyltransferase/IMP cyclohydrolase	involved in de novo purine biosynthesis
SACOL2146		5.48	PTS system, mannitol-specific IIBC components	identified by match to protein family HMM PF02302; match to protein family HMM PF02378; match to protein family HMM TIGR00851
SACOL2443		5.22	hypothetical protein	
SACOL1081	purN	4.98	phosphoribosylglycinamide formyltransferase	identified by similarity to EGAD:16303; match to protein family HMM PF00551; match to protein family HMM TIGR00639
SACOL0095	spa	4.31	immunoglobulin G binding protein A precursor	identified by similarity to SP:P02976; match to protein family HMM PF00746; match to protein family HMM PF01476; match to protein family HMM PF02216; match to protein family HMM PF03373; match to protein family HMM PF04650; match to protein family HMM TIGR01167; match to protein family HMM TIGR01168
SACOL1080	purM	4.22	phosphoribosylaminoimidazole synthetase	catalyzes the formation of 1-(5-phosphoribosyl)-5-aminoimidazole from 2-(formamido)-N1-(5-phosphoribosyl)acetamidine and ATP in purine biosynthesis
SACOL0008	hutH	4.11	histidine ammonia-lyase	catalyzes the degradation of histidine to urocanate and ammmonia

SACOL0882		4.02	ABC transporter ATP-binding protein	identified by match to protein family HMM PF00005
SACOL2422	hlgB	4.01	gamma hemolysin, component B	identified by similarity to SP:P31715; match to protein family HMM PF01117; match to protein family HMM TIGR01002
SACOL2395	narG	3.97	respiratory nitrate reductase subunit alpha	identified by similarity to EGAD:30702; match to protein family HMM PF00384; match to protein family HMM PF01568; match to protein family HMM TIGR01580
SACOL2421	hlgC	3.82	gamma hemolysin, component C	identified by similarity to SP:P31716; match to protein family HMM PF01117; match to protein family HMM TIGR01002
SACOL1477	ilvA1	3.71	threonine dehydratase	catalyzes the formation of 2-oxobutanoate from L-threonine; catabolic
SACOL2396		3.67	uroporphyrinogen III methylase SirB	identified by similarity to GP:4433641; match to protein family HMM PF00590; match to protein family HMM TIGR01469
SACOL0704		3.55	iron compound ABC transporter ATP-binding protein	identified by similarity to EGAD:37683; match to protein family HMM PF00005
SACOL0883		3.55	ABC transporter permease	identified by match to protein family HMM PF00528
SACOL2044		3.48	acetolactate synthase 1 regulatory subunit	with IlvI catalyzes the formation of 2-acetolactate from pyruvate, this subunit subunit is required for full activity and valine sensitivity; also known as acetolactate synthase small
SACOL1658		3.29	hypothetical protein	
SACOL1478	ald1	3.22	alanine dehydrogenase	identified by match to protein family HMM PF01262; match to protein family HMM PF05222; match to protein family HMM TIGR00518
SACOL0690		3.13	ABC transporter ATP-binding protein	identified by match to protein family HMM PF00005
SACOL0874		3.13	nitroreductase	identified by match to protein family HMM PF00881
SACOL2554		3.12	hypothetical protein	identified by match to protein family HMM PF04172
SACOL2024	agrD	3.08	accessory gene regulator protein D	identified by similarity to EGAD:18902; match to protein family HMM PF05931
SACOL2043	ilvB	3.04	acetolactate synthase large subunit	identified by match to protein family HMM PF00205; match to protein family HMM PF02776; match to protein family HMM TIGR00118
SACOL0768		3.04	hypothetical protein	identified by similarity to GB:AAO04078.1
SACOL0413		3.04	ribosomal-protein-serine acetyltransferase	identified by match to protein family HMM PF00583
SACOL1923		3.03	hypothetical protein	identified by match to protein family HMM PF06081
SACOL0404		3.02	MarR family transcriptional regulator	identified by match to protein family HMM PF01047
SACOL2716		3.02	hypothetical protein	identified by match to protein family HMM PF03551
SACOL1114		3.01	manganese transport protein MntH	identified by match to protein family HMM PF01566; match to protein family HMM TIGR01197

SACOL0994	oppF	3.00	oligopeptide ABC transporter ATP-binding protein	identified by match to protein family HMM PF00005
SACOL2258	sarV	2.95	hypothetical protein	identified by similarity to OMNI:SA2258; match to protein family HMM TIGR01889
SACOL2394	narH	2.95	respiratory nitrate reductase subunit beta	identified by similarity to EGAD:16236; similarity to EGAD:30703; match to protein family HMM TIGR01660
SACOL1428	lysC	2.91	aspartate kinase	catalyzes the formation of 4-phospho-L-aspartate from L-aspartate and ATP, in Bacillus, lysine sensitive; regulated by response to starvation.
SACOL2006		2.89	Aerolysin/leukocidin family protein	identified by match to protein family HMM PF01117
SACOL2734		2.89	hypothetical protein	identified by similarity to GB:AAO06055.1
SACOL1476		2.87	amino acid permease	identified by match to protein family HMM PF00324
SACOL2630		2.86	hypothetical protein	identified by similarity to GP:4574119
SACOL1475		2.86	drug transporter	identified by match to protein family HMM PF07690
SACOL0445		2.84	hypothetical protein	identified by similarity to GB:AAO06012.1
SACOL1741	icd	2.84	isocitrate dehydrogenase	Converts isocitrate to alpha ketoglutarate
SACOL2020		2.83	hypothetical protein	identified by match to protein family HMM PF00881
SACOL1429	asd	2.83	aspartate semialdehyde dehydrogenase	identified by similarity to EGAD:15165; match to protein family HMM PF01118; match to protein family HMM PF02774; match to protein family HMM TIGR01296
SACOL2042	ilvD	2.81	dihydroxy-acid dehydratase	catalyzes the dehydration of 2,3-dihydroxy-3-methylbutanoate to 3-methyl-2-oxobutanoate in valine and isoleucine biosynthesis
SACOL0884		2.75	ABC transporter substrate-binding protein	identified by match to protein family HMM PF03180
SACOL2023	agrB	2.73	accessory gene regulator protein B	identified by match to protein family HMM PF04647
SACOL2398	nirB	2.73	nitrite reductase [NAD(P)H], large subunit	identified by similarity to EGAD:30822; match to protein family HMM PF00070; match to protein family HMM PF01077; match to protein family HMM PF03460; match to protein family HMM PF04324
SACOL0152		2.71	heme-degrading monooxygenase IsdI	iron regulated; catalyzes the release of heme from hemoglobin allowing bacterial pathogens to use the host heme as an iron source
SACOL1846		2.71	hypothetical protein	
SACOL0119		2.71	cell wall surface anchor family protein	identified by match to protein family HMM PF00746; match to protein family HMM TIGR01167
SACOL1784	acuA	2.70	acetoin utilization protein AcuA	identified by similarity to EGAD:23882
SACOL2025	argC2	2.69	accessory gene regulator protein C	identified by match to protein family HMM PF02518
SACOL2393	narJ	2.68	respiratory nitrate reductase subunit delta	identified by match to protein family HMM PF02613; match to protein family HMM TIGR00684

SACOL2694	geh	2.66	lipase	identified by similarity to SP:Q02510; similarity to EGAD:17843; match to protein family HMM PF04650; match to protein family HMM TIGR01168
SACOL0707		2.63	dihydroxyacetone kinase subunit DhaK	with DhaL and DhaM forms dihydroxyacetone kinase, which is responsible for phosphorylating dihydroxyacetone; DhaK is the dihydroxyacetone binding subunit of the dihydroxyacetone kinase
SACOL1546	proC	2.63	pyrroline-5-carboxylate reductase	identified by similarity to EGAD:45894; match to protein family HMM PF01089; match to protein family HMM TIGR00112
SACOL0907	seb	2.62	enterotoxin B	identified by similarity to GP:3212819; match to protein family HMM PF01123; match to protein family HMM PF02876
SACOL0153		2.62	hypothetical protein	identified by match to protein family HMM PF04304
SACOL2386		2.59	nitrite extrusion protein	identified by similarity to EGAD:30454; match to protein family HMM PF07690
SACOL0995		2.58	oligopeptide ABC transporter oligopeptide-binding protein	identified by match to protein family HMM PF00496
SACOL1182	arcC1	2.58	carbamate kinase	catalyzes the reversible synthesis of carbamate and ATP from carbamoyl phosphate and ADP
SACOL0991	oppB	2.57	oligopeptide ABC transporter permease	identified by match to protein family HMM PF00528
SACOL2392	narI	2.56	respiratory nitrate reductase subunit gamma	identified by similarity to EGAD:30704; match to protein family HMM PF02665; match to protein family HMM TIGR00351
SACOL2628	betB	2.56	betaine aldehyde dehydrogenase	identified by similarity to EGAD:97843; match to protein family HMM PF00171; match to protein family HMM TIGR01804
SACOL2147		2.55	BglG family transcriptional antiterminator	identified by match to protein family HMM PF00874
SACOL2399	nirR	2.53	transcriptional regulator NirR	identified by similarity to GP:4433637
SACOL2145	glmS	2.52	glucosamine--fructose-6-phosphate aminotransferase	Catalyzes the first step in hexosamine metabolism, converting fructose-6P into glucosamine-6P using glutamine as a nitrogen source
SACOL1847		2.52	hypothetical protein	identified by similarity to EGAD:108623
SACOL2391		2.51	hypothetical protein	identified by similarity to GB:AAO05612.1
SACOL2531		2.51	MarR family transcriptional regulator	identified by match to protein family HMM PF01047
SACOL1711		2.50	DNA-3-methyladenine glycosylase	identified by similarity to EGAD:6433; match to protein family HMM PF03352
SACOL2521		2.49	transporter	identified by match to protein family HMM PF07690
SACOL2045	ilvC	2.49	ketol-acid reductoisomerase	catalyzes the formation of (R)-2,3-dihydroxy-3-methylbutanoate from (S)-2-hydroxy-2-methyl-3-oxobutanoate in valine and isoleucine biosynthesis
SACOL2397	nirD	2.48	nitrite reductase [NAD(P)H], small subunit	identified by similarity to EGAD:30823; match to protein family HMM PF00355

SACOL0993	oppD	2.47	oligopeptide ABC transporter ATP-binding protein	identified by match to protein family HMM PF00005; match to protein family HMM TIGR01727
SACOL2026	agrA	2.46	accessory gene regulator protein A	identified by similarity to EGAD:16137; match to protein family HMM PF00072; match to protein family HMM PF04397
SACOL0402		2.46	PTS system, IIA component	identified by match to protein family HMM PF00359
SACOL0205	pflA	2.45	pyruvate formate-lyase-activating enzyme	identified by similarity to SP:O68575; match to protein family HMM PF04055
SACOL2651		2.45	tributyrin esterase EstA	identified by similarity to GP:7453516; similarity to OMNI:NTL01LL1811; match to protein family HMM PF00756
SACOL2661		2.43	hypothetical protein	identified by similarity to GB:AAO05863.1
SACOL1432	dapD	2.43	2,3,4,5-tetrahydropyridine-2,6-dicarboxylate N-succinyltransferase	identified by similarity to EGAD:165602; match to protein family HMM PF00132
SACOL2046	leuA	2.42	2-isopropylmalate synthase	catalyzes the formation of 2-isopropylmalate from acetyl-CoA and 2-oxoisovalerate in leucine biosynthesis
SACOL1431	dapB	2.42	dihydrodipicolinate reductase	catalyzes the reduction of 2,3-dihydrodipicolinate to 2,3,4,5-tetrahydrodipicolinate in lysine and diaminopimelate biosynthesis
SACOL2199	budB	2.42	acetolactate synthase	catalyzes the formation of 2-acetolactate from pyruvate in stationary phase
SACOL0718		2.42	ABC transporter ATP-binding protein	identified by similarity to EGAD:108398; match to protein family HMM PF00005
SACOL1596	aroK	2.42	shikimate kinase	identified by similarity to EGAD:29699; match to protein family HMM PF01202
SACOL1430	dapA	2.41	dihydrodipicolinate synthase	catalyzes the formation of dihydrodipicolinate from L-aspartate 4-semialdehyde and pyruvate in lysine and diaminopimelate biosynthesis
SACOL2047	leuB	2.41	3-isopropylmalate dehydrogenase	catalyzes the oxidation of 3-isopropylmalate to 3-carboxy-4-methyl-2-oxopentanoate in leucine biosynthesis
SACOL0821		2.39	HD domain-containing protein	
SACOL2632	cudT	2.38	BCCT family osmoprotectant transporter	identified by similarity to EGAD:45763; match to protein family HMM PF02028; match to protein family HMM TIGR00842
SACOL2389		2.37	transcriptional regulatory protein DegU	identified by match to protein family HMM PF00072; match to protein family HMM PF00196
SACOL0516		2.37	PTS system, IIBC components	identified by match to protein family HMM PF00367; match to protein family HMM PF02378; match to protein family HMM TIGR00826; match to protein family HMM TIGR01992
SACOL2333		2.34	hypothetical protein	identified by match to protein family HMM PF02694
SACOL1350		2.34	hypothetical protein	identified by similarity to GB:AAO04593.1
SACOL1043		2.33	glycosyl transferase, group 1 family protein	identified by match to protein family HMM PF00534
SACOL2627	betA	2.33	choline dehydrogenase	catalyzes the oxidation of choline to betaine aldehyde and betain aldehyde to glycine betaine

SACOL2049	leuD	2.32	isopropylmalate isomerase small subunit	catalyzes the isomerization between 2-isopropylmalate and 3-isopropylmalate in leucine biosynthesis; forms a heterodimer of LeuC/D
SACOL2050	ilvA2	2.31	threonine dehydratase	catalyzes the formation of 2-oxobutanoate from L-threonine; biosynthetic
SACOL2390		2.30	sensory box histidine kinase	identified by match to protein family HMM PF02518
SACOL2458		2.30	amino acid permease	identified by match to protein family HMM PF00324
SACOL2167		2.28	iron compound ABC transporter iron compound-binding protein	identified by match to protein family HMM PF01497
SACOL1397	msrA	2.28	methionine sulfoxide reductase A	this stereospecific enzymes reduces the S isomer of methionine sulfoxide while MsrB reduces the R form; provides protection against oxidative stress
SACOL2535		2.27	D-lactate dehydrogenase	catalyzes the formation of pyruvate from lactate
SACOL2676		2.27	LPXTG cell wall surface anchor family protein	identified by match to protein family HMM PF00746; match to protein family HMM PF05345; match to protein family HMM TIGR01167
SACOL2565		2.26	FeoA domain-containing protein	identified by match to protein family HMM PF04023
SACOL2519		2.25	hypothetical protein	
SACOL2322		2.23	M20/M25/M40 family peptidase	identified by match to protein family HMM PF01546; match to protein family HMM PF07687; match to protein family HMM TIGR01891
SACOL0204	pflB	2.22	formate acetyltransferase	identified by similarity to SP:P09373; match to protein family HMM PF01228; match to protein family HMM PF02901; match to protein family HMM TIGR01255
SACOL0992	oppC	2.22	oligopeptide ABC transporter permease	identified by match to protein family HMM PF00528
SACOL2660	isaB	2.22	immunodominant antigen B	
SACOL1362	hom	2.21	homoserine dehydrogenase	catalyzes the formation of L-aspartate 4-semialdehyde from L-homoserine
SACOL1060		2.19	MarR family transcriptional regulator	identified by match to protein family HMM PF01047
SACOL1171		2.19	hypothetical protein	
SACOL0796		2.18	iron compound ABC transporter permease	identified by similarity to EGAD:37681; match to protein family HMM PF01032
SACOL0708		2.17	DAK2 domain-containing protein	identified by similarity to OMNI:NTL01BH3400; match to protein family HMM PF02734; match to protein family HMM TIGR02365
SACOL1816	putA	2.17	proline dehydrogenase	identified by match to protein family HMM PF01619
SACOL0007		2.17	hypothetical protein	identified by similarity to EGAD:21908; match to protein family HMM PF01256
SACOL2550		2.16	hypothetical protein	
SACOL1363	thrC	2.16	threonine synthase	catalyzes the formation of L-threonine from O-phospho-L-homoserine
SACOL0871		2.15	hypothetical protein	

SACOL0458	xpt	2.15	xanthine phosphoribosyltransferase	Catalyzes the transfer of the phosphoribosyl moiety from 5-phospho--D-ribosyl-1-pyrophosphate (PRib-PP) to the 6-oxo-guanine and -xanthine
SACOL2618	ldh2	2.13	L-lactate dehydrogenase	identified by similarity to EGAD:16887; match to protein family HMM PF00056; match to protein family HMM PF02866; match to protein family HMM TIGR01771
SACOL0176		2.13	hypothetical protein	identified by match to protein family HMM PF05913
SACOL2304		2.13	hypothetical protein	
SACOL2451		2.13	amino acid ABC transporter amino acid-binding protein	identified by match to protein family HMM PF04069
SACOL2048	leuC	2.13	isopropylmalate isomerase large subunit	dehydratase component, catalyzes the isomerization between 2-isopropylmalate and 3-isopropylmalate
SACOL1556		2.12	hypothetical protein	
SACOL1659		2.12	hypothetical protein	identified by similarity to GP:10174438; similarity to OMNI:NTL01BH1823
SACOL2569		2.12	1-pyrroline-5-carboxylate dehydrogenase	catalyzes the conversion of 1-proline-5-carboxylate dehydrogenase to L-glutamate
SACOL0660	adhP	2.11	alcohol dehydrogenase	similar to zinc-dependent eukaryotic ADH enzymes and distinct from fermentative ADHs
SACOL0009	serS	2.11	seryl-tRNA synthetase	catalyzes a two-step reaction, first charging a serine molecule by linking its carboxyl group to the alpha-phosphate of ATP, followed by transfer of the aminoacyl-adenylate to its tRNA
SACOL2453		2.10	amino acid ABC transporter ATP-binding protein	identified by match to protein family HMM PF00005; match to protein family HMM PF00571; match to protein family HMM TIGR01186
SACOL0599		2.09	hypothetical protein	identified by similarity to OMNI:NT01TA1215
SACOL2125		2.08	M20/M25/M40 family peptidase	identified by match to protein family HMM PF01546; match to protein family HMM PF07687; match to protein family HMM TIGR01891
SACOL1783	acs	2.07	acetyl-CoA synthetase	Acs; catalyzes the conversion of acetate and CoA to acetyl-CoA
SACOL1742	gltA	2.07	citrate synthase	catalyzes the formation of citrate from acetyl-CoA and oxaloacetate
SACOL0703		2.07	hypothetical protein	identified by similarity to EGAD:108622; match to protein family HMM PF02588
SACOL0111		2.06	acetoin reductase	identified by match to protein family HMM PF00106
SACOL1175		2.06	hypothetical protein	
SACOL1020		2.05	hypothetical protein	similar to 2'-5' RNA ligase
SACOL2324	hutU	2.04	urocanate hydratase	catalyzes the formation of 4-imidazolone-5-propanoate from urocanate during histidine metabolism
SACOL0689		2.04	ABC transporter permease	identified by match to protein family HMM PF00950
SACOL2319		2.03	Na+/H+ antiporter family protein	identified by similarity to OMNI:VCA0193; match to protein family HMM PF03553
SACOL1366		2.03	hypothetical protein	identified by similarity to GB:AAO04611.1

SACOL0934		2.03	hypothetical protein	identified by similarity to GB:AAO04220.1
SACOL0700	abcA	2.02	ABC transporter ATP-binding protein/permease	identified by match to protein family HMM PF00005; match to protein family HMM PF00664
SACOL2011		2.01	sodium transport family protein	identified by match to protein family HMM PF02386
SACOL2516	gntR	2.01	gluconate operon transcriptional repressor	identified by similarity to EGAD:17516; match to protein family HMM PF00392
SACOL2620		2.00	4-aminobutyrate aminotransferase	catalyzes the formation of succinate semialdehyde and glutamate from 4-aminobutanoate and 2-oxoglutarate
SACOL0688		1.98	ABC transporter substrate-binding protein	identified by match to protein family HMM PF01297
SACOL2448		1.98	2-dehydropantoate 2-reductase	ketopantoate reductase; catalyzes the NADPH reduction of ketopantoate to pantoate; functions in pantothenate (vitamin B5) biosynthesis
SACOL2718		1.97	anion transporter family protein	identified by match to protein family HMM PF00939; match to protein family HMM TIGR00785
SACOL2059		1.97	hypothetical protein	
SACOL0314		1.96	hypothetical protein	identified by similarity to EGAD:15022; match to protein family HMM PF01380
SACOL0494	nuoF	1.95	NADH dehydrogenase subunit 5	Catalyzes the transfer of electrons from NADH to ubiquinone
SACOL1151		1.95	hypothetical protein	identified by similarity to EGAD:107725; match to protein family HMM PF05164
SACOL0609	sdrD	1.95	sdrD protein	identified by similarity to GP:3550594; match to protein family HMM PF00746; match to protein family HMM PF02412; match to protein family HMM PF04650; match to protein family HMM PF05738; match to protein family HMM TIGR01167; match to protein family HMM TIGR01168
SACOL1981		1.95	isochorismatase	identified by match to protein family HMM PF00857
SACOL0245	lytS	1.94	sensor histidine kinase LytS	identified by similarity to EGAD:42940; match to protein family HMM PF02518; match to protein family HMM PF06580; match to protein family HMM PF07694
SACOL0709		1.94	phosphotransferase mannnose-specific family component IIA	identified by similarity to OMNI:NTL01LL0257; match to protein family HMM PF03610; match to protein family HMM TIGR02364
SACOL2407		1.93	lipoprotein	identified by similarity to EGAD:109043; match to protein family HMM PF01323
SACOL0027		1.93	hypothetical protein	
SACOL1181	arcB1	1.92	ornithine carbamoyltransferase	catalyzes the formation of L-citrulline from carbamoyl phosphate and L-ornithine in arginine biosynthesis and degradation
SACOL1660		1.91	LamB/YcsF family protein	identified by match to protein family HMM PF03746
SACOL2552		1.91	PTS system, IIABC components	identified by match to protein family HMM PF00358; match to protein family HMM PF00367; match to protein family HMM PF02378; match to protein family HMM TIGR00826; match to protein family HMM

				TIGR00830; match to protein family HMM TIGR02002
SACOL0961	gluD	1.91	glutamate dehydrogenase	identified by match to protein family HMM PF00208; match to protein family HMM PF02812
SACOL0546	pth	1.91	peptidyl-tRNA hydrolase	Enables the recycling of peptidyl-tRNAs produced at termination of translation
SACOL0960	rocD	1.91	ornithine--oxo-acid transaminase	identified by similarity to EGAD:21835; match to protein family HMM PF00202; match to protein family HMM TIGR01885
SACOL0208		1.90	hypothetical protein	
SACOL1033		1.90	hypothetical protein	
SACOL0766	saeR	1.90	DNA-binding response regulator SaeR	identified by similarity to GP:5726300; match to protein family HMM PF00072; match to protein family HMM PF00486
SACOL2021		1.90	carbon-nitrogen family hydrolase	identified by match to protein family HMM PF00795
SACOL1451	arlR	1.90	DNA-binding response regulator ArlR	identified by similarity to GP:9230552; similarity to OMNI:SA1451; match to protein family HMM PF00072; match to protein family HMM PF00486
SACOL0459	pbuX	1.89	xanthine permease	identified by similarity to EGAD:30678; match to protein family HMM PF00860; match to protein family HMM TIGR00801
SACOL1908	fumC	1.89	fumarate hydratase	class II family (does not require metal); tetrameric enzyme; fumarase C; reversibly converts (S)-malate to fumarate and water; functions in the TCA cycle
SACOL0403		1.89	BglG family transcriptional antiterminator	identified by match to protein family HMM PF00359; match to protein family HMM PF00874
SACOL0730		1.87	hypothetical protein	identified by similarity to EGAD:173390; match to protein family HMM PF04167
SACOL1113		1.86	hypothetical protein	
SACOL2154	rocF	1.86	arginase	identified by similarity to EGAD:14086; match to protein family HMM PF00491; match to protein family HMM TIGR01229
SACOL0012		1.85	homoserine O-acetyltransferase	identified by match to protein family HMM PF00561
SACOL2198	budA1	1.84	alpha-acetolactate decarboxylase	identified by similarity to EGAD:17067; match to protein family HMM PF03306; match to protein family HMM TIGR01252
SACOL1351	cls1	1.84	cardiolipin synthetase	identified by similarity to SP:O66043; match to protein family HMM PF00614
SACOL2331		1.84	hypothetical protein	
SACOL1988		1.84	hypothetical protein	identified by match to protein family HMM PF03417
SACOL0456		1.84	hypothetical protein	identified by similarity to GB:AAO05995.1
SACOL1349		1.83	hypothetical protein	identified by similarity to OMNI:PG0474
SACOL0460	guaB	1.83	inosine-5'-monophosphate dehydrogenase	identified by similarity to SP:P21879; match to protein family HMM PF00478; match to protein family HMM PF00571; match to protein family HMM TIGR01302

SACOL2188	lacR	1.83	lactose phosphotransferase system repressor	identified by similarity to SP:P16644; match to protein family HMM PF00455
SACOL1147		1.83	RNA methyltransferase	identified by match to protein family HMM PF00588
SACOL0301		1.82	formate/nitrite transporter family protein	identified by match to protein family HMM PF01226
SACOL0096	sarS	1.82	accessory regulator S	identified by similarity to OMNI:SA0096; match to protein family HMM TIGR01889
SACOL0750		1.82	anion transporter family protein	identified by match to protein family HMM PF00939; match to protein family HMM TIGR00785
SACOL0215		1.82	propionate CoA-transferase	identified by match to protein family HMM PF01144
SACOL0320		1.82	hypothetical protein	
SACOL1324		1.81	hfq protein	identified by similarity to EGAD:12661; match to protein family HMM PF01423
SACOL2615	panB	1.81	3-methyl-2-oxobutanoate hydroxymethyltransferase	catalyzes the formation of tetrahydrofolate and 2-dehydropantoate from 5,10-methylenetetrahydrofolate and 3-methyl-2-oxobutanoate
SACOL2086		1.81	TenA family transcription regulator	identified by similarity to EGAD:24145; match to protein family HMM PF03070
SACOL1450	arlS	1.81	sensor histidine kinase ArlS	identified by similarity to GP:9230553; similarity to OMNI:SA1450; match to protein family HMM PF00512; match to protein family HMM PF00672; match to protein family HMM PF02518
SACOL1308		1.81	pyruvate ferredoxin oxidoreductase subunit alpha	identified by match to protein family HMM PF01558; match to protein family HMM PF01855
SACOL2070	kdpD	1.80	sensor histidine kinase KdpD	identified by similarity to EGAD:149594; match to protein family HMM PF00512; match to protein family HMM PF02518; match to protein family HMM PF02702
SACOL2272	modA	1.80	molybdenum ABC transporter molybdenum-binding protein ModA	identified by similarity to EGAD:13554; match to protein family HMM PF01547; match to protein family HMM TIGR01256
SACOL2505		1.80	cell wall surface anchor family protein	identified by match to protein family HMM PF00746; match to protein family HMM PF04650; match to protein family HMM PF07501; match to protein family HMM TIGR01167; match to protein family HMM TIGR01168
SACOL0190	acpD	1.80	azoreductase	FMN-dependent; requires NADH; catalyzes the cleavage of azo bond in aromatic azo compounds
SACOL2514	gntP	1.79	gluconate transporter, permease	identified by similarity to EGAD:19179; match to protein family HMM PF02447; match to protein family HMM TIGR00791
SACOL0466		1.79	hypothetical protein	identified by match to protein family HMM PF06993
SACOL2452		1.79	amino acid ABC transporter permease	identified by match to protein family HMM PF00528
SACOL1434		1.79	alanine racemase	identified by match to protein family HMM PF00842; match to protein family HMM PF01168

SACOL2437	bcr	1.78	bicyclomycin resistance protein	identified by similarity to SP:P28246; match to protein family HMM PF00083; match to protein family HMM PF07690; match to protein family HMM TIGR00710
SACOL2585		1.77	hypothetical protein	
SACOL1338		1.77	hypothetical protein	
SACOL1661		1.76	acetyl-CoA carboxylase, biotin carboxylase	identified by similarity to SP:P49787; match to protein family HMM PF00289; match to protein family HMM PF02785; match to protein family HMM PF02786
SACOL0244	scdA	1.76	cell wall biosynthesis protein ScdA	involved in peptidoglycan cross-linking
SACOL1323	miaA	1.75	tRNA delta(2)-isopentenylpyrophosphate transferase	IPP transferase; isopentenyltransferase; involved in tRNA modification; in Escherichia coli this enzyme catalyzes the addition of a delta2-isopentenyl group from dimethylallyl diphosphate to the N6-nitrogen of adenosine adjacent to the anticodon of tRNA species that read codons starting with uracil; further tRNA modifications may occur; mutations in miaA result in defects in translation efficiency and fidelity
SACOL1165		1.75	hypothetical protein	
SACOL1321	glpD	1.75	aerobic glycerol-3-phosphate dehydrogenase	identified by similarity to EGAD:18115; match to protein family HMM PF01266
SACOL1850		1.75	hypothetical protein	
SACOL2449		1.75	drug transporter	identified by match to protein family HMM PF00083; match to protein family HMM PF07690
SACOL1010	relA1	1.74	GTP pyrophosphokinase	identified by match to protein family HMM PF04607
SACOL2587		1.74	hypothetical protein	
SACOL0724		1.74	hypothetical protein	identified by similarity to GB:AAO04031.1
SACOL1159	sdhA	1.74	succinate dehydrogenase flavoprotein subunit	part of four member succinate dehydrogenase enzyme complex that forms a trimeric complex (trimer of tetramers); SdhA/B are the catalytic subcomplex and can exhibit succinate dehydrogenase activity in the absence of SdhC/D which are the membrane components and form cytochrome b556; SdhC binds ubiquinone; oxidizes succinate to fumarate while reducing ubiquinone to ubiquinol
SACOL1072	folD	1.74	bifunctional 5,10-methylene-tetrahydrofolate dehydrogenase/ 5,10-methylene-tetrahydrofolate cyclohydrolase	catalyzes the formation of 5,10-methenyltetrahydrofolate from 5,10-methylenetetrahydrofolate and subsequent formation of 10-formyltetrahydrofolate from 5,10-methenyltetrahydrofolate
SACOL0506		1.74	ABC transporter substrate-binding protein	identified by match to protein family HMM PF03180
SACOL2294		1.73	hypothetical protein	
SACOL0959		1.72	Oye family NADH-dependent flavin oxidoreductase	identified by match to protein family HMM PF00724
SACOL2345		1.72	esterase	identified by similarity to EGAD:16024

SACOL1368	kataA	1.72	catalase	identified by similarity to EGAD:29401; match to protein family HMM PF00199
SACOL2133		1.71	hypothetical protein	identified by similarity to GB:AAO05339.1
SACOL1001	trpS	1.71	tryptophanyl-tRNA synthetase	catalyzes a two-step reaction, first charging a tryptophan molecule by linking its carboxyl group to the alpha-phosphate of ATP, followed by transfer of the aminoacyl-adenylate to its tRNA
SACOL1776		1.71	1-acyl-sn-glycerol-3-phosphate acyltransferase	identified by match to protein family HMM PF01553; match to protein family HMM TIGR00530
SACOL2019		1.70	sdrH protein	identified by similarity to GP:8101009
SACOL0667		1.70	HAD superfamily hydrolase	identified by match to protein family HMM PF00702; match to protein family HMM TIGR01509; match to protein family HMM TIGR01549
SACOL2323	hutI	1.70	imidazolonepropionase	catalyzing the hydrolysis of 4-imidazolone-5-propionate to N-formimidoyl-L-glutamate, the third step in the histidine degradation pathway
SACOL1812	rot	1.70	repressor of toxins	identified by similarity to GP:6651452; match to protein family HMM TIGR01889
SACOL2483		1.70	transporter	identified by match to protein family HMM PF03806
SACOL2534	frp	1.69	NAD(P)H-flavin oxidoreductase	identified by match to protein family HMM PF00881
SACOL0920		1.69	hypothetical protein	
SACOL0135		1.69	bifunctional acetaldehyde-CoA/alcohol dehydrogenase	identified by similarity to SP:P17547; match to protein family HMM PF00465
SACOL0271		1.69	hypothetical protein	identified by match to protein family HMM PF06013
SACOL1009		1.69	hypothetical protein	identified by similarity to OMNI:NTL01BH2853
SACOL2441		1.69	amino acid permease	identified by match to protein family HMM PF00324
SACOL1785	acuC	1.69	acetoin utilization protein AcuC	identified by similarity to EGAD:19784; match to protein family HMM PF00850
SACOL2332	galM	1.68	aldose 1-epimerase	identified by match to protein family HMM PF01263
SACOL0312	nanA	1.68	N-acetylneuraminate lyase	catalyzes the formation of pyruvate and N-acetylmannosamine from N-acetylneuraminic acid
SACOL1222	rpoZ	1.68	DNA-directed RNA polymerase subunit omega	Promotes RNA polymerase assembly; latches the N- and C-terminal regions of the beta' subunit thereby facilitating its interaction with the beta and alpha subunits
SACOL1167		1.68	hypothetical protein	
SACOL1158	sdhC	1.68	succinate dehydrogenase, cytochrome b558 subunit	identified by similarity to EGAD:20778; match to protein family HMM TIGR02046
SACOL0797		1.68	iron compound ABC transporter permease	identified by similarity to EGAD:37682; match to protein family HMM PF01032
SACOL2715		1.68	hypothetical protein	
SACOL0643		1.67	hypothetical protein	identified by similarity to GP:11230708
SACOL1935		1.67	hypothetical protein	identified by similarity to GP:10173504; match to protein family HMM PF04055

SACOL2607		1.67	hypothetical protein	
SACOL2644		1.66	ABC transporter ATP-binding protein	identified by match to protein family HMM PF00005
SACOL1393		1.66	transcription antiterminator	identified by similarity to SP:P39805; match to protein family HMM PF00874; match to protein family HMM PF03123
SACOL2619		1.66	amino acid permease	identified by match to protein family HMM PF00324
SACOL2363		1.65	L-lactate permease	identified by similarity to EGAD:8633; match to protein family HMM PF02652; match to protein family HMM TIGR00795
SACOL2439		1.64	hypothetical protein	identified by similarity to GB:AAO05643.1
SACOL1848		1.64	hypothetical protein	
SACOL0179		1.64	RpiR family phosphosugar-binding transcriptional regulator	identified by match to protein family HMM PF01380; match to protein family HMM PF01418
SACOL2143		1.64	hypothetical protein	identified by similarity to GP:10174364; match to protein family HMM PF00702; match to protein family HMM TIGR00099; match to protein family HMM TIGR01484
SACOL1436		1.64	hypothetical protein	
SACOL0505		1.64	ABC transporter permease	identified by match to protein family HMM PF00528
SACOL0307	pfoR	1.64	perfringolysin O regulator protein	identified by similarity to EGAD:33437
SACOL2124		1.64	hypothetical protein	identified by similarity to GB:AAO05329.1
SACOL1322		1.63	alpha/beta fold family hydrolase	identified by match to protein family HMM PF00561
SACOL1041		1.63	hypothetical protein	
SACOL1891		1.63	RNAIII-activating protein TRAP	identified by similarity to OMNI:SA1891
SACOL0818	prfB	1.63	peptide chain release factor 2	recognizes the termination signals UGA and UAA during protein translation a specificity which is dependent on amino acid residues residing in loops of the L-shaped tRNA-like molecule of RF2; in some organisms control of PrfB protein levels is maintained through a +1 ribosomal frameshifting mechanism; this protein is similar to release factor 1
SACOL1804		1.63	polysaccharide biosynthesis protein	identified by match to protein family HMM PF01943
SACOL1367		1.63	amino acid permease	identified by match to protein family HMM PF00324
SACOL0788		1.63	proton-dependent oligopeptide transporter family protein	identified by match to protein family HMM PF00854; match to protein family HMM PF07690; match to protein family HMM TIGR00924
SACOL1591		1.63	lipoate-protein ligase A family protein	identified by match to protein family HMM PF03099
SACOL2058		1.63	PemK family protein	identified by similarity to GP:10834755; match to protein family HMM PF02452
SACOL1161	murI	1.63	glutamate racemase	converts L-glutamate to D-glutamate, a component of peptidoglycan
SACOL0394		1.62	hypothetical protein	identified by match to protein family HMM PF00296

SACOL0600	ilvE	1.62	branched-chain amino acid aminotransferase	catalyzes the transamination of the branched-chain amino acids to their respective alpha-keto acids
SACOL2408		1.62	lipoprotein	identified by similarity to GB:AAO05629.1
SACOL2567		1.62	hypothetical protein	
SACOL1734	gapA2	1.62	glyceraldehyde 3-phosphate dehydrogenase 2	identified by similarity to EGAD:107759; match to protein family HMM PF00044; match to protein family HMM PF02800; match to protein family HMM TIGR01534
SACOL0720		1.62	ABC transporter permease	
SACOL0418		1.61	mttA/Hcf106 family protein	identified by match to protein family HMM PF02416; match to protein family HMM TIGR01411
SACOL1031		1.61	5' nucleotidase	identified by match to protein family HMM PF02872
SACOL1826		1.61	hypothetical protein	identified by similarity to GB:AAN32737.1
SACOL1396	fmtC	1.61	fmtC protein	identified by match to protein family HMM PF04329; match to protein family HMM PF04330; match to protein family HMM PF04331
SACOL0616	nagB	1.61	glucosamine-6-phosphate isomerase	identified by similarity to EGAD:107403; match to protein family HMM PF01182
SACOL0608	sdrC	1.61	sdrC protein	identified by similarity to GP:3550592; match to protein family HMM PF00746; match to protein family HMM PF04650; match to protein family HMM PF05738; match to protein family HMM TIGR01167; match to protein family HMM TIGR01168
SACOL0668		1.61	alpha/beta fold family hydrolase	identified by match to protein family HMM PF00561
SACOL1878	epiA	1.61	lantibiotic epidermin precursor EpiA	identified by similarity to EGAD:6281; match to protein family HMM PF02052
SACOL0281		1.61	hypothetical protein	
SACOL1412		1.61	hydrolase-like protein	identified by match to protein family HMM TIGR00099; match to protein family HMM TIGR01484
SACOL1772		1.61	class V aminotransferase	identified by match to protein family HMM PF00266
SACOL0513	gltC	1.60	transcriptional regulatory protein GltC	identified by similarity to EGAD:6257; match to protein family HMM PF00126
SACOL2064		1.60	hypothetical protein	
SACOL2338		1.60	hypothetical protein	
SACOL0319		1.60	hypothetical protein	
SACOL1539		1.60	hypothetical protein	identified by similarity to EGAD:12647; match to protein family HMM PF03745
SACOL0658		1.59	HD domain-containing protein	identified by match to protein family HMM PF01966
SACOL1662		1.59	acetyl-CoA carboxylase, biotin carboxyl carrier protein	identified by similarity to SP:P49786; match to protein family HMM PF00364
SACOL0171	brnQ1	1.59	branched-chain amino acid transport system II carrier protein	identified by match to protein family HMM PF05525; match to protein family HMM TIGR00796
SACOL2369		1.59	pyridine nucleotide-disulfide oxidoreductase	identified by match to protein family HMM PF00070

SACOL0072		1.59	hypothetical protein	identified by match to protein family HMM PF00126; match to protein family HMM PF03466
SACOL0632		1.59	hypothetical protein	identified by match to protein family HMM PF06738
SACOL1221	gmk	1.59	guanylate kinase	Essential for recycling GMP and indirectly, cGMP
SACOL0166		1.59	hypothetical protein	identified by match to protein family HMM PF07274
SACOL2541		1.59	acetyltransferase	identified by match to protein family HMM PF00583
SACOL2078		1.58	hypothetical protein	identified by match to protein family HMM PF02583
SACOL0161		1.58	hypothetical protein	
SACOL1842		1.58	hypothetical protein	identified by similarity to OMNI:NTL01BH2832; match to protein family HMM PF01809; match to protein family HMM TIGR00278
SACOL1797		1.58	metallo-beta-lactamase	identified by match to protein family HMM PF00753
SACOL2193		1.58	MerR family transcriptional regulator	identified by match to protein family HMM PF00376
SACOL2502		1.58	hypothetical protein	
SACOL1992		1.57	hypothetical protein	identified by similarity to GB:BAC14289.1
SACOL1304	recA	1.57	recombinase A	catalyzes the hydrolysis of ATP in the presence of single-stranded DNA, the ATP-dependent uptake of single-stranded DNA by duplex DNA, and the ATP-dependent hybridization of homologous single-stranded DNAs
SACOL0566	nupC	1.57	nucleoside permease NupC	identified by similarity to EGAD:6216; match to protein family HMM PF01773; match to protein family HMM PF07662; match to protein family HMM PF07670
SACOL1042		1.57	hypothetical protein	
SACOL2527		1.57	fructose-1,6-bisphosphatase	identified by similarity to EGAD:37656; match to protein family HMM PF06874
SACOL1364	thrB	1.57	homoserine kinase	catalyzes the formation of O-phospho-L-homoserine from L-homoserine in threonine biosynthesis from asparate
SACOL0514	gltB	1.57	glutamate synthase	identified by similarity to EGAD:109137; match to protein family HMM PF01493; match to protein family HMM PF01645; match to protein family HMM PF04897; match to protein family HMM PF04898
SACOL2442		1.57	Na+/H+ antiporter	identified by match to protein family HMM PF00999
SACOL1037		1.56	hypothetical protein	
SACOL1435	lysA	1.56	diaminopimelate decarboxylase	identified by similarity to SP:P23630; match to protein family HMM PF00278; match to protein family HMM PF02784; match to protein family HMM TIGR01048
SACOL0870		1.56	LysE/YggA family protein	identified by match to protein family HMM PF01810
SACOL2551		1.56	hypothetical protein	identified by similarity to OMNI:VC1938
SACOL2672		1.56	hypothetical protein	identified by similarity to GB:AAK17000.1

SACOL1374	lexA	1.56	LexA repressor	Represses a number of genes involved in the response to DNA damage
SACOL1164		1.56	fibrinogen binding-like protein	identified by similarity to EGAD:16905
SACOL2673		1.55	hypothetical protein	identified by similarity to GB:AAK16999.1
SACOL2142		1.55	SAP domain-containing protein	
SACOL2296		1.55	glycerate dehydrogenase	Catalyzes the reduction of hydroxypyruvate to form D-glycerate, using NADH as an electron donor
SACOL1689	relA2	1.55	GTP pyrophosphokinase	identified by similarity to EGAD:107375; match to protein family HMM PF01842; match to protein family HMM PF01966; match to protein family HMM PF02824; match to protein family HMM PF04607; match to protein family HMM TIGR00691
SACOL0611		1.55	glycosyl transferase, group 1 family protein	identified by match to protein family HMM PF00534
SACOL0317		1.55	lipase precursor, interruption-N	identified by similarity to EGAD:17843; match to protein family HMM PF04650; match to protein family HMM TIGR01168
SACOL2733		1.55	hypothetical protein	identified by similarity to GB:AAO06054.1
SACOL0455		1.54	hypothetical protein	identified by similarity to SP:Q8CQQ7
SACOL2549		1.54	hypothetical protein	identified by similarity to EGAD:16024
SACOL1645		1.54	comE operon protein 2	identified by similarity to EGAD:23914; match to protein family HMM PF00383
SACOL0756		1.54	ebsC protein	identified by similarity to SP:P36922; match to protein family HMM PF04073; match to protein family HMM TIGR00011
SACOL1058		1.54	aminotransferase, class I	identified by match to protein family HMM PF00155
SACOL2450		1.54	amino acid ABC transporter permease	identified by match to protein family HMM PF00528
SACOL1758	ald2	1.54	alanine dehydrogenase	identified by similarity to EGAD:15508; match to protein family HMM PF01262; match to protein family HMM PF05222; match to protein family HMM TIGR00518
SACOL0715		1.53	hypothetical protein	identified by similarity to GB:AAO04023.1
SACOL2639	cysJ	1.53	sulfite reductase (NADPH) flavoprotein alpha-component	identified by similarity to SP:P38038; match to protein family HMM PF00175; match to protein family HMM PF00258; match to protein family HMM PF00667; match to protein family HMM TIGR01931
SACOL2144		1.53	ABC transporter ATP-binding protein	identified by match to protein family HMM PF00005
SACOL0747		1.53	cobalamin synthesis protein/P47K family protein	identified by match to protein family HMM PF02492; match to protein family HMM PF07683
SACOL0666		1.53	iron compound ABC transporter permease	identified by match to protein family HMM PF01032
SACOL2658		1.53	ArgR family transcriptional regulator	identified by similarity to EGAD:18464; match to protein family HMM PF02863
SACOL2522		1.53	DedA family protein	identified by match to protein family HMM PF00597
SACOL1549	zwf	1.52	glucose-6-phosphate 1-dehydrogenase	catalyzes the formation of D-glucono-1,5-lactone 6-phosphate from D-glucose 6-phosphate

SACOL1448	sucB	1.52	dihydrolipoamide succinyltransferase	component of 2-oxoglutarate dehydrogenase complex; catalyzes the transfer of succinyl coenzyme A to form succinyl CoA as part of the conversion of 2-oxoglutarate to succinyl-CoA
SACOL2459	pnbA	1.52	para-nitrobenzyl esterase	identified by similarity to SP:P37967; match to protein family HMM PF00135
SACOL0180		1.52	type I restriction-modification enzyme, R subunit	identified by match to protein family HMM PF00270; match to protein family HMM PF04313; match to protein family HMM PF04851; match to protein family HMM TIGR00348
SACOL1339		1.52	hypothetical protein	
SACOL2491		1.51	hypothetical protein	identified by similarity to GB:AAO05679.1
SACOL2562	ogt	1.51	methylated-DNA--protein-cysteine methyltransferase	identified by similarity to EGAD:29038; match to protein family HMM PF01035; match to protein family HMM PF02870; match to protein family HMM TIGR00589
SACOL2400		1.51	acetyltransferase	identified by match to protein family HMM PF00583
SACOL1775		1.51	PTS system, IIBC components	identified by match to protein family HMM PF00367; match to protein family HMM PF02378; match to protein family HMM TIGR01998
SACOL2077		1.51	hypothetical protein	identified by similarity to GB:AAO05284.1; match to protein family HMM PF00403
SACOL1307		1.51	hypothetical protein	identified by similarity to EGAD:108574; match to protein family HMM PF00149; match to protein family HMM TIGR00282
SACOL0512		1.51	hypothetical protein	
SACOL0120		1.51	GntR family transcriptional regulator	identified by similarity to EGAD:37606; match to protein family HMM PF00392
SACOL2278		1.51	acyl-CoA dehydrogenase-like protein	identified by match to protein family HMM PF00441; match to protein family HMM PF02770
SACOL0612		1.51	glycosyl transferase, group 1 family protein	identified by match to protein family HMM PF00534
SACOL1883		1.51	hypothetical protein	
SACOL0751		1.50	deoxyribodipyrimidine photolyase	identified by match to protein family HMM PF03441
SACOL2063		1.50	hypothetical protein	identified by match to protein family HMM PF03703